UNIVERSIDAD COMPLUTENSE DE MADRID

FACULTAD DE CIENCIAS FÍSICAS

Departamento de Física Atómica, Molecular y Nuclear

TESIS DOCTORAL

Measurement of the inclusive production cross-section of W bosons in proton-proton collisions at √s=7 TeV in the CMS experiment at the LHC

MEMORIA PARA OPTAR AL GRADO DE DOCTOR

PRESENTADA POR

María Luisa Cepeda Hermida

Directoras:

María Isabel Josa Mutuberría
Begoña de la Cruz Martínez

Madrid, 2011

ISBN: 978-84-694-8486-9

Centro de Investigaciones Energéticas, Medioambientales y Tecnológicas

•

Departamento de Física Atómica, Molecular y Nuclear

Facultad de Ciencias Físicas

Universidad Complutense de Madrid

Measurement of the inclusive production cross-section of W bosons in proton-proton collisions at $\sqrt{s} = 7$ TeV in the CMS experiment at the LHC

Tesis presentada por

María Luisa Cepeda Hermida

para optar al grado de Doctor

(con mención europea)

Dirigida por:

Dra. María Isabel Josa Mutuberría

Dra. Begoña de la Cruz Martínez

Madrid, Marzo de 2011

Dra. María Isabel Mutuberría y **Dra. Begoña de la Cruz Martínez**, investigadoras titulares del Departamento de Investigación Básica del Centro de Investigaciones Energeéticas, MedioAmbientales y Tecnológicas (CIEMAT)

CERTIFICAN:

Que la presente tesis: "**Measurement of the Inclusive Production Cross-Section of W bosons in proton-proton collisions at $\sqrt{s} = 7$ TeV in the CMS experiment at the LHC**" ha sido realizada bajo nuestra dirección en el departamento de Física Atómica, Molecular y Nuclear de la Facultad de Físicas de la Universidad Complutense de Madrid, para optar al grado de Doctor en Ciencias Físicas.

Y para que así conste, en cumplimiento de la legislación vigente, presentamos ante la Univerisdad Complutense de Madrid esta memoria, firmando el presente certificado:

Madrid, 20 de Marzo de 2011

A mis padres y mi hermana

(y a la máquina de café,
auténtica autora de esta tesis)

Contents

Agradecimientos

Se acaban cuatro años de aventura buscando muones, dejando atrás mucho esfuerzo, y guardando el reconocimiento al esfuerzo de los demás para traerme hasta aqui. Cuatro años que se merecen muchos "gracias" para mucha gente:

Primero de todo, para mis maravillosas "jefas" Isabel y Begoña (aunque protesten por el título), por todo. Siempre disponibles para guiarme y ayudarme, siempre dispuestas a defenderme y tolerar mis locuras y mi carácter, y siempre tan cercanas que es cierto que el nombre "jefas" no les hace justicia.

Por supuesto, para Juan. Por tener siempre La Respuesta Perfecta a cualquier duda, por combinar conocimiento, esfuerzo y paciencia de ese modo tan suyo. Voy a intentar que no se me escape ningn "lo siento" en los agradecimientos, sólo por ésta vez.

Y para el CIEMAT al completo. Por haberme hecho sentir apoyada y protegida por todo el grupo (Marcos, Manuel, Cruz, Jesús, Mara, Silvia, Carlo, Pablo, Chema, Juan Pablo, Ignacio, Cristina...), especialmente por el equipo de CMS, desde el primer día. Muchísimas gracias a todos por hacer estos cuatro años tan agradables.

Tambien para Sridhara, Michael y Gautier como coordinadores del grupo de Física Electrodébil de CMS por la confianza puesta en mi; y para Jeff, Georgios y Luca, y todos aquellos otros con los que he tenido la suerte de trabajar en este periodo - y compartir la locura de los primeros datos y los primeros papers. Especialmente gracias a los estudiantes, Michele, Pieter, Phil y todos los demás. Por las noches delante de un ordenador "cazando" los primeros candidatos, y luchando contra reloj con luminosidades y eficiencias.

Para mis profesores, desde los primeros años de colegio hasta los últimos exámenes de la facultad, ya que les debo el seguir conservando el sueño de entender un poquito mejor el mundo.

Y cómo no, para las entregadas, por ser las mejores compañeras de despacho del mundo. Carmen por ser la más loca (aunque disimule); Cristina por siempre tener

una sonrisa a punto (y estar a punto ya de ser libre); María, la primera de todas, por toda la ayuda, y por esas largas conversaciones de vuelta a casa. Y para todos los demás, (Aurelio, Nacho, Dani, Javi, Julia, David, Antonio, Rafa, Jorge, Juanjo, Carlos) por contribuir a las discusiones y risas con o sin café que tanto voy a echar de menos.

Para mis amigos, porque lo que se merecen no son gracias sino un monumento por seguir estando a mi lado. Para los físicos (Flavio, Emilio, Mario, Nacho, Dani) por seguir considerandome la teórica después de cuatro años de tesis experimental. Para Rocío (miau) y para Edurne, por estar ahí siempre para traerme de vuelta al mundo real. Y a María, y a Marta, y a Virginia, y a Nat... y a todos los que no olvido, muchas gracias por ser vosotros.

Para mi segunda familia cernícola, porque no hace falta que os diga que sois los mejores - ya lo sabeís. Para Rebeca, por todas las conspiraciones y locuras, por la aspiradora incendiada... y por la argamasa. Para Lola y Paloma, por ser las únicas Lola y Paloma de Ginebra. Para Clara, porque creo que eres la única Clara del planeta. Y para todo el resto de la tropa: Alex, y Lara, y Pablo, y Ricci, y Alessio, y María, y Jorge...

Podría conseguir una lista de agradecimientos casi tan larga como la lista de autores de CMS.

Pero en algun lugar hay que poner punto y final.

Y mi último - o primer - gracias irá siempre para toda mi familia. Porque sin vosotros de esta tesis no existiría ni la portada; sabéis que estáis en cada una de estas páginas. Y no hay nada más que decir.

Chapter 1

Introduction

The Large Hadron Collider (LHC) entered into operation on November/December 2009 and delivered the first pp collisions at injection energy, at a center-of-mass energy of 900 GeV and soon after, at 2.36 TeV. Long time had passed since the first preparatory studies for the construction of a high energy, high luminosity hadron collider to be installed at the European Laboratory for Particle Physics (CERN) were carried out. These first collisions marked the end of almost twenty years of design, construction, installation and commissioning of the accelerator and the associated experiments. It was a gigantic and sometimes heroic joint effort of thousands of physicists, engineers, technicians and support personnel from hundreds of research institutes, laboratories and industries all over the world. We can proudly say now that the challenge is accomplished, the phase of physics exploitation of the machine and experiments has just started.

The beam energy raised to 3.5 TeV only few months later, on March 2010, signalling the start of LHC continuous running delivering pp collisions at $\sqrt{s} = 7$ TeV in a steady stable operation mode. The Compact Muon Solenoid (CMS) detector, a multipurpose experiment located in one of the four interaction points of the accelerator, was fully operational since the beginning of the run and accumulated an integrated luminosity of over 46 pb^{-1} in this 2010 run. The measurements presented in this thesis are the result of the analysis of this data.

The LHC unveils a previously unexplored energy regime where the particle physics community expects to find answers to many of the yet unresolved questions it has raisedi: from the quest of the long-awaited Higgs boson, predicted to explain the Electroweak Symmetry Breaking, to the search for new symmetries and particles.

This thesis presents the first measurement with the CMS detector of the inclusive W boson production cross-section in proton-proton collisions, in its muon decay channel $\sigma(\text{pp} \rightarrow$

$W^{\pm} + X) \times BR(W^{\pm} \to \mu^{\pm}\nu)$ at a centre-of-mass energy of 7 TeV. It is indeed one of the first measurements at the TeV scale. Already, it can be qualified as a precision measurement and will allow to check the validity of Standard Model predictions in this new energy regime, an essential test before more involved analysis can be undertaken. Once W boson production is properly characterized, plenty of other ElectroWeak studies will follow. Also, as they constitute a large background for many New Physics phenomena, a deep understanding of the mechanisms of W production and decay is a key element for the new discovery era we are just about to start.

From the detector point of view, the clean experimental signature of the physics channel studied makes it an invaluable testbench to understand and optimize the detector performance in terms of detector operation, reconstruction algorithms and analysis techniques.

The study presented here summarises the status of the experiment after the first months of data-taking, and the analysis strategy devised to perform this first Electroweak measurement.

The first part of the thesis sets the general picture in which this measurement has to be framed. The physics program the LHC aims for is briefly described in Chapter 2. A short description of the accelerator and the main characteristics of the CMS experiment are also included here. The experimental conditions of the 2010 run were somehow special, with the LHC still in commissioning mode. Several machine developments periods were needed to achieve the initial foreseen performance. The actual parameters of the accelerator in 2010 are given in Chapter 3. From the point of view of CMS, all the procedures long time exercised to run efficiently the experiment, were finally put into practice, now with data from pp collisions. The running experience of CMS during 2010 is also summarized there.

Chapter 4 provides a brief description of the characteristics of W boson production in hadron-hadron interactions. It also compiles some of the prospects of the measurement of W boson properties to be performed by the CMS experiment in the coming years.

The core of the analysis is reported in Chapters 5 to 8. The description of the different reconstruction techniques employed in the analysis, and their performance, evaluated with this first LHC data, are given in Chapter 5. Special attention was paid to muon momentum measurement, muon isolation and missing transverse energy measurement, since they constitute the distinct experimental signature to, first, identify W boson events, decaying into a muon and a neutrino and then, to determine its production cross section.

The analysis strategy followed is presented in Chapter 6. It starts with a detailed kinematic characterization of the signal process: $pp \to WX \to \mu\nu X$ events, and compared with other processes with a similar experimental signature that may constitute a background noise for

the measurement. An efficient selection procedure is thus established, to maximize the signal efficiency minimizing at the same time background contributions. The methods developed to evaluate the efficiency of this selection process are then addressed. Signal events and remaining background are further characterized in terms of the discriminant variable that will be used afterwards for the final cross section determination. A substantial effort was done to minimize analysis reliance on Montecarlo simulations, extracting almost all auxiliary information from independent data samples of well known processes or from data-samples selected in control regions extensively checked by other means.

Chapter 7 deals with the final W signal extraction. The validity of the method followed is first assessed making use of MC simulated samples. It is then applied for the W signal yield extraction and W cross section determination. The sources of any potential (experimental and theoretical) effects that may have an impact in the measurement are then analyzed and the size of the associated systematic uncertainties is quantified.

The final results of this thesis are given in Chapter 8: the inclusive production cross section of W bosons, $\sigma(pp \to W + X) \times BR(\mathrm{W} \to \mu\nu)$, as well as separated by charge, W^+ and W^-, in pp collisions at a center-of-mass energy of 7 TeV. From these values, the ratio of cross sections $\sigma(W^+)/\sigma(W^-)$ is determined. Making use of the CMS measured value of the inclusive production cross section of Z bosons, the ratio of cross-sections $\sigma(W)/\sigma(Z)$ is calculated. The values obtained are compared with the measurements published by the CMS and by the ATLAS collaborations, and with the latest Next-to-Next-to-Leading Order theoretical predictions. Finally, and based on the experience gained in this analysis, an outlook for possible future improvements of the measurement with a larger statistical sample is included.

The conclusions of this work are summarized in Chapter 9.

This is the first W cross section measurement carried out in CMS. Analysis started with the first bunch of collected data. Data was initially scrutinized almost on a daily basis to confirm the correctness of the analysis strategy deployed. The historical evolution of the analysis, from the first runs to the final result is summarized in Appendix A. Also, and in order to use the best-performance reconstruction algorithms in the analysis, this was carried out in parallel applying several reconstruction algorithms. Appendix B gives the results using an alternative reconstruction algorithm to measure the missing transverse energy of the event. The values obtained are in full agreement with the main results given in Chapter 8.

Chapter 2

The LHC program and the CMS Experiment

The Large Hadron Collider (LHC) [1; 2; 3] is a proton-proton collider located at CERN, in the frontier between Switzerland and France. It is housed in the 26.7 km long, 50-175 m deep tunnel originally used by the Large Electron-Positron collider (LEP, 1989-2000).

The design and construction of the LHC and its experiments began more than 20 years ago. It was officially introduced in 1984 in the ECFA (European Committee for Future Accelerators)-CERN meeting, and its construction was approved in 1994. The original starting date (2005) was postponed several times, and it finally started operation in late 2009.

The LHC was designed to operate at a centre-of-mass collision energy of $\sqrt{s} = 14$ TeV, therefore providing parton-parton collisions up to energies of about 1 TeV, and with a very high collision rate in order to favour the study of the production of rare particles.

This will allow us to extend the energy regime to explore beyond the Electro-Weak scale (200 GeV, already covered in former experiments). By opening the door to this new territory, we will be able to test the limits of the current Standard Model of Particle Physics. We expect that in the future years the LHC will find the answers to many of the currently unresolved questions of high energy physics.

2.1 Scientific scope of the LHC

The Standard Model (SM) of particles and fields is a quantum field theory which aims to describe the interactions of all elementary, point-like particles.

The model classifies particles into three families of constituents of matter (fermions, with half-integer spin) and carriers of the four fundamental interaction (bosons, with integer spin). For each particle in the model there is an associated antiparticle with the same mass and opposite electric charge. The fundamental forces are reduced to four. Electromagnetism, weak nuclear force, and strong nuclear force are explained by the model, while a quantified theory of gravity is still to come. Elementary particles are not known to have sub-structure (up to the present limits of $10^{-18} - 10^{-19}$ cm), and are summarised in Table 2.1.

	I	II	III	**Bosons**
Quarks	**u** up $m_u = 2.49$ MeV $q = +2/3e$ $s = 1/2$	**c** charm $m_c = 1.27$ GeV $q = +2/3e$ $s = 1/2$	**t** top $m_c = 172.0$ GeV $q = +2/3e$ $s = 1/2$	γ photon $m_\gamma = 0$ $q = 0$ $s = 1$
	d down $m_d = 5.05$ MeV $q = -1/3e$ $s = 1/2$	**s** strange $m_s = 101$ MeV $q = -1/3e$ $s = 1/2$	**b** bottom $m_b = 4.19$ GeV $q = -1/3e$ $s = 1/2$	**g** gluon $m_g = 0$ $q = 0$ $s = 1$
Leptons	**e** electron $m_e = 0.511$ MeV $q = -e$ $s = 1/2$	μ muon $m_\mu = 105.7$ MeV $q = -e$ $s = 1/2$	τ tau $m_\tau = 1777$ MeV $q = -e$ $s = 1/2$	$\mathbf{W^{\pm}}$,$\mathbf{Z^0}$ weak bosons $m_W = 80.4$ GeV $m_Z = 91.2$ GeV $q_{W^\pm} = \pm 1e$ $q_{Z^0} = 0$ $s = 1$
	$\nu_\mathbf{e}$ electron neutrino $m < 2$ eV $q = 0$ $s = 1/2$	ν_μ muon neutrino $m < 0.17$ MeV $q = 0$ $s = 1/2$	ν_τ tau neutrino $m < 15.5$ MeV $q = 0$ $s = 1/2$	

Table 2.1: Elementary particles of the Standard Model. [4]

The theory is invariant under local transformations of $SU(3)_C \times SU(2)_L \times U(1)_\gamma$. These three groups correspond roughly to the three interactions covered by the model. The $SU(3)$ gauge field corresponds to the strong interaction, described by quantum chromodynamics or QCD, which acts only on particles carrying colour charge "C" (quarks), by exchange of eight kinds of massless gluons. The $SU(2) \times U(1)$ group corresponds to the Electro-Weak interaction. Before electroweak-symmetry breaking, $SU(2)$ is mediated by three weak isospin, massless, bosons W^μ,

and $U(1)$ by a weak hypercharge massless boson B^0. After electroweak symmetry breaking, these gauge bosons are recombined and give raise to the massive carriers of weak force (W^+, W^-, Z^0) and the massless photon γ, carrier of the electromagnetic interaction ($U(1)_{em}$). This process requires the introduction in the model of a scalar field, the Higgs field, and its elementary scalar (spin-0) the Higgs boson.

The current formulation of the Standard Model was finalized in the 70s with the experimental confirmation of the existence of quarks. Many of its predictions have been experimentally confirmed. For example, the discoveries of the W and Z bosons (1983), the top quark (1995) or the tau neutrino (2000). The accuracy of these predictions is shown in Figure 2.1 [5; 6], which compares experimental measurements (the masses and widths of the weak bosons, the top quark mass, asymmetries) with the global fit result of the Electro-Weak theory. Almost all the measurements obtained with extremely high precision.

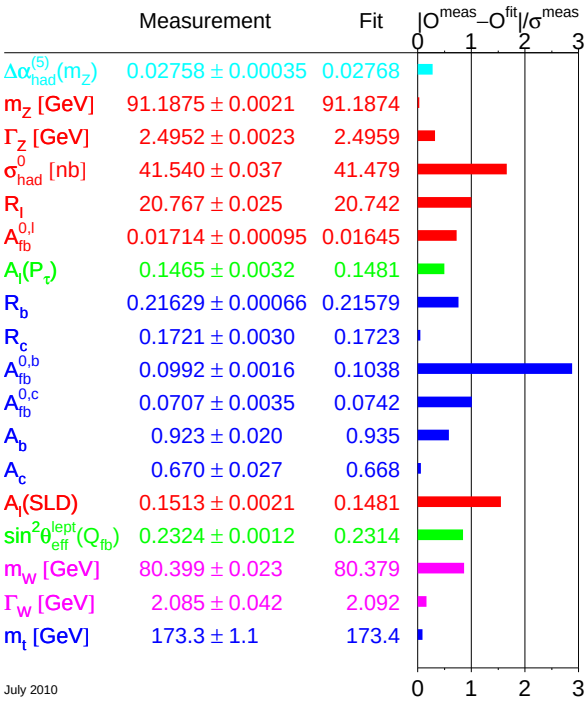

Figure 2.1: Parameters of the Standard Model. [5]

However, the Standard Model is not a complete theory of fundamental interactions. It does not incorporate the physics of general relativity, and it cannot provide an explanation for dark matter and dark energy. Therefore it is incompatible with the latest observational cosmological results. Nor does it give a solution for the masses of the neutrinos, originally massless in the theory but proved to be of discrete mass by the experimental observation of neutrino oscillations. Other mysteries are the origin of the widely different values spanned by the masses of elementary particles (six orders of magnitude, from $m_e = 0.511$ MeV to $m_t = 172$ GeV[1]); the Charge-Parity violation, responsible for the matter-antimatter asymmetry observed in our current universe; the existence of three and only three different families or "copies" of particles (e, μ, τ); or the so-called hierarchy problem, which refers to the orders of magnitude existing between the Electro-Weak scale

[1] In this thesis natural units ($c = 1$, $\hbar = 1$) are assumed. Momenta and masses will be therefore measured in GeV.

(≈ 100 GeV, unification of weak and electromagnetic forces) and the Planck scale ($\approx 10^{19}$ GeV, grand unification scale).

The Standard Model is therefore considered today an effective theory of another more fundamental one, valid only up to the energy range explored until now (~ 100 GeV, Electro-Weak scale).

Even restricted to this energy-range, one of its fundamental pieces remains undiscovered. The Higgs boson, needed to explain the mechanism by which W and Z bosons acquire mass in this model, has not yet been observed. The theory predicts all of its properties except its mass, which is is the only remaining free parameter of the Standard Model.

Theoretically the Higgs boson mass is bounded to be $M_H < 1$ TeV for unitarity reasons (preventing WW scattering to be divergent). Direct searches performed by the LEP experiments excluded its existence in a wide range of masses, providing a lower bound for its mass, $M_H > 114$ GeV at 95% confidence level [5; 6]. Tevatron at Fermilab has extended the excluded region. Combining data from CDF and D0 experiments was sufficient to exclude the existence of the Higgs boson in the mass range between 158 GeV and 175 GeV at the 95% confidence level. [7]

In addition to these direct searches, it is possible to probe the mass range indirectly, studying the effects of the Higgs boson in measurable quantities. These effects come through Higgs loop diagrams which result in small corrections to electroweak parameters (for instance, the mass of the weak bosons or the Fermi constant), which can be measured very accurately. These measurements exclude the Standard Model Higgs for values of the mass higher than 186 GeV at 95% confidence level, under the assumption of the validity of the model.

The full theoretically-allowed mass spectra is yet to be covered. Figure 2.2 a) presents the 95% Confidence Level exclusion plot from the Tevatron [7], for an integrated luminosity of $\sim 6\text{fb}^{-1}$. The expected exclusion limit (dashed line, green and yellow error bands) is shown together with the observed one (solid line). The vertical green bands show the area in which the observed limit goes below the 95% confidence level limit, and the red vertical band includes the limit given by LEP searches. Together, they reduce the allowed range for the Higgs boson mass to $114 < M_H < 158$ GeV and $M_H > 175$ GeV. Figure b) shows the latest update of the Electro-Weak fit, with calculates the preferred value for the Higgs boson mass given all the other measured parameters of the Standard Model, taking into account Electro-Weak corrections. Solid yellow areas represent the already excluded masses. The best value of the fit, below 100 GeV, has already been excluded experimentally [5; 6].

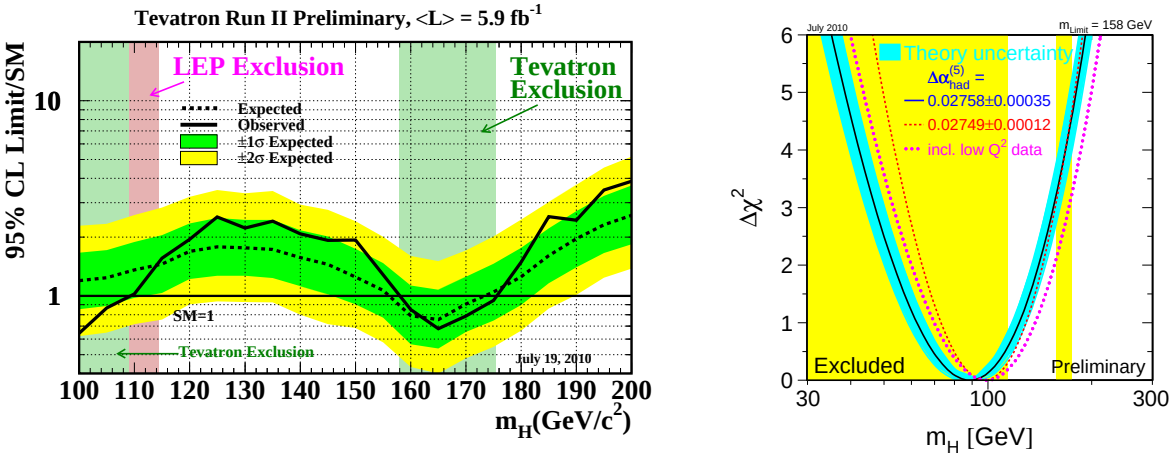

Figure 2.2: a) Most up-to-date Higgs exclusion plot prepared by the CDF and DO collaborations at Tevatron, with integrated luminosities up to 6.7 fb^{-1}. The sensitivity-weighted average luminosity is 5.9 fb^{-1} 95% C.L. exclusion for SM Higgs with mass mH between 158 and 175 GeV, and between 100 and 109 GeV. [7] B) ElectroWeak fit showing the theoretical preferred value for the Higgs boson mass in the Standard Model, and the current excluded region [5].

The LHC will be able to probe the full theoretically allowed mass range (up to 1 TeV). The elusive particle will necessarily have to be discovered - or proved nonexistent.

Figure 2.3 shows the foreseen exclusion limit that the CMS experiment of the LHC will provide at a centre-of-mass-energy of $\sqrt{s} = 7$ TeV with an integrated statistic of $1 - 2\text{fb}^{-1}$ (expected already by the end of 2011) [8].

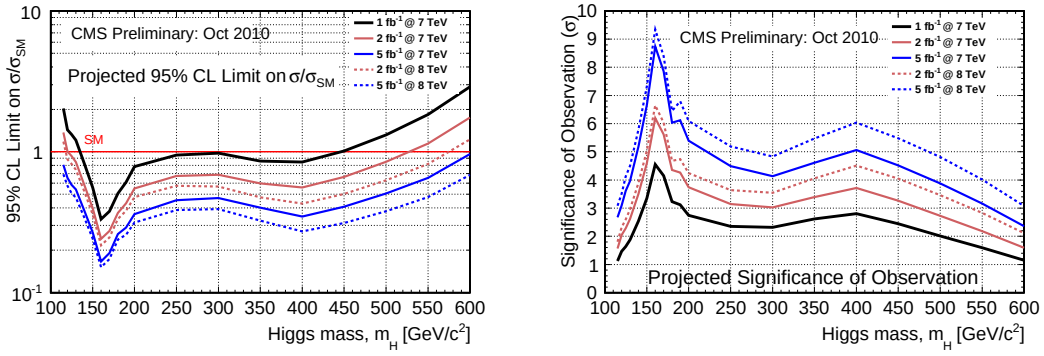

Figure 2.3: Foreseen exclusion limits and the expected observation significance for a SM Higgs search at $\sqrt{s} = 7$ and 8 TeV and a few selected luminosities.

If no trace of the Standard Model Higgs boson is found at the LHC, the model will have to be revised. There are different theories available which extend the model (allowing for different models of electroweak symmetry breaking, while still in agreement with the current experimental data). If no Higgs is found, the new data analysed in the LHC will allow us to verify or deny these models, or give us new insights on the behaviour of nature to construct new ones. These new theories also help to solve some of the other pieces of the puzzle which fail to fit within the Standard Model, for instance by providing a dark matter candidate particle.

One of the most famous extensions of the Standard Model is Supersymmetry, which maintains the general structure of the present model but introduces a new symmetry between fermions and bosons. Every particle of the Standard Model would require a supersymmetric partner, that differs by half a unit of spin. A new relation is established this way between particles of matter, half-integer fermions, and force carriers, integer bosons. For instance, leptons (fermions) would be paired with sleptons (bosons) and gluons (bosons) would be paired with gluinos (fermions). The Electro-Weak symmetry breaking problem is still solved through a Higgs mechanism, though in this case instead of a single Higgs scalar field, at least two Higgs doublets (paired to higgsinos) have to be introduced. This new symmetry gives a solution to the hierarchy problem of the Standard Model ensuring a finite Higgs boson mass by loop cancellation, but doubles the number of elementary particles in nature. Experimental signatures of these supersymmetric particles should be observed at the energies that the LHC will reach. There are many particular formulations of supersymmetry, the simplest one of them being the "Minimal SuperSymmetric Standard Model" (MSSM). In many of them there is a natural candidate to dark matter (the lightest supersymmetric particle, which is stable).

Other "beyond the standard" models include the existence of extra-dimensions (dimensions of extremely small size that could be unveiled at the TeV scale), little-Higgs type modes (new boson-boson and fermion-fermion symmetries) or the existence of new fundamental interactions. We do not know where and how will the signals for physics beyond the Standard Model appear, so the experiments need to be prepared to look everywhere.

The LHC is a versatile machine, not only oriented to searches. Known physical processes, like the production of bottom and top quarks, will also be studied. B-Physics is intimately related with CP-violation, and therefore with the matter-antimatter problem, and thus will be studied in detail. Top-quark processes can be studied for the first time in multi-TeV proton-proton collisions. pairs. With a $t\bar{t}$ production rate up to 5 orders of magnitude higher than in the Tevatron, the measurements of top-quark properties are a important part of the LHC program, due to its importance both as a background to many searches and as a precise test of

the SM predictions. Other areas that will be covered will be precise measurements of Electro-Weak physics quantities (such as W and Z asymmetries, or anomalous gauge couplings), or QCD studies on the behaviour of matter at very high energy and density.

This is a very succinct summary of the physics that the LHC will study. The successes and failures of the Standard Model are well documented in the literature and have not been detailed in this thesis.

A comparison of the cross-sections, and therefore the relative production rate, of the processes that will be studied in the LHC is shown in Figure 2.4, as a function of the centre-of-mass energy of the collision, $\sqrt{s}$. The rate varies greatly from the huge total σ_{pp} (10^8 nb) to the tiny Higgs production (10^{-3} nb) [9]. As we can see in this graphic, W and Z production ($\approx 10^2$ nb) is, after jet and $b\bar{b}$ production, the dominant process.

A very exciting era for Particle Physics has just started, for which the very first step is the precise measurement of familiar processes. To go beyond the Standard Model we first need to understand the properties of known particles in this new territory. In this thesis I have studied the production at 7 TeV of one of these fundamental pieces, the W boson. Chapter 4 gives a more detailed introduction to the theory behind Vector Boson production at the LHC.

2.2 General Description of the LHC

The LHC is composed of two synchrotron storage rings of superconducting magnets, with a common cryogenic system but independent vacuum pipes, and opposite magnetic dipole fields. Along them two beams of protons (or heavy ions such as Pb) circulate in opposite directions, intersecting at four interaction points where the experiments are located.

The very small production rate of the processes to be studied (see Figure 2.4) determined the design of the LHC. In order to favour the production of rare processes such as the Higgs and to cover the widest possible range of energies in the search for new Physics, a high centre-of-mass energy was required. Even meeting this requirement, the small production rate of interesting particles implied maximizing their collision rate, and therefore the intensity and collimation of the beams.

An schematic view of the CERN accelerator complex is shown in Figure 2.5. Different accelerators are chained so that the energy of the beams is increased progressively. Protons are initially obtained by ionising gaseous hydrogen, and then accelerated in bunches to the linear accelerator (LINAC2) to an energy of 50 MeV. From there they are injected into the Proton

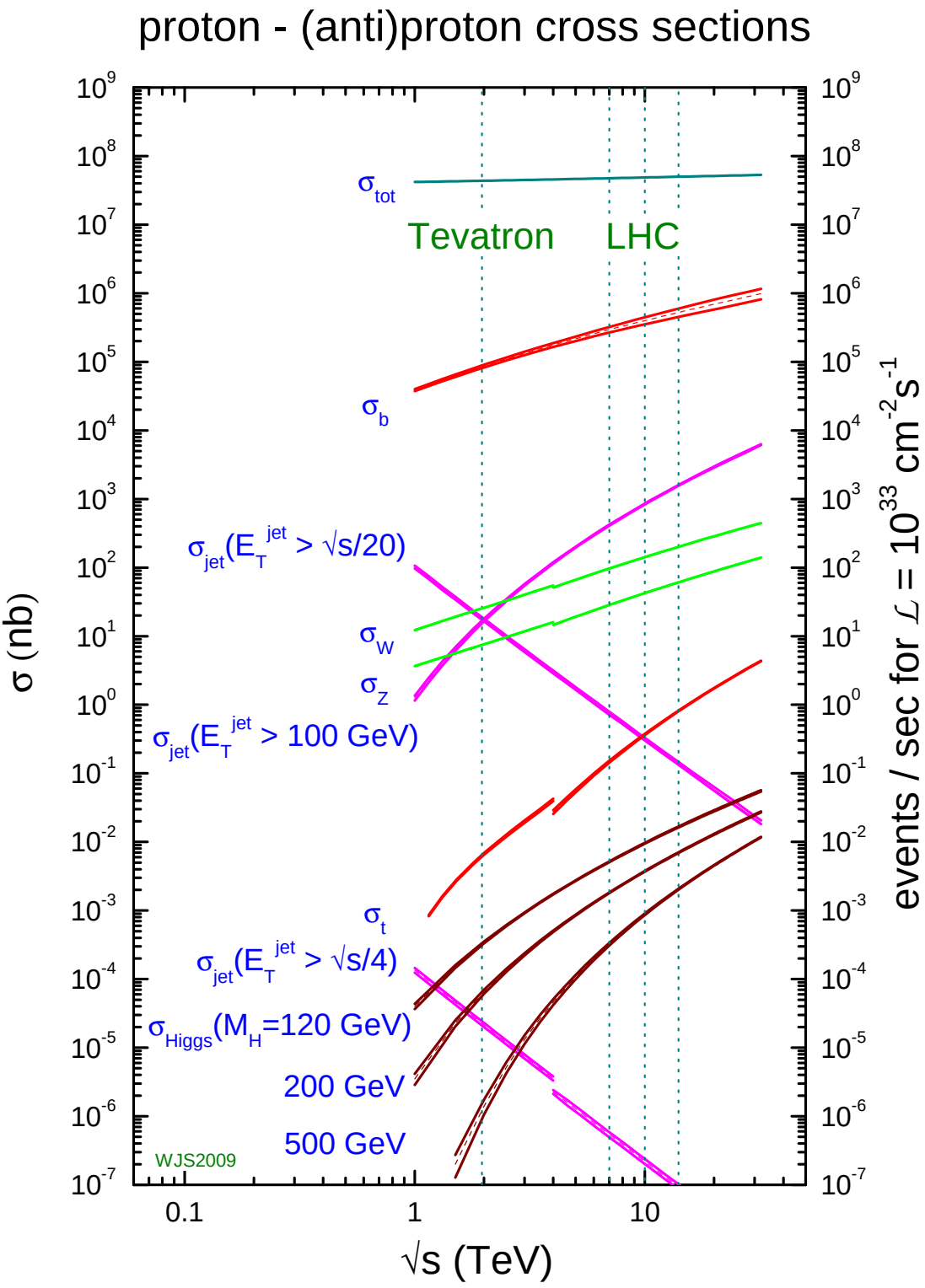

Figure 2.4: Hadronic cross-sections of different physic process with as a function of the centre-of-mass energy $\sqrt{s}$. Dotted lines mark the collision energies of the Tevatron and the LHC.

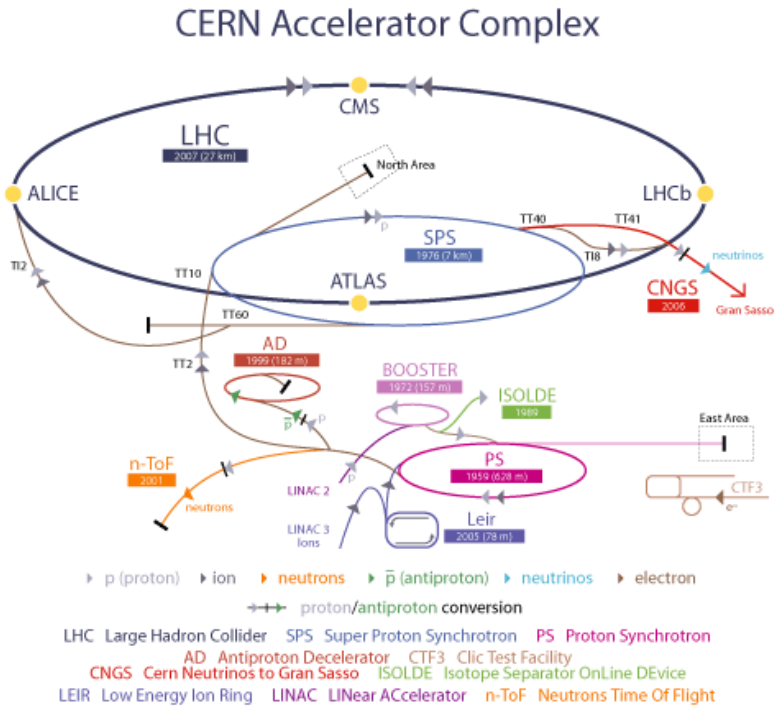

Figure 2.5: CERN accelerator complex.

Synchrotron Booster (PSB), and boosted to an energy of 1.4 GeV before being accelerated in the Proton Synchrotron (PS) to 26 GeV. The final step before the beams enter the LHC is done in the Super Proton Synchrotron (SPS), which pushes them up to the injection energy of 450 GeV.

Once they are injected into the LHC, the beams are accelerated up to collision energy (nominal $\sqrt{s} = 14$ TeV, in 2010 $\sqrt{s} = 7$ TeV). A 8.33 T magnetic filed generated by 12323 dipole magnets keeps the beams on their circular path. The beams are focused by 392 quadrupole magnets. Further corrections are obtained through other magnets of higher order, up to dodecapoles. These superconducting magnets need to be maintained at 1.9 K to operate using super-fluid helium, turning the LHC into the largest cryogenic system in the world.

The need for a high beam intensity made it necessary to have two independent magnetic fields for each proton beam. This could have been avoided replacing one of the proton beams with an anti-proton beam - hence allowing a simplification of the vacuum and magnet system. However, the difficulty of reaching high intensity anti-proton beams made this solution incompatible with the required design.

The collision rate can be quantified in terms of instantaneous luminosity (number of collisions

per unit time and transverse section of the beams), which depends on the configuration of the accelerator:

$$L = \frac{1}{4\pi \cdot m_0 c^2} \cdot \frac{f_{rev} N_p F}{\beta^\star \epsilon_n} E_{stored}$$

The protons circulate around the ring in the LHC in bunches of N_p particles. They have a revolution frequency f_{rev} which is geometrically fixed by design, and are spaced by 25 ns (≈ 7 m). The stored energy in the beam, E_{stored}, grows with the number of bunches, reaching 362 MJ at design level.

The transverse beam-sizes can be written in terms of the normalised transverse emittance and the betatron function at the interaction point: $\pi\sigma^2 = \epsilon_n \beta^\star$ The normalised transverse emittance ϵ_n is a beam property related to the area occupied by the particles of the beam in the space and momentum phase-space. It is constant along the ring for all the beam lifetime, and at design level values as low as 3.75 μm are achieved. The betatron function at the interaction point $\beta^\star$ is beam-optics property reduced thanks to collimation ("squeezing") of the beams close to the interaction points.

If the number of bunches in the beam is high ($N_b > 156$), a crossing angle of the order of $250 - 300$ μrad at the interaction point will be needed. This will introduce a geometrical luminosity reduction factor F, which depends on the crossing angle and the beam length and diameter at the interaction point. This is required to avoid parasitic collisions caused by beam-beam interaction away from the interaction point.

All these parameters and other design characteristics of the accelerator are summarised in Table 2.2.

Under nominal operating conditions, LHC will have 2808 bunches in each beam, with around 10^{11} protons in each bunch. The size of the bunch is not constant around the ring, it is squeezed and expanded. At the interaction points, they have a longitudinal size of 7.5 cm and a transverse size of 16 μm approximately.The design luminosity is 10^{34} cm^{-2}s^{-1}

The probability of more than one interaction occurring in the same bunch crossing increases with luminosity. The collision of two proton bunches with nominal parameters causes an average of about 20 collisions per bunch crossing. Bunches will cross about 30 million times per second. Hence at nominal conditions the LHC will generate up to 600 million particle collisions per second in each interaction point.

Experiments are located at the points where the beams intersect. The main experiments of the LHC are installed in underground caverns built in four of the eight possible interaction points

Design Parameters	
Circumference Length	26659 m
Depth	50 - 175 m
Total number of magnets	9600
Number of main Dipoles	1232
Time between collisions	25 ns
Bunch Crossing Rate f_{rev}	40.08 MHz
Temperature	1.9 K (-271.3C)
Injection energy	450 GeV
Dipole field	8.33 T
Nominal proton energy	7 TeV
Centre-of-mass energy $\sqrt{s}$	14 TeV
Number of bunches per proton beam	2808
Protons per bunch	1.1×10^{11}
Bunch spacing	25 ns
ϵ_n Norm. transverse emittance	3.75μm
Transverse beam size at IP5	16.7 μm
$\beta^\star$ IP5 beta value	0.55 m
Crossing angle	285 μrad
E_{stored} Stored energy	362 MJ
Design instantaneous luminosity	10^{34} cm^{-2}s^{-1}
Average number of collisions per crossing	20

Table 2.2: Design parameters of the Large Hadron Collider.

of the LHC: ALICE (A Large Ion Collider Experiment) [10], ATLAS (A Toroidal LHC ApparatuS) [11], CMS (Compact Muon Solenoid) [12] [13], LHCb (Large Hadron Collider beauty) [14]. Other two experiments, LHCf (Large Hadron Collider forward) and TOTEM (TOTal Elastic and diffractive cross-section Measurement), are situated in the tunnel, near ATLAS and CMS respectively.

ATLAS and CMS are the two multipurpose experiments of the LHC, prepared to work in the high luminosity regime. They have similar physics goals but different technical solutions and design, and are situated at opposite locations in the ring. ALICE is dedicated to the study of heavy ion collisions and the QCD phase diagram, and LHC-b to the study of the physics of the b-quark, intimately related with CP-symmetry violation. Given the characteristics of their physics programs, the optimal luminosity for ALICE and LHC-b is lower than the nominal LHC design luminosity, 10^{32} cm^{-2}s^{-1} for the former and 10^{27} cm^{-2}s^{-1} for the latter.

This thesis is based on data from the CMS experiment. In the following its main characteristics will be described in some detail.

2.3 The Compact Muon Solenoid

The Compact Muon Solenoid (CMS) [12], as its name suggests, is based in an intense solenoidal magnetic field of 3.8 T, and an excellent muon spectrometer. Different subdetectors aimed for detection, identification and reconstruction of charged particles, electrons, photons and hadrons are located inside the solenoid; while the muon detectors are situated in the return yoke of the magnetic field.

Despite its dimensions (21.6 meters of length x 14 meters of diameter) its weight of 12500 tons makes it a compact machine, especially compared to the enormous ATLAS.

To detect particles in the widest possible angular range, CMS covers all the azimuthal angle $-\pi < \phi < \pi$ and almost all the polar angle in θ (depending on the subdetector considered, from $|\eta| < 2.5 - \theta < 10^\circ$ up to $|\eta| < 5 - \theta < 0.8^\circ$ [1]).

In order to meet the goals signalled by the LHC physics programme, the design objectives of CMS can be summarised as follows [15; 16]:

1. A good and redundant muon detection and triggering system, able to provide excellent muon identification and resolution over a wide range of momenta and angles, good di-muon mass resolution ($\sim 1\%$ at 100 GeV) and unambiguous charge identification for muons up to 1 TeV.

2. The best possible electromagnetic calorimeter, to ensure excellent electromagnetic energy resolution over a wide range of energy and angles, good di-photon and di-electron mass resolutions (($\sim 1\%$ at 100 GeV), π^0 identification and rejection and efficient photon and lepton isolation at high luminosities.

3. A high-quality inner tracker, for excellent charged particle momentum resolution and reconstruction efficiency, and secondary vertex reconstruction for the identification of τ and b-jets.

[1] CMS coordinate system is a cylindrical one, based on (x,y,z) or (r,ϕ,η) where z is the direction along the beam pipe and x points to the centre of the LHC from the origin, $r = \sqrt{x^2 + y^2}$ is the radius in the transverse plane, and ϕ the azimuthal angle in it. The pseudorapidity $\eta = -\ln(\tan\frac{\theta}{2})$, is used instead of the polar angle θ.

4. Good hermeticity and fine lateral segmentation of the hadron calorimetry, to provide good missing-transverse-energy and jet energy resolution.

Technically the subdetectors are required to be radiation-resistant, highly granular and to provide a fast response. In order to distinguish interesting events a filtering (*trigger*) system is in place. It is technologically impossible to record on tape the 10^9 collisions produced per second, and therefore the trigger task is a crucial one: select the most interesting 10^2 collisions per second to store them for future analysis.

Figure 2.6 shows a sketch with the trajectory of photons, electrons, hadrons, muons and neutrinos created in a proton-proton collision travelling through the subdetectors that compose CMS. Photons only leave signals in the electromagnetic calorimeter, where their energy is completely absorbed and measured. Electrons on the other hand are first measured as charged particles in the tracker, and then absorbed in the electromagnetic calorimeter, allowing a precise measurement of their momentum and energy. Hadrons (charged and uncharged) are able to reach the hadronic calorimeter where they deposit their energy in a cascade process. The only particles able to escape through the material contained within the magnet yoke are muons and neutrinos. Muons are identified thanks to their signals in the muon spectrometer. The lack of interaction of neutrinos with matter allows them to escape direct detection - they can only be measured indirectly.

A more detailed drawing of the CMS detector is shown in Figure 2.7. Each subdetector is composed is described in the following.

2.3.1 Magnet

The intense solenoidal field provided by the CMS magnet is the central key of the design of the experiment. It is the responsible for its compactness and cylindrical symmetry. Subdetectors are situated concentrically around the interaction point, with the tracker and calorimeters within the solenoid bore and muon spectrometers outside of it, interleaved in the iron return yoke.

The superconducting solenoid is composed by a four-layers winding of NbTi conductor stabilised and reinforced by aluminium, 12.5 m long and with an inner radius of 4.9 m. It provides a uniform axial field of 3.8 T in the positive z direction in the inner detectors. This magnetic field curves the trajectory of charged particles, therefore making it possible to measure their momentum.

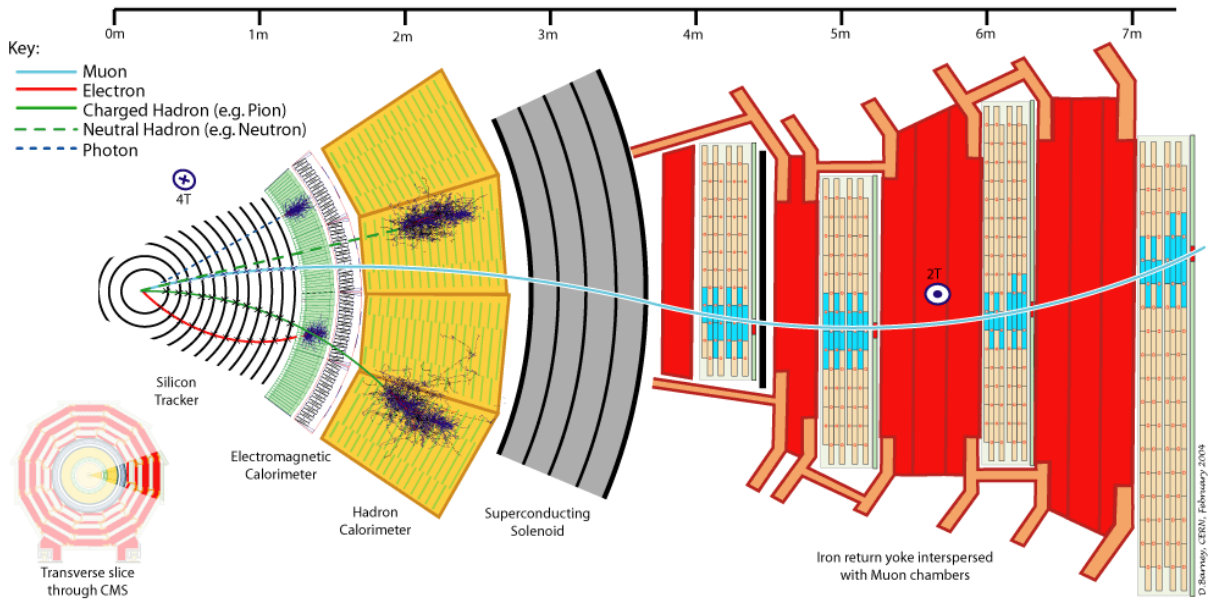

Figure 2.6: Slice of the CMS detector.

The return yoke is formed by five iron wheels and two endcaps (1000 ton in total), interleaved with the muon spectrometer stations. In this part of the detector the magnetic field is saturated at 2 T.

The predicted magnetic flux density on a longitudinal section of the CMS detector is shown in Figure 2.8. Approximately two thirds of the magnetic flux return through the barrel yoke, half of which enters directly into the barrel without passing through the endcap disks. One third of the total flux escapes radially, returning outside the steel yoke. The field in the tracker volume has been mapped with an accuracy better than 0.1%. In the CMS yoke, the map is estimated to be accurate to better than 3% in the steel of the three central barrel wheels, and to about 8% in the steel of the two outermost barrel wheels, satisfying the accuracy required for physics analysis and muon triggering in CMS [17].

2.3.2 Inner Detectors

The innermost detector of CMS is its all-silicon tracker [18; 19]. Its precise measurement of the trajectories of charged particles and reconstruction of secondary vertices makes it one of the biggest assets of the experiment. The need to address successfully the physics program required, in its design, a reconstruction efficiency higher than 95% for isolated tracks and 90% for tracks

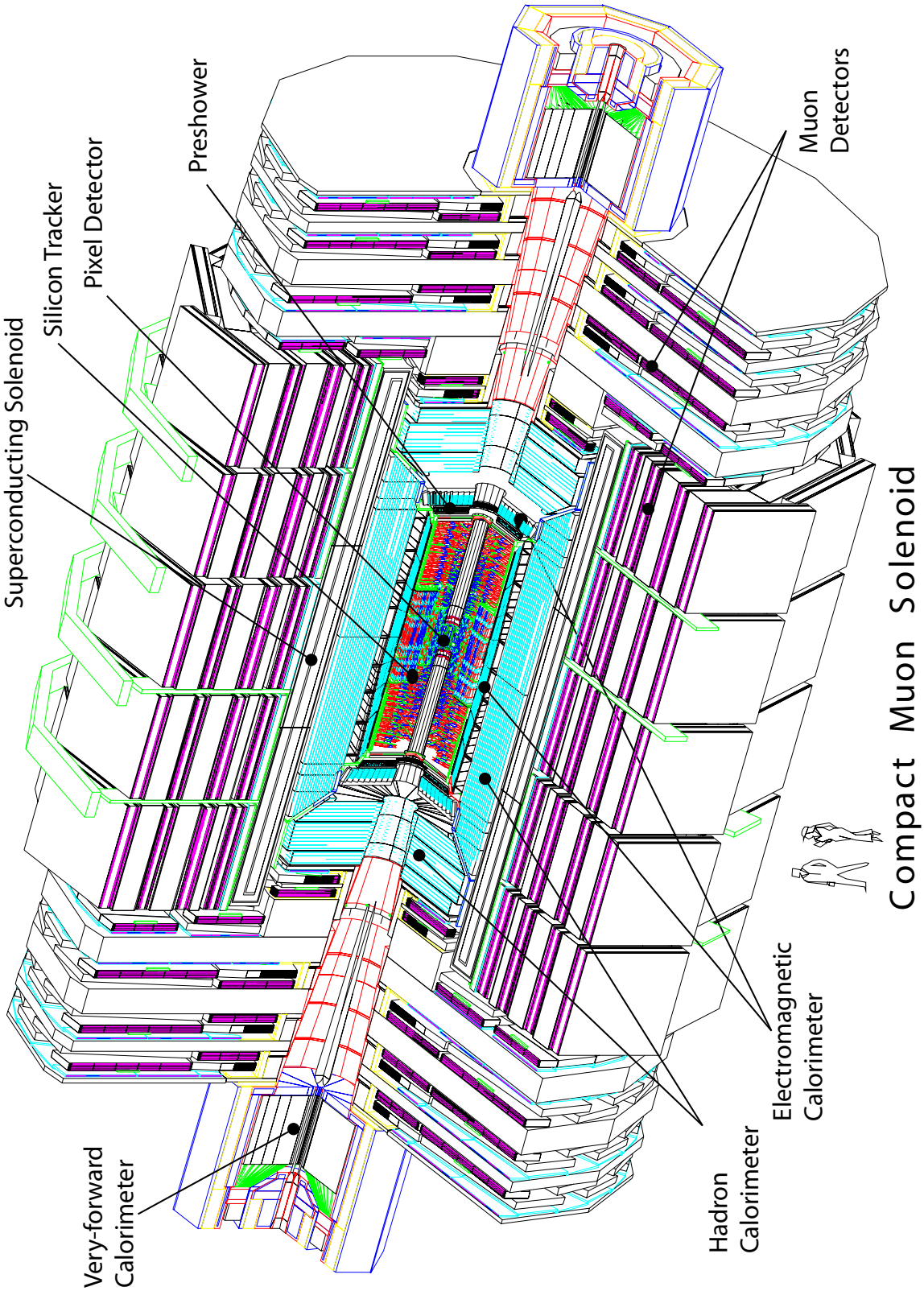

Figure 2.7: Layout of the CMS detector.

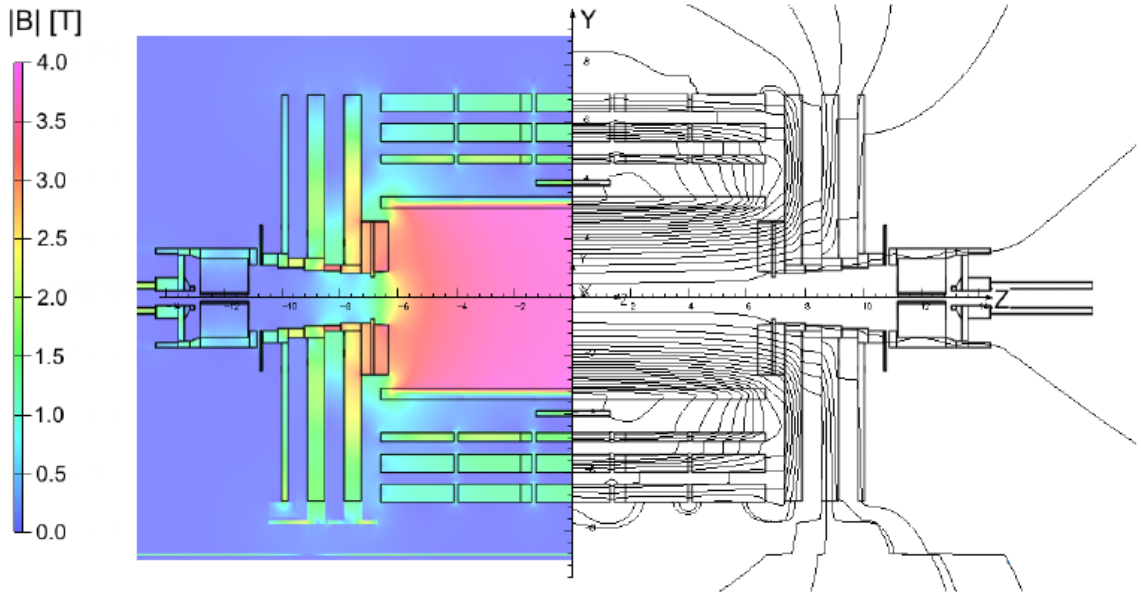

Figure 2.8: Value of the magnetic field B (left) and field lines (right) predicted on a longitudinal section of the CMS detector, for the underground model at a central magnetic flux density of 3.8 T. [17]

within jets in a pseudorapidity range $-2.5 < \eta < 2.5$, and a lepton momentum resolution of $\Delta p_t/p_t = 10\%$[1].

The homogeneous field in which the particles coming from the interaction point are immersed forces them to follow an helicoidal trajectory. This allows a measurement of their momentum, by the expression $p_t[\text{GeV}] = 0.3\ q\ \rho[\text{m}]\ B[\text{T}]$. The constant value 0.3 is an addimensional factor given by the geometry of the magnet, q the charge of the measured particle, ρ its radius of curvature and B the solenoidal field (3.8 T).

The large particle flux crossing the tracker in each bunch crossing requires a highly granular detector, able to distinguish trajectories reliably and fast enough to attribute them to the correct bunch crossing and provide a precise measurement of their momentum. However, a compromise must be reached between granularity and material budget. Increasing channel density implies increasing the associated cabling and piping for read-out and cooling, and this additional material budget increases multiple scattering, bremsstrahlung, photon conversion and nuclear interactions which worsen track momentum resolution.

In addition to this, the material of the tracker has to be specifically designed to resist

[1]The transverse momentum and transverse energy of particles are the projections in the transverse plane of their momentum and energy: $p_t = p\cos(\phi) = \sqrt{p_x^2 + p_y^2}$, $E_T = \sqrt{E_x^2 + E_y^2}$

radiation. This led to the design and construction of a two-parts all-silicon tracker, a inner subdetector composed of silicon pixels and an outer one composed of silicon strips. The overall length of the system is 5.8 m and its diameter 2.5 m. With about 200 m^2 of active silicon area, CMS is the largest silicon tracker ever built.

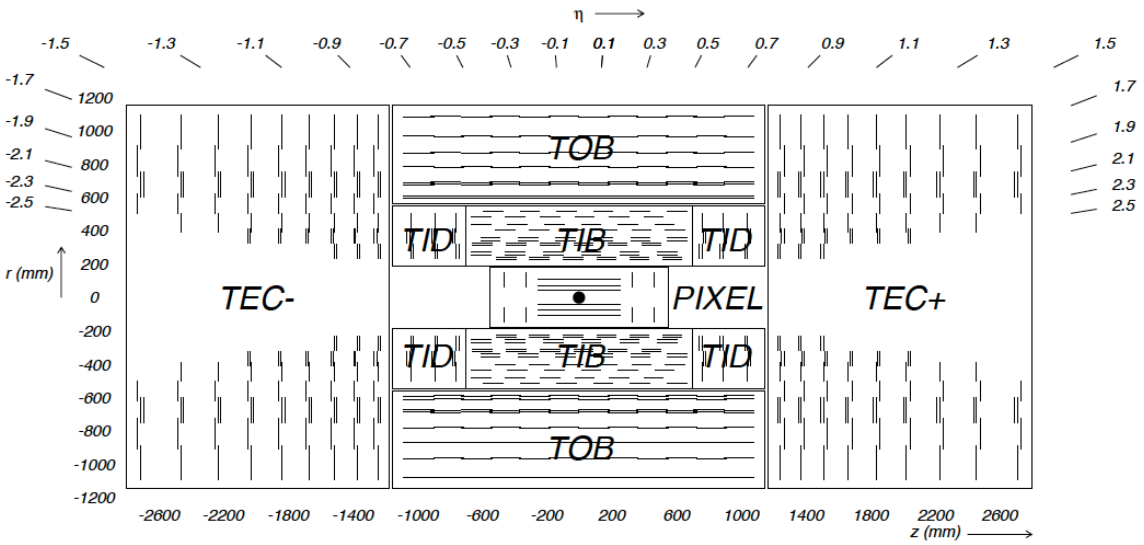

Figure 2.9: CMS inner tracker.

The structure of the two tracker subdetectors is shown in Figure 2.9. Their main characteristics are:

- The **Pixel Detector** is composed of 66 million pixels surrounding the interaction point, distributed in three barrel layers and two forward disks in each Z direction. Each pixel has a size of 125×125 μm^2, and a spatial resolution of ≈ 10 μm in $R-\phi$ and $\approx 15-20$ μm in Z is obtained. The signals detected by each individual pixel are collected, amplified and stored within the detector awaiting confirmation from the trigger system.

- The **Strip Detector** is composed of silicon microstrips, with widths ranging from 320 to 550 μm (depending on their localization). Strips are organized in modules. The particles transversing the detector produce an ionization, depositing charge in the different strips. The centre of the charge distribution provides a two-dimensional measurement of the position of the particle in the module. In the barrel there are 4+6 layers of such modules (parallel to the beam direction) and 3 disks (perpendicular to it), and in the endcap 9

additional perpendicular disks. The achieved single point resolution is 230 μm and 530 μm in the barrel layers, respectively, and varies with pitch in the disks of barrel and endcaps. The full subdetector extends up to a radius of 1.2 m and a length of 2.8 m from the interaction point, and has a total of 9.3 million strips and 198 m^2 of active silicon area.

In order to compute the intrinsic error in the measurement of the transverse momentum we have to take into account the error due to the determination of the position of the particle in the sensor. Approximating the radius of curvature to $\rho \approx d^2/8s$, where s is the sagita of the trajectory and d the distance transversed in the magnetic field, and considering that the error in the measurement of the covered distance is constant, we see that the associated error in the transverse momentum will be proportional to p_T^2: $\frac{\Delta p_T}{p_T}_{int} = \frac{\Delta \rho}{\rho} = \frac{\Delta s}{s} \approx \frac{\sigma_S}{d^2 B} p_T = k p_T$.

The granularity of the CMS tracker ensures good intrinsic momentum resolution. Figure 2.10 shows the material budget of the CMS tracker in units of radiation length. It increases from 0.4 X_0 at $\eta \approx 0$ to about 1.8 X_0 at $|\eta| \approx 1.4$, falling to about 1 X_0 at $|\eta| \approx 2.5$. Material effects deteriorate the measurement of the momentum. Multiple scattering and energy losses due to ionization give rise to non-gaussian tails to the measurement, adding a constant and a inverse term to the expression ($\frac{\Delta p_T}{p_T}_{MS} = \beta$ and $\frac{\Delta p_T}{p_T}_{I} = \frac{\gamma}{p_T}$).

Other material effects are bremsstrahlung (only relevant at high momentum) or delta rays. In addition to material effects, deviations from the ideal modelling of the detector also have to be considered. For instance, misalignment of the different subsystems or uncertainties in the measurement of the magnetic field.

All these effects are summarised in the expression:

$$\frac{\Delta p_T}{p_T} = k p_T \oplus \beta \oplus \frac{\gamma}{p_T}$$

The expected performance of the inner tracking system is shown in Figure 2.11, for single muons of transverse momenta of 1, 10 and 100 GeV. The three panels show the expected resolution of transverse momentum, transverse impact parameter and longitudinal impact parameter, as a function of track pseudorapidity η. For high momentum tracks (100 GeV) the transverse momentum resolution is around 1-2% up to $|\eta| \approx 1.6$. For higher η values it is degraded due to the reduced lever arm. At a transverse momentum of 100 GeV multiple scattering in the tracker material accounts for 20 to 30% of the transverse momentum resolution, while at lower

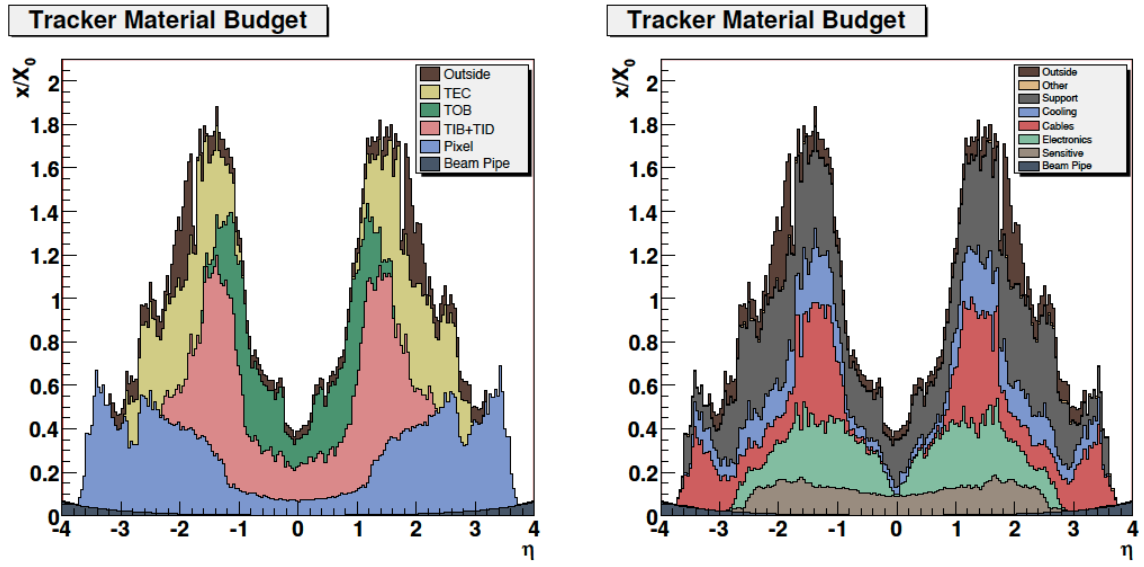

Figure 2.10: Material budget of CMS as a function of pseudorapidity.

momentum multiple scattering is the dominating factor. The transverse impact parameter resolution reaches 10 μm for high p_t tracks, dominated by the resolution of the first pixel hit, while at lower momentum it is degraded by multiple scattering (similarly for the longitudinal impact parameter).

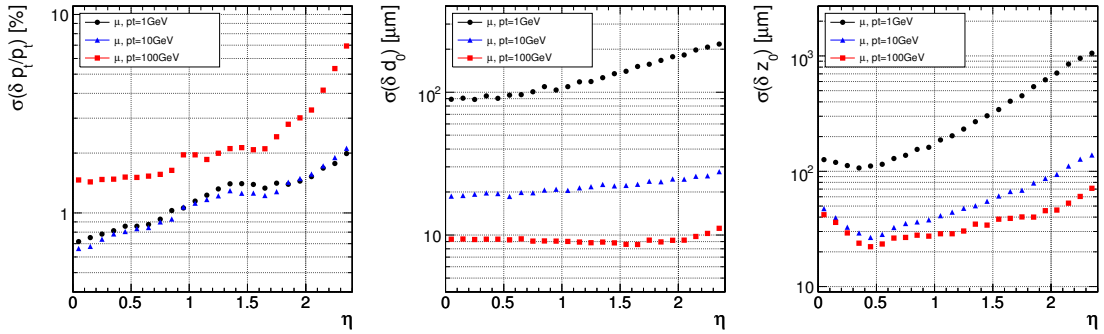

Figure 2.11: Resolution of several track parameters for single muons with transverse momenta of 1, 10 and 100 GeV: transverse momentum (left panel), transverse impact parameter (middle panel), and longitudinal impact parameter (right panel) [12].

2.3.3 Electromagnetic Calorimeter

The electromagnetic calorimeter (ECAL) [15; 20] is in charge of measuring the energy and position of photons and electrons, as well as aiding in the identification of electrons and pions and contributing to the measurement of the energy in hadronic showers. It is a hermetic, homogeneous calorimeter, composed of 75848 lead tungstate ($PbWO_4$) crystals, distributed in a central barrel (61200) and two endcaps (7324 each). They cover a pseudorapidity range up to $|\eta| < 3.0$.

The size of the crystals varies with their location. For the electromagnetic shower to be fully contained in the calorimeter, at least 26 radiation lengths are required in the crystals at $\eta \approx 0$. This implies a crystal length of only 23 cm. The presence of a preshower detector (two layers of lead each followed by a silicon strip detector) in front of the endcaps reduces this required length and improves the position determination of electrons and photons, as well as aiding in the identification of π^0.

The characteristics of the $PbWO_4$ crystals make them an appropriate choice for operation at LHC. The high density (8.28 g/cm3), short radiation length (0.89 cm) and small Moliére radius (2.2 cm) result in a fine granularity and a compact calorimeter. The scintillation decay time of these production crystals is of the same order of magnitude as the LHC bunch crossing time: about 80% of the light is emitted in 25 ns.

The electromagnetic calorimeter, shown in Figure 2.12, is divided into two structures:

- The **barrel ECAL** (**EB**) covers the pseudorapidity range $|\eta| < 1.479$, and is situated at $1.24 < r < 1.86$ meters from the interaction point and divided in two halves. Crystals are distributed in modules, each containing 400 or 500 crystals according to the position in η. Four modules are then assembled in a supermodule, which contains 1700 crystals. Eighteen supermodules, each covering 20° in ϕ, form a half barrel. The granularity obtained is $\Delta\eta \times \Delta\phi = 0.0175 \times 0.0175$, corresponding to a crystal front face of about 22×22 mm^2.

- The two **ECAL endcaps** (**EE**) cover the rapidity range $1.479 < \eta < 3.0$. They are formed by two half-disks ("Ds") situated at 3.154 m from the interaction point. Each D consists of 3662 identically shaped crystals grouped in mechanical units of 5x5 crystals (supercrystals, or SCs). The granularity decreases progressively up to $\Delta\eta \times \Delta\phi = 0.05 \times 0.05$ though the crystal front section does not change.

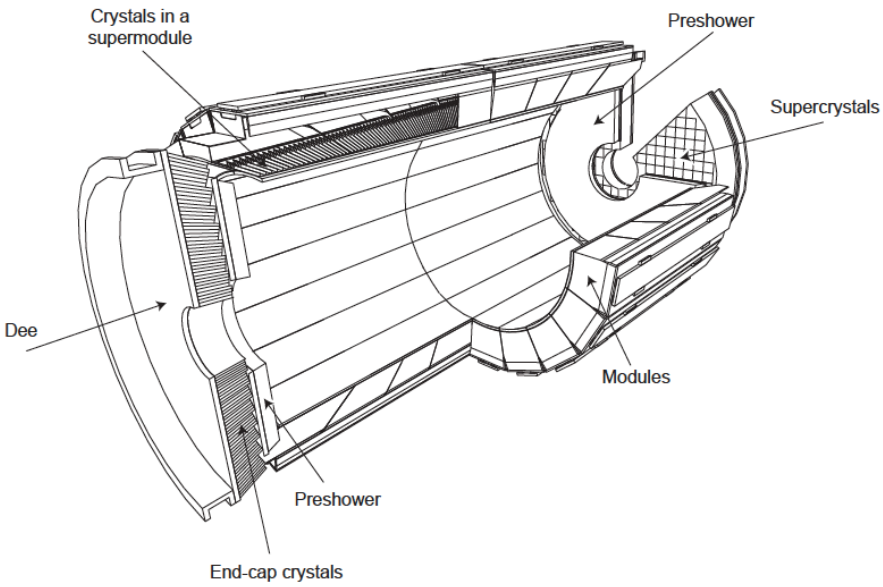

Figure 2.12: Layout of the CMS electromagnetic calorimeter showing the arrangement of crystal modules, supermodules and endcaps, with the preshower in front.

Electrons and photons deposit their energy in the crystals in the form of electromagnetic cascades. The light emitted is detected by avalanche photodiodes (APDs) in the barrel and vacuum phototriodes (VPTs) in the endcaps.

For energies below 500 GeV, where shower leakage from the rear of the calorimeter starts to become significant, the energy resolution can be parametrised as

$$\left(\frac{\sigma_E}{E}\right)^2 = \left(\frac{S}{\sqrt{E}}\right)^2 + \left(\frac{N}{E}\right)^2 + C^2$$

where S is the stochastic term, N the noise term, and C the constant term. The individual contributions are shown in Figure 2.13. The stochastic term includes fluctuations in the shower containment as well as a contribution from photostatistics. The noise term contains the contributions from electronic noise and pileup energy; the former is quite important at low energy, the latter is negligible at low luminosity. The curve labelled intrinsic includes the shower containment and a constant term of C of 0.55%. Terms representing the degradation of the energy resolution at extremely high energies have not been included.

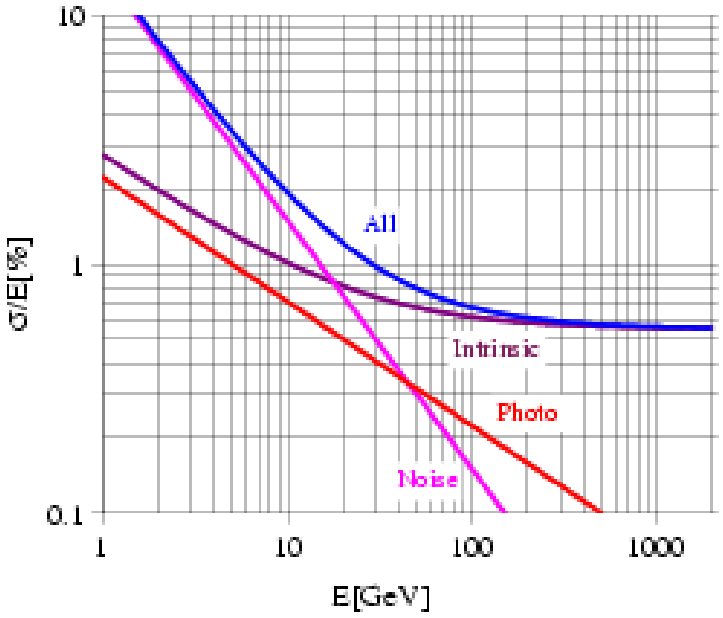

Figure 2.13: Different contributions to the energy resolution of the $PbWO_4$ calorimeter.

2.3.4 Hadronic Calorimeters

The calorimetric system of CMS is completed with a sampling hadronic calorimeter, the HCAL [15; 21]. It completely surrounds the ECAL, and covers a pseudorapidity range up to $|\eta| < 5.2$. The energy and direction of hadrons showers are measured in this subdetector.

Hermeticity is essential to accurately measure the missing energy of neutrinos or other exotic particles. The central barrel and endcap HCAL subdetectors are fully immersed in the magnetic field, and cover up to $|\eta| < 3.0$. Since the magnet restricts the size of the barrel subdetector to R = 2.95 m, an outer hadron calorimeter or tail catcher is placed outside the solenoid complementing the barrel calorimeter. In the forward direction, a Cherenkov-based, radiation-hard technology detector placed at 11.2 m from the interaction point extend the pseudorapidity coverage down to $|\eta| < 5.2$.

The **inner inner HCAL**, (**HB**), is a sampling calorimeter covering the pseudorapidity range $|\eta| < 1.3$. It is divided into two half-barrel sections, each half-section being inserted from either end of the barrel cryostat of the superconducting solenoid. They are composed of 18 identical azimuthal wedges, constructed out of flat brass absorber plates aligned parallel to the beam axis, interleaved with scintillation plastics. Each wedge is segmented into four ϕ sectors. The innermost and outermost plates are made of stainless steel for structural strength. The plastic

scintillator is divided into 16 η sectors, resulting in a segmentation of $(\Delta\eta, \Delta\phi) = (0.087, 0.087)$. The thickness of the absorber grows from 40 mm in the innermost plate to 75 mm in the outermost one.

The **HCAL endcaps**,(**HE**), cover a substantial portion of the rapidity range, $1.3 < \eta < 3.0$ (13.2% of the solid angle), a region containing about 34% of the particles produced in the final state. Brass plates are 79 mm thick with 9 mm gaps to accommodate the scintillators. The granularity obtained is identical to the one in the barrel up to $|\eta| < 1.6$ and increases to $(\Delta\eta, \Delta\phi) = (0.17, 0.17)$ for larger pseudorapidities.

The **outer barrel HCAL**, (**HO**), just before the muon spectrometer, uses the coil of the solenoid as an additional absorber and it is used to identify late starting showers and to measure the energy deposited beyond the coil. Absorber depth is minimal in the central region of the detector (less interaction lengths transversed) so the outer barrel calorimeter has two layers of scintillators in the central ring around $\eta = 0$ and one layer for the rest of the covered region ($|\eta| < 1.3$).

The **forward hadronic calorimeter**, (**HF**),consists of two modules situated in the forward directions, and is designed to resist unprecedented particle fluxes which concentrate around the highest rapidity region. This harsh environment conditioned its design, and quartz fibres were chosen as the active medium to detect the Cherenkov light emitted by showers. It is essentially a cylindrical steel structure with an outer radius of 130.0 cm. Its front face is situated 11.2 m from the interaction point. In addition to ensuring hermeticity, this subdetector plays a crucial role in the determination of luminosity, since coincidences between both directions along the z axis will indicate a collision has taken place.

Several parts of the various HCAL subsystems were exposed to beams of electrons, pions, protons and muons, to measure their characteristics and to obtain a reference calibration. An ECAL module was also included in the test beam setup. The hadronic energy resolution of the barrel HCAL and ECAL combination has been being parametrised as $\sigma/E = a/\sqrt{E} \oplus b$, where a corresponds to a stochastic term and b to a constant term. They were measured in the test beam to be $a = 0.847 \pm 0.016$ GeV$^{1/2}$ and $b = 0.074 \pm 0.008$ [22]. The energy resolution in the endcaps is similar to that in the barrel. The corresponding values for the outer calorimeter are $a = 1.98$ GeV$^{1/2}$ and $b = 0.09$ [23]. Since the forward jets typically have very high energies, the stochastic term can be higher for the outer calorimeter than for the other calorimeters, while still providing the required energy resolution.

2.3.5 Muon detectors

One of the main design objectives of the "Compact Muon Solenoid" was obtaining a high precision muon momentum measurement, given its key role both in New Physics searches and in Standard Model measurements.

Compared to other particles, such as electrons or photons, muons are characterized by their simplicity in identification: between the interaction point and the muon chambers there is a big amount of material (more than 10 interaction lengths) that absorbs practically all other particles. Only muons and neutrinos reach the muon chambers.

The CMS muon system [15; 24] (see Figure 2.14) is composed of three different kinds of gaseous chambers inserted in the segmented iron return yoke. The different particle flux and residual magnetic field found in the various angular regions covered by the muon detectors required the use of different technologies to build each subsystem. In the barrel, up to $|\eta| < 1.2$, the low occupancies and residual field lead to the construction of four *Drift Tube* (DT) stations are situated concentrically around the magnet. In the endcaps, up to $|\eta| < 2.5$, the higher particle density and magnetic field required four disks of finely segmentated *Cathode Strip Chambers* (CSC), situated perpendicular to the beam. DTs and CSCs determine the bending curvature of muons transversing them, and thus measure its inverse momentum and charge. The third kind of chamber, *Resistive Plate Chambers* (RPC), are situated both in barrel and endcaps. They aid in the triggering of muons up to $|\eta| < 1.6$ and complement the reconstruction of the muon trajectory.

- **Drift Tubes (DTs)**

The Barrel Detector consists of 4 concentric stations with a total of 250 chambers inside the magnet return yoke of CMS, distributed into 5 wheels along the Z direction. Each wheel is divided into 12 sectors, each covering a 30° azimuthal angle.

The basic unit of detection (cell) is a tube of 2.5 m of length and 4.2×1.3 cm^2 of section, filled with Ar/CO_2, which ionizes when a charged particle transverses it.

The two innermost stations consist of sandwiches made of a DT chamber placed between two RPCs. The two outermost stations consist of packages of a DT coupled to a RPCs, placed on the innermost side of the station.

Each DT in the three innermost stations, consists of 12 layers of drift tubes divided into 3 groups of 4 consecutive layers, called SuperLayers (SL). Two SLs measure the r-ϕ coordinate in

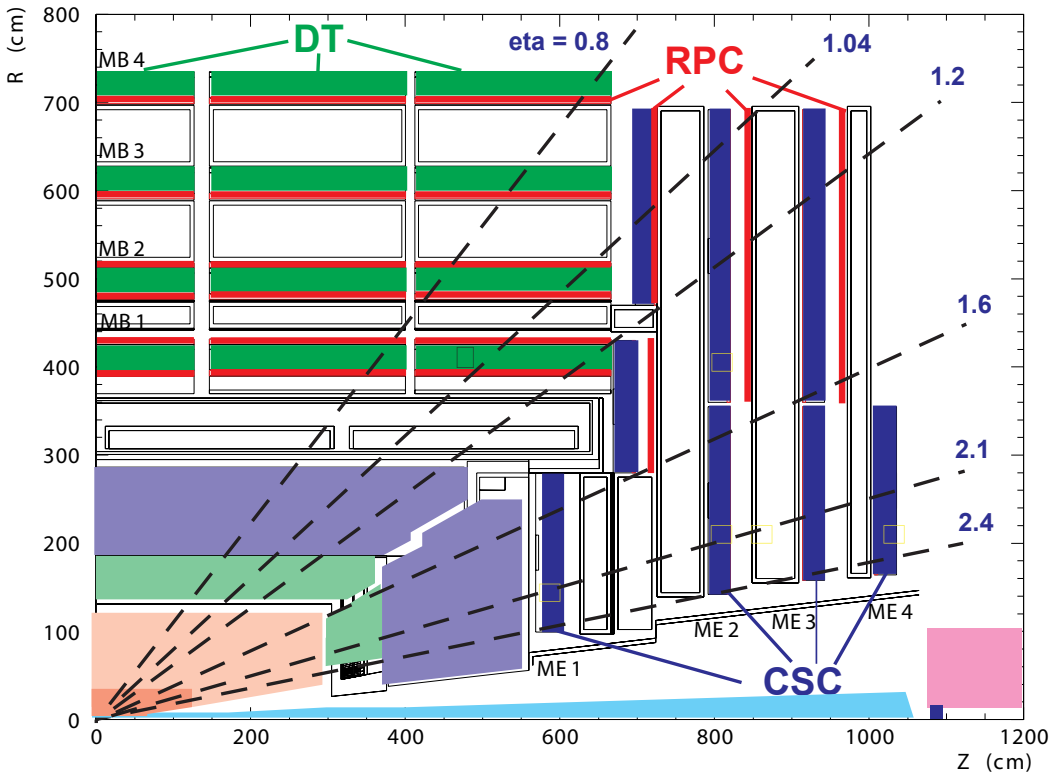

Figure 2.14: Layout of the different subdetectors of which the Muon Spectrometer is composed.

the bending plane (they have wires parallel to the beam line), and the third SL measures the z-coordinate (with wires perpendicular to the beam line). A honeycomb structure gives rigidity to the whole structure, providing a lever arm length of about 28 cm for the measurement of the track direction inside each chamber in the bending plane. In the outermost station, each DT has only the 2 SLs that measure the r-ϕ coordinate.

- **Cathode Strip Chambers (CSCs)**

There are 468 CSCs in the 2 Muon Endcaps. Each encap consists of 4 stations of chambers, which are mounted on the disks enclosing the CMS magnet, perpendicular to the beam direction. In each disk the chambers are situated in 2 concentric rings around the beam axis (3 for the innermost chambers).

Each CSC is trapezoidal in shape and consists of 6 gas gaps, each gap having a plane of radial cathode strips and a plane of anode wires running almost perpendicularly to the strips. All CSC chambers, except those in the innermost station, are overlapped in ϕ to avoid gaps in

the muon acceptance. There are 36 chambers in each ring of a muon station, except for the innermost (highest η) rings starting from the second station which have 18 chambers. The gas ionization and subsequent electron avalanche caused by a charged particle traversing each plane of a chamber produces a charge on the anode wire and an image charge on a group of cathode strips. Thus, each CSC measures the space coordinates (r,ϕ,z) in each of the 6 layers.

- **Resistive Plate Chambers (RPCs)**

The DT and CSC subsystems can both trigger on the passage of muons carrying a minimum momentum, with good efficiency and high background rejection. The Level-1 trigger p_T resolution is about 15% in the barrel and 25% in the endcap.

An additional, dedicated trigger system consists of Resistive Plate Chambers (RPC) both in the barrel and in the endcap regions. The RPCs provide a fast, independent, and highly-segmented trigger with a sharp p_T threshold over a large portion of the rapidity range ($|\eta| < 1.6$) of the muon system. The RPCs are double-gap chambers, operated in avalanche mode to ensure good operation at high rates. They produce a fast response, with good time resolution but coarser position resolution than the DTs or CSCs. They also help to resolve ambiguities in attempting to make tracks from multiple hits in a chamber, and provide additional points for the determination of the muon trajectory.

A total of 6 layers of RPCs are embedded in the barrel muon system, 2 in each of the first 2 stations, and 1 in each of the last 2 stations. The redundancy in the first 2 stations allows the trigger algorithm to work even for low-p_T tracks that may stop before reaching the outer 2 stations. In the endcap region, there is a plane of RPCs in each of the first 3 stations intended for using the coincidences between stations to reduce background, to improve the time resolution for bunch crossing identification, and to achieve a good p_T resolution at trigger level.

Muon identification and measurement is ensured in $10^\circ < \theta < 170^\circ$ thanks to the pseudo-rapidity coverage of the muon detector elements ($\eta < 2.5$, with no acceptance gaps). Offline reconstruction efficiency of simulated single-muon samples is typically 9599%, with some small efficiency drops in the regions between barrel wheels (around $\eta \approx 0.25$ and 0.8) and in the transition between the DT and the CSC systems ($\eta \approx 1.2$). Negligible punch-through reaches the system due to the amount of material in front of the muon system, which exceeds 16 interaction lengths.

The offline muon momentum resolution of the standalone muon system is about 9% for small values of η and transverse momenta up to 200 GeV, dominated by the multiple-scattering in the detector material situated before the first muon station. At 1 TeV the standalone momentum resolution varies between 15% and 40%, depending on η.

2.3.6 Trigger

The total proton-proton cross-section at $\sqrt{s} = 14$ TeV is roughly 100 mb. This implies that at design luminosity and centre-of-mass energy, CMS will observe an event rate of approximately 10^9 events per second. Experimentally this poses a huge challenge. It is technically impossible to record all produced collisions. Detectors must have a response fast enough to cope with a bunch crossing frequency of 40 MHz and rapidly reducing the rate, selecting about 100 events per second to store them for subsequent analysis. This is the mission of the trigger: select online interesting collisions, closing the 6 orders of magnitude gap between produced and recordable.

The CMS trigger and data acquisition system [12] consists of 4 parts: the detector electronics, the Level-1 trigger processors (calorimeter, muon, and global), the readout network, and an online event filter system (processor farm) that executes the software for the High-Level Triggers (HLT).

The size of the LHC detectors and the underground caverns imposes a minimum transit time for signals from the front-end electronics to reach the services cavern housing the Level-1 trigger logic and return back to the detector front-end electronics. The total time allocated for the transit and for reaching a decision to keep or discard data from a particular beam crossing is 3.2 μs. During this time, the detector data must be kept in buffers while trigger data is collected from the front-end electronics and decisions reached that discard a large fraction of events while retaining the small fraction of interactions of interest (nearly 1 crossing in 1000).

Of the total latency, the time allocated to Level-1 trigger calculations is less than 1 μs. Custom hardware processors form the Level-1 decision. The Level-1 triggers involve the calorimetry and muon systems, as well as some correlation of information between these systems. The Level-1 decision is based on the presence of trigger primitive objects such as photons, electrons, muons, and jets above certain E_T or p_T thresholds. It also employs global sums of energy and missing energy in the detector. Reduced-granularity and reduced-resolution data are used to form trigger objects.

During the Level-1 decision-making period, all the high-resolution data is held in pipelined memories. Computer processors make subsequent decisions using more detailed information

from all of the detectors in more and more sophisticated algorithms that approach the quality of final reconstruction. Upon receipt of a Level-1 trigger, after a fixed time interval of about 3.2 μs, the data from the pipelines are transferred to front-end readout buffers. After further signal processing, zero suppression and/or data-compression, the data are placed in dual-port memories for access by the data acquisition (DAQ) system. Each event, with a size of about 1.5 MB, is contained in several hundred front-end readout buffers. Through the event building switch, data from a given event are transferred to a processor. Each processor runs the same high-level trigger (HLT) software code to reduce the Level-1 output rate of 100 kHz to 100 Hz for mass storage. The use of a processor farm for all selections beyond Level-1 allows maximal benefit to be taken from the evolution of computing technology. Flexibility is maximised since there is complete freedom in the selection of the data to access, as well as in the sophistication of the algorithms.

Various strategies guided the development of the HLT code. Rather than reconstruct all possible objects in an event, whenever possible only those objects and regions of the detector that are actually needed are reconstructed. Events are to be discarded as soon as possible. This leads to the idea of partial reconstruction and to the notion of many virtual trigger levels, e.g., calorimeter and muon information are used, followed by use of the tracker pixel data and finally the use of the full event information (including full tracking).

Since this thesis is based on muons, muon triggers are described in some more detail in the following.

2.3.6.1 Muon Triggers

Muon triggers in CMS are based on a global reconstruction process.

Level−1 triggering is performed by the three muon subsystems. DTs in the barrel and CSCs in the endcap ensure sharp momentum thresholds due to their multilayered structure, while the timing resolution of the RPCs allows precise beam crossing identification. The RPC system covers only the region up to $|\eta| < 1.6$, and the CSC trigger provides a reliable p_T measurement up to $|\eta| = 2.1$.

Information is first interpreted locally, then in regions or subsystems and finally in the Global Muon Trigger (GMT). The CSC and DT system deliver one trigger primitive (vector of position, direction, bunch crossing and quality) per muon per station after local reconstruction. These primitives are collected by the Track Finder (TF, "regional trigger"), which build a track already with an estimation of the momentum according to pre-established look-up tables. In the overlap

region, both subsystem exchange segment information. Finally, the four candidates with highest p_T and quality in each subsystems are selected for the final combination in the GMT. The RPCs collect hits from all stations into a Pattern Comparator Trigger logic, which look for aligned hits to form tracks with a momentum estimation. Up to eight best candidates (four in barrel, four in endcap) are sent to the GMT.

The combination of all these regional triggers into a final ensemble of muons, without duplicates, is sent to the global trigger. The momentum measured at this level is discrete.

Reconstructed objects are then filtered by minimal momentum requirements. Each Level−1 object passing this first filters is used as a seed for the Level−2 reconstruction in the muon spectrometer, akin to the reconstruction of standalone tracks offline. After a filtering in p_T and a removal of tracks with shared hits, final Level−2 muons are constrained to pass through the beam spot and injected as seeds into the Level 3 reconstruction, Since tracker track reconstruction is too time consuming to be completely done at trigger level for each event, regional pattern reconstruction in the silicon tracker are produced only in a small slice around the Level−2 muon. An inner track is therefore reconstructed, and matched to the Level−2 muon. The final combined fit yields a Level−3 muon track, on which the final requirements can be applied, for instance the final p_T threshold.

2.3.7 Computing at CMS

The CMS software and computing systems cover a broad range of activities. It organizes the storage, reconstruction and distribution of the data; it also takes care of generation and simulation of Monte Carlo samples needed for the physics analysis; and finally provides the necessary framework for data analysis.

Even after the trigger system has reduced the collision rate enough to be stored in tape, CMS still produces a huge amount of data that must be analysed: more than five petabytes per year when running at nominal luminosity. To meet this challenge, the LHC employs the Worldwide LHC Computing Grid (WLCG), a distributed computing and data storage infrastructure.

The CMS computing model [25] is structured in a series of "Tiers" or computer centres, from the *Tier 0* centre at CERN and the large *Tier 1* centres in seven countries around the world (including Spain), to smaller, institute based, *Tier 2* centres. In this way information branches out from each Tier, and the analysis of the final data can be performed locally all around the world.

Before the data enters in the Tier system, calibration and express stream analysis are performed in the CERN Analysis Facility, CAF. The CAF is dedicated to latency critical activities like Calibration and Alignment, Detector/Trigger Commissioning or High Priority Physics Analysis.

The CMS software framework (CMSSW) is an object-oriented structure based on C++ and python. The data formats used are compatible with ROOT [26], and consist on "trees" organising the event information.

To facilitate development, CMS consolidates its code base regularly into releases. Different releases are grouped into release cycles (for example, data taking and reconstruction in a particular LHC collision period or integration of a new ROOT version) to aggregate specific feature sets of the software stack. The fast development cycle of the CMS software and the resulting high number of releases requires a thorough quality assurance process. To guarantee stable releases while supporting fast development, CMS implemented an advanced central release validation process.

Chapter 3

The 2010 LHC Run

The first proton-proton collisions of the LHC took place at injection energy ($E_b = 450$ GeV), the 23^{th} of November of 2009. This first pilot run, followed by a first beam acceleration a week later to an energy to $E_b = 1.18$ TeV was intended for commissioning and testing the accelerator chain. Beams with an intensity of $I_{beam} \approx 10^9$ protons collided one to one in the four LHC experiments.

In order to guarantee a safe operation of the accelerator as well as competitiveness for the scientific results obtained, the collision energy for the first year of operation was set at $\sqrt{s} = 7$ TeV. Beams accelerated to 3.5 TeV and composed of a single bunch with 10^{10} protons collided for the first time the 30th of March of 2010 in the four LHC experiments. First physics results (charged particle distributions and low mass resonances) were produced promptly by the four experiments marking the start of the so called "2010 Run".

All through 2010 the LHC was in continuous commissioning of the beam parameters, the most important entering the mathematical formulation of the instantaneous luminosity delivered to the experiments, already presented in the previous chapter:

$$L = \frac{1}{4\pi \cdot m_0 c^2} \cdot \frac{f_{rev} N_p F}{\beta^\star \epsilon_n} E_{stored}$$

The low initial luminosity, $L \approx 10^{25}\ cm^{-2}s^{-1}$, was in continuous increase through the seven months of operation towards a final value seven orders of magnitude higher. Geometrical factors such as the frequency (described in section 2.2) are fixed by design. Therefore this increase was achieved through the reduction or "squeeze" of beam size ($\beta^\star$), the increase of the number of particles per bunch (N_p), and the increase of the energy stored in the beam (E_{stored}), via the increase of the number of colliding bunches.

Data-taking was not continuous through the year. Periods of "stable beams" dedicated to data taking for physics alternated with short "technical stops" dedicated to machine development. Each one of this stops signified a clear improvement in the instantaneous luminosity, and typically a factor of two increase in the integrated luminosity available for later analysis.

This first period of the LHC program has been therefore characterised by the commissioning of the beams and the accelerator components, which performed well beyond the initial expectations. Design intensity of the beams (1.1×10^{11} protons per bunch) was achieved, and a peak luminosity of $2 \times 10^{32}\ cm^{-2}s^{-1}$ was reached at the end of the run. The last step in the luminosity increase towards the 2010 goal was the increase in the number of bunches per collision, from 1x1 until 368x368. The length of the "fills" (time period from the injection of the beams until they are safely dumped to initiate a new cycle) also increased through the year, the longest of them exceeding 24 hours. Final values of the collider parameters are shown in Table 3.

Table 3.1: LHC Beam Parameters during 2010, at the end of the two periods in which the run can be divided: "A" until September (data presented in this thesis) and "B" until the end of the proton run in November.

Parameter	March-September	September-November
E_{beam}	3.5 TeV	
Dipole field B	4.17 T	
Protons per bunch	1.15e11	
ϵ_n Norm. transverse emittance	3.75μm	2.5μm
$\beta^\star$ IP5 beta value	3.5 m	
Max. number of bunches per beam	50	368
Peak E_{stored} Stored energy	2.8MJ	28 MJ
Average collisions per crossing	1.5	2.7
Peak Luminosity	10^{31} cm^{-2}s^{-1}	2×10^{32} cm^{-2}s^{-1}

Figure 3.1 shows the integrated luminosity and the peak luminosity as a function of time delivered to the 4 LHC experiments during year 2010. Both luminosity plots show an increasing steepness versus time, being essentially correlated one to the other. The total integrated luminosity delivered to the experiments was of $\approx 47\text{pb}^{-1}$ to ATLAS, CMS and LHC-b and $\approx 0.8\text{pb}^{-1}$, to ALICE. The plateaus in the integrated luminosity plot correspond to the above mentioned machine development technical stops, which can be seen in the instantaneous luminosity plot.

On the 5th of November of 2010, the LHC changed mode from proton-proton collision to

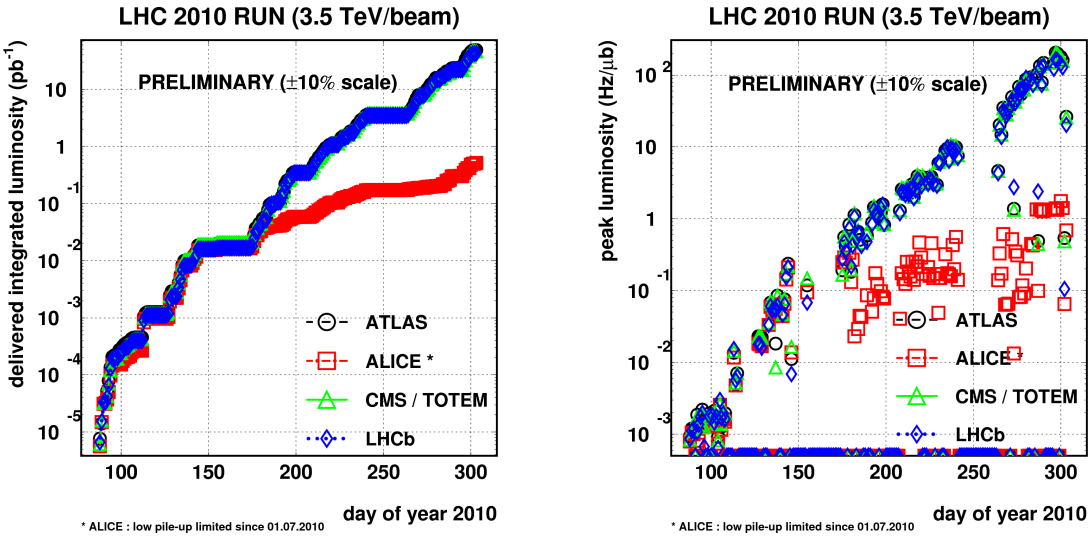

Figure 3.1: Luminosity delivered by the LHC. a) Increase of delivered integrated luminosity as a function of day of year 2010. b) Peak instantaneous luminosity also as a function of time.

Pb-Pb nucleus collisions for a month. Approximately an integrated luminosity of $10\mu b^{-1}$ of collision data were delivered to the experiments during this run.

After a short stop at the end of the year, proton-proton collisions will be resumed in 2011 with the aim of recording an integrated luminosity of $\approx 5 - 10\text{fb}^{-1}$ through the years 2011 and 2012. This goal will mark the end of the first low energy run, and will be followed by a shutdown in which the LHC will be commissioned for its design energy of 14 TeV.

3.1 Operation of the CMS detector

Although the first collisions of the LHC were recorded in late 2009, the CMS detector had been operational long before this date. CMS exploited cosmic ray muons as a calibration and commissioning tool for the data-taking chain and the performance of the detectors. These runs started as early as 2006 with the detector partially assembled on surface, followed with two other data-taking campaigns in 2008 and 2009 once the detector was already installed in the underground experimental cavern. Each of these runs recorded more than 300 million cosmics muons. In addition more than a million beam halo muons were recorded during 2008, 2009 and 2010 during LHC commissioning.

All the analysis performed using this cosmic and halo muons events were invaluable:

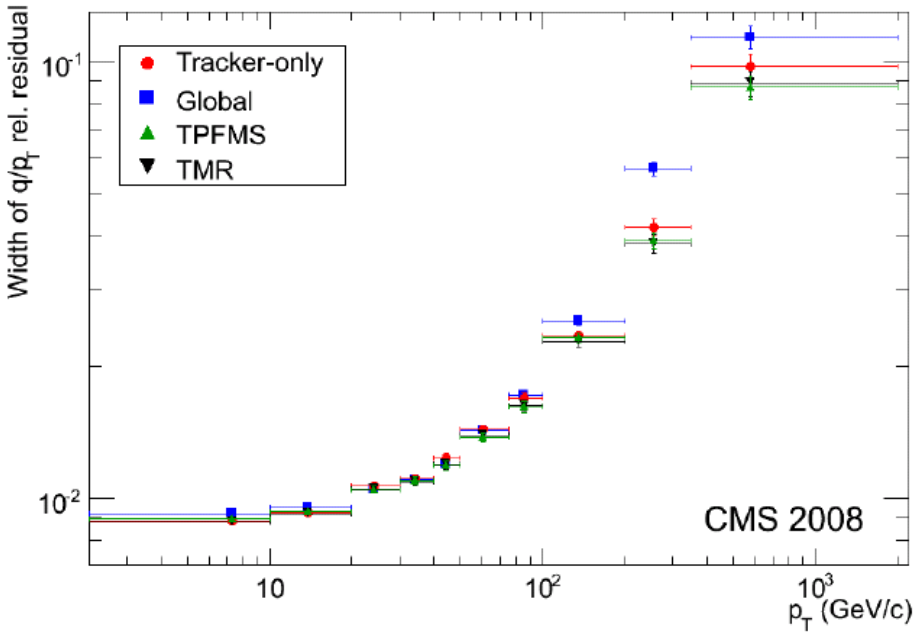

Figure 3.2: Muon Momentum Resolution measured on cosmic muons during the Cosmic Run At Four Tesla (CRAFT) as a function of transverse momentum of the reference track. [27]

- To establish the alignment of the detector to the level previously foreseen only after the first 10 pb^{-1} of collision data had been analysed [28; 29]
- To improve the modelling of the magnetic field. The new map is estimated to be accurate to better than 0.1% in the tracker volume, 3% in the steel of the three central barrel wheels, and to about 8% in the steel of the two outermost barrel wheels [17],
- To test the response of the different components of the detector.

An example of the importance of these studies is shown in Figure 3.2. The momentum resolution of cosmic muons measured during 2008 is shown here for different muon reconstruction algorithms, including the one used in this thesis (section 5.2.1). The resolution obtained, of the order of 1% for transverse momenta smaller than 100 GeV, is already at design-level. [27].

The calibrations obtained were incorporated to the reconstruction software before the pilot run at $\sqrt{s} = 900$ GeV and $\sqrt{s} = 2.36$ TeV in 2009.

In this first pilot run, CMS collected approximately 350 thousand collision events ($L_{int} \approx 10\ \mu b^{-1}$) at $\sqrt{s} = 0.9$ TeV and 20 thousand events ($L_{int} \approx 0.40\ \mu b^{-1}$) at $\sqrt{s} = 2.36$ TeV. Even though this recorded data-sample is very small compared to the size of the Run2010 data set, it

was still extremely useful to test the detector performance reconstructing and analysing the first collision events, in addition to providing the first physics results of CMS (measurement of the charge-hadron transverse-momentum and pseudo-rapidity distributions on pp collisions) [30].

The expertise obtained in the 2009 run was also incorporated to the detector simulation, and reconstruction algorithms were tuned accordingly to prepare for the 2010 Run.

The 2010 CMS Run can be divided in three main periods, separated by two relatively large technical stops of the LHC. A commissioning period before the technical stop in June, with several minor machine development stops in between, in which the integrated luminosity recorded was very low (≈ 8 nb^{-1}). A second long data-taking period in the summer (Run2010A), recording a considerably higher integrated luminosity (≈ 3 pb^{-1}). The final stretch of data-taking after the technical stop in September, Run2010B, despite being the shortest in time, collected most of the statistics of 2010 (≈ 44 pb^{-1}). These two stops were critical for increasing the instantaneous luminosity.

In usual operation mode CMS is always active and recording data. Only while the accelerator is in development mode, and also while the LHC prepares for collisions (injecting, ramping and squeezing the beams), the most delicate detectors are brought to a safe "stand-by" status. Otherwise the instabilities of the beams could harm the equipment. Once the beam conditions are stable and the beginning of a physics run is declared, the high voltage of the different subsystems is raised from this safe status to operation mode.

The integrated luminosity delivered to CMS during Run2010A was 3.6 ± 0.4 pb^{-1} (3.3 ± 0.4 pb^{-1} recorded), as shown in Figure 3.3 (left). The overall data taking efficiency of the experiment during this period was of $\epsilon = \frac{L(recorded)}{L(delivered)} = 92\%$. This data collected by CMS is organized in "runs", experimental collections of data corresponding to stable periods of data taking.

Detector problems can also force the detector to stop momentarily before data-taking is re-assumed. This minimal stops, together with the intrinsic turning on of the detector, cause small periods of "down-time". A graphical example, where the origin of downtime is split by subdetectors, is shown in Figure 3.4. Downtime during the Commissioning and Run2010A periods was remarkably small, being dominated by data-acquisition errors from the inner detectors.

The overall data taking efficiency CMS experiment during all of 2010 was 91.72%. The integrated luminosity delivered in total to CMS was of 46.36 pb^{-1} (42.52 pb^{-1} recorded), as shown in logarithmic scale in Figure 3.3 (right).

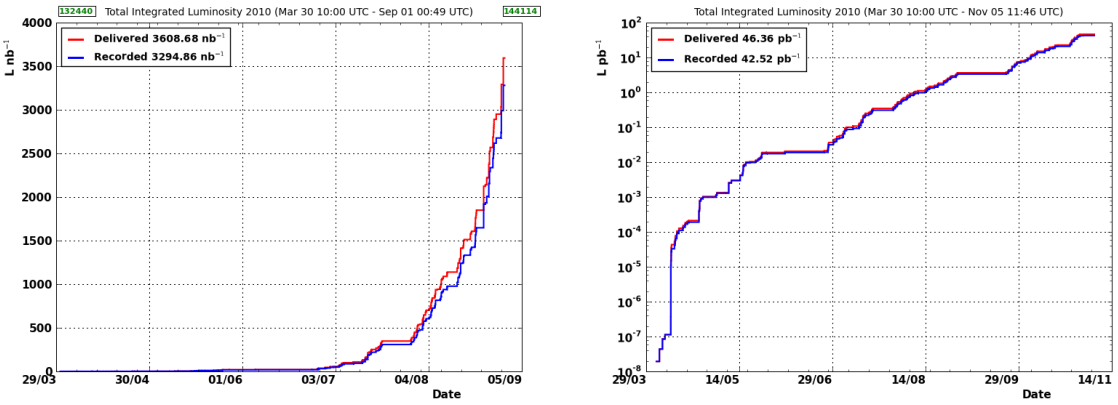

Figure 3.3: Luminosity collected by CMS during 2010: for Run2010A (left), in which this thesis is based, and for the total 2010 dataset (right).

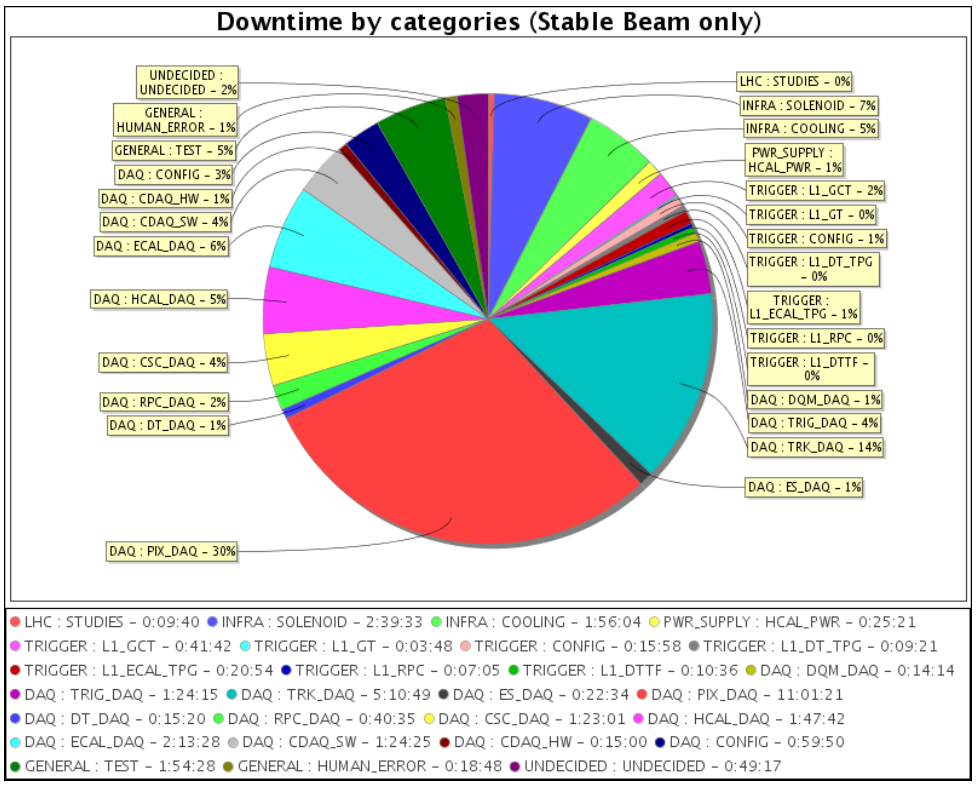

Figure 3.4: Downtime graphic split by subdetector during Run 2010A

3.1.1 Datasets

As explained in Section 2.3.6, the experiment employs a trigger system composed of several steps to filter online all collision events produced at the interaction point. Only interesting events pass a first online selection which depends on fast object identification are saved in different "streams" or "datasets". These streams are defined by the characteristics of the events recorded, according to some pre-defined criteria or "menus". For example, "muon" streams record events in which the online reconstruction has identified one or more muons.

A first *Express* reconstruction of these events is performed within hours of data-taking for fast validation of the data. A second reconstruction with updated calibrations and software is performed afterwards, still in a time scale appropriate for first analysis. This *Prompt* reconstruction may be re-reprocessed later to incorporate new calibrations and code improvements.

The rapidly changing conditions of the accelerator during the 2010 Run is reflected in the evolution of the data-taking conditions. Since trigger rates in the first months were very low compared to expected nominal ones, the first collisions were recorded using very open trigger requirements, and collected in a single-dataset which gathered all kinds of events ("MinimumBias"). As instantaneous luminosity was increased, data-taking evolved accordingly classifying events into streams ("Primary Datasets") based on analysis objects (muons, electrons/photons and Jets/Missing Energy/Taus).

The evolution of the Primary Datasets during Run2010A is shown in Figure 3.1.1. In particular for the Muon triggers, the comprehensive "MinimumBias" dataset was soon split into a dedicated commissioning primary dataset ("MuMonitor", consistent on trigger paths based in detector activity) and a main, analysis stream ("Mu"), which was subsequently branched into a stream dedicated to low momentum studies (including J/Ψ and Υ studies, "MuOnia", which requires the presence of two muons of low momentum), and a more general stream ("Mu", which demands at least one muon of relatively high momentum).

This thesis is based on the data collected during Run2010A, between 31st of March and September 3rd, and corresponds to runs numbers 132440 up to 144114. The datasets used are summarised in Table 3.2. The integrated luminosity accumulated in this first run is of $3.3 \pm 0.4\text{pb}^{-1}$.

3.1.2 Data Quality Monitoring

The quality of the data used in all CMS analysis is guaranteed by a careful and prompt control of the detector conditions and the reconstruction chain and objects.

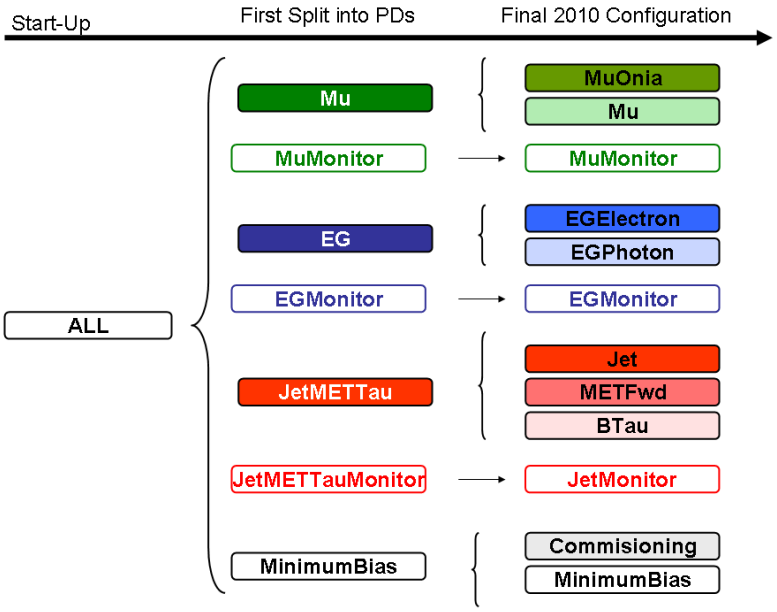

Figure 3.5: Schematic evolution of the Primary Datasets.

Table 3.2: Analysed data, reprocessed with the CMS software version $CMSSW\_3\_6\_1\_patch4$

DataSet Name	L ($cm^{-2}s^{-1}$)	Run Range	$\int Ldt$ (recorded)
/MinimumBias/Commissioning10-SD _Mu-Jun14thSkim_v1	10^{29}	132440 - 135802	8.9 nb^{-1}
/Mu/Run2010A-Jun14thSkim _v1	10^{29}	135821 - 137435	8.8 nb^{-1}
/Mu/Run2010A-Jul16thReReco _v1	10^{30}	139779 - 140159	123 nb^{-1}
/Mu/Run2010A-PromptReco-v4	10^{30}-10^{31}	137426 - 139459, 140160 - 144114	3.105 pb^{-1}

The "Data Quality Monitoring" (DQM) system of CMS is an archive of the information of each run taken in CMS. This information is stored in the form of one-dimensional and two-dimensional histograms, for different levels of granularity. This catalogue permits fast access to information from the performance of hardware (for instance, individual channel efficiencies and occupancies) to high level object variables (such as the beam-spot position, the momentum distribution of charged particles or the reconstructed energy of the event). Plots are stored hierarchically and allow the computation of trends as a function of time and comparison with reference histograms.

It can aid to detect malfunctioning of the detectors online, just as the data is being recorded.

It is used as the first alert level to stop the run if needed and take actions to correct the faulty subsystem.

The plots stored are further scrutinised by experts in order to provide a quality assessment of the data recorded. This task is performed as the data is being recorded, controlling of the detector performance "online" (first hardware-related control that everything performs as expected) and also on the first, fast, data delivered to the "offline" analysis (second control performed on the first Express reconstruction, not only at detector-level, but also on the basic reconstructed objects such as muons).

This assessment is not performed on a run-by-run basis, but as a function of smaller units, lumisections (defined as the longest period in which both the accelerator and the detectors can be assumed to be stable).

Lumisections are certified if no anomaly or faulty behaviour is found. Depending on the nature of the test failed, these excluded lumisections may be recovered in further reprocessings of the data (if they are due to noisy channels or wrong calibrations easily circumvented at reconstruction level).

This certification procedure is performed in several steps, from the first fast look at the control room in the experimental area to a offline careful expert validation. The production of a common list of "good lumisections" for all CMS detectors and objects is centralised for all CMS analysis.

As an example, muon certification online monitors the status of the efficiencies, occupancies, rates and pulse shapes of the three muon subsystems (DT, CSC, RPC), comparing with a stable reference. Offline, a further check on reconstructed quantities such as the muon momentum is performed, controlling that resolution and momentum validity is comparable with previous data.

Taking into account these quality tests 3.1 ± 0.4 pb^{-1} of data have been certified as optimal for physics analysis out of the 3.35 ± 0.4 pb^{-1} recorded during Run 2010A. The certification efficiency during this first part of the data taking is therefore $\epsilon_{cert} = \frac{certified}{recorded} = 88\%$.

The individual certification efficiency, split by subdetectors (DT, RPC, ECAL...) and offline objects (Muons, Jets, Missing Transverse Energy, Electrons...) was over 80% (with respect to delivered luminosity) for all subsystems, as shown in Figure 3.1.2. Both online and offline certification are taken into account. Good runs are shown in green, bad runs in red, runs in which the system was excluded in grey.

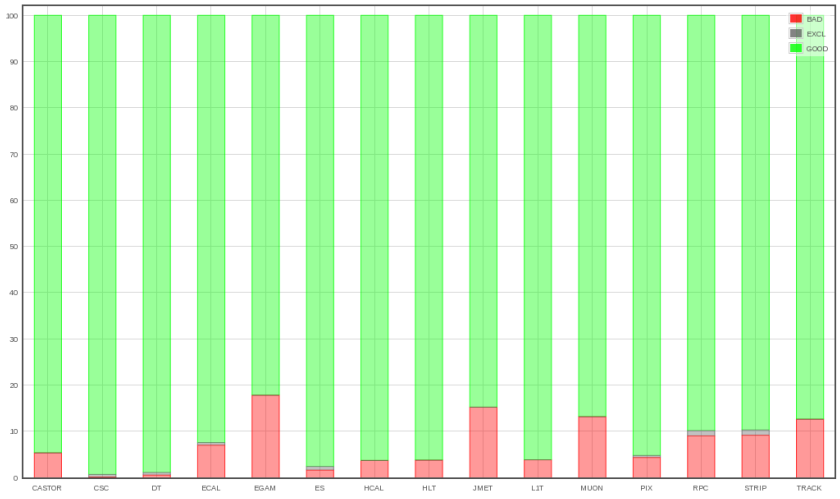

Figure 3.6: Certification Efficiency by subsystem in Run 2010 A, with respect to all collision runs. The faulty periods (red) include downtime of detectors

Besides the DQM programs oriented to detector and basic object monitoring at data-taking level, there is a further level of Data Quality Monitoring oriented to physics. Basic analysis can be performed on this data, with the constraints of keeping techniques simple enough not to require complex tools. One of the physics channels with a dedicated area in DQM is the Vector Boson (W,Z) decay into muons. Some information about this system is found in the Appendix.

3.2 First CMS Results at 7 TeV

For all subdetectors and physics groups, this first data has served not only as the first calibration tool to improve the quality of the physical objects reconstruction (electrons, muons, met, jets), but also to produce the first physic results.

Most physical objects were validated within the first four months of LHC operation, with only 0.3 pb^{-1} of data.

As an example of the excellent performance of the muon systems Figure 3.7 shows the reconstruction of the dimuon spectra, from the ρ and ω resonances to the Z peak, with the full 2010 data-sample. An equivalent plot for the dielectron spectra is shown in Figure 3.8.

The process analysed in this thesis, the muonic decay of the W boson, has been one of the benchmark examples of this performance.

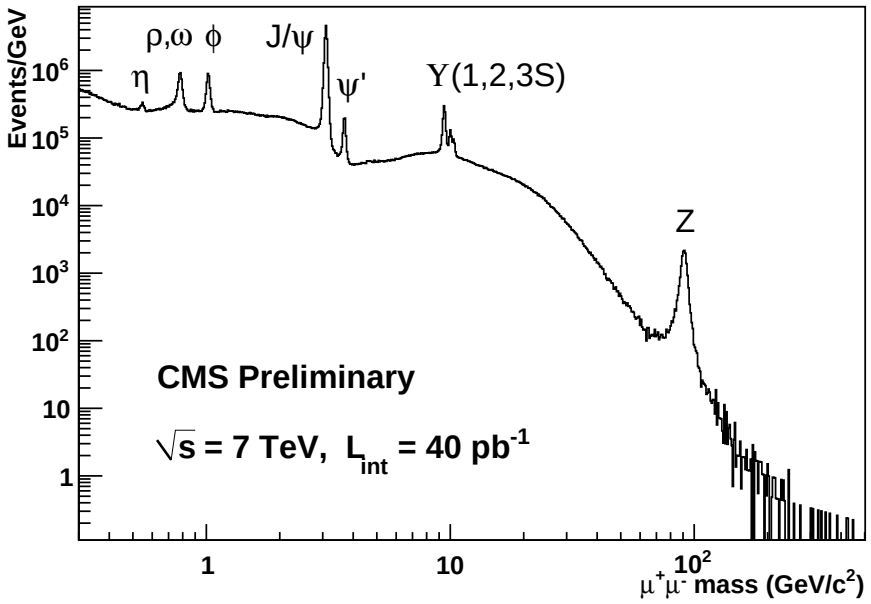

Figure 3.7: Dimuon Spectra reconstructed by CMS for an integrated luminosity of 40 pb^{-1}

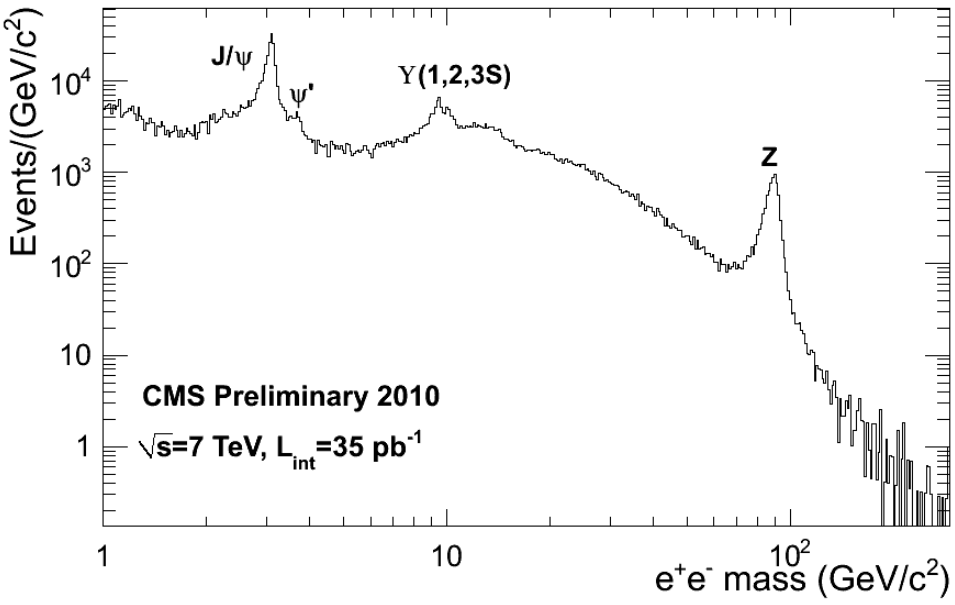

Figure 3.8: Dielectron Spectra reconstructed by CMS for an integrated luminosity of 35 pb^{-1}

Chapter 4

The physics of W and Z at the LHC

The LHC physics program is large and ambitious, its ultimate goal answering many of the unresolved questions of particle physics. The area of ElectroWeak Physics, already tested in past experiments, will provide some of the first improvements in our knowledge of the physics at the TeV scale.

W and Z bosons ("weak bosons") are the elementary particles that mediate the weak interaction. They have an extremely short half-life ($\approx 3 \times 10^{-25}\ s$) and decay almost immediately into other particles at the typical energies of accelerators.

They are amongst the heaviest elementary particles. With masses of $M_W = 80.399 \pm 0.023$ GeV and $M_Z = 91.1876 \pm 0.0021$ GeV [4], related by the expression $M_W = M_Z \sin(\theta_W)$, W and Z bosons are almost 100 times more massive than the proton, and only lighter than the top quark ($M_{top} \approx 175$ GeV).

Although the electroweak domain has been extensively studied in LEP, SLAC and Tevatron, the LHC implies a large step forward in energy and luminosity. As a result the LHC will be a W and Z factory, with over 100 bosons produced per second in nominal conditions. W and Z observables will constitute unique tools for testing the validity of the Standard Model in proton-proton collisions at 7 TeV scale.

The cross-section versus centre of mass energy of different processes at the LHC was already presented in Chapter 2 (see Figure 2.4) [9]. As we can see in this graphic, W and Z production ($\sigma_V \approx 10^2$ nb) is, after jet and $b\bar{b}$ production, the dominant process at the LHC. It will constitute a non-negligible (and sometimes irreducible) background for most of the searches foreseen. It is then clear that without a solid understanding of the physics of W, Z, none of the discoveries the LHC is aiming for can be attained.

The data collected by the LHC in 2010 has provided electroweak measurements which can already be checked against theoretical predictions, such as the inclusive production cross-section or the ratio of W/Z or W^+/W^- cross-sections. Further precision measurements, such as the mass of the W boson, require a higher integrated luminosity to be performed, and will ultimately provide important inputs for internal consistency checks of the Standard Model.

We can safely conclude that a solid understanding of the production of the W and Z bosons at the LHC will set the foundations of our knowledge of particle physics in the new energetic regime.

4.1 Production of Vector Bosons in the LHC

W and Z bosons are produced in electroweak processes, by interaction of two weakly charged particles. However, in order to describe the physics involved in their production at the LHC, we cannot only restrict ourselves to the study of the electroweak effects. QCD will play a mayor role in the study of the production of any particle in a proton-proton collider, and its effects will have to be taken into account.

Particles at the LHC are produced in parton-parton interactions. Partons (quarks and gluons) are the constituents of the colliding hadrons, and carry a fraction x of their momentum.

Since the LHC is a proton-proton collider, and the ground state for protons is (uud), partons can primarily be the u or d quarks composing the proton ("valence" quarks). Due to their asymptotic freedom, these u and d quarks radiate gluons which can in turn split into quark-antiquark pairs, forming a "sea" of particles. The probability of radiation grows with the energy of the partons, and therefore the influence of sea quarks and gluons will be enhanced as the centre-of-mass energy of the proton-proton collision increases.

Therefore at the LHC W and Z bosons are produced by interaction of all flavours of quarks and antiquarks. Z bosons are mainly produced in $u\bar{u}$ and $d\bar{d}$ annihilation, while the dominant diagrams for W production is $u\bar{d}$ (W^+) and $d\bar{u}$ (W^-).

These tree or *leading order* (LO) diagrams are shown in Figure 4.1.

The leading order diagrams for W and Z production in quark-quark collision ($q(p_1)q'(p_2) \rightarrow W(p)$ or $Z(p)$) correspond to the following matrix element, where $V_{qq'}$ is the appropriate element of the CKM matrix:

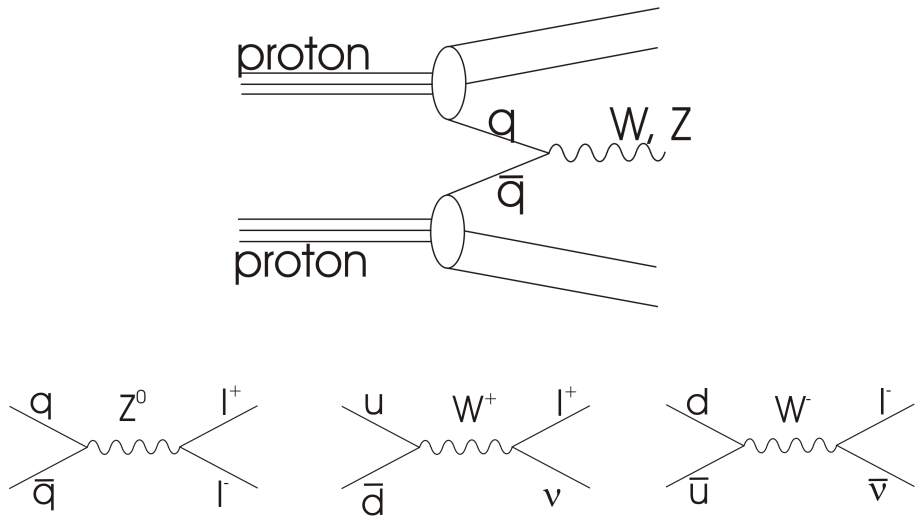

Figure 4.1: a) The upper figure shows the Feynman diagram for the interaction between two protons resulting in two partons which collide to form a weak boson. b) The lower image shows the main Feynman diagrams for W and Z production, and the subsequent leptonic decay.

$$\mathcal{M}(W) = -iV_{qq'}\frac{g}{\sqrt{2}}\epsilon_\alpha \bar{v}(p_2)\gamma^\alpha \frac{1}{2}(1-\gamma_5)u(p_1)$$
$$\mathcal{M}(Z) = -ig\epsilon_\alpha \bar{v}(p_2)\gamma^\alpha (g_V + g_A\gamma_5)u(p_1)$$

These matrix elements lead to expressions for the partonic cross-sections (σ_{ab}), which depend on the flavour of the colliding quarks (in this notation, the partons will be labelled a and b). The hard interaction that describes the parton-parton process is computable as a power series expansion in the QCD coupling α_s. If μ_R represents the renormalisation scale for the QCD running coupling, and k depends on the final state of the interaction, [31]:

$$\begin{aligned}\sigma_{ab}(x_1, x_2, Q^2) &= \alpha_s^k(\mu_R)\sum_l \alpha_s(\mu_R)\sigma_{ab}^l \\ &= \alpha_s^k(\mu_R)\left(\sigma_{ab}^{(LO)} + \alpha_s(\mu_R)\sigma_{ab}^{(NLO)} + \alpha_s(\mu_R)^2\sigma_{ab}^{(NNLO)} + ...\right)\end{aligned}$$

If this calculation of the hard cross section was performed at all orders, it would be independent of the renormalization scale. However, it has to be truncated. The lowest term of the cross-section, σ_{ab}^{LO} (leading order or LO), gives only a rough estimate of the cross-section. W and Z production is a well understood theoretically process, and current estimates of the hard

cross-section go up to next-to-next-to leading order (NNLO) in QCD. As an example, in the case of W production the cross-section is increased by a 30% when moving to the NNLO prediction from the tree level LO cross-section.

Given that at the LHC collisions of all flavour combinations will take place, in order to obtain the total cross-section these contributions will have to be integrated for all possible energies and momentum fractions of the incoming partons taking into account their relative abundance.

In general, the production cross-section of any particle at a hadron collider can be theoretically described as the convolution of the described hard scattering cross-section of the two partons σ_{ab} with the parton density functions (PDFs, parametrizations of the proton internal structure, $f_a(x_1, Q^2)$ and $f_b(x_2, Q^2)$) at a given energy scale, summed over all possible initial partonic states [32]:

$$\sigma_{pp\to VX} = \sum_{a,b} \int dx_1 dx_2 f_a(x_1, Q^2) f_b(x_2, Q^2) \sigma_{ab\to VX}(x_1, x_2, Q^2, \alpha_s(Q))$$

For momentum fractions x_1 and x_2 and momentum transfer Q^2.

The factorisation theorem for short-distance inclusive processes allows us to separate parton scattering (high-energy, short-range) from the rest of the hadronic interaction (low-energy, long-range). This way the partonic interaction can be calculated from perturbative QCD as described, and the low-energy part is included into the parton density functions themselves.

Parton luminosity ($f_a \otimes f_b$) is given as the convolution of the parton distribution functions in the proton. The PDFs are universal, and thus can be computed from data of existing experiments (HERA data) and extrapolated to higher centre-of-mass energies. They cannot be calculated perturbatively, and need to be obtained from a parametrisation of the partonic content of the proton obtained from global fits to data. The x dependence of the PDFs is parametrised at a given scale Q_0^2 (1-10 GeV^2) and then evolved using the DGLAP equations to obtain the $f_i(x_a, Q^2)$. The evolution of the PDFs is governed by the perturbatively calculable Altarelli-Parisi splitting functions P_{ij}, known to NNLO in QCD [33].

$$Q^2 \frac{df_a(x, Q^2)}{dQ^2} = \sum_b \int_x^1 \frac{dz}{z} P_{ab}(\alpha_s(Q), z) f_a(x/z, Q^2) \quad (DGLAP\ eqn)$$

$$P_{ab}(\alpha_s, z) = \alpha_s P_{ab}^{(LO)}(z) + \alpha_s^2 P_{ab}^{(NLO)}(z) + \alpha_s^3 P_{ab}^{(NNLO)} + O(\alpha_s^4) \quad (AP\ splitting\ functions)$$

The relative contribution of the different partons $a = q, g$ to the final integral are controlled by the kinematics (rapidity y and momentum Q) of the hard scattering process. There is a smooth but non-negligible dependence in the energy scale of the process, $Q^2 = x_1 x_2 s$. The

dominant values of the momentum fractions are $x_{a,b} \approx M\ e^{\pm y}/\sqrt{s}$, where $s = (p_a + p_b)^2$ is the square of the centre-of-mass energy of the collision. Increasing the energy we probe the parton density functions in a range that extends towards larger values of Q and smaller values of $x_{a,b}$. This is illustrated in Figure 4.2[9], which shows the value of Q^2 versus x in the LHC, for the production of objects with mass M and rapidity y.

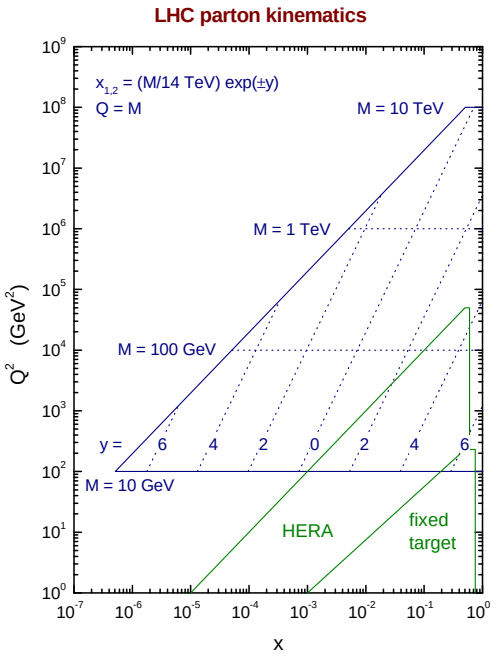

Figure 4.2: Values of x and Q^2 probed in the production of an object of mass M and rapidity y at the LHC ($\sqrt{s} = 14$ TeV).

As explained, in proton-proton collisions W and Z bosons are produced by "Valence-Sea" and "Sea-Sea" interactions [34]. The energy range under study at central rapidities corresponds to the low momentum fraction x regime ($10^{-4} < x < 10^{-2}$, at 7 TeV) of the participating partons. The predictions are dominated by uncertainties on the parametrization of sea quarks and gluons, since at $Q^2 \sim M_{W(Z)}$ the sea quark comes mainly from the gluon (via gluon splitting), and is far less precisely determined than valence quarks for all x values.

The NNLO PDF scale for the different partons at $Q^2 = 10$ GeV^2 (original Q_0 value from HERA experiments to which DGLAP equations are applied) and $Q^2 = 10^4$ GeV^2 ($Q^2 \sim M_{W(Z)}$) is shown in Figure 4.3, calculated by the MSTW group using NNLO pdfs at 68% of C.L. [9]. The figure shows the behaviour of $xf_a(x, Q^2)$ for the different partons, as a function of the momentum fraction x. It can be seen that for the low momentum fraction regime the uncertainties on the gluon and sea quarks bands are much larger than the ones corresponding to u and d valence quarks.

Besides this hard scattering process ($u\bar{d} \to W^+$, $d\bar{u} \to W^-$), the proton remnants give rise to additional activity, identified as "initial state radiation". This ISR is mostly of hadronic type, with a smaller contribution of photons. To go beyond the LO collinear (radiation close to the beams) and soft (small energy emission) limits, a NLO treatment is necessary, including the calculation of the production of W bosons accompanied by jets [35]. Higher order effects (NNLO) should only affect the total cross-section of the process, having a minimal impact on the angular distribution of the resulting particles [36].

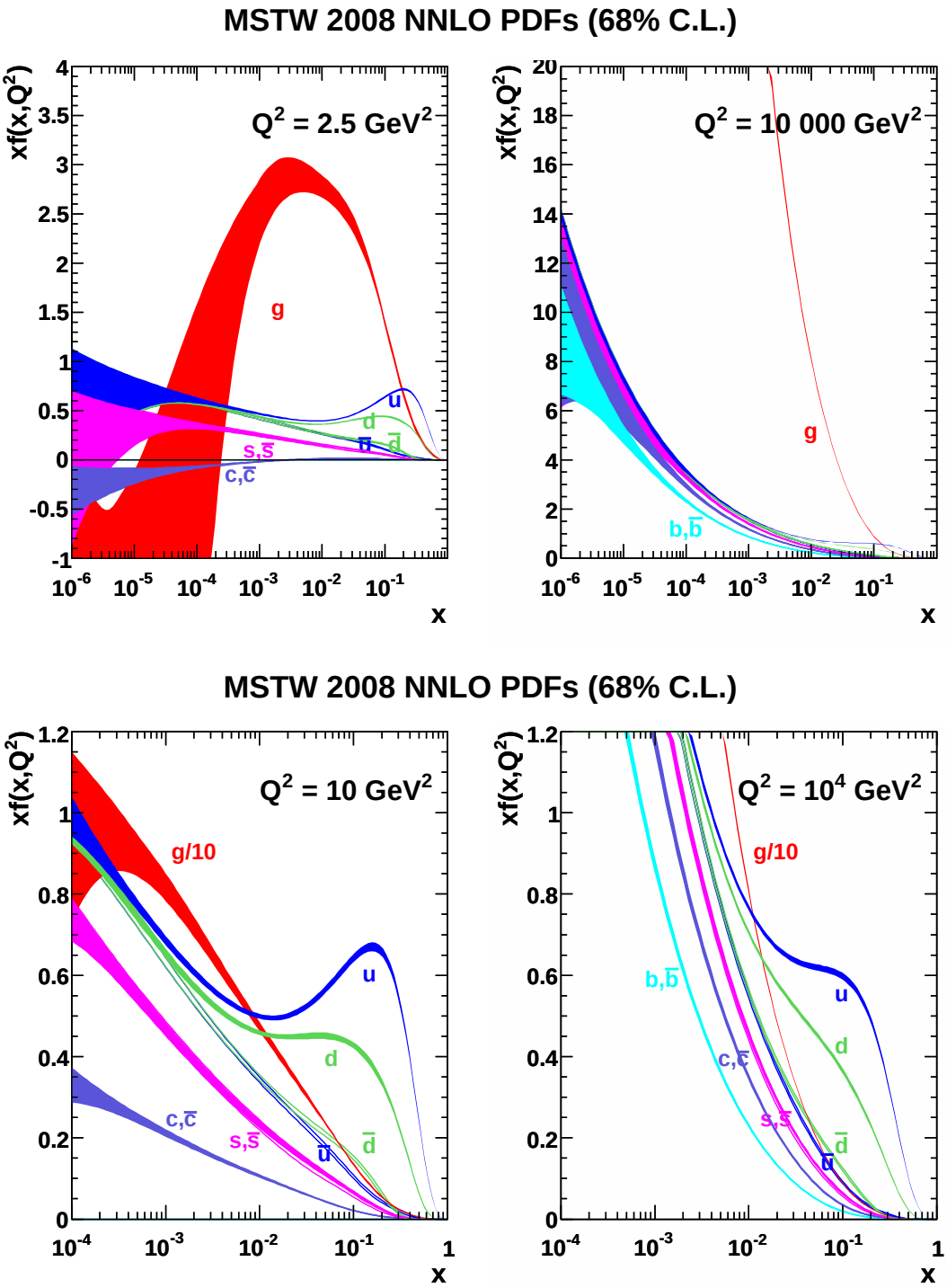

Figure 4.3: Values of x and Q^2 probed in the production of an object of mass M and rapidity y at the LHC (at a centre-of-mass energy, $\sqrt{s} = 14$ TeV) [9].

4.2 Theoretical predictions of the inclusive production cross-section at 7 TeV

At a centre-of-mass energy of $\sqrt{s} = 7$ TeV, the total production cross-section of W and Z bosons are $\sigma_W \sim 100$ nb and $\sigma_Z \sim 30$ nb, as shown in Figure 2.4. The W and Z bosons decay to fermion−antifermion pairs of lower mass. Experimentally, we can distinguish between $V \to q\bar{q}'$ (hadronic decays) and $V \to \ell\ell'$ (leptonic decays).

Neglecting phase space effects and higher order corrections, simple estimates of their branching fractions can be theoretical calculated from the coupling constants.

The leptonic branching ratios of the W boson are approximately $BR(e, \nu_e) = BR(\mu, \nu_\mu) = BR(\tau, \nu_\tau) = 1/9$ ($\approx 11.11\%$). The hadronic branching ratio is dominated by the CKM-favoured ud and cs final states, and the sum of the hadronic branching ratios is roughly $BR(hadrons) = 2/3$ (66.67%). Experimentally, this branching ratios have been measured to be $BR(\ell, \nu_\ell) = 10.80 \pm 0.09\%$ (per flavour) and $BR(hadrons) = 67.60 \pm 0.27\%$, as quoted by the Particle Data Group[4].

The leptonic branching ratios of the Z boson have been experimentally measured to be $BR(\ell^-, \ell^+) = (3.3658 \pm 0.0023)\%$, while the "invisible" decay into two neutrinos is $BR(\nu, \nu) = (20.00 \pm 0.06)\%$. The branching ratio into hadrons is similar to the corresponding W one, $BR(hadrons) = (69.91 \pm 0.06)\%$.

Despite their smaller branching ratio, leptonic decays are preferred for the experimental measurement of the cross-section. This is due to the different identification and reconstruction of hadrons and quarks (which are observed in the detector as jets of particles) and leptons. Vector boson decays into muons and electrons are much cleaner and simpler to identify and measure than those involving jets, therefore compensating for their smaller production rate.

This thesis studies the decay of W bosons into muon−neutrino pairs, measuring its cross-section $\sigma(\mathrm{pp} \to \mathrm{W}^\pm + X) \times BR(\mathrm{W}^\pm \to \mu^\pm\nu)$. An experimental sample of Z bosons decaying into muons is used as an auxiliary tool. Taking into account the mentioned 11% and 3% branching ratios into leptons, the total W and Z production cross-sections is reduced to around $\sigma(W) \sim 10$ nb and $\sigma(Z) \sim 1\mathrm{nb}^{-1}$when the prediction is restricted to the leptonic channels.

The current uncertainties on the theoretical predictions for $\sigma(\mathrm{pp} \to \mathrm{W}^\pm + X) \times BR(\mathrm{W}^\pm \to \mu^\pm\nu)$ are smaller than 5%, and due to PDF parametrization and uncertainties on the QCD scale

α_s. The predictions are computed from theoretical programs choosing a particular parametrisation for the parton density functions. For instance, FEWZ [37], which can give predictions up to NNLO order in QCD, or MCFM [38], up to NLO.

Figure 4.4 shows the comparison of the theoretical predictions of different PDF sets, for $W^{\pm}$, W and Z bosons, as computed by the MSTW group [9] at NLO. The recommended Parton Density Functions by the PDF4LHC [39] working group are currently MSTW08 [9], CTEQ66 [40] and NNPDF2.0 [41][1]. The differences between the cross-sections calculated using these three PDF parametrizations at NLO are smaller than 4%, as shown in the Figure.

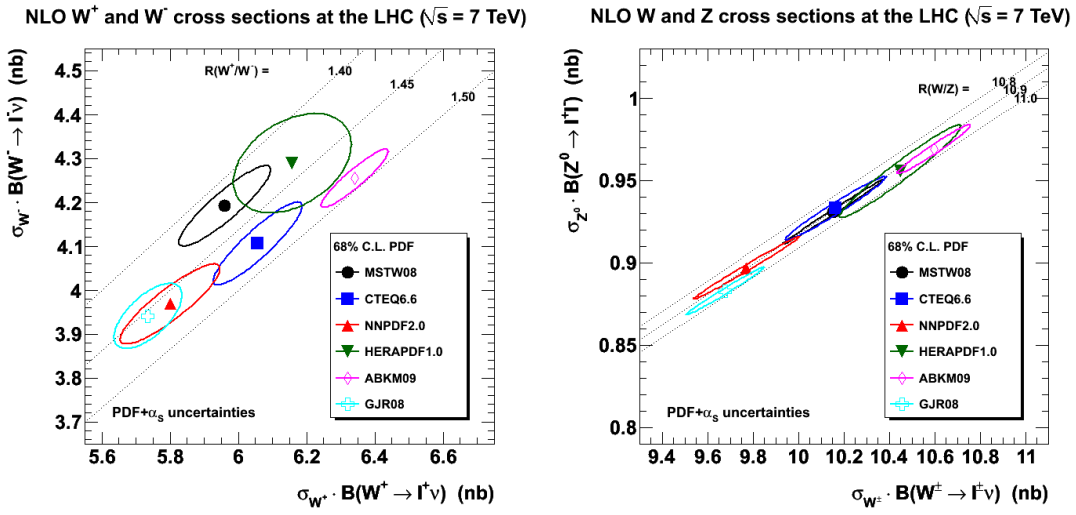

Figure 4.4: NLO cross-section x branching ratio for inclusive $W^{\pm}$ and Z production at the LHC at a centre of mass energy of 7 TeV, computed by the MSTW08 collaboration [9; 43]. Two comparisons are shown: W^- versus W^+ (left) and Z versus W (right), using different PDF parametrizations (including CTEQ66, NNPDF2.0 and MSTW, as recommended by the PDF4LHC group).

The theoretical reference used in this thesis to compare with our measured cross-section value is has been computed at NNLO with the program FEWZ [44; 45]) and the MSTW set of PDFs. The uncertainties come from 68% confidence levels obtained by combining the NLO PDF and α_s errors from the MSTW08, CTEQ6.6 and NNPDF2.0 groups and adding the NNLO scale uncertainties in quadrature, as prescribed by the PDF4LHC working group [39].

The reference values are summarised in Table 4.1. [46]

[1]Further studies by the CMS community will also include CT10 [42], which was released after the study presented in this thesis was completed.

Table 4.1: Theoretical predictions for the $\sigma(\mathrm{pp} \to \mathrm{W}^{\pm} + X) \times BR(\mathrm{W}^{\pm} \to \mu^{\pm}\nu)$ and $\sigma(\mathrm{pp} \to \mathrm{Z} + X) \times BR(\mathrm{Z} \to \mu^{+}\mu^{-})$ cross-sections at 7 TeV. This reference has been computed with FEWZ at NNLO in α_s, using MSTW08 also at NNLO.

Boson	$Z/\gamma*$ ($60 < M_{\mu\mu} < 120$ GeV)	W^+	W^-	W
$\sigma \times BR$	0.97 ± 0.04 nb	6.15 ± 0.29 nb	4.29 ± 0.23 nb	10.44 ± 0.52 nb

4.3 Measurement of W and Z observables at the LHC

The leptonic decay of W and Z bosons is one of the experimentally simplest signatures in a hadronic collider.

Due to charge conservation, Z bosons decay to a pair of opposite-charged leptons (or to two neutrinos), with resonant invariant mass centred around the Z peak. W bosons decay products are a charged lepton and a neutrino. It is experimentally impossible to compute the invariant mass of the (lepton, neutrino) pair[1], and therefore a related variable (such as the transverse mass of the muon pair or the lepton and the neutrino momentum) will be used as final discriminating variable. The produced leptons are typically produced back-to-back in the transverse plane and are characterised by their high transverse momentum.

Some of the properties of vector bosons which are going to be measured at the LHC are described in what follows. This is not a complete list of electroweak observables, but rather one tailored to the theme of this thesis.

4.3.1 Cross-Section measurement

The inclusive measurement of the W and Z cross-sections ($\times$ branching ratios) has been the first electroweak observable precisely measured in the LHC. In this thesis a first measurement of the W cross-section at 7 TeV is presented, using data from the CMS experiment and using an integrated luminosity of $\int \mathcal{L} dt = 3$ pb^{-1}.

Differential measurements of the cross-section ($d\sigma_W/dp_T$, $d\sigma_W/d\eta$, $d\sigma_W/dp_T(W)$) will soon follow this first measurements to provide further insight on the associated production mechanisms and distinguish between different Monte Carlo Generators and PDF predictions.

Once the production process of weak bosons is thoroughly studied, their cross-sections will also serve as a luminosity monitor for the LHC. Since the combined experimental and theoretical

[1]For the sake of brevity, in this thesis "leptons" will be used generically to refer to (e,μ,τ) - and neutrinos (ν) will in many cases generically refer to all flavours of neutrinos and antineutrinos, (ν_e,$\bar{\nu}_e$,ν_μ,$\bar{\nu}_\mu$,ν_τ,$\bar{\nu}_\tau$) unless otherwise specified.

errors are much lower than the luminosity uncertainty provided by the LHC, the measurement can be reversed. Integrated luminosity can be extracted by counting the observed number of W and Z candidates in a datasample, thus obtaining a luminosity error which can be close to $\approx 5\%$ to propagate to other analysis.

Furthermore, using the $\ell^{\pm}$ pseudo-rapidity distributions of the decay products of weak bosons, a very accurate estimate of the parton luminosity can be obtained, and propagated to other analysis. For instance, the strong correlation between the weak boson pair production and the single boson production may lead to an estimated experimental luminosity accuracy at the $\pm 1\%$ level [33; 47].

4.3.2 W charge asymmetry

The study of the charge asymmetry in W production, due to the different amount of $u\bar{d}$ and $d\bar{u}$ in proton-proton collisions, can also give insight on the quark and antiquark PDFs at the $Q^2 \sim 10^4$ GeV^2 scale.

This asymmetry can be approximated as

$$A_W \approx \frac{u\bar{d} - \bar{u}d}{u\bar{d} + \bar{u}d} \approx \frac{u_{val} - d_{val}}{u_{val} + d_{val} + 2\bar{q}}$$

This W asymmetry is directly related to the lepton asymmetry, which is an experimentally simpler observable. Both asymmetries can studied in different rapidity (or pseudorapidity) bins, due to the relation of the rapidity of the produced particles with the momentum fractions of the incoming partons ($M^2 = x_1 x_2 s$, $Y = 1/2ln(x_1/x_2)$, $x_{1,2} = (M/\sqrt{s})e^{\pm y}$).

Moreover, the V-A interaction causes a difference in the y (or η) distributions of μ^+ and μ^-, especially at large values of η. Left-handed leptons (μ^-) are emitted preferentially in the direction of the incoming quark, while right-handed leptons (μ^+) are emitted opposite to the quark direction [47]. The observed charged lepton η reflects not only the x distributions of quarks and antiquarks, but also a distinction between valence and sea quarks at a given x [47].

Mathematically, these asymmetries are expressed as a function of rapidity / pseudorapidity as:

$$A_W(y) = \frac{\frac{d\sigma}{dy}(W^+) - \frac{d\sigma}{dy}(W^-)}{\frac{d\sigma}{dy}(W^+) + \frac{d\sigma}{dy}(W^-)}$$

$$A_\ell(\eta) = \frac{\frac{dN}{d\eta}(\ell^+) - \frac{dN}{d\eta}(\ell^-)}{\frac{dN}{d\eta}(\ell^+) + \frac{dN}{d\eta}(\ell^-)}$$

A first observation of this W charge asymmetry by the CMS collaboration will be soon published, using the data collected through 2010 ($\mathcal{L} \sim 36$ pb^{-1}) and combining the muon and electron decays of the W boson [48].

4.3.3 W Mass and Width measurement

The mass and the width of the W boson are two basic parameters of the Standard Model. The current world average of the W mass and width combines measurements from LEP2 and Tevatron experiments [5]. These combined values $m_W = 80.399 \pm 0.023$ GeV and $\Gamma_W = 2.085 \pm 0.042$ GeV are shown in Figure 4.5, which also shows the comparison of this average to past measurements.

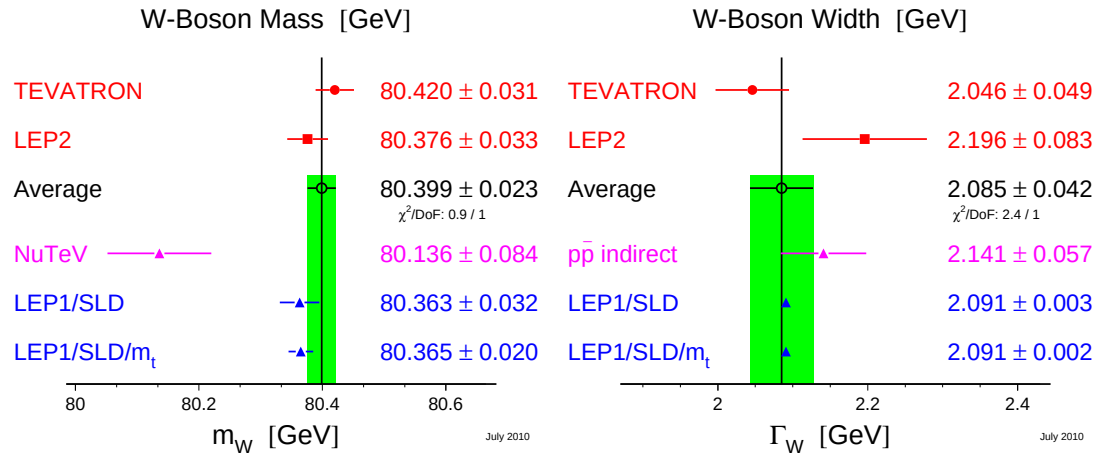

Figure 4.5: Average of the different measurements of the W Boson mass and width.

The measurements of the W and the top quark mass provide a constraint on the mass of the Higgs boson in the Standard Model as well as a consistency check of the theory. The most recent update by the LEP Electroweak group, including the latest Tevatron measurements, is shown in Figure 4.6. The area marked by the blue ellipse shows the $m_t - m_W$ region compatible at 68% with the experimental measurements from LEP2 and Tevatron. The green band marks the allowed values for the Higgs mass (the white gap corresponds to the $158 < M_H < 175$ GeV region excluded by Tevatron searches). At 68%, this check indicates a preference for a low Standard Model Higgs mass.

Therefore, since the current uncertainty on the W mass is $\Delta M_W = 23$ MeV, in order to improve this constraint on the Higgs mass the measurement of the W mass in the LHC is required to have an uncertainty smaller than 20 MeV.

To reach the desired precision implies a extremely good control of all the systematical errors involved in the measurement. An excellent understanding of the detector (lepton identification,

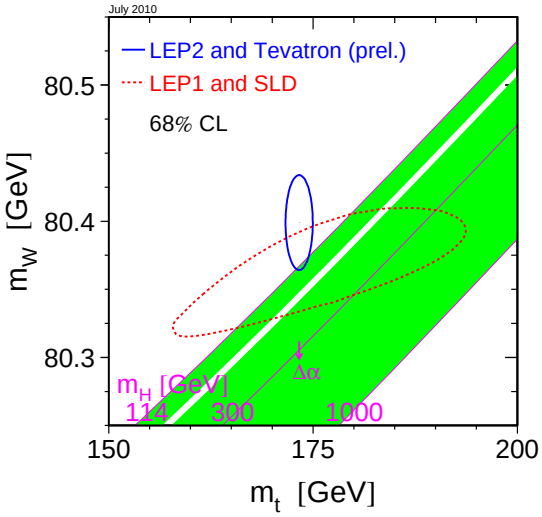

Figure 4.6: Constraints on the Higgs Boson Mass from the measured mass of the W boson and the top quark.

lepton efficiencies, energy reconstruction) and the theoretical effects involved (PDFs, radiative decays, EWK corrections) is required.

Therefore, although the current knowledge of the CMS detector is already very good, a competitive measurement of the W mass and width cannot be obtained with the data collected in 2010.

Preliminary studies done at CMS at 14 TeV with an integrated luminosity of 10 fb^{-1} show that a total instrumental systematic uncertainty below 20 MeV should be within reach[16].

4.3.4 Anomalous gauge couplings

In the Standard Model, the Non-Abelian nature of the $SU(2)_L \times U(1)_\gamma$ gauge symmetry allows charged triple gauge-couplings (TGCs, couplings between three gauge bosons such as $W^+W^-Z^0$, $W^+W^-\gamma$) to exist. On the other hand, neutral couplings (such as ZZZ) are forbidden. New physics beyond the Standard Model may introduce *anomalous* couplings (aTGCs), which allow neutral TGCs or modify charged TGCs, modifying the production cross-section of dibosons in proton-proton collisions [16].

The study of these TGCs (allowed and forbidden alike) can be performed thanks to the measurement of the production cross-section of pairs of gauge bosons: $pp \rightarrow WWX$, $pp \rightarrow$

WZX, $pp \to ZZX$, $pp \to W\gamma X$, $pp \to Z\gamma X$ where the W, Z or γ bosons decay into lepton pairs.

In addition to this, diboson production is one of the main backgrounds in the search for the Higgs boson, SuperSymmetry and other new physics models (such as the production of extra gauge bosons, Z'), and therefore a correct normalization of its production is essential.

Prospective studies for the measurement of the WW, WZ^0, $W\gamma$, Z^0Z^0 cross-sections [16; 49; 50] have been done in CMS, at centre-of-mass energies of 14 and 10 TeV.

The first experimental measurement of the WW, $W\gamma$ and $Z\gamma$ production cross-sections in proton-proton collisions at 7 TeV is about to be published by the collaboration [51; 52], together with the first limits on anomalous $WW\gamma$, $Z\gamma\gamma$ and $ZZ\gamma$ couplings.

4.3.5 Other electroweak measurements

Other measurements that will be performed in the CMS experiment in the future:

- **Drell-Yan Cross Section Measurement** - The production of lepton pairs in hadron-hadron collisions (*Drell-Yan processes*) will be studied over the full range of $M_{\ell^+\ell^-}$. This $d\sigma(Z/\gamma*)/dM_{\ell^-\ell^+}$ measurement may allow to discover new di-lepton resonances at high-mass. [53]

- **Measurement of the** $\mathrm{Z} \to \tau^+\tau^-$ **and** $\mathrm{W} \to \tau\nu$ **production cross-sections** - Tau τ leptons are more difficult to measure experimentally than electrons and muons, due to their immediate decay in the detectors. The production of Z bosons decaying into τ pairs serves as an important bench- mark for τ reconstruction and constitutes a reference process for Higgs searches. [54]

- **W polarization at high** q_T - W bosons preferentially exhibit left-handed helicity states for both charges of the W boson. This effect increases with the transverse momentum of the W bosons, and leads to very distinct and charge dependent decay kinematics. These properties will allow to distinguish them from other physics searches which have high transverse momentum W bosons as one of the sources of background [55].

- A_{FB} **asymetry of the Z boson** - Measurement of the forward-backward asymmetry of of the $\mathrm{Z} \to \ell\ell$ process, caused by the vector and axial-vector couplings of electroweak bosons to fermions. The A_{FB} depends on the di-lepton invariant mass, quark flavour and $\sin(\theta_W)$ and is sensitive to deviations from the Standard Model (for instance, caused by extra neutral gauge bosons). [56]

4.4 Monte Carlo description of W events

The production of W bosons in a proton-proton collision is implemented in Monte Carlo event generators, which are used to predict event rates and topologies.

Event generators allow theoretical and experimental studies of complex multiparticle physics. They randomly generate events as those produced in particle accelerators, incorporating the kinematics of the products of the hard collision as well as the evolution of the underlying event. Initial and final state radiation effects are also taken into account.

The final-state particles generated (i.e, the products of the W decay, muon and the neutrino) can be fed through the full GEANT4 [57; 58] detector simulation, trigger emulation and event reconstruction chain of the CMS experiment. This way a precise prediction and verification of the entire system of experimental setup is obtained.

Two different generators of electroweak events are used in this thesis. The baseline Monte Carlo used for this analysis is POWHEG, since it is computed at NLO and therefore expected to provide more accurate precisions, while PYTHIA was used a as cross-check.

1. **PYTHIA** [59] - Considered the basic reference for many analysis, PYTHIA is a widely used program for the generation of high-energy physics events. It is a event generator, based on a shower Monte Carlo which contains theory and models for a number of physics aspects, including hard and soft interactions, parton distributions, initial- and final-state parton showers, multiple interactions, fragmentation and decay. It can provide modelling to basically any process at a hadron collider. On the other hand, it can only provide results at leading-order (or leading-order plus leading-log) in QCD. Events are then characterised by a small number of high-p_T, well-separated, final-state partons (the ones described by the tree-level Born amplitude) plus many collinear partons, whose collinear divergences have been correctly resumed.

2. **POWHEG** ("POsitive-Weight Hardest Emission Generator") [60] - The POWHEG program is a hard interaction event generator for hadronic collisions. It is accurate at the next-to-leading order in QCD, and it must be interfaced to shower Monte Carlo programs like HERWIG and PYTHIA (p_T ordered), in such a way that both the leading logarithmic accuracy of the shower and the NLO accuracy are ensured in the output.

The parton density functions used in generation are cteq6l (leading order) for the PYTHIA samples, and cteq66 (NLO) for the POWHEG samples.

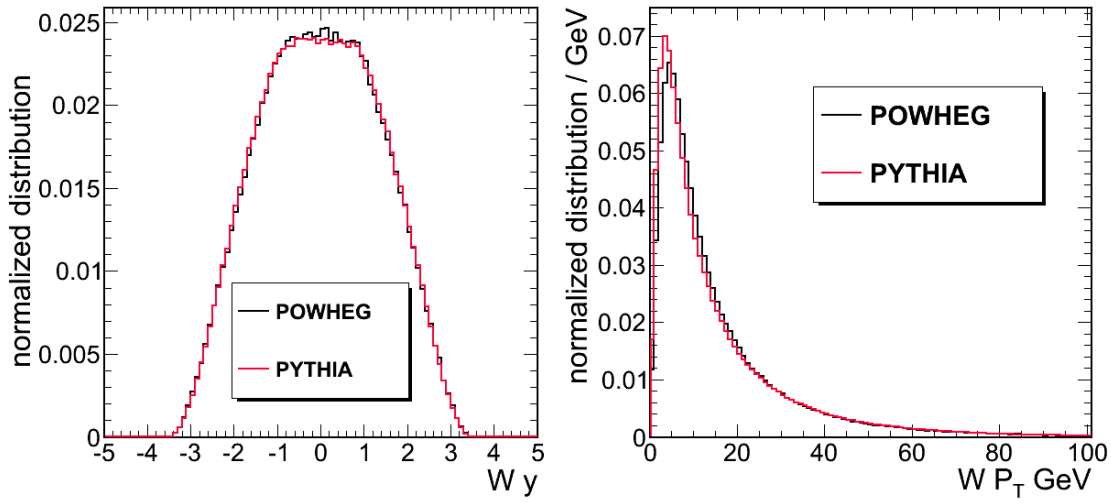

Figure 4.7: Comparison between PYTHIA and POWHEG expected distributions: Expected rapidity (left) and transverse momentum (right) for the W boson.

Figure 4.7 shows the expected distributions at generator level for transverse momentum and rapidity of the W in these two Monte Carlo samples, Figure 4.8a and 4.8b shows them for the muon and the neutrino which result from its decay. In both cases the phase-space is restricted to those events in which the pseudorapidity of the muon is inside the fiducial volume of the detector ($|\eta| < 2.5$).

Note that W bosons are produced mostly in the central rapidity (y) region, and have a transverse momentum spectra which falls abruptly, peaking at 4−5 GeV. On the other hand muons and neutrinos coming from a W decay tend to be energetic (p_T peaks around 40 GeV) and have a relatively flat distribution in η. This features will be important for the description of the analysis strategy in further chapters.

Despite the differences present in generation, the resulting distributions are in general very similar. The most evident difference in shape appear in the W rapidity and pseudorapidity distribution, due to the different PDF parametrizations used in the generation of the two Carlo samples.

The other differences are mainly present in the peak of the p_T, both for the W and for the muon. These differences are nevertheless small enough that they will not have an impact on the measurement.

Figure 4.9 shows the jacobian peak of the generated transverse mass, for both generators:

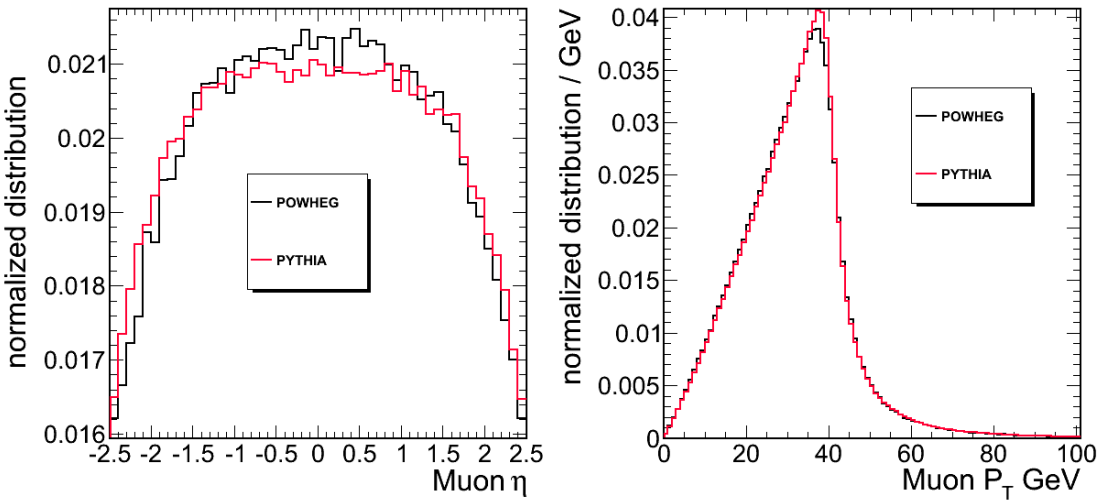

(a) Expected Pseudorapidity (left) and transverse momentum (right) for the muon product of the W decay.

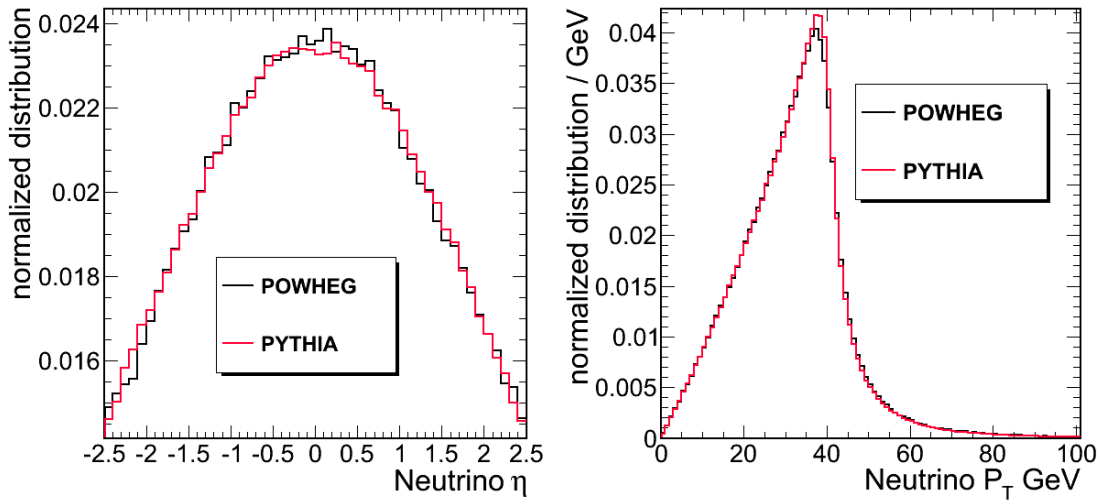

(b) Expected Pseudorapidity (left) and transverse momentum (right) for the neutrino product of the W decay.

Figure 4.8: Comparison between PYTHIA and POWHEG expected distributions: Muon and Neutrino transverse momentum and pseudorapidity

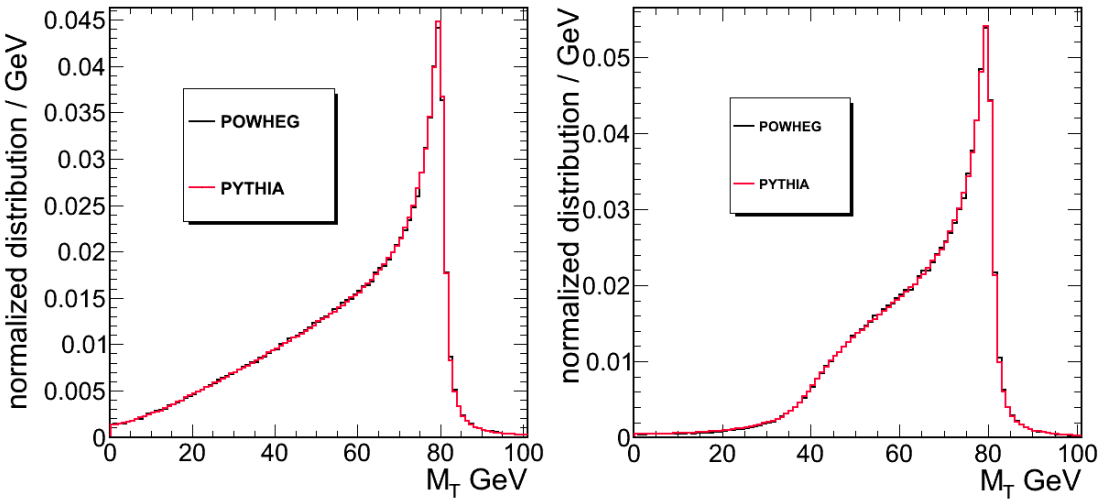

Figure 4.9: Comparison between PYTHIA and POWHEG expected distributions: Expected Transverse Mass (M_T) both before and after the kinematic cuts $p_T > 20$ GeV and $|\eta| < 2.1$ are applied.

$$m_{T(\mu,\nu)}(W) = \sqrt{2p_T^{\mu}p_T^{\nu}(1-\cos(\Delta\phi(\mu,\nu)))}$$

The left plot considers the fiducial phase-space already described, covering all the momentum spectra and restricting the pseudorapidity of the muon up to $|\eta| < 2.5$. The right plot considers a restricted phase-space close to the one used later in the analysis (Chapters 6,7,8), applying a kinematic cut on the transverse momentum of the muon of $p_T > 20$ GeV and on its pseudorapidity of $|\eta| < 2.1$. This restricted phase-space distorts the lower part of the M_T spectra, leaving mostly unchanged the higher region and the peak itself. The difference between the POWHEG and the PYTHIA expected distributions is again negligible.

Chapter 5

Building blocks of the analysis

As mentioned in Chapter 4, the signature of Vector Boson production in proton-proton collisions, followed by their leptonic decay, is a simple and experimentally clean one. Experimentally, Z events are characterized by two opposite charged, high momentum leptons with an invariant mass in the vicinity of the Z peak. The typical signature of W events is a single high momentum lepton. As the neutrino cannot be detected, the event will be energetically unbalanced, with a sizeable amount of "missing transverse energy" or $\overrightarrow{E_T}^{miss}$. Therefore we will look for energetic, isolated leptons reconstructed in the fiducial volume of the detector.

The study of W $\rightarrow \ell\nu$ and Z $\rightarrow \ell\ell$ makes use of many of the reconstruction techniques of CMS. A good performance of all the subsystems of CMS and excellent object reconstruction algorithms are required for the basic elements of analysis: muons, electrons, photons, jets, missing transverse energy and tracks.

In the case of W $\rightarrow \mu\nu$ and Z $\rightarrow \mu^+\mu^-$ events, the performance of the algorithms used to reconstruct muons and $\overrightarrow{E_T}^{miss}$ is particularly relevant. A brief description of these follows.

5.1 Monte Carlo Samples

Several large Monte Carlo (MC) simulated samples have been used in order to predict the behaviour of signal and backgrounds events and compare to the theoretical predictions. They will be used to evaluate signal and background efficiencies and to validate the analysis techniques deployed.

Samples of electroweak processes with Z and W production are produced with POWHEG [60; 61; 62] interfaced with the PYTHIA [59] parton-shower generator, as mentioned in Chapter 4.

QCD events with a muon in the final state and $t\bar{t}$ events are generated with PYTHIA.

The analysed samples are reported in Table 5.1. Signal samples simulated with PYTHIA are used as cross-check with respect to POWHEG samples. Further details on the MC collections processed are available in Ref. [63].

Table 5.1: Summary of analysed Monte Carlo samples for the various signal and background processes. At generator level, cross-sections correspond either to LO (PYTHIA) or NLO (POWHEG), for the PDF set indicated. The CMS reference value has been computed at NNLO using FEWZ for W and Z, using PDFs from MSTW08 at NNLO, and with MCFM at NLO for WW, WZ, ZZ [46]. The $t\bar{t}$ reference cross-section (NNLL) has been taken from Ref. [64].

Generator	Process	Kin. cuts (in GeV,$c=1$)	σ^{GEN} (pb)	Events	PDF set	σ^{NNLO} (pb)
POWHEG	$W^+ \to \mu^+\nu$	no cuts	5825	∼700k	CTEQ66	6152
POWHEG	$W^- \to \mu^-\bar{\nu}$	no cuts	3954	∼700k	CTEQ66	4286
POWHEG	$Z \to \mu^+\mu^-$	$m_{\mu\mu} > 20$	1631	> 1M	CTEQ66	1666
PYTHIA	$t\bar{t}$	no cuts	94.3	500k	CTEQ6L1	165
PYTHIA	Inclusive μ	$\hat{p}_T > 20$, $p_T^\mu > 15$, $\lvert\eta_\mu\rvert < 2.5$	79688	6M	CTEQ6L1	-
PYTHIA	WW	no cuts	28	100k	CTEQ6L1	43
PYTHIA	WZ	no cuts	10.5	100k	CTEQ6L1	18.2
PYTHIA	ZZ	no cuts	4.3	100k	CTEQ6L1	5.9
PYTHIA	$W \to \mu\nu$	$\lvert\eta_\mu\rvert < 2.5$	5861	2M	CTEQ6L1	10438
PYTHIA	$W \to \tau\nu$	no cuts	7899	2M	CTEQ6L1	10438
PYTHIA	$Z \to \mu^+\mu^-$	$m_{\mu\mu} > 20$	1300	2M	CTEQ6L1	1666
PYTHIA	$Z \to \tau^+\tau^-$	$m_{\tau\tau} > 20$	1300	2M	CTEQ6L1	1666

5.2 Muons in CMS

Muons are identified unequivocally by their presence in the muon spectrometers. They are reconstructed as tracks both in the silicon inner detector (just like any other charged particle) and in the muon detectors in two independent processes. Combining the information provided by muon spectrometers and tracker, a very precise measurement of the muon momentum and trajectory is obtained. Different reconstruction algorithms are employed to ensure full coverage of low and high momentum objects, and are detailed in Section 5.2.1.

The spectra of inclusive muons produced in proton-proton collisions falls rapidly with transverse momentum. The low p_T region, populated mostly by muons coming from minimum bias processes, is the most abundant one. Therefore it has been used in the first months of 7 TeV

collisions to finally test reconstruction algorithms and Monte Carlo modellings on proton-proton collisions.

The sample is mostly composed of muons coming from light flavour processes with a smaller component of muons from decays of heavy flavour hadrons, as can be seen in the p_T and η distributions of Figure 5.1. In this plot we can also see a small contribution of hadrons traversing the detector and being reconstructed as muons in the chambers (punch-through) and duplicate muons. Overall, the agreement of the Monte Carlo predictions and the data is excellent [65].

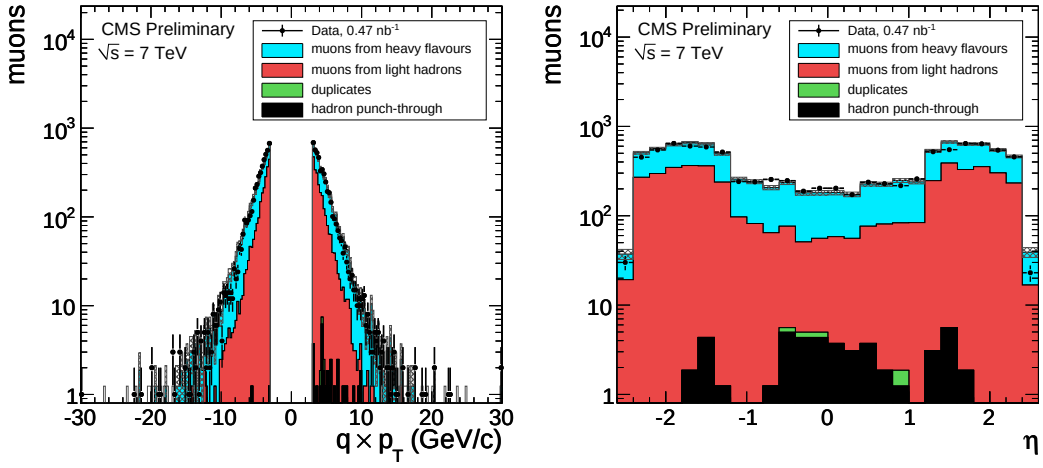

Figure 5.1: Muon momentum and Muon pseudorapidity in a sample of low p_T muons compared to the expected contributions of different sources of muons in a Minimum Bias Monte Carlo simulation [65].

At high p_T the amount of soft muons coming from minimum bias is reduced exponentially, and new sources of muons start to dominate. The sources of muons at high momentum are mainly decays of heavy flavour ($b\bar{b}$) and electroweak ($W \to \ell\nu$, $Z \to \ell\ell$, $t\bar{t}$) processes. Besides these physical sources of muons there are also other objects mis-identified as muons (fake muons or hadron punch-trough) or other muon sources not coming from a proton-proton interaction (cosmic muons or decays in flight of pions and kaons).

5.2.1 Muon Reconstruction

CMS aims for an excellent muon reconstruction along three orders of magnitude: from the low momentum muons present in B Physics studies (peaking at transverse momenta lower than 10 GeV), to relatively energetic muons such as the ones coming from electroweak processes studied in this thesis (typically peaking at $p_T \approx 40$ GeV), to the very high momentum muons

that are a distinctive signature of some new physics models (TeV muons, as in heavy vector bosons W' and Z' decays into muons).

This wide energetic range calls for a flexible and versatile muon reconstruction, which makes use of two different elements:

- **Tracker** reconstruction

As described in Section 2.3.2, the impact left by charged particles in the inner detector of CMS are combined into trajectories. Their curvature in the magnetic field of CMS is used to compute their momentum.

Track reconstruction in CMS is an iterative process. Starting from the reconstructed hits, the track reconstruction is decomposed in three logical parts: a) finding the starting points for tracks in the inner detectors ("Seed Finding"), b) collecting all measurements corresponding to a single track ("Pattern Recognition") c) performing a combined fit of the collected measurements ("Final Fit") into a helicoidal function to produce tracks.

The pattern recognition is based on a combinatorial Kalman Filter method which takes into account multiple scattering and energy loss in the traversed material. The Filter proceeds iteratively from the seed layer, starting from a coarse estimate of the track parameters provided by the seed, and including the information of the successive detection layers one by one.

All resulting trajectory candidates are then grown in turn to the next compatible layer(s), and the procedure is repeated until either the outermost layer of the tracker is reached or a stopping condition is satisfied. To avoid an exponential increase of the number of trajectory candidates the total number of candidates is truncated at each layer.

On each layer, i.e. with every new measurement, the track parameters are known with a better precision, up to the last point, where they include the full tracker information [66].

- **Muon-Spectrometer** reconstruction

A muon going through the muon spectrometer leaves physical signals or hits in the chambers it transverses. These hits are reconstructed as digitised electronic signals. Hits within each DT or CSC chamber are fitted to a straight line to form a segment (track-stub). This process is known as "Local Muon Reconstruction".

These segments constitute the "seeds"(direction, position) for the next step in the reconstruction chain, a fit combining the information of the full muon system. This fit is performed

by means of an iterative Kalman filter, by updating the trajectory parameters at each step taking into account scattering due to material crossed. Once the hits are fitted and fake-trajectories removed, the remaining objects are extrapolated to the point of closest approach to the beam line. In order to improve the muon-momentum resolution, they are constrained to pass through the beam-spot of the event.

Combining these **tracks** and **segments** a reconstruction of the muon is obtained. Different algorithms have been developed in CMS for the different p_T ranges.

The reconstruction process of these categories of identified muons depends on the combination of tracker and muon spectrometer information used in the final objects. The two main ones are known as "global muons" and "tracker muons":

1. **Global muons** - Muon reconstruction algorithm which starts from the outer part of the detector and moves inwards, reconstructing a stand-alone track in the Muon Spectrometer which is then matched to the inner tracker track to obtain the best combined fit. This combination is done through the Kalman filtering technique, using the hits from both inner and outer tracks. The resulting combined, "global" muon is the basic object for the analysis in most CMS studies.

2. **Tracker muons** - Reconstruction of muons from the innermost point of the detector to the Muon Spectrometers. It starts from a tracker track with $p_T > 0.5$ GeV and $p > 2.5$ GeV which is extrapolated to the muon chambers, taking into account the expected energy loss and multiple scattering due to the material crossed. If at least one muon segment reconstructed locally matches in position the extrapolated track, the corresponding object is labelled "tracker-muon". This very loose algorithm is very useful to reconstruct low momentum muons, such as the ones coming from decays of J/Ψ or Υ, not energetic enough to reach the outer part of the muon spectrometer.

Both of these algorithms will be used in this thesis.

Alternative reconstruction strategies have been devised for **High p_T muons**. As the muon traverses the iron yoke, multiple scattering and/or showers can give rise to high hit occupancies in the chambers, where the reconstruction algorithms may get distorted. This affects particularly the measurement of the trajectory of very energetic muons. CMS has developed specific optimisations of the refitting procedure to address this problem through a selective use of the

available hits. For example, using all hits both in the tracker and in the innermost muon station crossed, or hits both in the tracker and in those muon stations which do not appear to contain electromagnetic showers.

As an alternative reconstruction completely independent from the muon system, the energy deposited in the calorimeters in the direction of a tracker-track is also evaluated to see if it is compatible with a minimum-ionizing particle. Since the fake rate of these muon candidates is very high compared to the other categories, they are seldom used in analysis.

The combination of all these algorithms provides a robust and efficient muon reconstruction over the very wide range of momentum required by CMS. The majority of muons from collisions with sufficient momentum ($p_T > 5$ GeV) are reconstructed either as Global Muons or Tracker Muons. Reconstruction efficiencies are close to 100%.

5.2.2 Muon Momentum Resolution

Figure 5.2 compares the ideal momentum resolution of tracker track reconstruction and global muon reconstruction as a function of the transverse momentum of the muon. Below 200 GeV the measurement of the momentum is dominated by the tracker resolution, while at very high momentum bremsstrahlung dominates and the combination of the tracker with the muon spectrometer gives a better momentum estimation.

Therefore in this thesis, due to the range studied, muon momentum will be defined to be the one measured in the inner detector.

Muon momentum resolution is expected to be measured with a relative accuracy better than 1% up to 10 GeV and 2−3% up to 100 GeV. As shown in Chapter 4, this design resolution has been essentially reached for all the momentum range, studying cosmic muons, with the exception of very high momentum muons.

Studies done on 7 TeV data show that track-resolution is already at the same level as this expectation. This is shown in Figure 5.3, which shows the muon momentum resolution $\sigma(p_T)/p_T$ as a function of the muon pseudorapidity, obtained using muons from the J/Ψ mesons peak. It shows as a black line the result of the resolution fit in data, from the small deviation (0.2% shift) in the position of this dimuon peak with respect to the expected PDG value. The filled area is the experimental uncertainty associated to this measurement. There is a slight parabolic dependence on the pseudorapidity which is reproduced on MonteCarlo (dots represent both the MonteCarlo-based measurement of resolution and the application of the method to a Monte Carlo J/Ψ sample) [67].

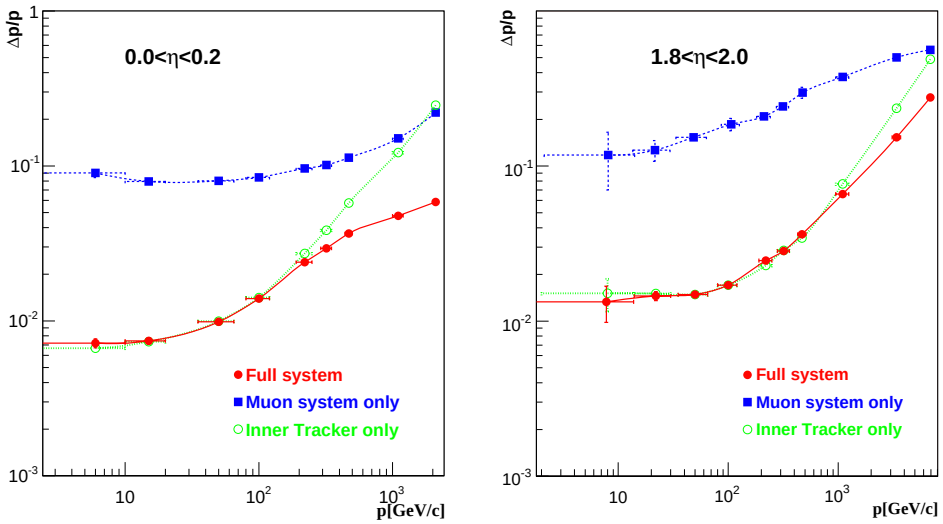

Figure 5.2: Muon Momentum Resolution in Monte Carlo, as a function of p_T, comparing the results of the tracker track fit, the stand-alone fit and the global fit. [16].

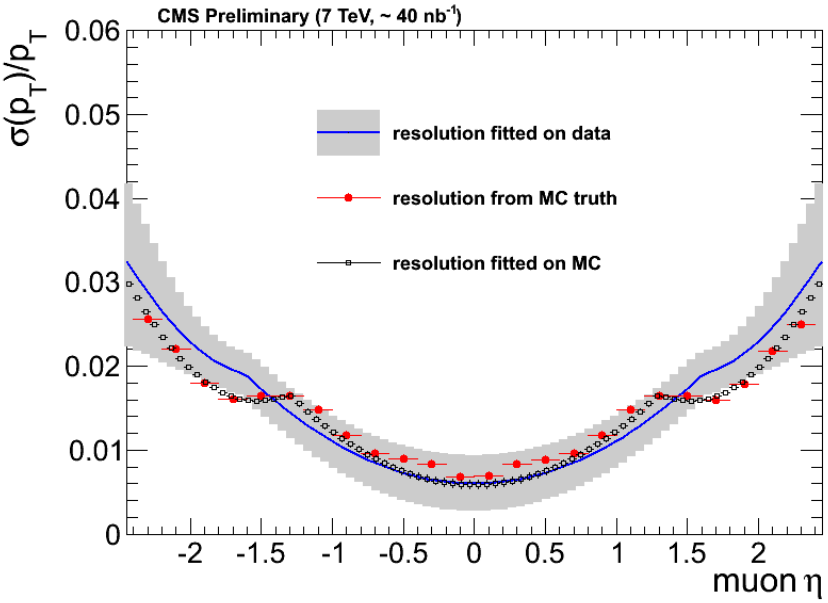

Figure 5.3: Resolution on transverse momentum measured on J/Ψ events with 40 nb^{-1} of data, compared with Monte Carlo results [67].

5.2.3 Muon Triggers

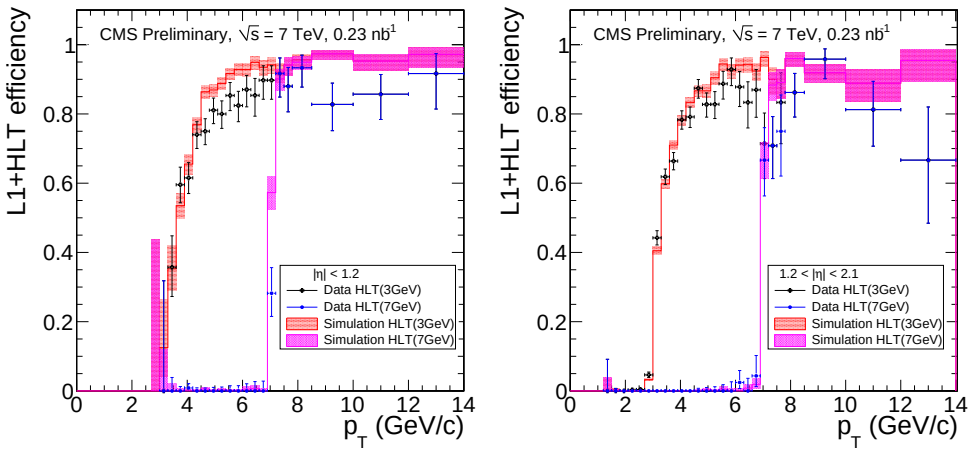

Figure 5.4: Sharp L1+HLT Turn-On Curves for barrel (a) and endcap (b), with first data, comparing thresholds (3 GeV vs 7 GeV) [65]

The trigger menu used during 2010 provided a variety of muon triggers for the study of the first data analysis, depending on the momentum requirements of each analysis. This trigger menu evolved as described in 3.1.1. The lower rate of the first months of data taking allowed for the existence of muon triggers of relatively low transverse momenta thresholds to record a maximum number of events.

The lowest, unprescaled pt threshold for muons available for the data used in this thesis was "HLT_Mu9". This means that the selected muon must have been detected in two of the muon detectors and be seeded at Level 1 (hardware trigger) with a p_T threshold of 7 GeV. A final threshold of 9 GeV is applied in the last triggering step (software).

5.2.4 Muon from W/Z decays

Muons coming from the decay of Z and W bosons have relatively high momentum (typically peaking at 30-40 GeV) and they are originated from the vertex of the event.

In order to guarantee an excellent reconstruction, the muon is required to have fired the muon triggers, and then to continue through offline reconstruction as a global muon. In addition, we suppress instrumental background, badly reconstructed muons and muons coming from decays in flight by examining the quality of the fits, their distance from the vertex and their penetration in the muon system . W candidate events will be identified as those with only one high momentum muon in the event, while Z candidates require two high momentum muons to be reconstructed.

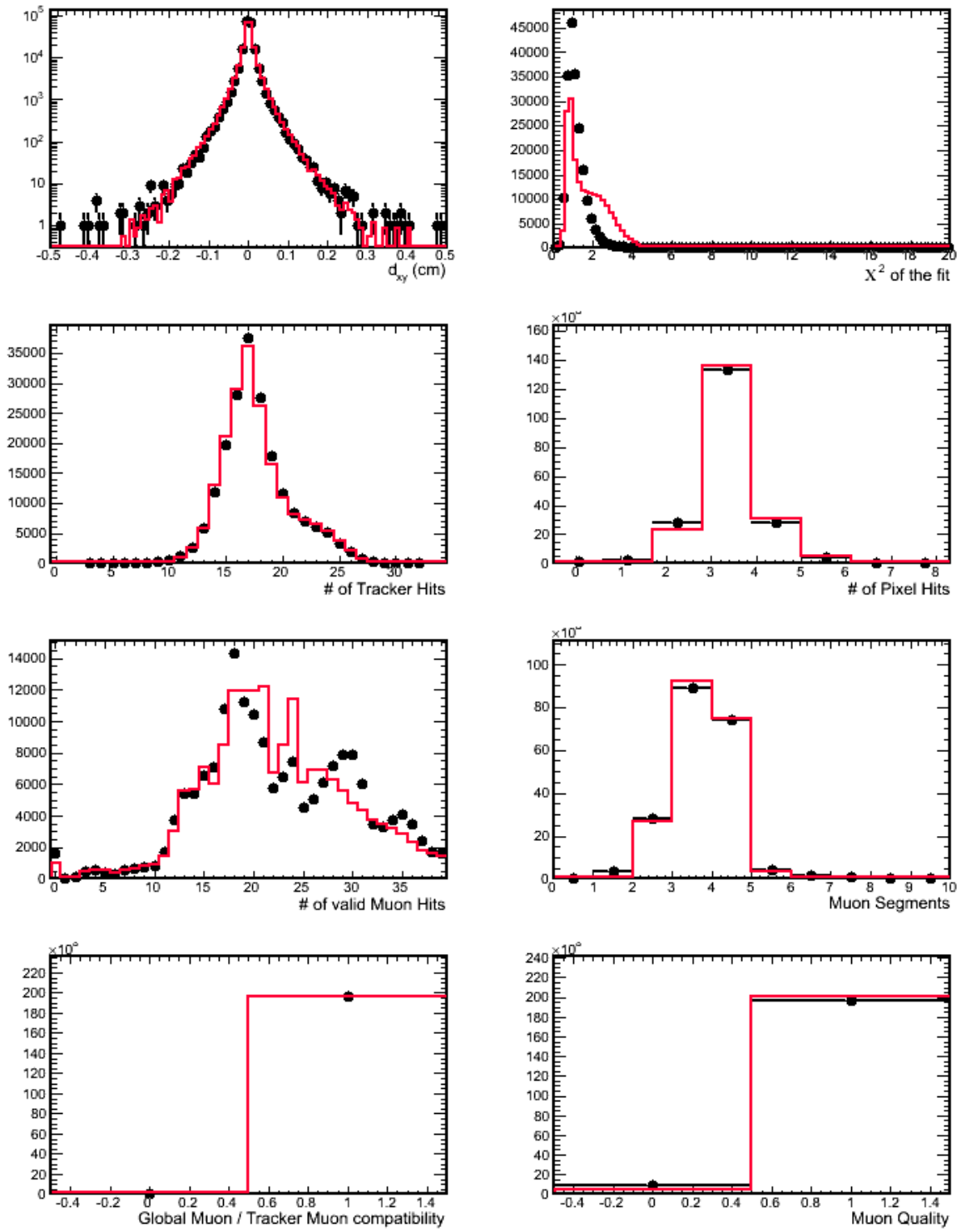

Figure 5.5: Comparison of quality criteria in Data (dots) and Monte Carlo (red line), for a sample of global muons with $p_T > 15$ GeV triggered by the HLT_Mu9. The final plot shows a boolean combination of all the quality criteria applied. Monte Carlo distributions are normalized to the events in data.

Other physical processes give rise to "good muons", of the same general characteristics to the ones coming from W and Z decays. To suppress them we will need to study the kinematics and topology of the event. The dominant $b\bar{b}$ contribution are typically characterised by a high number of tracks and jets in the event (which will be quantified in the analysis through "isolation variables"), and electroweak events, with a topology much similar to our signal.

5.2.4.1 Quality Criteria

In order to guarantee that the selected muons come indeed from vector boson decays, several simple quality criteria have been established over the base of the muon fit:

1. The muon must be identified both by the global and tracker muon algorithms to ensure good consistency between inner detector and muon spectrometer reconstructions. This is essential to ensure good momentum reconstruction, and additionally it reduces the contamination from muons produced in decays in flight of hadrons and from punch-through particles. Muon momentum is obtained from the inner tracker measurement.

2. The combined global fit is requested to have good quality, expressed in terms of its normalised χ value ($\chi^2/\text{ndof} < 10$)

3. To ensure good momentum and impact parameter determination the track reconstructed in the inner detector is required to contain at least 10 hits. At least one of them should be in the innermost part of the tracker, the Pixel Detector.

4. Good muons in general will cross the whole muon detector due to their high momentum. In order to suppress punch-through candidates (unable to penetrate deeply into the iron yoke), the muon is requested to enter deep enough in the muon system. The global muon fit must have incorporated at least one good muon chamber hit, and must have crossed at least two chambers.

5. The residual contamination from cosmic muons is rejected by requiring the impact parameter of the track measured in the transverse plane with respect to the primary vertex to be $|d_{xy}| < 2$ mm.

The experimental distributions of all these variables are shown in Figure 5.5 for events fullfilling all the requirements except for the plotted one, comparing data with a Monte Carlo mix of the processes mentioned in Section 5.1. The overall data-MC agreement is very good. In the Muon Hits and χ^2 plots there is some observed difference due to the different versions

of reconstruction software used in the data and in the generation of the Monte Carlo samples. They do no have any effect on the analysis.

These quality selection criteria are simple a particle, specially designed for removing misreconstructed muons and reducing the presence of cosmic muons and punch-through to a negligible level, while maintaining an excellent efficiency for reconstructing "good" electroweak muons (measured to be 98% in a high statistics Monte Carlo $W \to \mu\nu$ sample).

5.2.4.2 Muon isolation

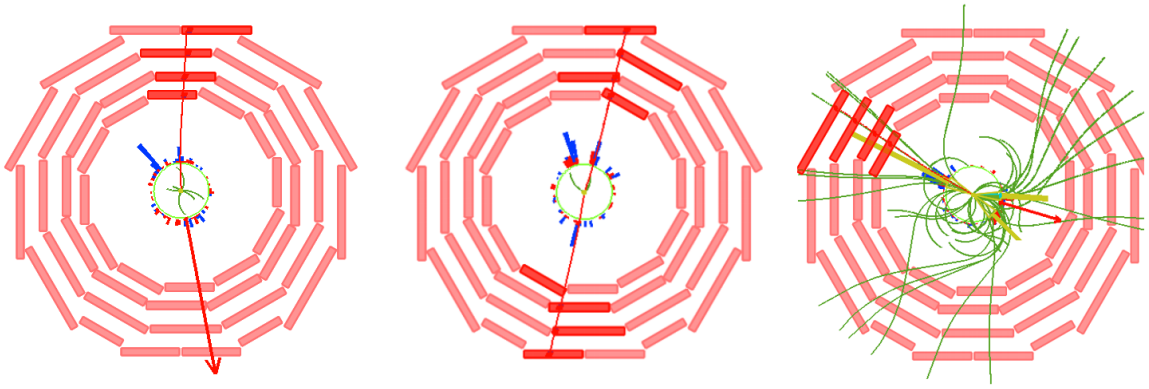

Figure 5.6: Simulated events displays for electroweak (left: $W \to \mu\nu$, centre: $Z \to \mu^+\mu^-$) and hadronic (right: $pp \to \mu + X$) processes.

Isolation is a measurement of the detector activity around an object, an extremely useful tool which allows discriminating between different physical processes in terms of the amount of energy or momentum surrounding a given particle, for example a muon.

Particles coming from electroweak processes are expected to be isolated in the detector, not surrounded by other particles. This characteristic turns out to be one of the key features to distinguish signal events from hadronic processes in which a high p_t lepton is produced.

These hadronic events (often labeled "QCD" events) typically have a much higher track and calorimeter occupancy, and produce an elevated number of low momentum jets. The muon is therefore surrounded by other tracks and energy depositions in the calorimeter.

Typical simulated $Z \to \mu^+\mu^-$, $W \to \mu\nu$ and $pp \to \mu + X$ events are shown as examples in Figure 5.6. While the two muons coming from the Z and the single muon coming from the W are not surrounded by any particle, the muon coming from the QCD event is immersed in a sea of tracks and jets.

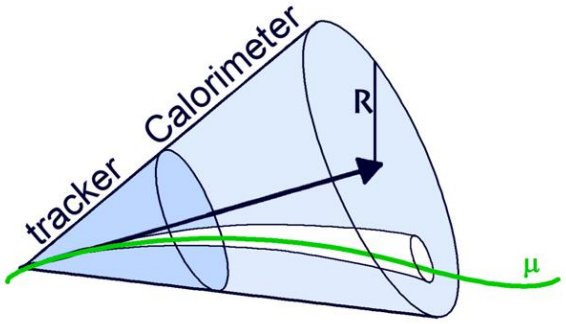

Figure 5.7: Cone defined around the muon line of flight to determine its isolation.

There are several ways to implement this idea. One of the basic elements to quantify this variable is the activity in a cone $R = \sqrt{\delta\phi^2 + \delta\eta^2}$, (typically, $R = 0.3 - 0.7$ radians) around the muon.

The definition of muon isolation in tracker and calorimeters is sketched in Figure 5.7:

- **Track isolation**: $I_{\text{Track}} = \sum_{\text{tracks}} p_T$, is defined as the sum of the momentum of all reconstructed tracks in the defined region around the muon, with momentum above a $p_T > 1$ GeV threshold. The momentum of the muon itself is removed of the counting. This is technically done disregarding the sum of those tracks in a narrow cone of 0.01 radians around the muon.

- **Calorimetric isolation**: $I_{\text{Cal}} = \sum_{\text{ECal}} E_T + \sum_{\text{HCal}} E_T$, is defined as the sum of the energy deposits in the calorimeters, in the defined region around the muon. In this case the energy depositions originated by the muon are removed defining a veto cone of 0.07 radians around it in the Electromagnetic Calorimeter and of 0.1 radians in the Hadronic Calorimeter.

Distributions comparing isolation on a $R = 0.3$ and a $R = 0.5$ cone are shown in Figure 5.8, for good quality muons with $p_T > 15$ GeV. The performance is similar, so the smaller cone radius was chosen in order to minimise possible influences of Pile-Up.

Figure 5.9 compares the behaviour of isolation in data and in Monte Carlo (electroweak+QCD), for tracker-only isolation (I_{Track}), calorimetric-only isolation (I_{Cal}) and a combination of the two variables $I_{\text{Track}} + I_{\text{Cal}}$. The agreement with Monte Carlo is remarkably good for each one of the defined variables.

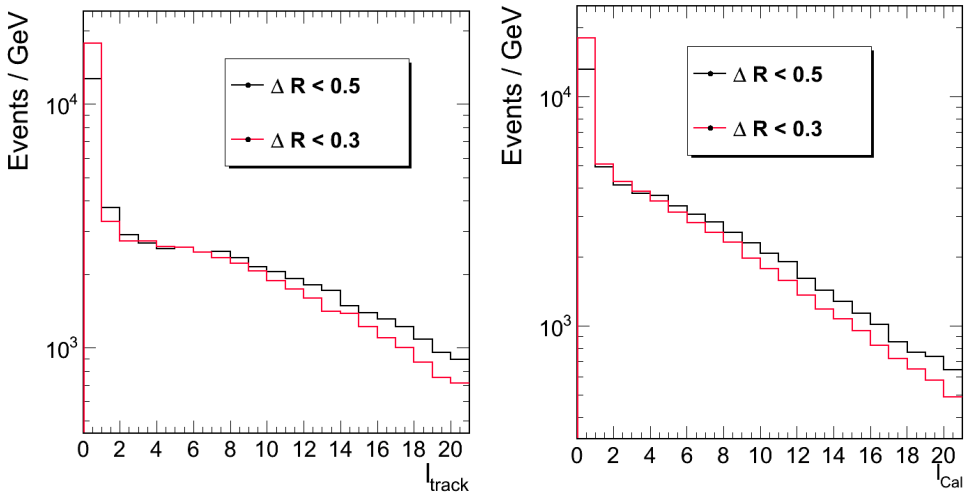

Figure 5.8: Distributions of the Track-Only and Calorimetric-Only isolation variable on data, for well reconstructed muons with $p_T > 15$ GeV, estimated with different cone sizes of $R = 0.3$ and $R = 0.5$ radians

As anticipated in Figure 5.6, muons from electroweak processes concentrate in the low part of the isolation distribution, while the ones coming from hadronic events tend towards a more or less uniform distribution in the higher values of the isolation variable. Therefore the isolation distribution is divided into "isolated" (I <threshold) and "anti-isolated" (I >threshold') regions, for a thresholds which depends on the final isolation variable chosen in the analysis. The chosen thresholds can be different, this way introducing a safety intermediate region (threshold< I <threshold') which minimizes the possibility of leakage of electroweak events in the defined "anti-isolated" region.

Combining information from the tracker and the calorimeters demonstrates a bigger rejection power against hadronic events while keeping the signal efficiency intact, when compared to simpler track-only isolation, in the lower part of the momentum spectra where hadronic background is concentrated.

In addition to this, a more uniform rejection power as a function of p_T is obtained if instead of presenting the amount of energy around the muon as an absolute quantity, it is presented as a relative variable (dividing by the transverse momentum of the muon). The fraction of events surviving after the application of the isolation criteria (efficiency) is shown in Figure 5.10, in which the signal efficiency (roughly $\epsilon_{eff} \approx 1$) is compared to the selection efficiency on QCD events (lower than $\epsilon_{rej} = 10\%$, also called rejection power), using high statistics Monte Carlo samples. The efficiencies are plotted versus the transverse momentum of the muon. This

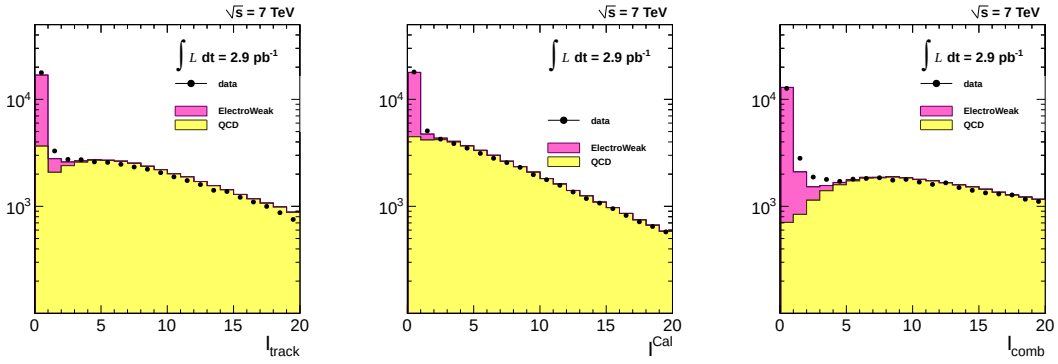

Figure 5.9: Distributions of isolation, on a high momentum ($p_t > 20$ GeV) sample of single muons passing the trigger and ID criteria. Left: track-only isolation ($I_{\text{Track}} = \sum_{\text{tracks}} p_T$). Middle: Calorimetric-isolation $I_{\text{Cal}} = \sum_{\text{ECal}} E_T + \sum_{\text{ECal}} E_T$. Right: Combined isolation: $I = \sum_{\text{tracks}} p_T + \sum_{\text{Cal}} E_T$. Data is compared with Monte Carlo expectation, normalised to the predicted cross-sections and integrated luminosity of the data.

comparison is done for four definitions of isolation: $I_{rack} < 3$ GeV, $I^{rel}_{rack} < 0.10$ $I_{comb} < 5$ GeV $I^{rel}_{comb} < 0.15$.

All these considerations lead the choice of combined, relative variable which will be used in the rest of the analysis:

$$I^{rel}_{comb} = \frac{\sum_{\text{tracks}} p_T + \sum_{\text{Cal}} E_T}{p^{\mu}_t}$$

The isolation threshold value was chosen comparing simulated W and QCD samples, balancing signal efficiency on the former and rejection power on the latter. The rejection power of isolation on hadronic events versus signal selection efficiency yields a rather smooth curve as shown in Figure 5.11 (right), in which each point corresponds to a threshold value from 0.05 to 0.30. Figure 5.11 (left) shows the distributions of signal and background, and the threshold value chosen. Muons will be considered isolated if the activity around the muon is less than 15% of its transverse momentum: $I^{rel}_{comb} < 0.15$.

The final distribution comparing data to Monte Carlo predictions is shown in Figure 5.12. The red arrow signals this $I^{rel}_{comb} < 0.15$ cut.

5.3 Missing Transverse Energy in CMS

The lack of interaction of neutrinos with the materials of the detectors renders them invisible. They do not leave any physical signal and their presence in a collision has to be inferred indirectly studying energy and momentum conservation.

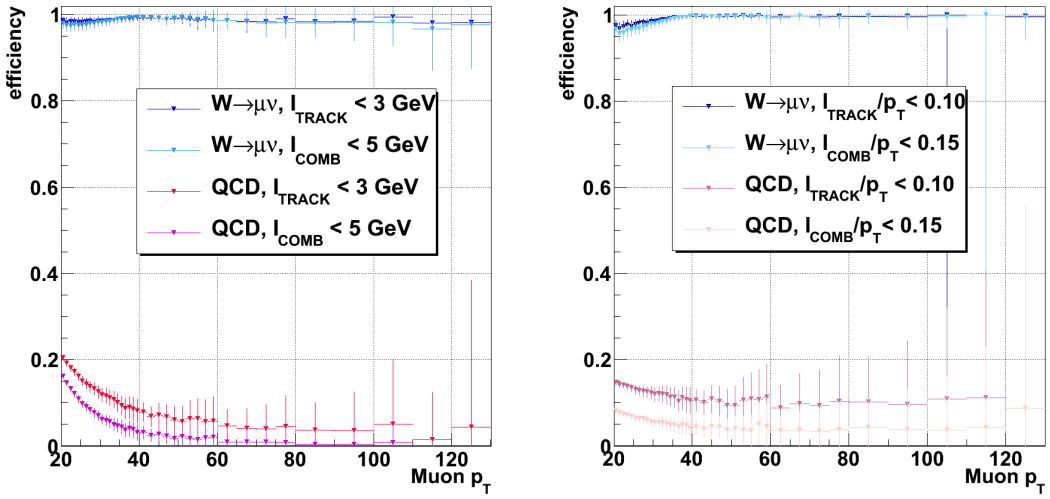

Figure 5.10: Isolation efficiency on W and QCD Monte Carlos, as a function of muon p_T, for absolute (left) and relative (right) isolation. Relative isolation have a flatter response versus p_T for QCD events, and have a greater rejection power for lower momenta - where most of the hadronic muons concentrate. The four kinds of isolation have a similar signal efficiency.

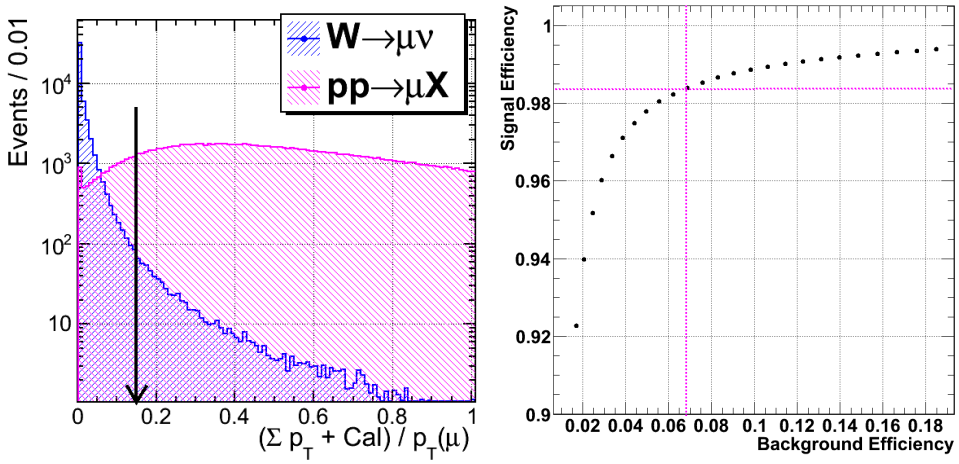

Figure 5.11: Isolation evaluated in Monte Carlo samples, comparing muons coming from W $\rightarrow \mu\nu$ and QCD processes. Left: Distributions normalised to the expected theoretical cross-sections. The arrow at $I^{rel}_{comb} < 0.15$ indicates the threshold value chosen. Right: Variation of signal efficiency vs background efficiency for 25 different values of the I^{rel}_{comb} threshold. Pink lines signal the threshold chosen.

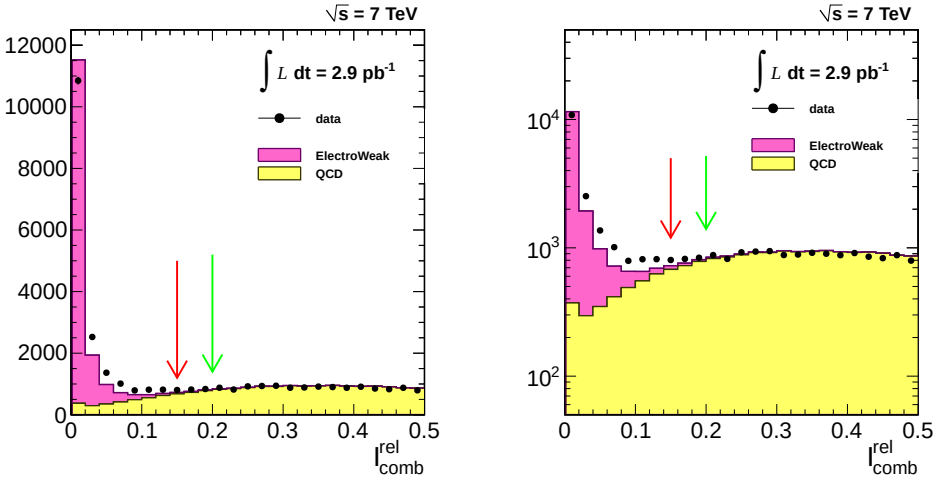

Figure 5.12: Relative Combined Isolation, in lineal and logarithmic formats, comparing data and Monte Carlo. The red arrow at $I^{rel}_{comb} < 0.15$ marks the defined signal region. The green arrow at $I^{rel}_{comb} > 0.20$ marks a region dominated by QCD background.

Thanks to the hermeticity of the CMS detector almost any particle in an ample angle coverage can be detected. The event should therefore be balanced energetically. An imbalance in the momentum in the plane transverse to the beam direction signifies the presence of undetected particles (which can be neutrinos, but also objects escaping the fiducial volume of the detector).

Reconstruction of $\sum E_T$ (scalar sum of all the energy in the event in the transverse plane) and $\overrightarrow{E_T}^{miss}$ (vectorial imbalance in the transverse plane) is challenging. It is very sensitive to detector miscalibration and noise. In addition to this it can be mismeasured if otherwise identifiable particles pass through poorly instrumented parts of the detector.

The magnitude $E_T^{miss} = |\overrightarrow{E_T}^{miss}|$ is one of the most important variables for many processes. In particular it is a clear discriminator for any physical process involving the production of neutrinos, or in any super-symmetric search involving weakly interacting particles. In this thesis E_T^{miss} reconstruction plays a key role, since good resolution is crucial not only to obtain a narrow jacobian peak for the W signal in the M_T spectrum but also to distinguish it from background events which do not contain neutrinos.

CMS has designed three main algorithms to reconstruct $\overrightarrow{E_T}^{miss}$, involving all of the sub-detectors to ensure the required performance is obtained. They are briefly described in this section.

5.3.1 E_T^{miss} Algorithms

The basis for a global energy reconstruction in a detector like CMS is the sum of all the energy in the event. This energy can be merely measured in the calorimeters, or incorporate corrections using other subdetectors. In particular, CMS is particularly interested in using the tracker, given its excellent momentum determination.

- **Calorimetric** $\overrightarrow{E_T}^{miss}$ (CaloMet)

It uses exclusively the energy deposited in the ECal and HCal towers. The $\overrightarrow{E_T}^{miss}$ variable is computed as the negative vector sum of these calorimeter depositions

The energy collected in the calorimeters does not take into account muon energy, since muons are minimum ionising particles that traverse them almost unaffected (in average, they deposit only ≈ 2 GeV). Therefore the contribution of the momentum of all the muons in the event has to be subtracted vectorially for the final calculation.

$$\overrightarrow{E_T}^{miss} = -\sum_{\text{CaloTowers}} \overrightarrow{E_T} - \sum_{\text{muons}} \overrightarrow{p_T}^{\mu} + \sum_{\text{muons}} \overrightarrow{E_T}^{\mu}$$

Further corrections can be applied to this CaloMET. Final states with jets require that the E_T^{miss} is corrected by the Jet Energy Scale. These corrections take the measured raw energy values and adjust them for the difference between corrected and raw energy scales. Uninstrumented regions of the detector, and effects of underlying event, can also be considered.

- **Track-Corrected** $\overrightarrow{E_T}^{miss}$ (tcMet)

The performance of the CMS tracker is superior to the one of the calorimeters for the measurement of the momentum of charged particles. The overall resolution and tails of the $\overrightarrow{E_T}^{miss}$ reconstruction can be greatly improved by combining the information provided by the CaloTowers as a basis with momentum measurement in the tracker, in the cases in which this is possible.

"Track-corrected" E_T^{miss} or "tcMET" is calculated replacing for all well reconstructed tracks the expected energy deposition in the calorimeters with the corresponding measured track momentum. This correction is applied to all tracks not identified as muons or electrons.

Charged particles are assumed to be pions, and their expected energy deposit is determined from a response function derived from a single pion Monte Carlo sample, mapped in bins of

η and p. Tracks with $p_T < 2$ GeV are fully compensated for assuming no response from the calorimeters ($\overrightarrow{E_T}^{miss} = 0$). Tracks with $p_T > 100$ GeV receive no correction since at that energy the measurement of calorimetric energy for charged hadrons is already good enough not to gain anything from the tracker resolution.

Identified muons are corrected in a similar way to CaloMET. No correction is applied for identified electrons as their energy is already correctly measured in the electromagnetic calorimeter.

$$\overrightarrow{E_T}^{miss} = -\sum_{\text{CaloTowers}} \overrightarrow{E_T} - \sum_{\text{muons}} \overrightarrow{p_T}^{\mu} + \sum_{\text{muons}} \overrightarrow{E_T}^{\mu} - \sum_{\text{good tracks}} \overrightarrow{p_T}^{track} + \sum_{\text{good tracks}} \overrightarrow{E_T}^{track}$$

The aim behind the design of this algorithm is the control of the tails of the $\overrightarrow{E_T}^{miss}$ distributions in events with no real E_T^{miss}.

- **Particle-Flow** $\overrightarrow{E_T}^{miss}$ (pfMet)

A final step comes from the full reconstruction and interpretation of the event through Particle-Flow techniques [68], which aim to identify all stable particles in the event (electrons, muons, photons, neutral hadrons and charged hadrons) through the combination of all CMS-subdetectors. Jets and τs are built from these identified objects.

Once all particles in the event are identified by the algorithm, $\overrightarrow{E_T}^{miss}$ is determined by building the vectorial sum of transverse momentum over all reconstructed particles in the event and then taking the opposite of this azimuthal 2D vector.

$$\overrightarrow{E_T}^{miss} = -\sum_{\text{All PF-Particles}} \overrightarrow{p_T}$$

There is no need to apply corrections for muons or tracks since they are directly taken into account in this inclusive approach.

5.3.2 Performance of E_T^{miss}

The performance of the missing transverse energy reconstruction has been studied in detail with the first 7 TeV data, using samples of minimum bias events or events with two identified jets.

The agreement of the three E_T^{miss} algorithms with Monte Carlo events is shown in Figure 5.13, for an integrated luminosity of 11.7 nb^{-1} [69]. The agreement is remarkable, specially taking

into account the early phase of the experiment (the first few months) in which the analysis was performed, and the sensitivity to noise of the $\overrightarrow{E_T}^{miss}$.

These studies served to identify and "clean" sources of noise. Hits in ECal and HCal which correspond to anomalous signals are identified by their timing (pulse shapes are different for physical and unphysical signals) and by examining neighbouring channels. Other sources of noise can only be identified and removed at higher levels of reconstruction (for example, jets with only hadronic energy are unlikely and may be removed from the calculation).

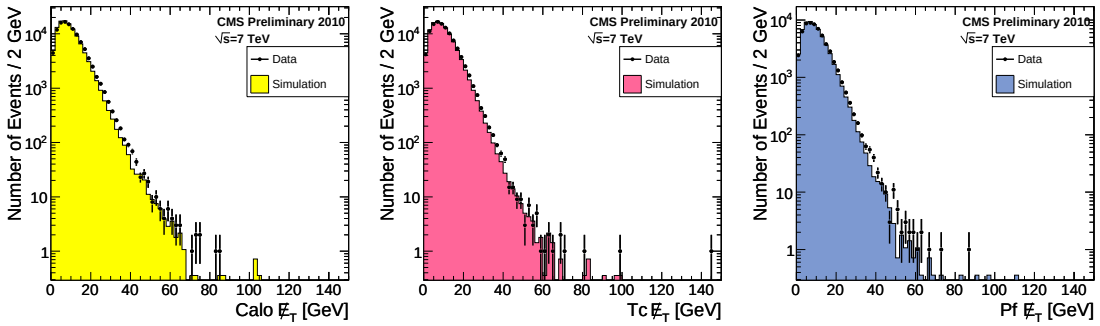

Figure 5.13: E_T^{miss} evaluated in data compared with Monte Carlo predictions, for a di-jet sample, for an integrated luminosity of 11.7 nb^{-1} [69]. Left (Yellow): caloMet, Center (Pink): tcMet, Right (Blue): pfMet.

5.3.3 E_T^{miss} in W and Z events

Vector bosons are excellent benchmark process to study E_T^{miss} performance on collision data [70]. W and Z events have very similar production and decay mechanisms. However, they are experimentally very different, since no $\overrightarrow{E_T}^{miss}$ is expected in Z events.

Z boson events should be completely balanced energetically, with two clearly identified muons and no energy deposited in the calorimeters[1]. There should be no $\overrightarrow{E_T}^{miss}$ in these events. Therefore they can be used as a calibration tool for E_T^{miss} algorithms, since the presence of E_T^{miss} in $Z \rightarrow \mu^+\mu^-$ would indicate mis-reconstruction or noise in the event. A data / Monte Carlo comparison of the E_T^{miss} algorithms in a sample of two isolated muons as described in Section 5.2.4 is shown in Figure 5.14.

The agreement data-MC is rather good, although not perfect. For the three algorithms the E_T^{miss} reconstructed is very close to zero, but in the case of CaloMet the spread of the distribution is broader. pfMet and tcMet provide a better reconstruction.

[1]Except in the case of production of Z+N jets, which corresponds to less than a 10% of the total Z production.

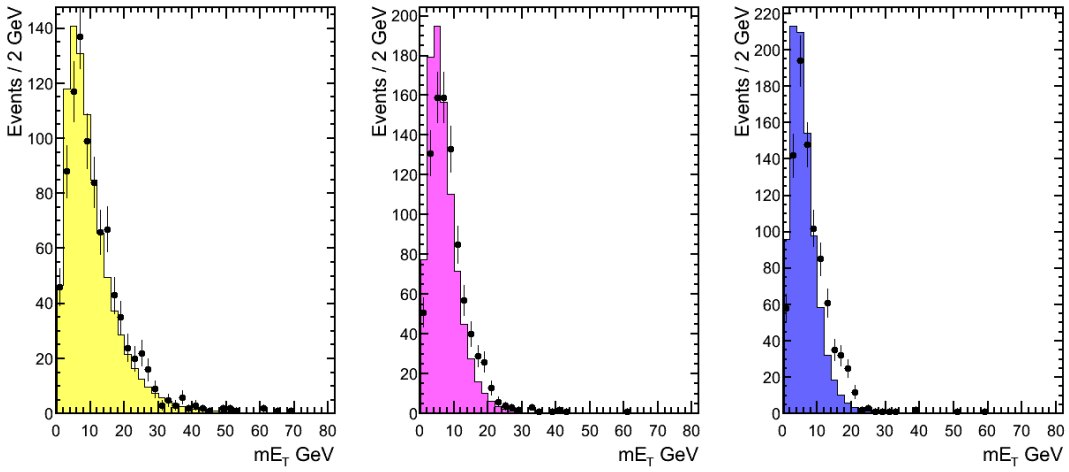

Figure 5.14: E_T^{miss} in data (dots) compared to $Z \rightarrow \mu^+\mu^-$ Monte Carlo (solid colour), for a sample of isolated dimuons of high momentum. Left (Yellow): CaloMet, Center (Pink): tcMet, Right (Blue): pfMet

In the case of W bosons, there is a natural source of E_T^{miss} in the event. The neutrino cannot be detected, and it has to be estimated through the missing transverse energy vector of the event. Figure 5.15 presents three different variables. The top row of plots shows the neutrino momentum, experimentally measured as E_T^{miss}, for each reconstruction algorithms. The central row of plots shows the angle between the E_T^{miss} and the muon in the transverse plane ($acop = \pi - \Delta\phi(\mu, \overrightarrow{E_T}^{miss})$). Finally the transverse mass of the $(\mu, \overrightarrow{E_T}^{miss})$ pair $m_T = \sqrt{2p_T^{\mu}E_T^{miss}(1 - \cos(\Delta\phi(\mu, \overrightarrow{E_T}^{miss})))}$ is shown in the bottom row of plots. In all of them a Monte Carlo sample of W bosons is compared to a data sample of single isolated muons as described in Section 5.2.4. The agreement is not perfect: data is broader than Monte Carlo for the 3 variables, which implies a slightly worse experimental resolution than the one expected from simulation.

The distributions show that the two algorithms which incorporate information from the full system (pfMet and tcMet) yield narrower, clearer peaks both for E_T^{miss} and m_T. This observation confirms what was observed in Z events. Looking solely at Monte Carlo information, the expected resolutions of the three algorithms can be obtained comparing the reconstructed E_T^{miss} and M_T distributions to the generator level information in the event (momentum of the generated neutrino and transverse mass of the generated W). This resolution is shown in Figure 5.16 in a high-statistics Monte Carlo sample of W events. Resolution for the Particle Flow and Track Corrected algorithms are comparable, but a clear broadening of the resolution

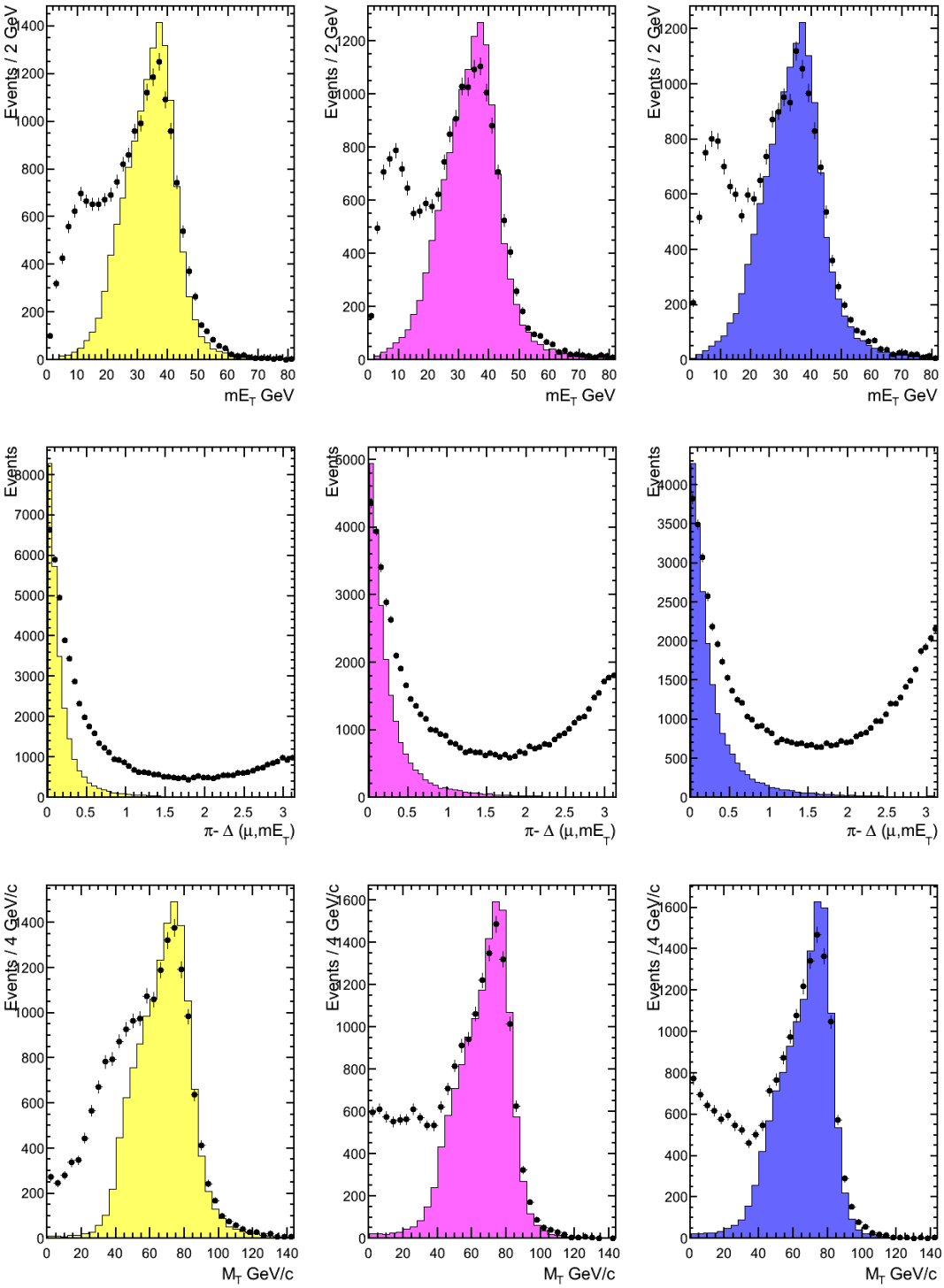

Figure 5.15: E_T^{miss}, acoplanarity (ϕ angle between the muon and the E_T^{miss}) and transverse mass (M_T) in data compared to a W $\rightarrow \mu\nu$ Monte Carlo, for an isolated sample of high momentum muons (dots). Monte Carlo distributions are normalized the number of events in data over $mE_T > 25$ GeV, $acop < 0.1$, $M_T > 50$ GeV respectively. Left (Yellow): CaloMet, centre (Pink): tcMet, Right (Blue): pfMet.

distributions is seen when comparing to the plain calorimetric estimation (caloMET).

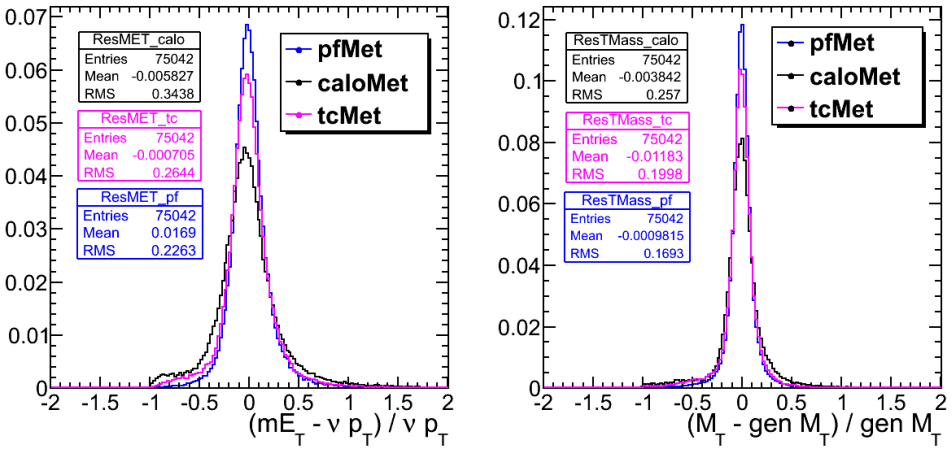

Figure 5.16: E_T^{miss} and M_T resolution obtained on a simulated W $\rightarrow \mu\nu$ sample comparing reconstructed variables with generator level information, for the three reconstruction algorithms.

The analysis will therefore be kept in parallel for both particle flow and track corrected E_T^{miss} reconstruction, with a preference towards particle flow due to the more inclusive nature of the algorithm.

In order to properly model the response and resolution of E_T^{miss} and M_T these variables will be extracted from experimental data themselves, with a procedure based on clean samples of $Z \rightarrow \mu^+\mu^-$ events. This method is described in detail in the next chapter.

Chapter 6

Analysis strategy

The measurement of the W production cross-section can be summarized as a counting of the events observed with a topology distinctive of the signal in a given time interval, once the contamination from the other processes is properly subtracted and any potential losses of signal events are accounted for.

This procedure can be translated into the following mathematical expression for the cross-section:

$$\sigma(\mathrm{W} \to \mu\nu) = \frac{N^{obs} - N^{bckg}}{\epsilon_\mu A_{kin} \times \int \mathcal{L} dt}$$

An efficient selection process has to be defined in order to obtain a clean sample of candidate events (N^{obs}) and reduce the contamination of other processes which resemble the final state under study. The remaining background events (N^{bckg}) must be quantified and subtracted, so that the signal yield will be $N^{obs} - N^{bckg}$.

In spite of the ample coverage of the CMS detector, the full production phase-space is not available for measurement. A restricted phase-space for the analysis has to be defined, and the corresponding kinematic acceptance factor (A_{kin}, the fraction of the phase-space covered) will be computed.

The selection process, together with certain instrumental inefficiencies, will induce a reduction of the number of signal events observed with respect to the total produced. The efficiency of the selection, ϵ_μ, has to be carefully evaluated. The final fraction of events analysed can be expressed through a global factor A_W = selected/total = $\epsilon_\mu \times A_{kin}$, that includes kinematic acceptance and selection efficiency.

Finally, the number of events corrected for acceptance and efficiency has to be normalized to the collisions the accelerator has delivered in that time period, dividing by the integrated luminosity $\int \mathcal{L}dt$ of the sample.

All these issues are addressed in this chapter. An efficient signal selection strategy is defined, evaluating the remaining sources of background. Kinematic acceptance is determined from Monte Carlo, and muon efficiencies from an independent data-sample. Finally, both signal and backgrounds are further characterized in terms of the final variables to be used for the extraction of the signal yield.

6.1 Event kinematics and expected background contributions

6.1.1 $W \rightarrow \mu\nu$ signal selection

W boson production, followed by its decay into a muon and a neutrino, is characterised by the presence of a high momentum, isolated muon in the detector. There will be an imbalance in the energy of the event, driven by a significant amount of $\overrightarrow{E_T}^{miss}$ yielded by the neutrino.

The $W \rightarrow \mu\nu$ candidate sample is selected online by the trigger system, through the HLT_Mu9 selection path, that basically requires an identified muon with a p_T over 9 GeV in the muon system, as described in previous sections.

Offline, the selection continues by requiring that the event has a reconstructed global muon,

- within the volume in which the L1 trigger response is reliable, ($|\eta| < 2.1$),
- which fulfils all the reconstruction quality criteria for muons described in the previous chapter (section 5.2.4.1),
- with $p_T > 20$ GeV,
- and which is isolated in the detector, $I^{rel}_{comb} < 0.15$.

Events with a second muon with a transverse momentum $p_T > 10$ GeV are vetoed, as they are identified as Z boson candidates.

As mentioned, W events are characterised by the high missing transverse energy (typically, $E_T^{miss} > 20,25$ GeV). Since the muon and the neutrino tend to be generated back-to-back, the angle between this $\overrightarrow{E_T}^{miss}$ and the muon will be close to π, and thus the acoplanarity of the $(\mu, \overrightarrow{E_T}^{miss})$ pair ($acop = \pi - |\phi_\mu - \phi_{\overrightarrow{E_T}^{miss}}|$) will be low, peaking at zero. Finally,

Table 6.1: Number of events passing each step of the selection criteria per pb^{-1} for signal and backgrounds. The Monte Carlo samples used and the expected values for the production cross-sections were summarised in Table 5.1. (VV=WW, WZ, ZZ. Z includes photon exchange for $M_{ll} > 20$ GeV. QCD corresponds to inclusive muon production, with generator level cuts of $\hat{p}_T > 20$ GeV, $p_T(\mu) > 15$ GeV and $|\eta| < 2.1$.)

Sample		$W \to \mu\nu$	QCD	$Z \to \mu^+\mu^-$	$W \to \tau\nu$	$Z \to \tau^+\tau^-$	$t\bar{t}$	VV
Produced		10438	79688	1666	10438	1666	165	61
$\geq$1 global muon		7751	76796	1379	1694	361	95	19
Triggered		6306	65418	1100	648	123	49	9
Z Rejection		6298	64910	579	647	120	43	8
Muon Quality		6155	62334	566	631	117	41	8
$\lvert\eta\rvert < 2.1$		5826	60336	521	597	111	40	8
$P_T > 20$ GeV		4902	18650	228	231	40	26	6
$I^{rel}_{comb} < 0.15$		4823	1281	224	224	39	19	6
M_T	pfMet	4040	6	127	99	5	13	4
> 50 GeV	tcMet	4060	10	134	99	5	13	4

the reconstructed transverse mass M_T of the system will be large (peaking at 80 GeV). No requirements are applied on these three variables, and they are used for the final description of the signal.

After this selection has been applied, we obtain a rather clean sample of W events. The effect of each one of the requirements on the signal, evaluated with the high statistics Monte Carlo described in Chapter 5 (Table 5.1), is shown in Table 6.1. Approximately a 46% of the produced signal events are finally selected. The major losses of selection efficiency are driven by the pseudorapidity and momentum criteria (already contained partially in the reconstruction and triggering requirements). The rest of the criteria has very little impact on the signal yield.

The main source of background contamination are hadronic QCD events, mostly decays of heavy ($b\bar{b}$, $c\bar{c}$) and light (π, K) flavour. Selection criteria are established to reduce significantly the contamination of these background processes, but their very high production rate makes them a sizeable background even after applying them.

Typically, these muons do not have a large momentum and have a large number of jets of low energy. As shown in Chapter 5, this implies that they are usually not isolated. In addition to this, only neutrinos coming from semi-leptonic decays of b and c hadrons can provide some

true missing energy. This implies QCD events have little intrinsic E_T^{miss} and M_T, peaking at lower values than the signal.

This background is difficult to model with Monte Carlo techniques, since there is no available prediction for the NNLO cross-section of inclusive muon production. Therefore its contribution will be determined jointly with the signal. Table 6.1 shows the effect of each one of the selection criteria on the sample, based on Monte Carlo simulations, normalized to the LO cross-section. The contribution of this process after all criteria have been applied, compared to the expected yield of W events, is $N_{QCD}/N_{\mathrm{W}\to\mu\nu} \approx 26\%$.

The remaining backgrounds come from other electroweak processes. They are irreducible, since they have very similar kinematics to those of the signal. Luckily they are very well understood theoretically, and thus they can be reliably modelled from Monte Carlo.

The next two contributions from background processes, in quantitative order, are Drell-Yan events ($Z/\gamma* \to \mu^+\mu^-$), in which one of the muons falls out of the fiducial volume of the detector and thus is not reconstructed; and W bosons decaying into tau leptons ($\mathrm{W} \to \tau\nu$) in which the τ decays to a muon. Each one of them represent a similar fraction ($N_{\mathrm{Z}\to\mu^+\mu^-}/N_{\mathrm{W}\to\mu\nu} \approx N_{\mathrm{W}\to\tau\nu}/N_{\mathrm{W}\to\mu\nu} \approx 5\%$) of the final candidate sample, according to Monte Carlo simulations, as shown in Table 6.1.

The contribution of Z bosons decaying into taus, with at least one of the taus decaying leptonically into a muon, is considerably smaller ($N_{\mathrm{Z}\to\tau^+\tau^-}/N_{\mathrm{W}\to\mu\nu} < 1\%$). The remaining background contributions are negligible: production of top-anti-top pairs ($N_{t\bar{t}}/N_{\mathrm{W}\to\mu\nu} < 0.5\%$) and dibosons (WW, WZ, ZZ, $N_{WW+WZ+ZZ}/N_{\mathrm{W}\to\mu\nu} \approx 0.1\%$).

The expected distributions of several variables used in the analysis, after the selection process here described has been applied, are shown in Figures 6.1 and 6.2 as predicted by Monte Carlo simulations. In the first one, the p_T, η, d_{xy} and isolation distributions of the different signal and background processes are shown after all the other requirements have been applied. In the latter, M_T, E_T^{miss}, *acop* are shown for the final candidate sample. It is clear in the plots how the final sample is dominated by signal events, and how the distributions from the main background contribution, QCD, differ from the signal ones.

The optimisation of the selection procedure is always a delicate issue. The highest possible Signal to Background (S/B) ratio is always desirable. However, for this very first measurement, due to the limited statistics available, a compromise was reached. Signal efficiency was optimised, thus obtaining a large candidate sample, while keeping the background at manageable level. A careful signal extraction process was devised to deal with the unavoidable loss of purity.

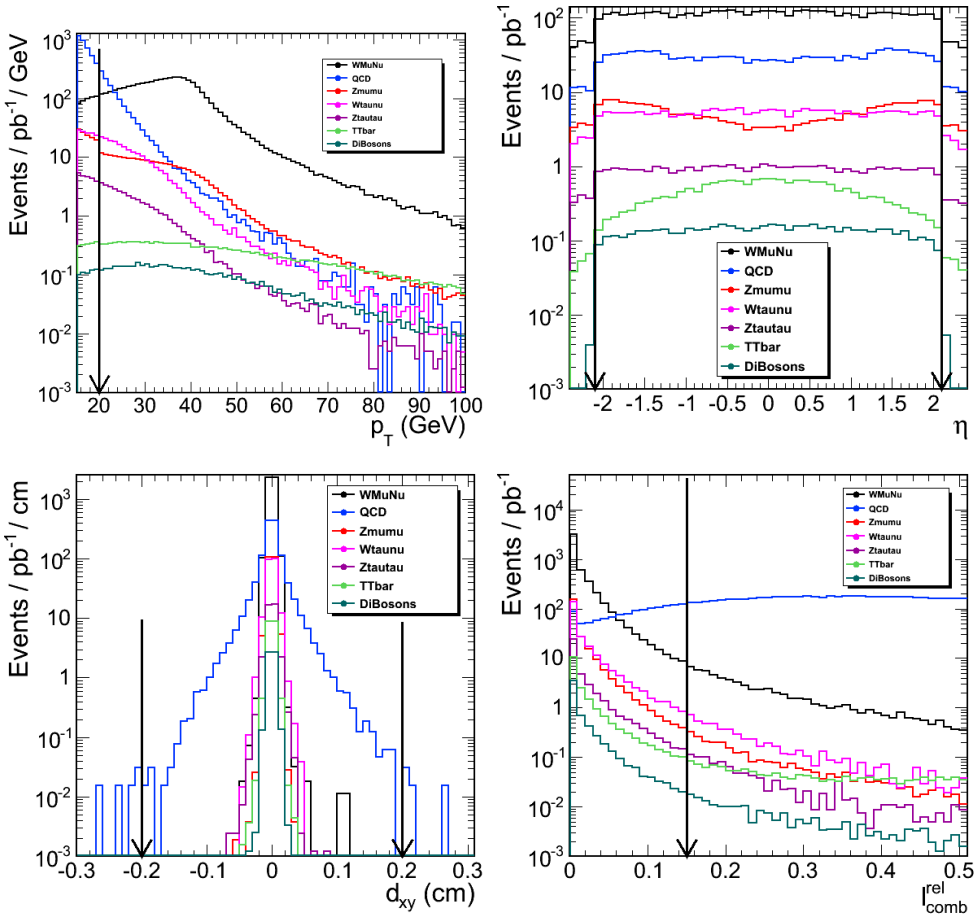

Figure 6.1: Muon p_T, pseudorapidity, impact parameter and isolation distributions once all the selection criteria, except the one corresponding to that variable, are applied. The contributions from the W signal and from the different backgrounds are shown explicitly, normalised to their predicted cross-sections.

Alternative tighter selections were also explored. Several strategies to further suppress QCD background can be devised. For example, imposing tighter kinematic (e.g, higher momentum cut, such as $p_T > 25$ GeV) and topological cuts (e.g: acoplanarity, $acop < 2$) (as in [71; 72]); or tightening the existing isolation (e.g, $I^{rel}_{comb} < 0.10$)) and impact parameter cuts (e.g, $|d_{xy}| < 200\ \mu m$).

The background rejection power of these alternative selections compared to the one used in this thesis is shown in Table 6.2.

Tightening the isolation criteria decreases QCD background, still dominant over the sum of electroweak backgrounds. Tightening the impact parameter threshold is a less successful

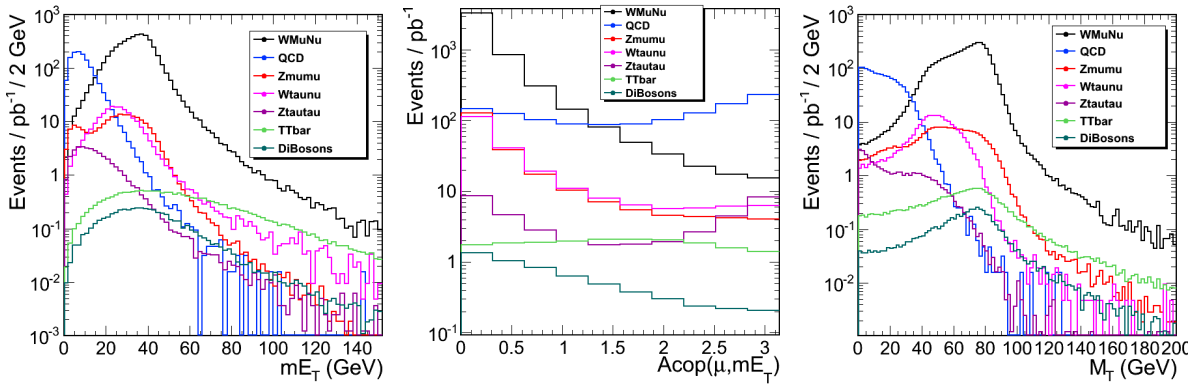

Figure 6.2: Final variables used in the description of the signal (E_T^{miss}, acoplanarity and M_T), computed using particle flow algorithms to reconstruct the missing energy of the event, once all the selection criteria are applied. The contributions from the W signal and from the different backgrounds are shown explicitly, normalised to their predicted cross-sections.

strategy, since setting it at a value low enough as to suppress appreciably the QCD background has also a significant impact on the signal efficiency.

Increasing the p_T threshold is very effective to reduce the contamination of low-momentum hadronic decays. Drell-Yan becomes thus the dominant background. However, it may significantly increase signal shape uncertainties.

Placing requirements on the acoplanarity between the muon and the $\overrightarrow{E_T}^{miss}$ will affect only the lower part of the M_T distribution. Since the high acoplanarity region is basically QCD background only (populated by events in which the muon is reconstructed in the same direction as the $\overrightarrow{E_T}^{miss}$), with a very small contribution of W and Z bosons boosted along the beam direction, the cut basically affects QCD events. Nonetheless, it may also increase the theoretical uncertainties associated to the acceptance.

The final comparison of these three alternative selections is shown in Figure 6.3. The W peak has a clearer separation from the QCD background in the tighter selections, but the event yield is lower. While the first two figures have a similar signal shape, the third one is different due to the higher transverse momentum required and the acoplanarity cut applied.

Therefore for this low luminosity study the optimal selection is the loosest one, with highest signal efficiency. The result of applying this selection criteria on data is shown on Figure 6.4 (left) the observed M_T distribution is plotted after each step of the process on a preselected sample of triggered high momentum muons. The event yields in each step are detailed in Table 6.3.

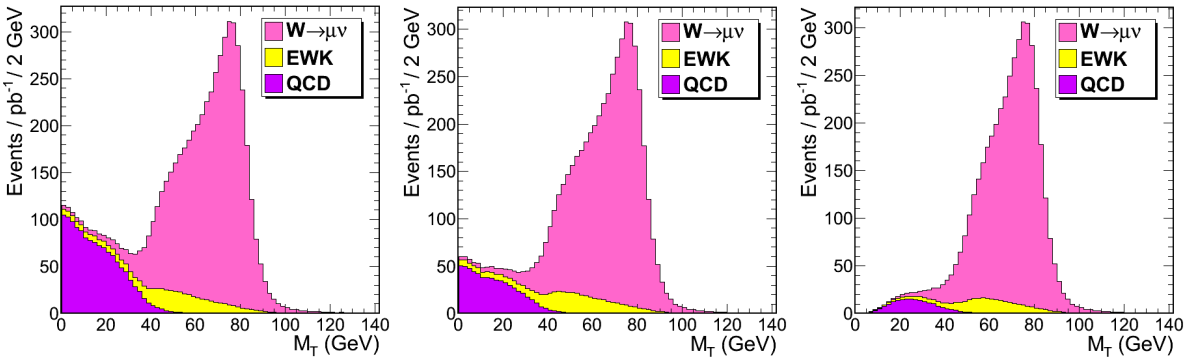

Figure 6.3: M_T distribution after applying all selection criteria, for the selection used in this thesis (left), compared to two tighter selections (centre: tighter isolation I^{rel}_{comb} and d_{xy}, right: tighter p_T and *acop*). The distributions are normalised to the expected contributions at $L_{int} = 1$ pb^{-1} for the different processes.

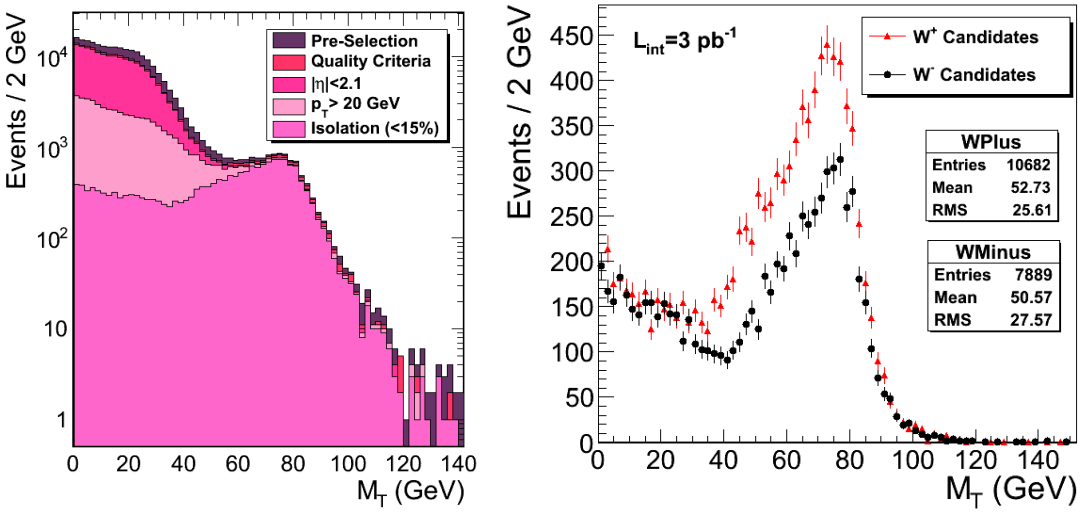

Figure 6.4: Left: M_T after each selection criteria in Data. The initial sample is pre-selected by requesting a high momentum muon ($p_T > 15$ GeV) selected online by the muon trigger path HLT_Mu9. Right: M_T distributions for the experimental data sample of $L_{int} = 2.88$ pb^{-1} after applying all selection criteria, for positive (red) and negative (black) candidates.

Table 6.2: Comparison between the selection used in this analysis and alternatives based on the tightening of several criteria individually, and all together ("tight selection"). The fraction of events selected after the whole process (A_W) is given.

Monte Carlo	$\epsilon_\mu * A_{kin}$			N_{bckg}/N_{sig}	N_{QCD}/N_{EWK}
	W	QCD	EWK		
Selection used in this thesis	46.21%	1.61%	3.65%	37 %	2.5
$d_{xy} < 200\mu m$	46.19 %	1.39 %	3.64%	33%	2.2
$I^{rel}_{comb} < 0.10$	45.60%	0.90%	3.58%	26 %	1.4
$p_T > 25$ GeV	39.94%	0.48%	2.45%	17 %	1.1
$acop < 2$	45.48%	0.85%	3.22%	24 %	0.51
Tight Selection	38.90%	0.12%	2.11%	10 %	0.32

Table 6.3: Observed number of W $\rightarrow \mu\nu$ candidates in $L_{int} = 2.88$ pb^{-1}, compared to Monte Carlo expectations after applying each selection step. The lower number of events in data compared to the expectation is due to an overall lower selection efficiency in data (see section 6.3).

	Predicted (All Processes)	Predicted (W signal)	Observed Events
Preselected	201465	16884	232286
$\lvert d_{xy}\rvert < 2\ mm$	201172	16884	231507
Quality Criteria	194235	16504	192297
$\lvert\eta\rvert < 2.1$	187797	15606	185503
$p_T > 20$ GeV	69358	14117	63346
Iso ($I^{rel}_{comb} < 0.15$)	19053	13890	18571
$M_T > 50$ GeV (pfMet)	12364	11635	11011

The final candidate sample available for the $L_{int} = 2.88$ pb^{-1} analysed consists on 18571 events (10682 positive candidates and 7889 negative candidates). The M_T distributions for positive and negative candidates are shown in Figure 6.4 (right), where the differences in yield ($N^+_W \approx 1.4\ N^-_W$) and shape of the positive and negative sub samples are already evident.

6.1.2 Z $\rightarrow \mu^+\mu^-$ selection

The kinematics of the muons coming from a Drell-Yan decay is very similar to the one of those coming from W bosons. The typical signature of this processes is the presence of two

opposite charge isolated muons of high transverse momentum, with an invariant mass around the Z peak.

Therefore we can benefit from the fact that once a event is identified as a Z, we can obtain a very pure sample of muons that can be used either for efficiency measurements or to provide a clean sample in which to study E_T^{miss} response and resolution.

Z events will be selected online by the HLT_Mu9 muon trigger path and characterised offline by the presence in the detector of two muons with at least $p_T > 20$ GeV reconstructed within $|\eta| < 2.1$, fulfilling the muon reconstruction quality criteria described in Chapter 5 (section 5.2.4.1), and isolated ($I_{comb}^{rel} < 0.15$).

The reconstructed invariant mass of the dimuon must be in the range $M_{\mu\mu} \in (60, 120)$ GeV. This mass constraint is a powerful identification criteria, which in fact will allow us to relax one by one the other selection criteria and still obtain a very pure sample. This way we can study the properties of muons in the event, through "Tag and Probe" techniques (described later in this chapter).

Residual backgrounds are very small ($N_{bckg}/N_{sig} < 1\%$) after this selection. The effect of selection cuts is shown in table Table 6.4.

Table 6.4: Number of events passing each step of the Z selection criteria per pb^{-1} for Z signal and backgrounds. The Monte Carlo samples used and the expected values for the production cross-sections were summarised in Table 5.1. (VV=WW, WZ, ZZ. Z includes photon exchange for $M_{ll} >$ 20 GeV. QCD corresponds to inclusive muon production, with generator level cuts of $\hat{p}_T > 20$ GeV, $p_T(\mu) > 15$ GeV and $|\eta| < 2.5$.)

Sample	W $\to \mu\nu$	QCD	Z $\to \mu^+\mu^-$	W $\to \tau\nu$	Z $\to \tau^+\tau^-$	$t\bar{t}$	VV
Produced	1666	79688	10438	10438	1666	165	61
2 global muons	767.22	5178.71	53.12	8.51	15.76	12.85	1.48
Triggered	719.16	4419.25	45.09	4.637	11.35	10.42	1.28
Muon Quality	672.37	3113.15	26.86	2.48	9.76	7.62	1.10
$p_T > 20$ GeV, $\|\eta\| < 2.1$	357.11	32.48	0.53	0.02	0.87	1.74	0.57
$I_{comb}^{rel} < 0.15$	347.77	0.08	0.03	0	0.84	0.94	0.54
$M_{\mu\mu} \in (60, 120)$ GeV	333.78	0.02	0.03	0	0.35	0.43	0.42

The expected di-muon mass distribution is shown in 6.5. This selection yields a Z data sample of 911 events in the $M_{\mu\mu} \in (60, 120)$ GeV range.

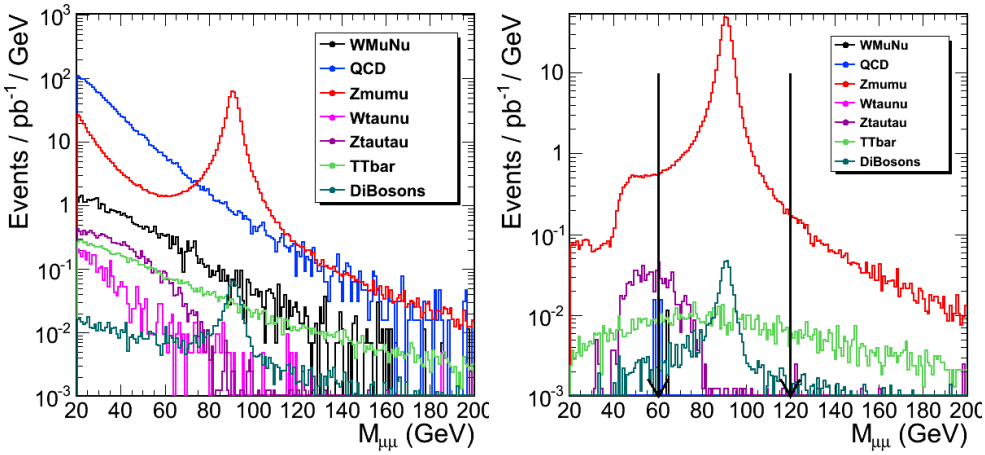

Figure 6.5: Dimuon invariant mass distribution of the Z $\rightarrow \mu^+\mu^-$ candidates. The expected contribution from the different processes, signal and background, are shown before (left) and after (right) selection criteria have been applied.

6.2 Kinematic acceptance

The measurement of the cross-section will be carried out experimentally in a reduced phase-space, where CMS is expected to be highly efficient for the process under study; and then extrapolated to the full phase-space to allow for comparison with the theoretical predictions.

This acceptance region is defined at generator level: a W is defined to be within acceptance if it has a muon with $p_T(GEN) > 20$ GeV in the pseudorapidity region $|\eta| < 2.1$. The kinematic acceptance is then defined as:

$$A_{kin} = \frac{\text{Generated events with } p_T > 20 \text{ GeV}, |\eta| < 2.1}{\text{Generated events in the full phase-space}}$$

A_{kin} values are computed with a W sample generated with our baseline NLO Monte Carlo, POWHEG [60], interfaced with PYTHIA [59] for parton-showering (see Table 5.1). Signal samples with PYTHIA have also been considered for cross-checks. They are given in Table 6.5 for positive and negative bosons independently. This definition takes into account final-state QED radiation effects.

The production mechanisms and kinematics of positive and negative W bosons are not identical. As a result, the p_T and η spectra are slightly different for W^+ and W^- (Figure 6.6), and there is a small difference between the A_{kin} factors for each process.

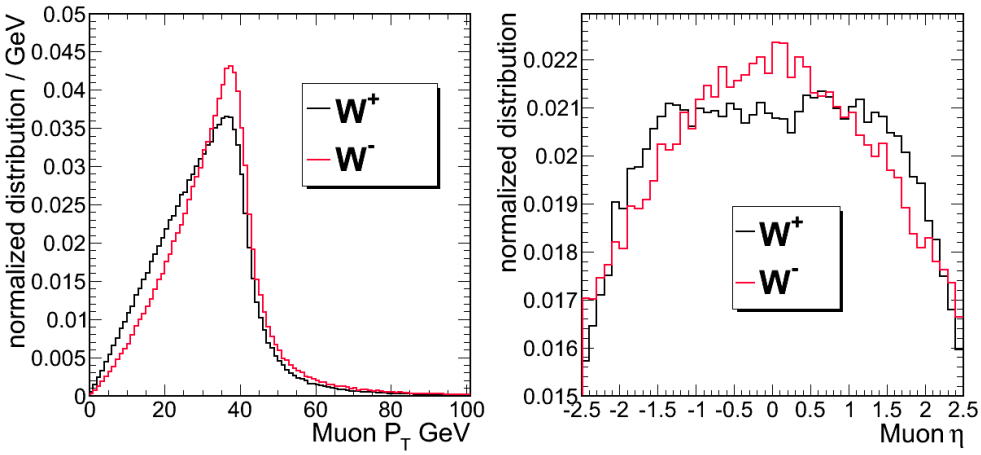

Figure 6.6: Muon p_T and pseudorapidity η at generator level in a high-statistics POWHEG sample, before any selection criteria is applied. The differences between the distributions of the positive W^+ bosons (black) and the negative W^- (red), origin of the difference in kinematic acceptance of the processes, are evident.

For simplicity, in this analysis the kinematic acceptance (A_{kin}) and the muon efficiency (ϵ_μ) will be integrated in a full "selection efficiency" term, which can be factorised as follows:

$$A_W = A_{kin} \times \epsilon_\mu = \frac{\text{Selected Events after cuts}}{\text{Generated Events (in the full phase space)}}$$

Table 6.5: Final selection efficiency and generator level kinematic acceptance. Errors are statistical only.

	Generator level Acceptance (A_{kin})		Selection Efficiency (A_W)	
	W^+ (%)	W^- (%)	W^+ (%)	W^- (%)
POWHEG (cteq66)	54.13 ± 0.07	50.23 ± 0.06	47.65 ± 0.07	44.13 ± 0.06
PYTHIA (cteq6L)	53.94 ± 0.08	50.46 ± 0.08	46.69 ± 0.07	43.64 ± 0.07

This global "acceptance × efficiency" factor includes all the muon efficiencies, from reconstruction to isolation, and can be derived from Table 6.1. It will be first evaluated with the mentioned high-statistic POWHEG samples. Muon efficiencies ϵ_μ will be later evaluated in data, and this value of A_W will be corrected for any differences with the real performance of the detector.

The original Monte Carlo values for the global selection efficiency factor for positive and

negative bosons for both Monte Carlos are also shown in Table 6.5. There is again a slight difference in the A_W factors by charge, which comes solely from A_{kin}. Selection efficiencies (isolation, reconstruction, triggering) are expected to be identical for positive and negative muons.

The equivalent selection efficiencies A_{EWK} for electroweak backgrounds ($Z \to \mu^+\mu^-$, $W \to \tau\nu$, $t\bar{t}$) are summarised in Table 6.6, ordered by their quantitative importance in the final candidate sample. The have been computed in the same way as the signal A_W, making use of the high statistics Monte Carlo samples presented in Chapter 5. This acceptances will be needed in Chapter 7 for the signal extraction procedure.

Table 6.6: Acceptance × efficiency factors (A_{EWK}) for electroweak backgrounds, needed in the equations of the template method. Errors are statistical only.

	$Z \to \mu^+\mu^-$ (%)	$W \to \tau\nu$ (%)	$Z \to \tau^+\tau^-$ (%)
Positive muons	7.019 ± 0.019	2.192 ± 0.013	1.220 ± 0.009
Negative muons	6.454 ± 0.018	2.074 ± 0.015	1.124 ± 0.009

6.3 Muon efficiencies

In this section we address the determination of single muon efficiencies in Run 2010 A data.

The description of the CMS detector used in Monte Carlo simulation is already very close to reality, both in terms of geometry and performance. However, subtle effects difficult to be modelled may still produce residual differences between the predicted behaviour and the observed one. Therefore, muon efficiencies (reconstruction, identification, isolation and triggering) need to be evaluated in data in order to provide precise measurements.

The performance of the detector is not uniform over all the kinematic range allowed for the relevant muon variables. A differential determination of the corresponding efficiencies, specially as a function of the muon pseudorapidity, would be optimal for the analysis. Given the limited statistics available such a measurement is not possible at the moment. Instead, an averaged efficiency will be computed combining all the independent factors, both in data and in Monte Carlo. A correction factor $\rho_{eff} = \frac{\epsilon_{data}}{\epsilon_{MonteCarlo}}$ is calculated and incorporated in the analysis.

The differential behaviour of the efficiencies is modelled according to Monte Carlo predictions, but the overall efficiency value observed in data is used to correct the A_W parameter defined in

the previous section.

Muon efficiencies are evaluated using a Tag and Probe method, as explained in the following section.

6.3.1 Tag and Probe method

In order to measure each one of the muon efficiencies in the analysis directly from data, we need to select a sample as close as possible to the selected events themselves. As explained before, this is possible due to the similarity of the kinematics of muons coming from W and Z bosons.

The "Tag and Probe" method starts by obtaining a clean sample of $Z \rightarrow \mu^+\mu^-$ events, using as a basis the selection described above. In order to estimate each efficiency the event will be requested to fulfil all selection criteria but the one under study. For example, a sample of well reconstructed, isolated, high momentum global muons will be used to compute the trigger efficiency.

This way we still obtain a sample of dimuons with very little contamination from other processes. We then require one of the muons to be "tagged", i.e, to pass the criteria that defines the efficiency we want to measure, and then "probe" the same condition on the other muon. If "X" is the property we are studying, N_{XX} is the number of events in which both muons pass the selection criteria, and $N_{X\bar{X}}$ are the events in which only one of the muons passes the criteria and the other one fails, the efficiency of "X" is deduced to be:

$$\epsilon_X = \frac{2 \times N_{XX}}{2 \times N_{XX} + N_{X\bar{X}}}$$

The validity of the method is established using Monte Carlo samples. In Monte Carlo we can always obtain the real value of each one of the efficiencies: the fraction of the muons which pass each selection criteria, or mathematically $\epsilon_X = N_X/(N_X + N_{\bar{X}})$. Therefore we can compute for a same sample the "Tag and Probe" efficiencies and compare them to the "Monte Carlo truth" ones [71].

Figure 6.7 shows the isolation and trigger efficiencies of muons at $\sqrt{s} = 14$ TeV, calculated for the corresponding W/Z analysis before the centre of mass energy for the first LHC run was brought down to $\sqrt{s} = 7$ TeV. The value of the efficiency obtained with the Tag and Probe method clearly agrees with the Monte Carlo value of the efficiency over all the rapidity range, thus confirming the validity of the method.

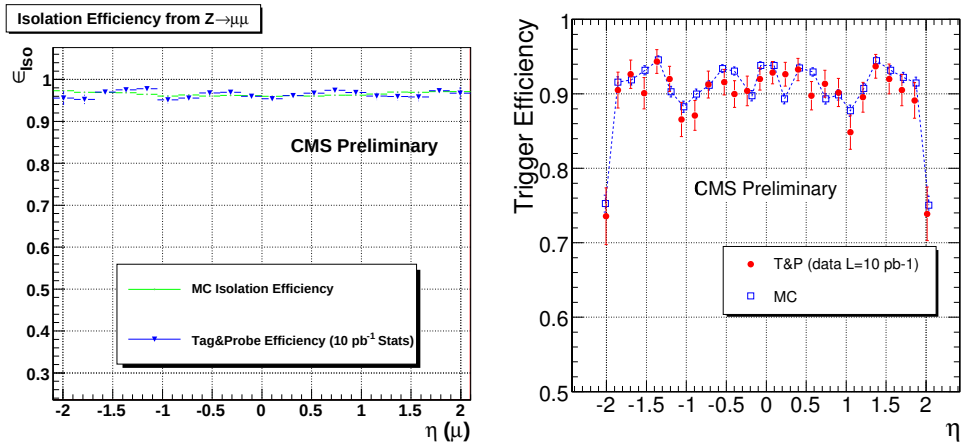

Figure 6.7: Isolation and trigger efficiencies as a function of pseudorapidity, computed for the Monte Carlo exercise on W and Z cross-section measurement at $\sqrt{s} = 14$ TeV and an integrated luminosity of $L = 10$ pb^{-1}, performed in 2007. Monte Carlo truth efficiencies are compared to the result of the Tag and Probe method. The agreement is very good over the full pseudo-rapidity range probed, thus confirming the validity of the method [71]

Using Monte Carlo samples we can also study possible differences between the efficiencies computed in a W sample and in a Z sample. The efficiencies in both samples are shown to agree better than 0.5% in average [73], due to the slightly different kinematical distributions of the two samples.

6.3.2 Muon efficiencies in Run 2010 A

The Z selection process described in section 6.1.2 rendered a sample of 911 golden Z $\rightarrow \mu^+\mu^-$ events. For muon efficiency determination, selection criteria are loosened one by one for one of the muons, in order to probe the corresponding muon efficiency. The total Z sample used to determined the efficiencies amounts to 1075 events [74].

This rather limited statistics imply that a differential determination of the efficiency is not appropriate, since bin by bin fluctuations are larger than any physical effect. An average efficiency is computed both in data and Monte Carlo to evaluate the relevant correction factors, and its behaviour as a function of η and p_T is directly taken from Monte Carlo predictions.

Efficiencies in Monte Carlo and in data are computed in the same way. The results of efficiencies are summarized in Table 6.7. Data and Monte Carlo agree at the percent level in almost all of the cases. The only significant difference is found in the muon trigger efficiency, which shows a 5% of difference due to syncronization mismatches between DT, CSC and RPC

detectors in the overlap region between the barrel and the endcaps. This inefficiency will be reduced once there is enough data to intercalibrate the three systems.

The correction factor $\rho_{eff} = \epsilon_{Data}/\epsilon_{MC}$, which accounts for the differences in data and in Monte Carlo, is also given in Table 6.7. The uncertainty on this ρ_{eff} correction will be propagated as a systematic uncertainty in the cross-section measurement.

Table 6.7: Efficiencies and correction factors, computed through a clean dimuon sample in data and in Monte Carlo simulation [74; 75]

	Data	Simulation	Correction ρ_{eff}
ϵ_{HLT}	$88.3 \pm 0.8\%$	$93.19 \pm 0.14\%$	$94.7 \pm 0.9\%$
$\epsilon_{stand-alone}$	$96.4 \pm 0.4\%$	$97.24 \pm 0.06\%$	$99.2 \pm 0.5\%$
ϵ_{track}	$99.4 \pm 0.5\%$	$99.27 \pm 0.07\%$	$99.8 \pm 0.3\%$
$\epsilon_{isolation}$	$98.5 \pm 0.4\%$	$99.14 \pm 0.04\%$	$99.4 \pm 0.4\%$
ϵ_{id}	$99.7 \pm 0.3\%$	$99.67 \pm 0.05\%$	$100.0 \pm 0.3\%$
$\epsilon_{\mu}(W)$	$82.8 \pm 1.1\%$	$88.74 \pm 0.13\%$	$93.3 \pm 1.2\%$

Muon efficiencies and correction factors are independently determined for positive and negative muons, and presented in Table 6.8, and no difference is observed. A coarse binning in η is obtained by splitting the measurement in terms of regions of the detector (barrel-overlap-endcaps). The results are also given in Table 6.8, and show that most of the discrepancy Data-MC is concentrated in the overlap region between barrel and endcaps.

The Tag and Probe method just described does not account for inefficiencies where the full event is lost. This may happen if by any reason the event is triggered at a wrong bunch crossing. Trigger rules forbid triggering an event at consecutive bunch crossings. Therefore if a given event is assigned a wrong bunch crossing by the muon system (one bunch crossing before the real one),

Table 6.8: Correction factors for several subsets of muons.

Subset	Data/Simulation (ρ_{eff})
Positive muons	$(93.5 \pm 1.8)\%$
Negative muons	$(93.1 \pm 1.9)\%$
Barrel ($\lvert\eta\rvert < 0.9$)	$(95.5 \pm 2.4)\%$
Transition ($0.9 < \lvert\eta\rvert < 1.2$)	$(89 \pm 4)\%$
End cap ($1.2 < \lvert\eta\rvert < 2.1$)	$(92 \pm 3)\%$

it will not be selected, as the time info of the event will be incorrect and the tracker information will not be read. No HLT muon candidate will be built, and therefore the event will be lost.

The probability of pre-firing an event has been studied using a muon sample independently triggered by the presence of jets or missing energy in the event. The global correction factor is found to be $0.5 \pm 0.5\%$ for W events and $1. \pm 0.5\%$ for Z events [76; 77; 78]. The uncertainty on this correction will be incorporated as a systematic uncertainty on the crosssection measurement.

Therefore the overall correction factor to be used for the W cross-section measurement is of 0.933×0.995, with an associated systematic uncertainty of $1.2\%(\rho_{eff}) \otimes 0.5\%(pre - trigg) \otimes 0.5\%$(W-Z kinematics).

6.4 Signal and Background modelling

Once we have selected a sample of candidates $N_{sel} = N_{signal} + N_{bckg}$, and we have computed the kinematic acceptance of the process and the efficiency associated to the selection process applied, we need to extract the W signal yield from the total candidate sample.

The strategy followed is o take the distribution of the discriminant variable (M_T or E_T^{miss}) as a sum of several components, each of them corresponding to a different physical process (signal, hadronic background, and the combination of all the other electroweak processes involved). The yield of each one of the components is obtained from a binned fit to the experimental distribution. This fit is described in detail in Chapter 7. It requires a previous adequate modelling of the several variables considered for all the processes involved.

The production of W bosons is well understood theoretically. The general kinematic of the events is properly reproduced by Monte Carlo generators, and the distributions predicted in simulation are expected to reproduced successfully the data. The only correction needed will therefore account for possible experimental discrepancies in event reconstruction.

As it was seen in Chapter 5, muon momentum scale and resolution determined in data is in very good agreement with the prediction from Monte Carlo simulation. However, the agreement between Monte Carlo descriptions of E_T^{miss} related variables and data is not perfect, with noticeable discrepancy in the resolution.

In the following section the description of these variables (E_T^{miss}, $acop$, M_T) will be improved using information extracted from the data.

This argument also applies to electroweak processes different to the signal ($Z \rightarrow \mu^+\mu^-$, $W \rightarrow \tau\nu$, etc). However due to their small contribution to the final data sample the net effect of this correction will be negligible.

For hadronic backgrounds the task is more complicated. The Monte Carlo predictions for these processes are not reliable enough, and therefore the template shapes used in the fit will be entirely modelled using data themselves.

6.4.1 E_T^{miss} resolution and W signal template

As described, in order to obtain a realistic description of the signal shape (either in M_T or in E_T^{miss}) we will need to incorporate the worsening of the E_T^{miss} resolution observed in data to the Monte Carlo.

Once again we can make use of a $Z \rightarrow \mu^+\mu^-$ sample for this task. We will model E_T^{miss} response and resolution using Z data, and then incorporate it to our high-statistics baseline $W \rightarrow \mu\nu$ Monte Carlo. This way, since the kinematic of the event is already reliably modelled at generator level and muon reconstruction is properly reproduced by simulation, we will finally obtain a satisfactory description of the W signal.

Z events have no physical source of $\overrightarrow{E_T}^{miss}$, aside from detector related resolution effects or mismeasured particles. Therefore we can use a clean $Z \rightarrow \mu^+\mu^-$ sample to obtain information about the response and resolution of the missing energy reconstruction.

The fact that muons pass basically undetected through the calorimeters, leaving only a small energy deposition, aids to separate the Z boson from the rest of the event. E_T^{miss} has been corrected by the muons in the event, so to compare the kinematics of W and Z bosons we have to go back to the "raw" measurement $\overrightarrow{E_T}^{miss\,raw} = \overrightarrow{E_T}^{miss} + \sum_\mu \vec{p}_T$.

Figure 6.8 shows the 2D scatter plot of missing E_T^{miss} with respect to the boson p_T, for the $Z \rightarrow \mu^+\mu^-$ events in the left panel and for the $W \rightarrow \mu\nu$ events in the middle one, computed with high statistics Monte Carlo sample. The last panel compares the profile of both distributions. Note that while the Z p_T is computed using the momenta of the two reconstructed muons, the W-p_T uses the momentum of the reconstructed muon together with that of the generated neutrino. Both spectra are in perfect agreement over the full p_T range shown. This comparison is shown here for particle flow, other E_T^{miss} algorithms give similar agreement.

For a given value of the boson p_T we obtain a experimental E_T^{miss} distribution from $Z \rightarrow \mu^+\mu^-$ data. This distribution is used to sample a realistic E_T^{miss} value for a W Monte Carlo event of that boson p_T. The same process is repeated for the angular distribution of the $\overrightarrow{E_T}^{miss}$

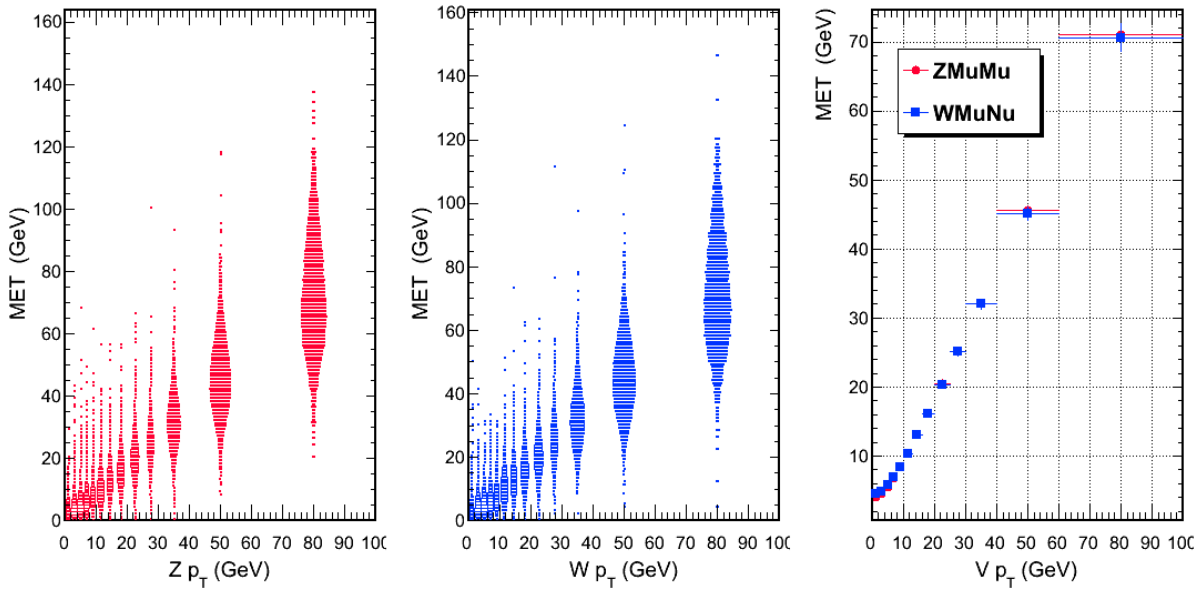

Figure 6.8: Monte Carlo predictions of the $E_T^{miss\,raw}$ distribution versus boson p_T for Z (left) and W (centre) events. The selection criteria described in this chapter have been applied to the samples. Both distributions are in perfect agreement, as better seen in the profiles shown in the right plot.

direction with respect to the Z p_t. This sampled $\overrightarrow{E_T}^{miss}$ is then combined with the simulated (and reconstructed) muon from the high statistics W Monte Carlo sample.

The method gives better results if instead of sampling directly the direction of the $\overrightarrow{E_T}^{miss}$ of the event, we decompose $\overrightarrow{E_T}^{miss}$ into two orthogonal variables, one parallel and other perpendicular to the transverse momentum of the Z boson. This projections will be labelled ${E_T^{miss}}_{\perp}$ and ${E_T^{miss}}_{||}$, and are shown in Figure 6.9.

The parallel component of the E_T^{miss} is due to initial state gluons radiated from the quarks that produce the Z. This emission balances the p_T of the boson, and therefore the average ${E_T^{miss}}_{||}$ is expected to increase with the Z p_T. The perpendicular component is caused by multiple interactions and remnants of the boson particles involved in the Z production. The distribution of ${E_T^{miss}}_{\perp}$ is thus centred at zero, showing only resolution effects and remaining roughly constant as Z p_T increases.

The performance of the method has been tested on Monte Carlo. The method is expected to perform accurately if there is enough statistics of $Z \to \mu^+\mu^-$ data accumulated. Therefore two different scenarios were tested, one modelling E_T^{miss} from a very high statistics Z sample, and another modelling E_T^{miss} from a 3 pb^{-1} sample (approximately $\approx$ 900 Z candidates), which is

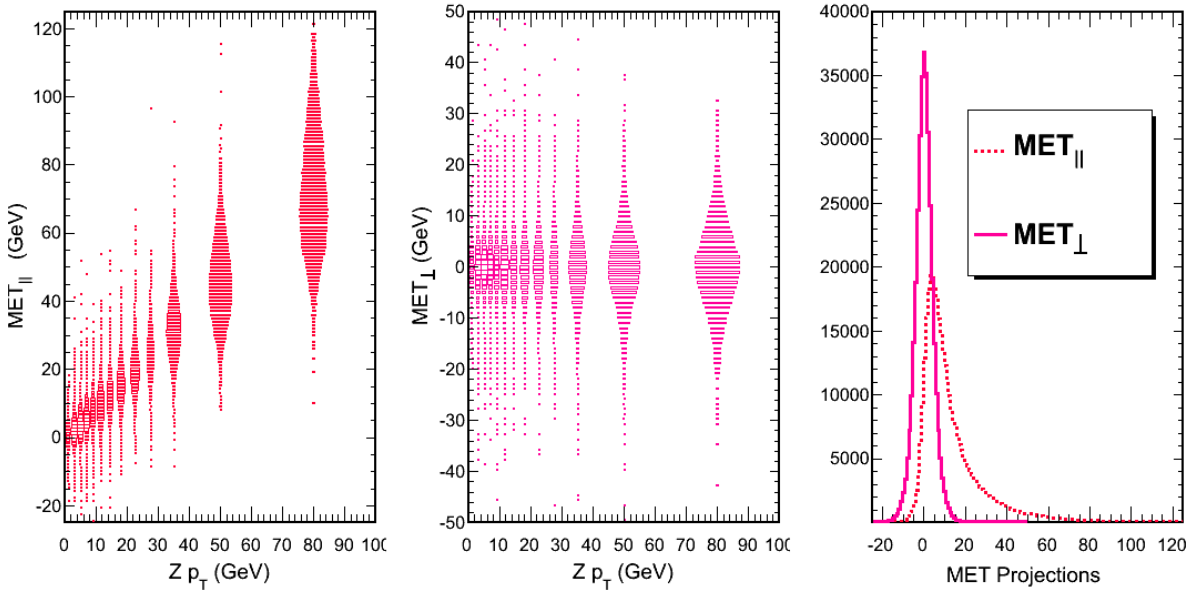

Figure 6.9: ${E_T^{miss}}_{\perp}$ and ${E_T^{miss}}_{||}$ versus boson p_T in a high statistics Monte Carlo sample.

the size of the experimental data sample collected during Run 2010A. Figure 6.10 compares the templates obtained from the two Z samples with the original W distributions in Monte Carlo, for E_T^{miss} and M_T, in linear and in logarithmic scales.

It is shown how the three shapes are in excellent agreement. No degradation of the method is observed when using a 3 pb^{-1} data sample to derive the templates, which implies the Z statistics already available for analysis are is sufficient to describe precisely the signal shape. Discrepancies around the peak among the three templates are negligible There is slight disagreement in shape in the low and high tails of the distributions, but these regions are barely populated and they will have no effect on the cross-section measurement. This guarantees the method will present no bias due to statistics when applied to real data.

The method has been applied to the experimental data analysed in this thesis. The Z candidates have been selected as described in section 6.1.2. Figure 6.11 shows the 2D distributions of ${E_T^{miss}}_{||}$ and ${E_T^{miss}}_{\perp}$ versus Z p_T from which the Z E_T^{miss} information is sampled. Although statistics is low, they follow the same pattern than the one predicted by the MC.

This information is plugged in the W Monte Carlo. The resulting template can be seen in Figure 6.12, compared to Monte Carlo expectations. In the linear plot we can see how there is a clear broadening of the shapes in data, due to a different E_T^{miss} scale and resolution with

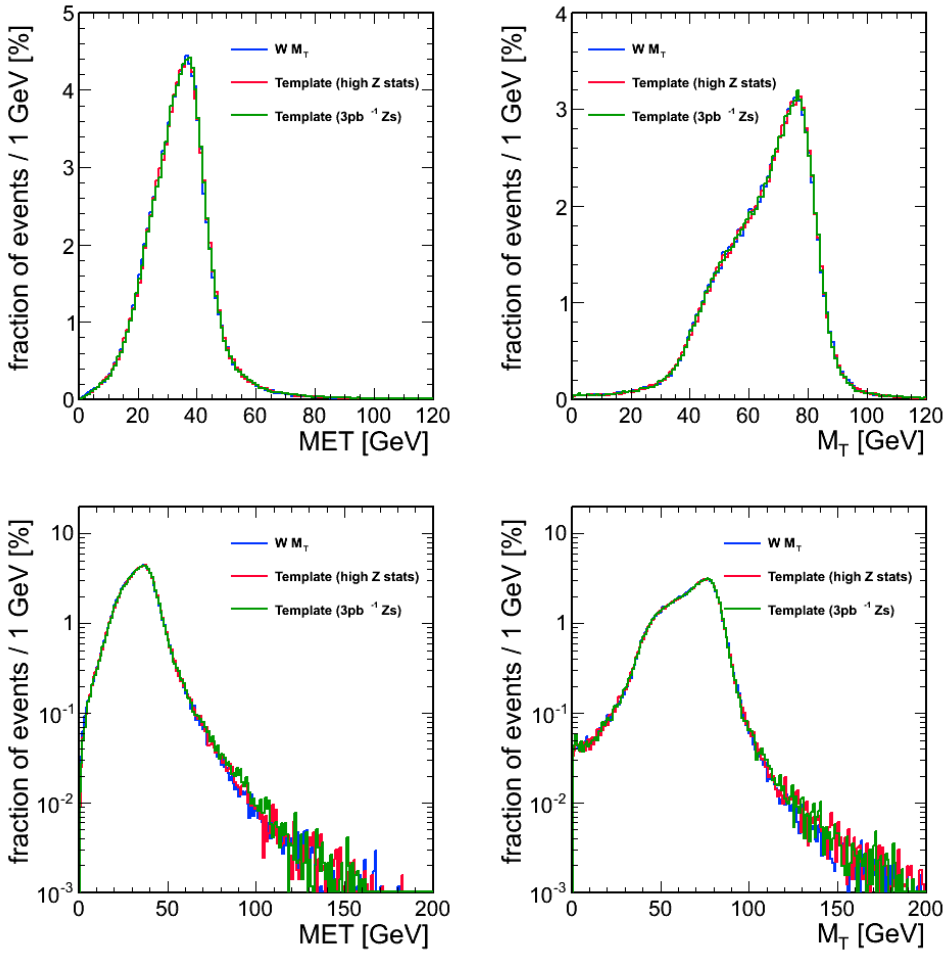

Figure 6.10: High-Statistics Monte Carlo test for the modelling of the signal shape. Distributions of E_T^{miss} (left) and m_T (right). Reconstructed distributions from the original W Monte Carlo are the blue ones. Two templates are compared, one from a high statistics Z sample (red histogram) and other from a sample statistically equivalent to 3 pb^{-1} (green histogram). Comparing the linear and logarithmic version of the plots we can see how the agreement is very good over the full range considered.

respect to the one predicted by Monte Carlo. In the logarithmic plot we can see how the tails agree reasonably well, although this part of the distribution will have virtually no effect on the cross-section measurement. The broadening of the E_T^{miss} and M_T distributions observed in data (see Chapter 5) is well reproduced by this template.

These templates are the ones used in Chapter 7 for signal extraction. Different templates are produced for $W^+ \to \mu^+\nu$ and $W^- \to \mu^-\bar{\nu}$ due to the kinematic differences between positive and negative W bosons. The comparison of shapes between these two templates (using once

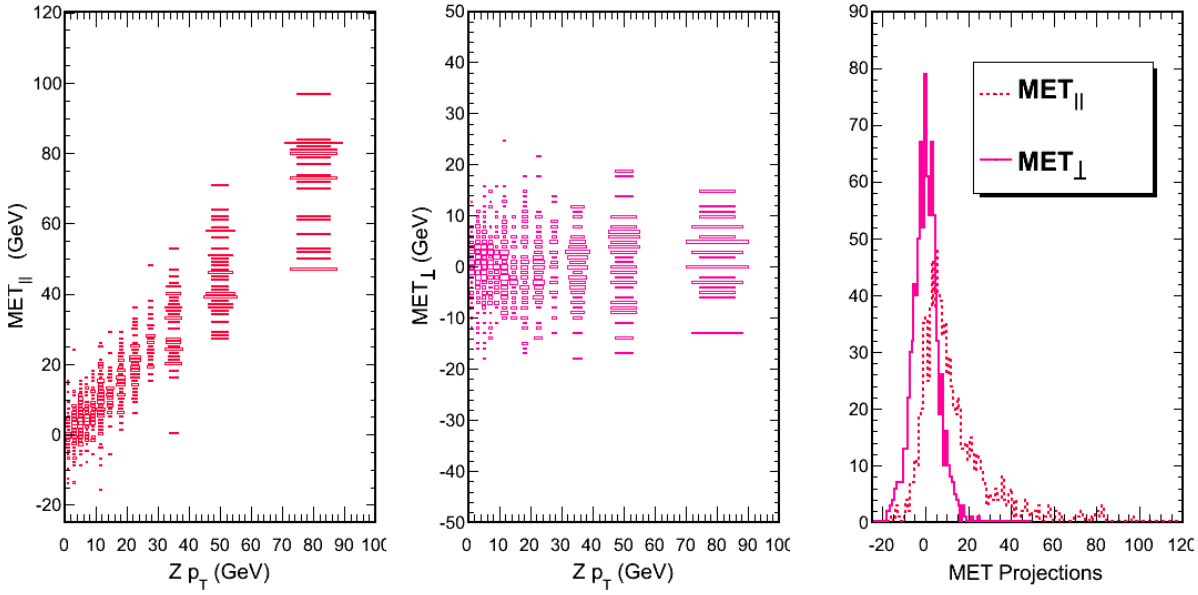

Figure 6.11: 2D distributions of ${E_T^{miss}}_{||}$ and ${E_T^{miss}}_{\perp}$ versus Z boson momentum in 2.9 pb^{-1} data, and their 1D projections.

again particle-flow E_T^{miss}) is shown in figure 6.13 (left).

Missing E_T and transverse mass are not the only variables which can be modelled using this approach. Any $\overrightarrow{E_T}^{miss}$-related variable (acoplanarity, W p_T) can be obtained using the same technique. The p_T of W bosons is shown in Figure 6.13 (right).

Electroweak backgrounds are well understood theoretically, and small enough that at this level of statistics, the effect of these shape distortions in the cross-section can be neglected and their shapes taken from Monte Carlo simulation. These shapes are shown in Figure 6.14, comparing the relative fractions per mass bin of each one of the backgrounds. It can be noticed how for those those backgrounds that include a W in the decay chain (W $\rightarrow \tau\nu$, $t\bar{t}$, dibosons) the resulting exhibits a Jacobian peak, just as the W signal; while processes involving the decay of a Z boson do not. For a comparison taking into account the relative contributions of each process, normalised to the predicted theoretical cross-sections, see Figure 6.2.

Once E_T^{miss} is properly modelled, an estimation of the real performance of the response and resolution of the missing transverse energy reconstruction can be obtained. They can be determined as the width of the distributions $\sigma(M_T(reco) - M_T(gen)/M_T(gen))$ and $\sigma(E_T^{miss}(reco) - p_T(gen\ \nu)/p_T(gen\ \nu))$. The resolutions so obtained are shown in Figure 6.15, as a function of the generated values of the neutrino momentum and the transverse mass of the W boson. The

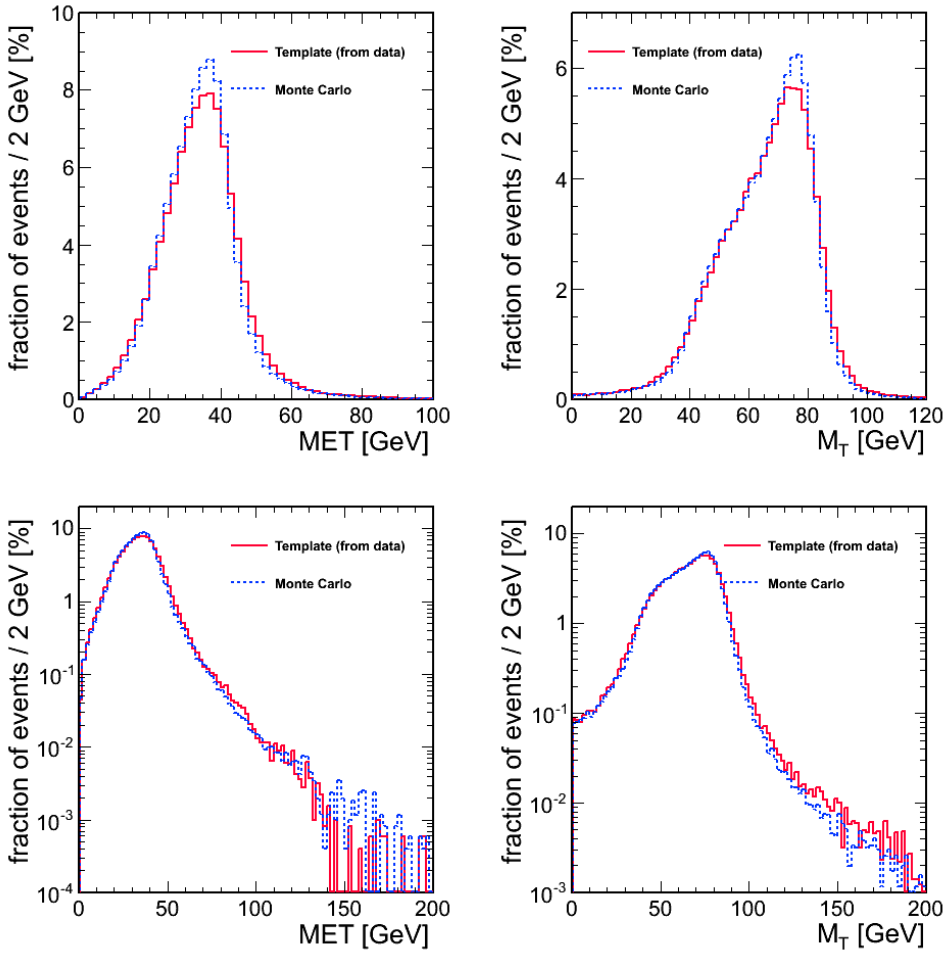

Figure 6.12: Linear and logarithmic E_T^{miss} (left) and M_T (right) shape comparison. W Monte Carlo (POWHEG) in blue and the template from a $Z \rightarrow \mu^+\mu^-$ data-sample in red.

values derived using the information from the templates are indeed slightly worse than the MC truth values.

6.4.2 QCD background template

The approach followed to arrive to an appropriate description of the E_T^{miss} / M_T distribution for hadronic processes is rather different.

Monte Carlo simulations of the QCD background are not accurate enough to rely on their predictions for the description of the relevant distributions. There is no NLO prediction available for the multi-jet simulation required in the analysis. Therefore the modelling of the QCD shapes

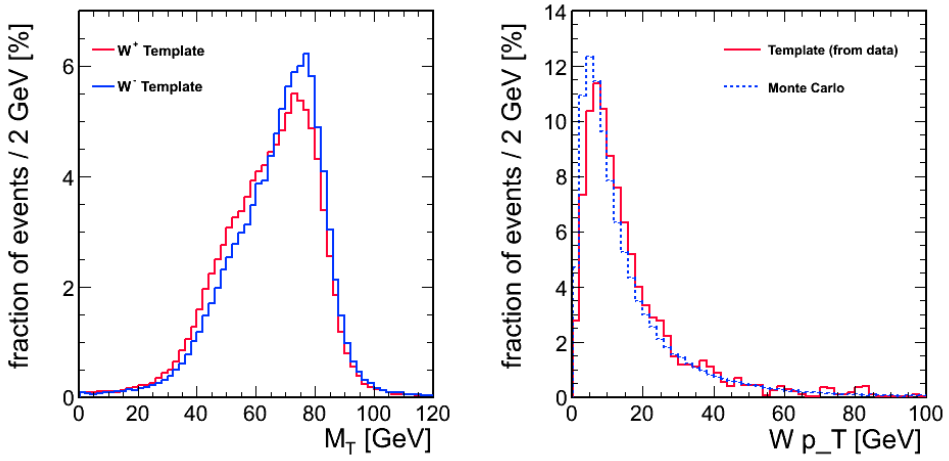

Figure 6.13: Left: M_T template for $W^+ \to \mu^+\nu$ (red) and $W^- \to \mu^-\bar{\nu}$ (blue). Right: Shape for the W p_T, compared to Monte Carlo prediction.

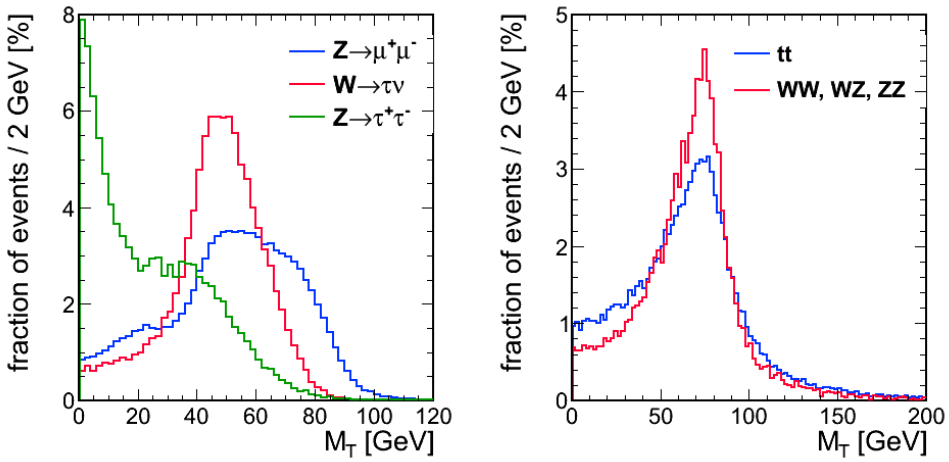

Figure 6.14: Estimation of the normalised M_T distributions of the electroweak backgrounds involved in the analysis, needed in Chapter 7. The left plot shows the main three contributions ($Z/\gamma*$ decays and W decays into τ), which will be fitted together with the signal shape (details in Chapter 7). The right plot shows the two less abundant backgrounds, whose size will be fixed to the expectations according to the theoretical predictions of their cross-section.

(E_T^{miss} and M_T) needed in the analysis will be exclusively extracted from control data samples.

The method proposed will be nevertheless first tested using Monte Carlo samples, since they reproduce the general features of the data even if full agreement between data and simulation is not expected.

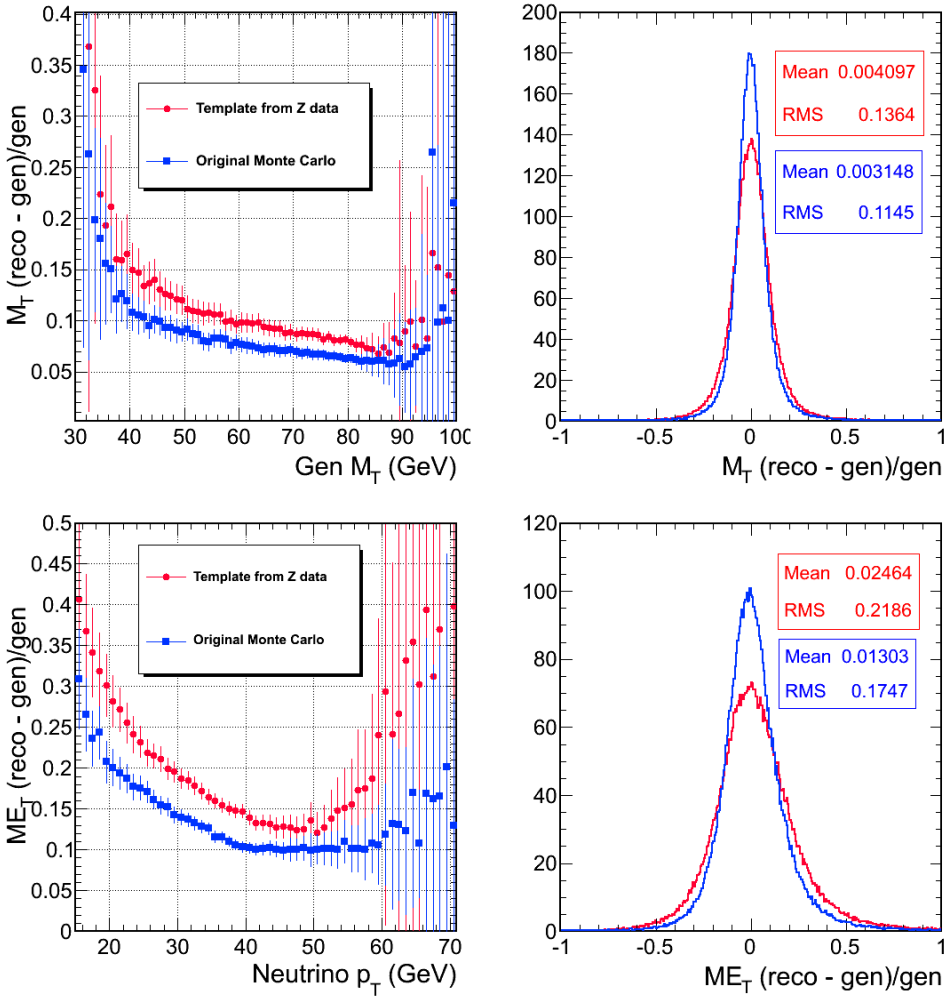

Figure 6.15: Estimation of the M_T resolution versus generated transverse mass (top) and E_T^{miss} resolution versus generator level neutrino momentum (bottom) (computed through the width of the distribution in an event by event basis). In blue, from the original Monte Carlo information and in red, from the described sampled template in data.

The first step consists in selecting a pure QCD data sample, from which a template can be derived. This control region of pure hadronic events can be obtained choosing a variable with no correlation with the distribution we want to model, which is able to cleanly separate signal and background.

In this analysis the variable chosen is isolation. As shown in Chapter 5, the region with a value of the isolation variable over $I_{comb}^{rel} > 0.2$ is essentially a pure QCD sample, with no residual presence of signal (or other electroweak backgrounds). The M_T (or E_T^{miss}) distribution of the QCD events so selected can serve to model the corresponding distribution in the isolated

region. However, E_T^{miss}/M_T and isolation are not fully independent variables in an hadronic sample: events in which the muon is within a jet are more likely to bias the measurement of E_T^{miss} related variables. This correlation appears in the two-dimensional distribution shown in Figure 6.16 for data and Monte Carlo, in terms of a rather linear dependence of E_T^{miss} with isolation.

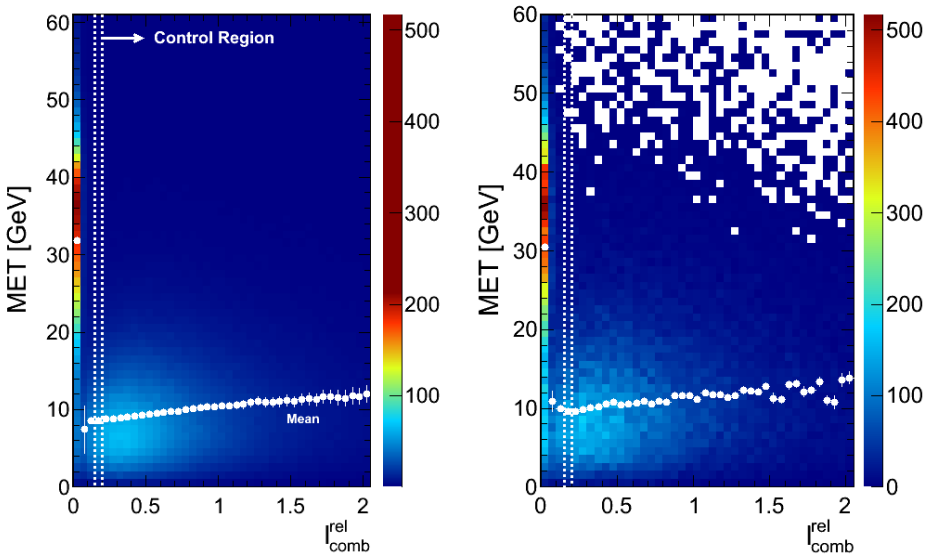

Figure 6.16: Isolation-E_T^{miss} distributions, for a fake-data sample constructed using Monte Carlo samples mixed in the right proportions (left) and data (right). Dashed lines separate the "signal region" (below 15% in isolation) and the "background control region" (above 20%). A visible shift of the E_T^{miss} distribution is observed as isolation increases. The mean of the E_T^{miss} distribution is superimposed to the two-dimensional plot to show this soft tendency upwards.

The physical reason for this correlation is the dependence of the isolation quantity (energy in the calorimeters and momentum of the tracks) on the total activity of the event (ΣE_T). Figure 6.17 shows this variation, both for a Monte Carlo simulation of QCD events (left) and for data (right).

The fact that this correlation can be characterized in terms of a "slope" indicates that we can parametrize the variation of the E_T^{miss} distribution in the non-isolated region. With the correction factor obtained we can extrapolate to the isolated region through an event-by-event correction of the control region.

The method is first studied with a QCD Monte Carlo sample. Figure 6.18 illustrates the different steps of the procedure. The average value of the $\overrightarrow{E_T}^{miss}$ distribution as a function

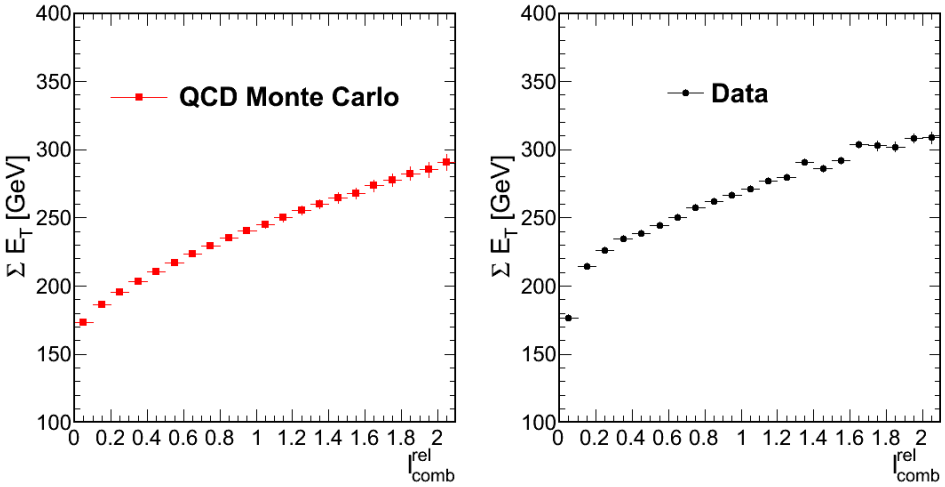

Figure 6.17: Variation of the ΣE_T of the event as a function of the isolation of the muon, for a QCD Monte Carlo simulation (left) and data (right). A visible increase of the mean ΣE_T distribution is observed as isolation increases.

of isolation is shown in the top left figure (red squares). The result of a Gaussian fit to the E_T^{miss} distributions for different intervals of the isolation variable are also shown (for each fit, the mean and width of the Gaussian function are shown as black and green dots respectively). In the three cases a rather linear behaviour is observed. The result of a linear fit to these sets of data is shown in the boxes of the figure. The average slope is $\alpha = 0.24 \pm 0.02$. This value is used to correct E_T^{miss}, and recompute the value of the M_T of the event.

The top right plot shows the effect of this correction on the mean and the width of the M_T distribution. It is seen how the behaviour is now rather flat, which implies that the original M_T-isolation correlation has been successfully removed.

The middle plots on the same Figure show the Monte Carlo truth prediction for the E_T^{miss} and M_T distributions in the isolated region (black histogram and inverted triangles), compared to the corresponding templates. The distributions obtained directly from the non-isolated region (pink open squares) are significantly different from the predicted shape in the isolated part, due to the correlation just discussed. Once this correlation is removed applying the correction described above, the "corrected" template obtained (blue dots) shows good agreement with the prediction from the isolated region.

The two bottom plots display more clearly this improvement in the modelling of the isolated region using the templates, by showing the ratio with respect to the original Monte Carlo truth prediction. While the anti-isolated shapes (pink open squares) deviate from the Monte Carlo

prediction, the corrected templates (blue dots) follow closely the isolated distribution over all the variable range, with only small discrepancies at high E_T^{miss} / M_T (where the amount of residual QCD background contamination is anyway very reduced).

Additional event information has to be considered in order to obtain a elaborated correction, such as the study of the variation of the M_T distribution with the angle between the reconstructed $\overrightarrow{E_T}^{miss}$ and the muon. The high acoplanarity ($acop > 2.0$) region is populated by events in which the muon is reconstructed in the direction of the missing energy. This behaviour is extremely unlikely for signal events (only possible in the case of very boosted W production).

The two-dimensional distribution (M_T, *acop*) is shown in Figure 6.19 (left) after the isolation requirement is applied, using the already mentioned Monte Carlo fake-data sample built mixing signal and backgrounds in the right proportions. The superimposed contours corresponds to the W signal (pink) and QCD background (white) distributions. As already discussed, it can be noticed how the W signal concentrates at high values of M_T and low values of acoplanarity, while QCD events populate mainly the low M_T, high *acop* region. A closer look at the QCD Monte Carlo sample shows how two different M_T shapes can be expected for low acoplanarity events (a smooth peak or dome, not entirely Gaussian in shape) and for high acoplanarity events (a decreasing slope). These M_T projections are shown in Figure 6.19 (right).

These different behaviours must be integrated when building the final template. A different correction is applied to events with high and with low acoplanarity. This effect was in fact already applied to the corrected M_T templates shown in Figure 6.18. The $\alpha = 0.24$ factor was applied to the full E_T^{miss} spectrum, but in order to compute the transverse mass distribution the M_T of events with $acop > 2.0$ was directly obtained from the anti-isolated region without any correction ($\alpha = 1.0$).

Some small differences between the corrected template and the Monte Carlo true shape can still be seen, and could be further corrected using a more complicated formula (quadratic corrections, extra α values for $acop > 2.0$, using two different templates to model high and low acoplanarity). Given the small statistics available on data, this higher order corrections will have no effect on the final cross-section value, and therefore have been not considered here.

The same behaviour is observed in data. The two-dimensional (M_T, *acop*) distribution observed in data is presented in the middle plot of Figure 6.19. Data follows the same trend described for the Monte Carlo sample: it is mainly clustered in the high M_T, low *acop* region (presumably corresponding to W events). Data with low M_T lies mainly in the high acoplanarity region, although a small contamination for lower acoplanarities can also be observed.

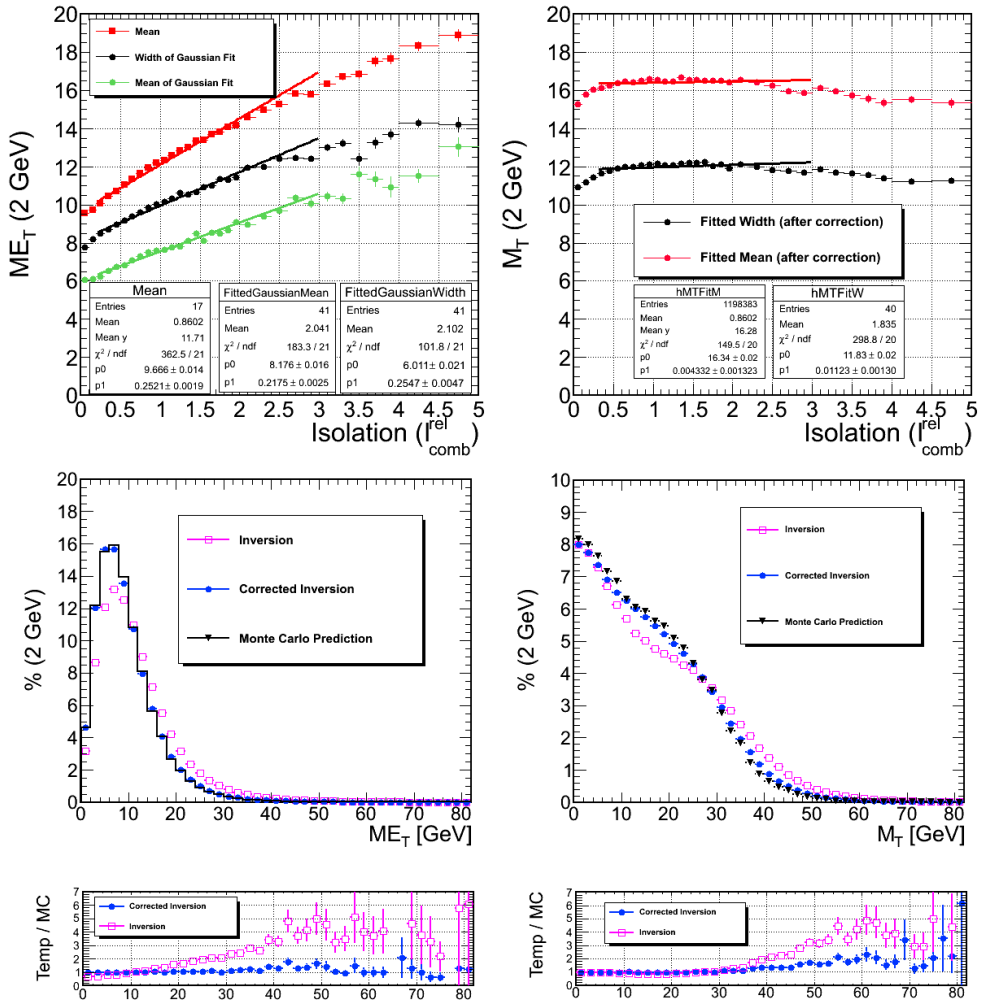

Figure 6.18: Proof of the method in Monte Carlo, using particle-flow E_T^{miss}. Top left shows the fitted slopes used to obtain the correction. Top right shows the mean and width of the M_T distribution after the correction to E_T^{miss} has been applied. Bottom compares Monte Carlo predictions with the templates, for E_T^{miss} (left) and M_T (right).

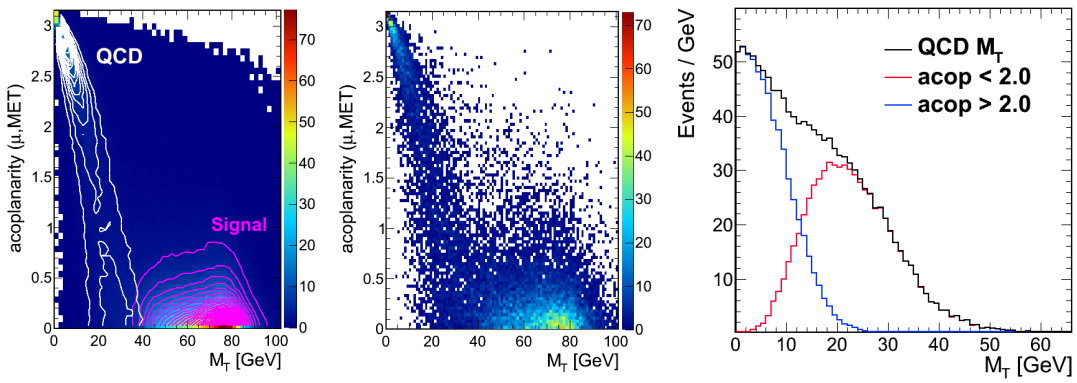

Figure 6.19: 2D *acop*-M_T distributions after isolation has been applied, for Monte Carlo simulation (left) and data (middle). Contours are shown superimposed to the two dimensional distribution (in the Monte Carlo plot, pink corresponds to signal and white to QCD background). Right: M_T distribution for isolated events in a high statistics QCD Monte Carlo sample, for low ($acop < 2.0$, red) and high ($acop > 2.0$, blue) acoplanarity regions. The high acoplanarity region distribution is concentrated at very low M_T and is different in shape from the low acoplanarity region.

The left plot in Figure 6.20 shows the mean (green) and width (black) from the already described Gaussian fits to the E_T^{miss} shape for different intervals of isolation, together with the mean (red) of the E_T^{miss} distribution in said interval. The first point in the three distributions (below the isolation threshold) is at a higher value than in the corresponding Monte Carlo (QCD-only) plots due to the dominant contribution of signal events in this region.

A rather linear behaviour is observed once again. No need of higher order corrections (for example, a quadratic fit) is appreciated. From the results of these three linear fits (shown in the boxes in the plots), an average slope of $\alpha = 0.19 \pm 0.02$ is obtained. This value is used to correct E_T^{miss}, and recompute the value of the M_T of the event. The top right plot shows the effect of this correction on the mean and the width of the M_T distribution. A flat behaviour of the M_T distribution as a function of isolation is recovered.

In Figure 6.21a the resulting templates for the E_T^{miss} (left) and M_T (right) spectra are shown, in linear and in logarithmic scale. The distributions obtained directly from the non-isolated region are represented with pink open squares, while the corrected templates are given by the blue dots. They are compared with the Monte Carlo prediction for the isolated region (black histogram and black inverted triangles). The corrected template lies in between the plain-inversion template and the pure Monte Carlo prediction for both variables.

The fact that there is a clear difference between the predicted distribution in Monte Carlo and the corrected template just obtained was expected. As already discussed, the differences

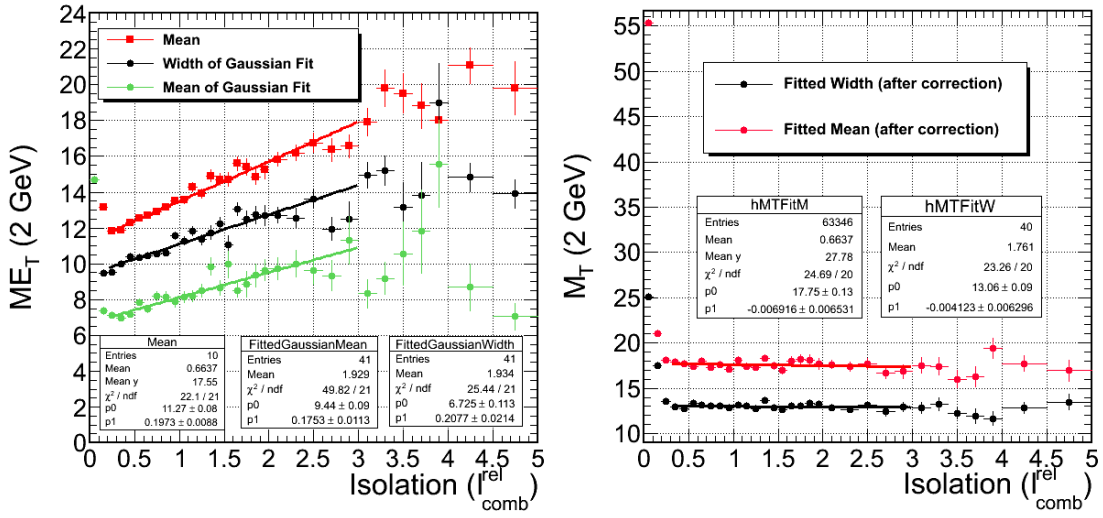

Figure 6.20: Left: Fitted slopes used to obtain the correction. Right: Mean and width of the M_T distribution after the correction to E_T^{miss} has been applied.

come both from the different E_T^{miss} resolution observed in data and in Monte Carlo, and from the imperfect simulation of hadronic processes in Monte Carlo.

These corrected templates (represented by blue dots in the Figure) will be used for the cross-section determination in the following chapter. The final correction used is therefore of the kind:

$$\alpha = 0.19 \pm 0.2$$

$$E_T^{miss}(cor) = E_T^{miss}/(1 + \alpha \times I_{comb}^{rel})$$

$$M_T(cor) = \begin{cases} \sqrt{2p_T E_T^{miss}(cor) \times (1 + \cos(acop))} & \text{if } acop < 2.0 \\ \sqrt{2p_T E_T^{miss} \times (1 + \cos(acop))} & \text{if } acop > 2.0 \end{cases}$$

For the sake of brevity, this study was presented using a particular E_T^{miss} reconstruction algorithm (particle flow), since it is the one which will be used for the final cross-section measurement. The behaviour here observed is also found for the other E_T^{miss} algorithms, and the corresponding results using track-corrected E_T^{miss} can be found in Appendix B.

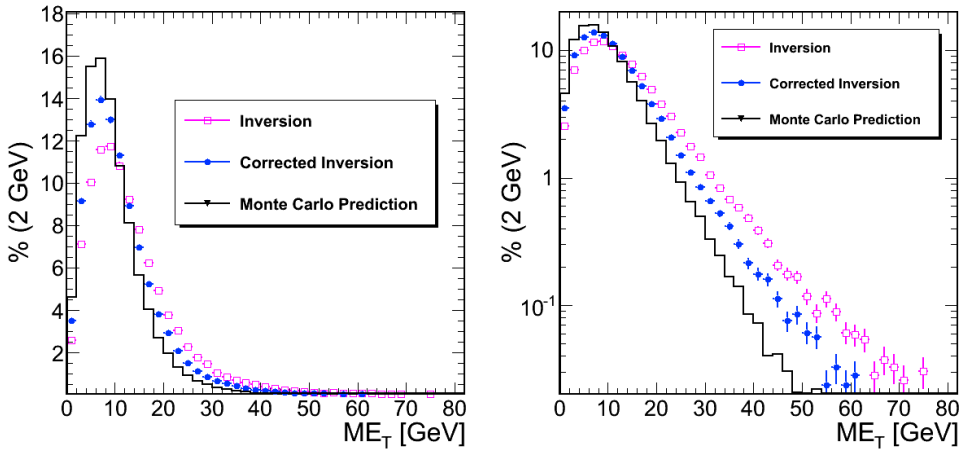

(a) Comparison of Monte Carlo predictions with the templates E_T^{miss} in linear (left) and logarithmic (right) scale.

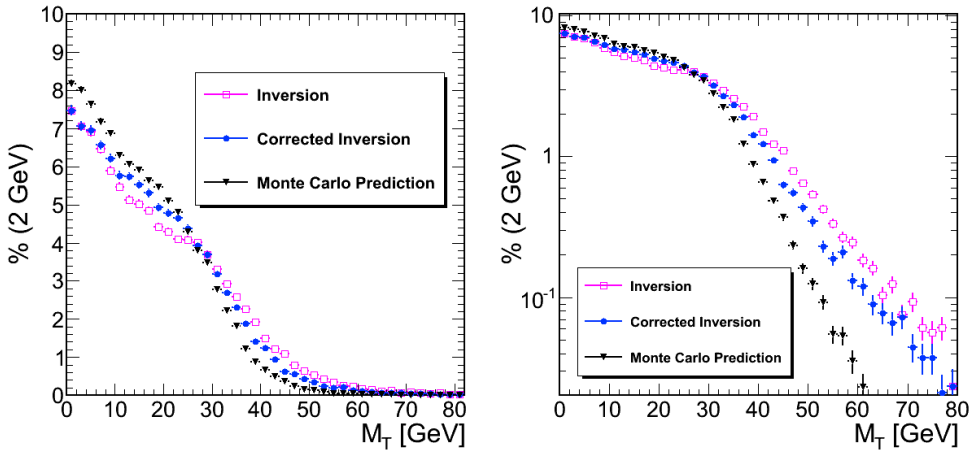

(b) Comparison of Monte Carlo predictions with the templates, for M_T in linear (left) and logarithmic (right) scale.

Chapter 7

Cross-Section measurement

This chapter presents the procedure performed to determine the W production cross-section $\sigma(W)$, in its muonic decay, as well as evaluating the independent positive and negative contributions $\sigma(W^+)$ and $\sigma(W^-)$ and their ratio $\sigma(W^+)/\sigma(W^-)$.

The signal extraction method developed is based on a fit of the experimental M_T distribution to the sum of the contributions from the different physics channels involved. The M_T shape for each of them is fixed to the templates presented in the previous chapter. Cross-section is extracted directly, turning the signal yield into a derived quantity.

The details of the fitting method and its validity (tested in Monte Carlo) are presented in the first part of the Chapter, and followed by the results obtained with the Run 2010 A dataset.

Finally, the estimation of the systematic uncertainties involved in the cross-section measurement is explained.

7.1 Template Fit method

The W $\rightarrow \mu\nu$ yield is extracted from a binned log likelihood minimization to the observed M_T distribution, which is taken to be the sum of different "templates" for each one of the physical processes in play: W signal, QCD backgrounds and the different EWK backgrounds.

$$N(DATA) = N(W) + N(QCD) + \sum_i N(EWK_i)$$

Signal yield (N_W) and the three main electroweak background contributions (Z $\rightarrow \mu^+\mu^-$, W $\rightarrow \tau\nu$, Z $\rightarrow \tau^+\tau^-$) are expressed in terms of their production cross-section and their Accep-

tance × Efficiency factors (A_W, A_{EWK}), using their associated M_T templates($\mathcal{F}(M_T)$, $\mathcal{G}_i(M_T)$, as described in Chapter 6).

The value of the ratio of production cross-sections ($k_{EWK_i} = \sigma_{EWK_i}/\sigma_W$, where i=Z $\rightarrow$ $\mu^+\mu^-$, W $\rightarrow \tau\nu$, Z $\rightarrow \tau^+\tau^-$) is not affected by theoretical uncertainties, since PDF effects and other theoretical effects largely cancel in the ratio. Therefore cross-sections for the electroweak processes can be normalizedd to the W $\rightarrow \mu\nu$ one, on the basis of theoretical expectations:

$$\begin{aligned} N(W)(M_T) &= A_W \mathcal{F}(M_T)\sigma_W \int \mathcal{L}dt \\ N(EWK_i)(M_T) &= A_{EWK_i}\mathcal{G}_i(M_T)\sigma_{EWK_i} \int \mathcal{L}dt \\ &= A_{EWK_i}\mathcal{G}_i(M_T)\sigma_W k_{EWK_i} \int \mathcal{L}dt \\ &(i = \mathrm{Z} \rightarrow \mu^+\mu^-, \mathrm{Z} \rightarrow \tau^+\tau^-, \mathrm{W} \rightarrow \tau\nu) \end{aligned}$$

The two remaining sources of electroweak backgrounds ($t\bar{t}$ and diboson production WW, WZ, ZZ) are very small compared to signal. The predicted cross-section for W bosons is ≈ 10 nb at NLO, to be compared with ≈ 0.165 nb for $t\bar{t}$ and ≈ 0.006 nb for WW also at NLO (see Table 6.1). In addition to this, the $t\bar{t}$ production cross-section does not necessarily scale with the $\sigma(W)$. Therefore these two background components ($N(Other)$, $Other = t\bar{t}$, WW, WZ, ZZ) will be estimated directly from Monte Carlo predictions.

The shape from the QCD contribution ($\mathcal{H}(M_T)$ is modelled from the anti-isolated sample as described in Chapter 6, and its normalization f_{QCD} is left as a free parameter in the fit.

$$N(QCD) = f_{QCD}\mathcal{H}(M_T) \int \mathcal{L}dt$$

In fact, as the W^+ and W^- bosons production cross-section is different, the previous expressions have to be written independently for candidates with positive and negative muons.

$$\begin{aligned} N_{Data^+} &= N(W^+) + N(QCD^+) + \sum_i N(EWK(i)^+) + N(Other^+) \\ N_{Data^-} &= N(W^-) + N(QCD^-) + \sum_i N(EWK(i)^-) + N(Other^-) \end{aligned}$$

QCD background is assumed to be symmetric with respect to charge, that is, the number of QCD events with a positive muon ($N(QCD^+)$) is taken to be equal to the QCD contribution with a negative muon ($N(QCD^-)$).

The fit will therefore have three free parameters: the QCD background normalization factor f_{QCD}, the total W cross-section $\sigma(W)$ and the ratio of positive and negative boson production

$R = \sigma(W^+)/\sigma(W^-)$. Alternatively these two latter parameters can be expressed as the $\sigma(W^+)$ and $\sigma(W^-)$ cross-sections.

The log-likelihood function to be minimised (using MINUIT [79]) is built taking into account Poisson statistics:

$$-\frac{1}{2}\log L = \sum_{M_T\ bins} \left(N_{DATA^+} \log\left(N_{fit^+}\left(f_{QCD}, \sigma_W, R\right)\right) - \left(N_{fit^+}\left(f_{QCD}, \sigma_W, R\right)\right)\right) + \sum_{M_T\ bins} \left(N_{DATA^-} \log\left(N_{fit^-}\left(f_{QCD}, \sigma_W, R\right)\right) - \left(N_{fit^-}\left(f_{QCD}, \sigma_W, R\right)\right)\right)$$

The output of the fit is the numerical value of the W cross-section and the QCD background yield, but also the graphical interpretation of data in terms of signal and background components, giving a direct and simple indication of the goodness of the fit.

It may be noted that this fit structure is independent of the variable chosen for the fit. It can technically be performed on E_T^{miss} instead of on M_T, but since the signal-background separation is more powerful using M_T this option it was preferred.

7.1.1 Validity of the method

The stability of the fits was checked on Monte Carlo, using 1000 random "fake-data" samples or "pseudo-experiments" each with an integrated luminosity of 3 pb^{-1}.

These fake data-samples are constructed sampling randomly a data-like mix of signal and background events, computed using high statistics Monte Carlo samples. Signal and electroweak backgrounds contributions are obtained from the theoretical predictions of their cross-section and the desired integrated luminosity. Since we only have a LO prediction for the QCD cross-section, and in data we observe a hadronic contribution almost a 30% larger than this, the contribution of QCD is enhanced to match more closely the observations.

Each of these 1000 samples was fitted with the method presented in the previous section.

A first test of the method was done using templates derived directly from Monte Carlo. An example of one of these fits is shown in Figure 7.1 (left). The agreement between the fake-data and the fitted function is, as expected, very good over the full range of M_T. This figure shows each one of the fitted templates for the different components (signal and background processes). Introducing templates to model both signal and background and repeating the fit we obtain Figure 7.1 (centre). In this case once again the fit agrees very well with the fake-data, but the W cross-section obtained is slightly lower (-0.7%). Both fits are compared to the fake-data and

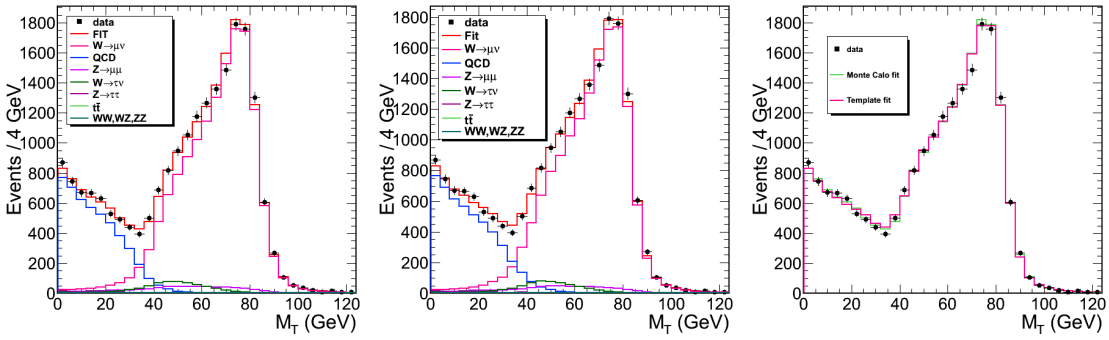

Figure 7.1: Example of a fit to a pseudo-experiment with an equivalent statistic of 3 pb^{-1}. The left panel shows the result of the fit using Monte Carlo to model signal and background. The central panel shows the result of the fit using templates to describe W and QCD. In both cases points represent the fake data, and lines the different components of the fit. Finally, the right panel shows the comparison of both fits to the data.

shown in the same Figure, in the right panel. Although both results are almost identical, the fit with the templates is slightly lower overall.

The same procedure is repeated over the remaining 999 sets of $\mathcal{L}_{int} = 3$ pb^{-1} luminosity, and the results are summarized in Figure 7.2. The results of these fits using the original Monte Carlo distributions as shapes are shown in blue; and the results of the fits using the templates described in Chapter 6 for signal and for QCD background in red. The use of templates instead of Monte Carlo shapes deviates the output parameters obtained slightly towards lower cross-sections and higher ratios.

These differences between the fits are systematic effects, to be taken into account (and re-computed) in data. Table 7.1 summarises the results, comparing fits with signal modelled directly from Monte Carlo as well as from a data-like template, and with QCD modelled with Monte Carlo and with the hadronic template described in Chapter 6 (both for different normalizations for positive and negative muons and for a single normalisation).

The input cross-section and ratio are recovered within 0.7% and 0.8% respectively, due to the modelling of QCD background. This bias is not a systematic effect to be directly ported to the measurement on data. E_T^{miss} behaviour in data and in Monte Carlo is different, and therefore the corrections applied to the QCD template change. As seen in Chapter 6, in Monte Carlo this very simple correction had room left for improvement (using a more complicated parametrization) - while in data further corrections had no effect.

The 0.8% bias on the determination of the ratio $\sigma(W^+)/\sigma(W^-)$ is not only due to the

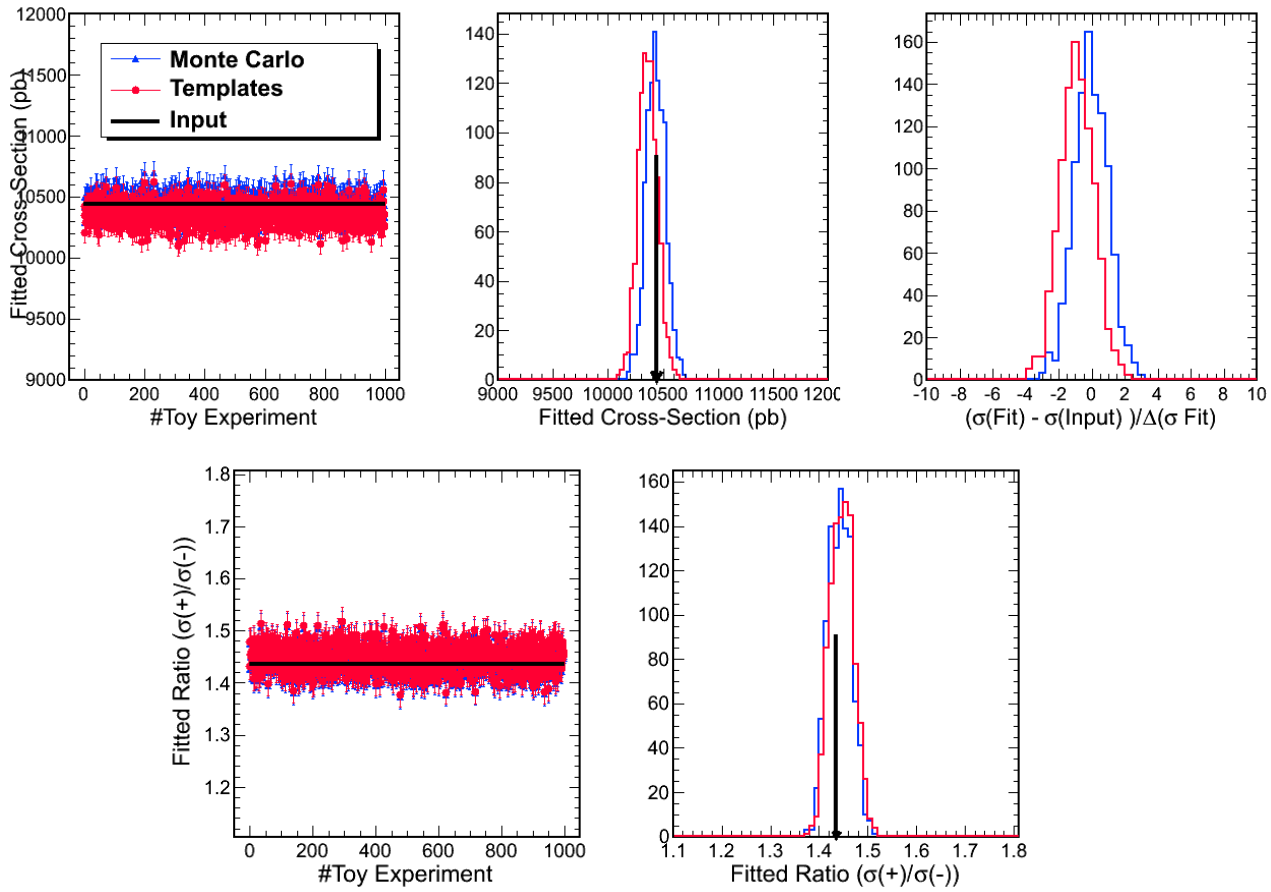

Figure 7.2: Results from the fit, in 1000 pseudo-experiments. Blue: fitting with the original Monte Carlo shapes, and using two different normalizations for negative and positive QCD contributions. Red: fitting with templates for signal and background, with a single normalization of QCD background.

Table 7.1: Summary of the means values of the fits performed over the 1000 fake-data samples, using Monte Carlo distributions to model the shapes (MC), modelling the signal from a template but background from Monte Carlo (W Temp) and using templates both for signal and QCD background. The fits have been performed both under the assumption that QCD background is symmetric with respect to charge (1xQCD) and using independent normalizations for positive and negative muons (2xQCD).

W	QCD	σ_W (pb)	Pulls σ_W	Ratio	Yield (W^+)	Yield (W^-)
W MC	MC	10436 ± 3	-0.03 ± 0.03	1.4363 ± 0.0007	8795 ± 3	5672 ± 2
	2xQCD	RMS=88	RMS$=1.02 \pm 0.02$	RMS=0.0236	RMS=92	RMS=75
	MC	10435 ± 3	-0.04 ± 0.03	1.4429 ± 0.0007	8810 ± 3	5656 ± 2
	1xQCD	RMS=87	RMS$=1.02 \pm 0.02$	RMS=0.0236	RMS=92	RMS=75
	Temp	10361 ± 3	-0.91 ± 0.03	1.4400 ± 0.0008	8741 ± 3	5622 ± 2
	2xQCD	RMS=88	RMS$=1.02 \pm 0.02$	RMS=0.0239	RMS=92	RMS=75
	Temp	10360 ± 3	-0.91 ± 0.03	1.4460 ± 0.0008	8755 ± 3	5607 ± 2
	1xQCD	RMS=88	RMS$=1.03 \pm 0.02$	RMS=0.0238	RMS=92	RMS=74
W Template	MC	10440 ± 3	0.01 ± 0.03	1.4364 ± 0.0008	8798 ± 3	5674 ± 2
	2xQCD	RMS=92	RMS$=1.01 \pm 0.02$	RMS=0.0253	RMS=96	RMS=77
	MC	10438 ± 3	0.01 ± 0.03	1.4423 ± 0.0008	8815 ± 3	5656 ± 2
	1xQCD	RMS=87	RMS$=1.01 \pm 0.02$	RMS=0.0256	RMS=92	RMS=74
	Temp	10363 ± 3	-0.88 ± 0.03	1.4413 ± 0.0008	8746 ± 3	5621 ± 2
	2xQCD	RMS=88	RMS$=1.02 \pm 0.02$	RMS=0.0239	RMS=92	RMS=75
	Temp	10362 ± 3	-0.89 ± 0.03	1.4474 ± 0.0008	8760 ± 3	5607 ± 2
	1xQCD	RMS=88	RMS$=1.02 \pm 0.02$	RMS=0.0238	RMS=92	RMS=74
Input		10438	-	1.4354	8795	5675

modelling of the M_T distribution, but also to the assumption that QCD background contains the same proportion of positive and negative muons. If the fit is performed with independent normalizations for the QCD positive and negative contributions, this bias is reduced to 0.4%. This implies that QCD in Monte Carlo is not completely symmetric with respect to charge. However, since the modelling of QCD in Monte Carlo is not reliable enough, this asymmetry does not necessarily have to be the same in data. This effect will have to be verified later, directly on the experimental data-sample.

On the other hand, the variation due to the modelling of signal is negligible ($< 0.1\%$), as expected. In data the difference between the signal template and Monte Carlo truth will therefore provide insight on the uncertainty associated to the E_T^{miss} scale.

Table 7.2: Summary of numbers needed for the extraction of the cross section values.

	$W \to \mu\nu$	$W^+ \to \mu^+\nu$	$W^- \to \mu^-\bar{\nu}$
A_W	46.20 ± 0.07	47.65 ± 0.07	44.13 ± 0.06
ρ_{eff}	$(92.83 \pm 1.4)\%$		
$\mathcal{L}$	2.88pb^{-1}		

In summary, we conclude that in ideal conditions the method works perfectly well ($< 0.1\%$). In more realistic conditions where both signal and background are modelled from template, the fit method still works very well, recovering the signal cross-section within 0.7% of its input value, and the ratio of cross-sections within 0.8%, due to well understood sources of bias.

7.1.2 Cross-Section Results

The described method is applied to the data recorded by CMS, using the signal and hadronic background templates described in Chapter 6. The Acceptance × Efficiency factors which enter in the calculation were already addressed in Section 6.2, and the global correction factor was presented in Section 6.3. They are summarized in Table 7.2.

The result of performing the fit over the experimental distribution is shown in Figure 7.3. The template shapes used for each one of the physical processes involved are shown, together with the final fit result. Data agrees well with the fitted shape over the full range of M_T, with small discrepancies in the tails, due to the lack of statistics available.

The values of the fitted cross-section, ratios and QCD normalization are:

$$\begin{aligned}
\sigma(\text{pp} \to \text{W}^\pm + X) \times BR(\text{W}^\pm \to \mu^\pm\nu) &= 9.93 \pm 0.09(\text{stat}) \text{ nb}, \\
\sigma(\text{pp} \to \text{W}^+ + X) \times BR(\text{W}^+ \to \mu^+\nu) &= 5.84 \pm 0.07(\text{stat}) \text{ nb}, \\
\sigma(\text{pp} \to \text{W}^- + X) \times BR(\text{W}^- \to \mu^-\bar{\nu}) &= 4.09 \pm 0.06(\text{stat}) \text{ nb}, \\
\frac{\sigma(\text{pp} \to \text{W}^+ + X) \times BR(\text{W}^+ \to \mu^+\nu)}{\sigma(\text{pp} \to \text{W}^- + X) \times BR(\text{W}^- \to \mu^-\bar{\nu})} &= 1.43 \pm 0.03(\text{stat}) \\
f_{QCD} &= 868 \pm 13(\text{stat})
\end{aligned}$$

The yields for the different processes involved in the full M_T range are shown in Table 7.3. The log-likelihood functions obtained in the final fit (total cross-section, W^+ and W^- cross-

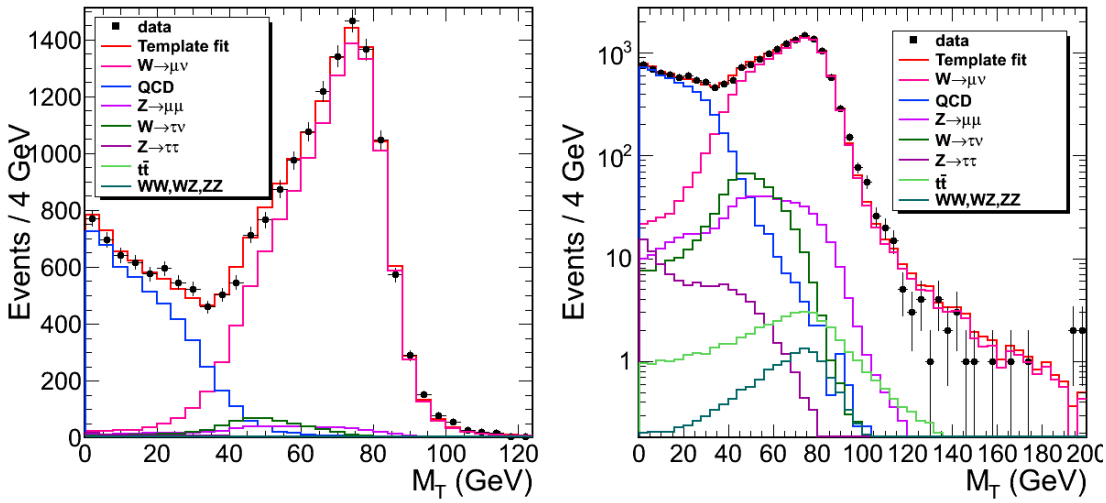

Figure 7.3: Fit to the full M_T distribution, showing individual contributions, in linear (left) and logarithmic (right) scale.

sections, and their charge ratio) are shown in figure 7.4. A line shows the statistical uncertainty (-0.5 over the minimum value).

7.2 Summary of systematical uncertainties

The uncertainty assigned to the measurement in the previous section, given by Minuit, is of statistical nature only. Different systematic effects, associated to the different methods used along the analysis, the measurement.

Theoretical uncertainties (PDFs, ISR, FSR...) affect our measurement only through the kinematic acceptance of the process (A_{kin}). The effect of each one of them has been studied using dedicated programs.

Experimental systematic uncertainties will cover the errors in the determination of the selection efficiency; the current knowledge of the muon momentum and missing energy scale and resolution; and the errors associated to our background modelling and subtractions techniques. Their study will be summarized in the next section.

The final uncertainty to be considered (and also the largest) is the measurement of the integrated luminosity of the data provided by the accelerator. It is independent of the particular measurement performed.

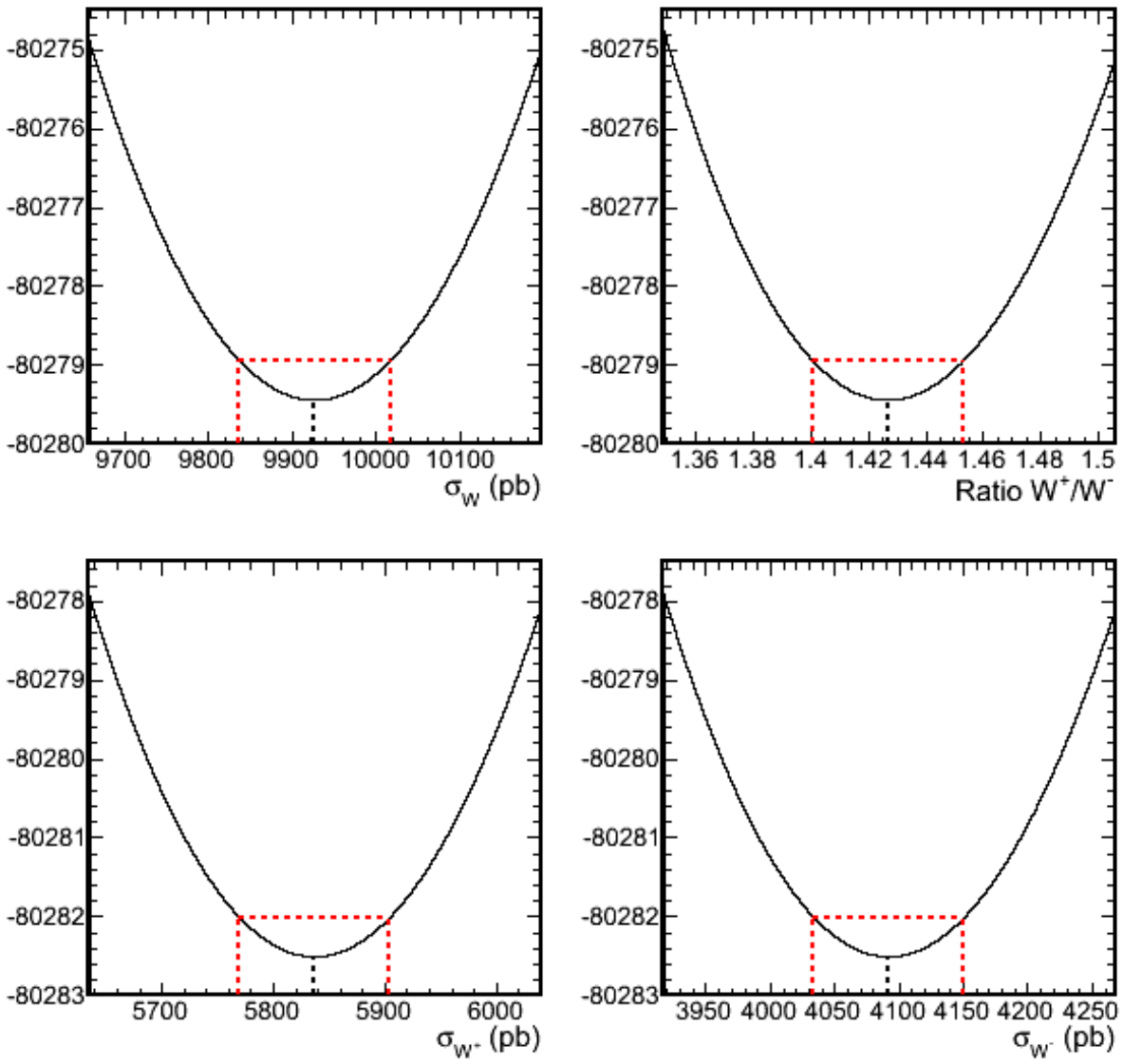

Figure 7.4: Log-Likelihood functions for the final template fit, for the four measurements involved, σ_W and the ratio of $R = \sigma_W^+/\sigma_W^-$ in one fit, and σ_W^+ and σ_W^- in an identical fit with a change of variables for proper correlation handling.

Table 7.3: Total, negative and positive yields obtained from the fit for each one of the physical processes considered.

	$W \to \mu\nu$	$W^+ \to \mu^+\nu$	$W^- \to \mu^-\bar{\nu}$
Observed Candidates	18571	10682	7889
Fitted Result	18575 ± 142	10663 ± 98	7912 ± 83
$W \to \mu\nu$ yield	12269 ± 111	7439 ± 86	4830 ± 69
QCD yield	5002 ± 80	2501 ± 40	2501 ± 40
$Z \to \mu^+\mu^-$ yield	571 ± 24	297 ± 17	275 ± 17
$W \to \tau\nu$ yield	569 ± 24	342 ± 18	227 ± 15
$Z \to \tau^+\tau^-$ yield	99 ± 10	52 ± 7	48 ± 7
$t\bar{t}$ yield	49 ± 7	24 ± 5	24 ± 5
WW, WZ, ZZ	15 ± 4	8 ± 2	7 ± 2

7.2.1 Muon Efficiencies

One of the main sources of experimental systematic uncertainties comes from the uncertainties on the correction factors for lepton reconstruction, identification, isolation and trigger requirements, obtained by the Tag-and-Probe method as discussed in Chapter 6.

The statistical uncertainty on the correction factors (ρ_{eff}) amounts to 1.2%. This uncertainty will be propagated as the systematic uncertainty on muon efficiency. See Table 6.7. An additional uncertainty of 0.5% due to pre-triggering effects is added in quadrature.

Finally, since efficiencies are determined on a $Z \to \mu^+\mu^-$ sample, another additional 0.5% uncertainty accounts for the different kinematic distributions predicted for W and Z events, estimated from high statistic Monte Carlo samples.

Therefore, the final muon efficiency uncertainty to be propagated to the W cross-section is of 1.5% (relative to the global efficiency correction ρ_{eff}).

Dedicated tag-and-probe studies have been repeated using only positive or negative muons as probes. There is no observed efficiency bias with respect to charge within statistical uncertainties. However, the statistical error on this difference in correction factors (2.8% relative to the mean efficiency correction ρ_{eff} applied) is propagated as a systematic uncertainty in the measurement of the W^+/W^- cross section ratio. See Table 6.8.

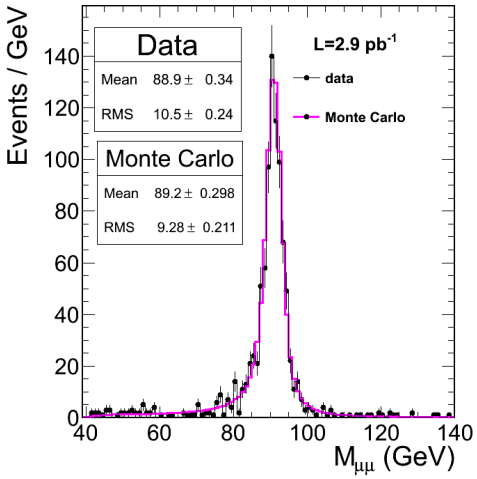

Figure 7.5: Comparison of the DiMuon peak in data and in Monte Carlo simulation (normalizedd to the observed yield in data).

7.2.2 Muon Momentum Scale and Resolution

Muon momentum reconstruction affects the measurement as it enters directly or indirectly at different steps of the analysis: directly, in the signal selection criteria (through the $p_T > 20$ GeV requirement, potentially modifying the A_W factor), but also in the modelling of signal using E_T^{miss} (muon momentum corrections) and M_T. Therefore any uncertainty on the measurement of the momentum of muons will be propagated to the final cross-section determination.

One of the most sensitive observables to possible mismeasurements of the muon momentum is the position and width of the dimuon mass resonances. Studying possible displacements and/or broadening of the peaks of J/Ψ, Υ and Z decaying into muons, a measurement of the muon momentum scale and resolution can be obtained.

Figure 7.5 shows the position of the Z dimuon peak compared to the predicted shape in Monte Carlo events, normalizedd to the observed yield in data. There is no visible displacement of the peak.

The comparison of data and Monte Carlo allows to place an upper limit on these effects. A dedicated study indicates that scale shifts above 0.40% for muons with $p_T \approx 40$ GeV can be excluded at the level of one standard deviation [67; 80].

An effect of this size would induce a small uncertainty on the W cross-section measurement. This systematic effect has been calculated by re-processing all the signal and background Monte Carlo samples used in the analysis [81]. The reconstructed muon is modified with a scale factor of

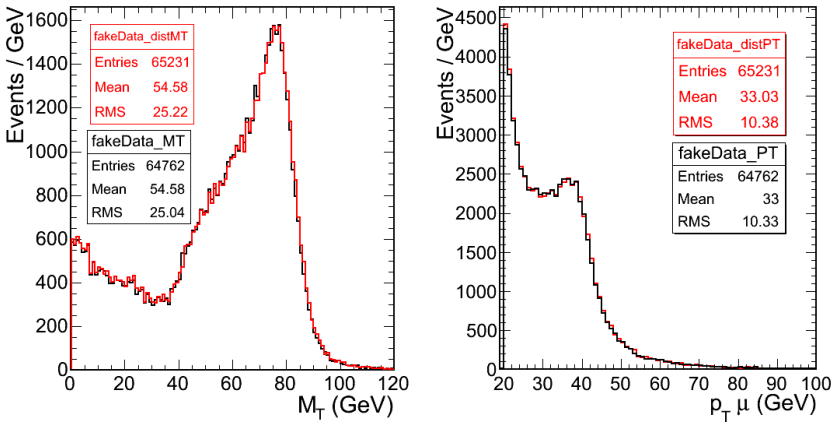

Figure 7.6: Impact of the muon momentum scale effect on the reconstructed M_T and p_T shape for a fake-data sample (including all possible background contributions), distorted (red) and without distortion (black).

the kind $p'_T = \alpha p_T$, where $\alpha = 1.004$. The E_T^{miss} variable is recomputed to take into account this modification of the muon contribution (as described in Chapter 5), and the effect is propagated to the M_T distribution. The impact of this distortion is shown in Figure 7.6 for a fake-data sample generated using a Monte Carlo simulation which incorporates this observed deviation, compared to the original sample. The effect is very small, and may best be noticed in the different number of entries in the plot (0.7% difference in the total number of events) since the shapes are barely modified.

The fit is repeated in the two fake-data distributions, and a 0.3% shift between both measurements is found. This shift is propagated as the upper limit on the systematic error on the cross-section due to momentum scale uncertainty.

7.2.3 E_T^{miss} scale and resolution

As we saw in Chapters 5-6, the Monte Carlo description of E_T^{miss} resolution does not completely reproduce the data. This will have an impact on the determination of the cross-section due to the modelling of the signal shape.

This uncertainty has been evaluated comparing the results obtained using with the signal template developed in Chapter 6, or the original Monte Carlo shape. This way it is possible to obtain an upper limit on the impact of the signal shape (E_T^{miss} scale and resolution) on the result. The effect is 0.4% on the three measured cross-sections, as shown in Table 7.4 (where different versions of the fit are reported).

7.2.4 Background subtraction

The estimation of the electroweak background contribution is assigned a 0.2% uncertainty which covers both the theoretical error on the acceptances (which affects the normalization used in the fits) and the effect of the imperfect modelling of the E_T^{miss}. The theoretical error on the k factors used ($k = \sigma_{EWK}/\sigma_W$) is negligible.

The errors due to QCD backgrounds are obtained by comparing the fits done using the templates obtained from the non-isolated sample and the Monte Carlo prediction. The actual shape of the QCD background is impossible to determine from data. Three different fits to the experimental M_T spectrum are performed:

a) Using the shapes predicted by Monte Carlo the quality of the fit is visually bad. The worsening of E_T^{miss} resolution in data affects clearly both background and signal, deviating from the observed shape. In particular, QCD background is underestimated, which results in an upper-limit for the cross-section measurement.

b) Using a QCD template directly obtained from the non-isolated sample overestimates the amount of QCD background contamination, therefore underestimating the signal.

c) The corrected QCD template provides an intermediate value between both limits. The systematic uncertainty associated to this modelling is obtained from the full difference between Monte Carlo and corrected template.

The comparative results of these fits are shown on Figure 7.7. The techniques developed for template modelling yield improve the agreement with data significantly, as seen in the fit residuals (difference data-fit) and ratio (fit / data) plots.

Further checks are performed to ensure the stability of the fit. The constraint that QCD background is symmetric with respect to charge (which had an impact on the Monte Carlo tests performed to validate the method) is released, fitting independent normalizations for the positive and negative QCD contributions. While this constraint was significant on the measurement of the cross-section ratio using Monte Carlo pseudo-experiments, it is not the case in data and for the available statistics. These results are summarized in Table 7.4, and provide an upper limit of the systematic error on QCD modelling that can be taken as uncertainty on the cross-section: 2% for the total spectrum, 1.7% for positive Ws and 2.3% for negative Ws (this includes a check on the charge symmetry of this background contribution). The effect on the charge ratio is measured to be of 0.7%.

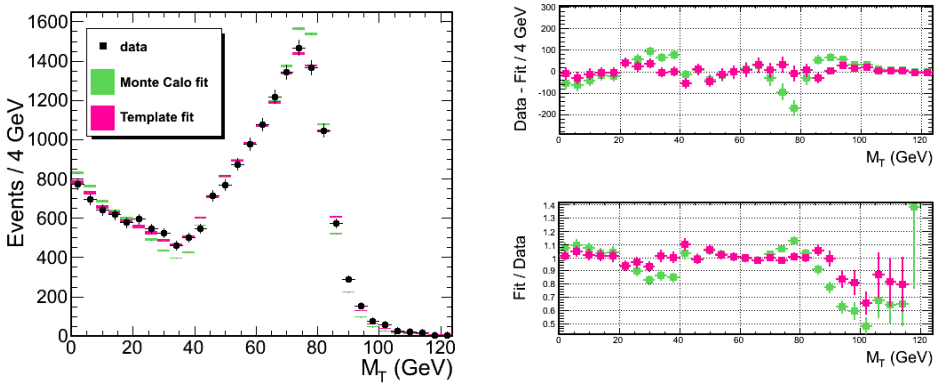

Figure 7.7: Left: Comparison of the data M_T spectra with two versions of the fit: modelling background and signal from Monte-Carlo (green), and modelling QCD background and signal from corrected templates (pink). Right: Difference between M_T results and data (top) and their ratio (bottom), as a function of M_T.

Table 7.4: Systematic study on background and signal shape, comparing the results obtained with different template shapes for signal (with and without E_T^{miss} modelling) and QCD background (Monte Carlo predicted shape, M_T distribution for the anti-isolated sample, and corrected M_T distribution). The results are shown floating one and two parameters for QCD background normalization in order to measure the impact of any charge asymmetries in this background.

pfMet	QCD	MonteCarlo	Inverted Isolation	Corrected Template
Symm.	MC Signal	$\sigma_W = 10.08 \pm 0.09$ nb $\sigma_{W^+} = 5.91 \pm 0.07$ nb $\sigma_{W^-} = 4.17 \pm 0.06$ nb $R = 1.42 \pm 0.03$	$\sigma_W = 9.75 \pm 0.09$ nb $\sigma_{W^+} = 5.74 \pm 0.07$ nb $\sigma_{W^-} = 4.11 \pm 0.06$ nb $R = 1.43 \pm 0.03$	$\sigma_W = 9.88 \pm 0.09$ nb $\sigma_{W^+} = 5.81 \pm 0.07$ nb $\sigma_{W^-} = 4.07 \pm 0.06$ nb $R = 1.43 \pm 0.03$
QCD	Template Signal	$\sigma_W = 10.12 \pm 0.09$ nb $\sigma_{W^+} = 5.94 \pm 0.07$ nb $\sigma_{W^-} = 4.18 \pm 0.06$ nb $R = 1.42 \pm 0.03$	$\sigma_W = 9.79 \pm 0.09$ nb $\sigma_{W^+} = 5.77 \pm 0.07$ nb $\sigma_{W^-} = 4.03 \pm 0.06$ nb $R = 1.43 \pm 0.03$	$\sigma_W = 9.93 \pm 0.09$ nb $\sigma_{W^+} = 5.84 \pm 0.07$ nb $\sigma_{W^-} = 4.09 \pm 0.06$ nb $R = 1.43 \pm 0.03$
Assym.	MC Signal	$\sigma_W = 10.08 \pm 0.09$ nb $\sigma_{W^+} = 5.91 \pm 0.07$ nb $\sigma_{W^-} = 4.17 \pm 0.06$ nb $R = 1.41 \pm 0.03$	$\sigma_W = 9.75 \pm 0.09$ nb $\sigma_{W^+} = 5.73 \pm 0.07$ nb $\sigma_{W^-} = 4.02 \pm 0.06$ nb $R = 1.43 \pm 0.03$	$\sigma_W = 9.88 \pm 0.09$ nb $\sigma_{W^+} = 5.80 \pm 0.07$ nb $\sigma_{W^-} = 4.08 \pm 0.06$ nb $R = 1.42 \pm 0.03$
QCD	Template Signal	$\sigma_W = 10.12 \pm 0.09$ nb $\sigma_{W^+} = 5.93 \pm 0.07$ nb $\sigma_{W^-} = 4.19 \pm 0.06$ nb $R = 1.42 \pm 0.03$	$\sigma_W = 9.79 \pm 0.09$ nb $\sigma_{W^+} = 5.76 \pm 0.07$ nb $\sigma_{W^-} = 4.03 \pm 0.06$ nb $R = 1.43 \pm 0.03$	$\sigma_W = 9.93 \pm 0.09$ nb $\sigma_{W^+} = 5.83 \pm 0.07$ nb $\sigma_{W^-} = 4.09 \pm 0.06$ nb $R = 1.43 \pm 0.03$

Finally, the results were checked using track-corrected E_T^{miss} instead of particle flow E_T^{miss}. The results using this alternative E_T^{miss} description are summarized in Appendix B, and are compatible with the ones presented here.

7.2.5 Theoretical errors

The kinematic acceptance of the process, A_{kin} can only be computed in Monte Carlo. The current theoretical knowledge of the production of W bosons affects this factor, and a theoretical uncertainty has to be taken into account to cover Parton Density Function uncertainties, Initial and Final State radiation effects and higher order electroweak and QCD effects.

The effect of these uncertainties has been calculated for the specific set of selection criteria applied in the analysis:

- **Parton Distribution Functions (PDFs)** - The POWHEG Monte Carlo sample used as baseline for this analysis uses CTEQ6.6. In order to compute the uncertainty on the acceptance due to the parton density function used, instead of generating, simulating and reconstructing different samples (a heavy computing task), a reweighting procedure was applied to the events already generated with our baseline Monte Carlo. For each event, the PDF information was recomputed using the values of Q and x for each one of the interacting partons. The final weight was computed comparing these new values with the original information, by $w = (PDF_1' \times PDF_2')/(PDF_1 \times PDF_2)$. Three different NLO pdfsets have been used: MSTW08 [9], CTEQ66 [40] and NNPDF2.0 [41], as recommended by the PDF4LHC [39] group. Following the recommended recipes for each set of calculations, the 68% CL positive and negative uncertainties obtained with each pdfset were considered to compute each uncertainty. The final systematic error assigned corresponds to half of the maximum difference observed between positive and negative variations for any combination of the three sets.

- **Higher Order QCD Corrections and Initial State Radiation (ISR)** - ISR is studied comparing the baseline Monte Carlo with ResBos [82] at NNLO. The effect of the QCD factorization scale dependence on NNLO calculations is studied with FEWZ [37] program.

- **Electroweak Corrections and Final State Radiation** - These effects are studied comparing the HORACE [83; 84; 85; 86] generator with PYTHIA, since FSR is modelled in the baseline Monte Carlo through its interface with PYTHIA.

These theory errors are summarized in Table 7.5, and explained in detail in Ref. [87].

Table 7.5: Theoretical systematic uncertainties on the acceptance

	W^+	W^-	W^+/W^-
PDFS	1.3%	1.9%	2.1%
ISR	$-1.39 \pm 0.09\%$	$-1.17 \pm 0.14\%$	$0.22 \pm 0.17\%$
α_S	$0.23 \pm 0.22\%$	$0.37\% \pm 0.32$	$1.13 \pm 0.63\%$
FSR	$0.11 \pm 0.12\%$	$0.01 \pm 0.17\%$	$-0.08 \pm 0.19\%$
EWK	$-0.02 \pm 0.12\%$	$0.26 \pm 0.17\%$	$0.28 \pm 0.19\%$
Total	1.42%	1.26%	1.19%

7.2.6 Luminosity

The largest uncertainty source in this measurement comes from the estimation of the luminosity of the dataset. The luminosity is obtained from a measurement of the event rate observed compared to the visible cross-section ($L(t) = N(t)/\sigma_{vis}$). The absolute normalization factor has to be determined experimentally [88; 89].

The CMS detector uses signals from the forward hadronic (HF) calorimeters to determine the event rate, and therefore the instantaneous luminosity, in real time. This information is stored for offline use.

The HF covers the pseudorapidity range $3 < |\eta| < 5$. The real-time relative instantaneous luminosity is extracted based on two techniques. The first one computes the mean number of interactions per bunch crossing based on the average of the fraction of empty towers ("zero counting"), and the second one is based on the linear relationship between the average transverse energy per tower and the luminosity. This second measurement is better performed by limiting the coverage to a pseudorapidity range of $3.5 < |\eta| < 4.2$ to avoid non-linear effects.

This luminosity estimates are afterwards cross-checked with an offline analysis of the data. Two different methods are applied to the offline data: one based in the HF (coincidence of energy depositions of at least 1 GeV in the forward and backward subdetectors), and one based in tracking and vertex finding (at least one vertex with at least 2 tracks in the event). These two methods have the drawback of a longer latency in the processing of the data, but on the other hand allow for better background rejection than the online methods.

The absolute normalization of the luminosity estimation is determined through a method originally proposed by Simon Van der Meer and first exploited at the CERN ISR [90]. The "Van der Meer scans" determine the size of the colliding beams, and thereby the luminosity,

with minimal reliance on simulations. The procedure consists in scanning one beam against the other in the transverse plane to determine their overlap region. Horizontal and vertical separation scans are performed to optimize the delivered luminosity and measure the beam size in the interaction area.

Two of these Van der Meer scans were performed in July 2010, allowing for a preliminary estimation of the luminosity of the LHC in the 2010 Run, with an uncertainty of 11% [88]. This uncertainty was quoted in all the analysis published along 2010, including the one presented in this thesis.

Other two Van der Meer scans were performed in October 2010. A detailed study of the uncertainties on the measurement of the luminosity has been performed with this additional information [89]. The final results were available in March 2011 (well after the analysis performed in this thesis was finished). The new calibrations obtained for the absolute luminosity normalization do not affect greatly the luminosity estimations, but lead to a considerable reduction of their uncertainty. The integrated luminosity measured with this new calibration is a factor of 0.7% lower than the one measured with the previous calibration, and the uncertainty of the measurement is reduced to 4%.

However, even though this second measurement is clearly more precise, the results in this thesis include the previous, larger uncertainty on the luminosity measurement. The reason for this is one of consistency with the published papers in 2010 (in particular, to [91]). The changes in the new central values of the integrated luminosity are minor (cross-sections should only be increased by a factor of 0.7%). And even with this reduction in the luminosity error, it is still the dominant systematic effect.

Therefore it has been preferred to use the calibrations available at the time the analysis was performed, and leave the update of this particular systematic to future improvements of the measurement.

7.2.7 Summary

All sources of uncertainty (including statistical) are summarized in Table 7.6. The measurement is dominated by systematical uncertainties. Not taking into account the 11% (or 4%) due to luminosity, the statistical uncertainty associated to the $W \to \mu\nu$ cross-section is of 0.9%, compared to a total combined systematic uncertainty of 3.1%.

Table 7.6: Uncertainties in percent for charged W cross sections and ratios in the $W \to \mu\nu$ analysis. The luminosity uncertainty corresponds to the one applied to 2010 analysis [88].

Source	$W \to \mu\nu$	$W^+ \to \mu^+\nu$	$W^- \to \mu^-\bar{\nu}$	$\frac{W^+ \to \mu^+\nu}{W^- \to \mu^-\bar{\nu}}$
Statistical	0.9	1.2	1.5	2.1
Muon reconstruction & identification	1.5	1.5	1.5	2.8
Momentum scale & resolution	0.3	0.3	0.3	0.3
$\overrightarrow{E_T}^{miss}$ scale & resolution	0.4	0.4	0.4	-
Background subtraction / modelling	2.0	1.7	2.3	0.7
PDF uncertainty for acceptance	1.1	1.3	1.9	2.1
Other theoretical uncertainties	1.4	1.4	1.3	1.2
Systematical (Theory+Experimental)	3.1	3.0	3.6	3.8
Luminosity	11.	11.	11.	-

Chapter 8

Results and Outlook

The main results of this work are summarised in this chapter. We report here the inclusive production cross-sections of W bosons, inclusively and separated by charge (W^+, W^-), as well as the ratio of the charged cross-sections, $\sigma(\mathrm{pp} \to \mathrm{W}^+ + X \to \mu^+\nu + X)/\sigma(\mathrm{pp} \to \mathrm{W}^- + X \to \mu^-\bar{\nu} + X)$.

Cross-sections are given in the phase space defined by the kinematic restrictions applied in the analysis ($p_T > 20$ GeV and $|\eta| < 2.1$). They are also extrapolated to the full phase-space.

The W boson cross-section is combined with the $\mathrm{pp} \to \mathrm{Z}(\gamma^*) + X \to \mu^+\mu^- + X$ production cross-section measured by CMS to evaluate the ratio $\sigma(\mathrm{pp} \to \mathrm{W} + X \to \mu\nu + X)/\sigma(\mathrm{pp} \to \mathrm{Z}(\gamma^*) + X \to \mu^+\mu^- + X)$.

The most relevant kinematical distributions characterizing the W sample are also presented.

The results are also compared to the recently published results by CMS and ATLAS, and with the latest theoretical predictions.

Finally, the experience gained in this work is projected towards the coming analysis of the data collected in the Run 2010 B.

8.1 Measurement of the inclusive W production cross-section

The production cross-section of W bosons in proton-proton collisions, at 7 TeV and multiplied by the branching ratio of the decay of the W into a muon and a neutrino, $\sigma(\mathrm{pp} \to \mathrm{W}^\pm + X) \times BR(\mathrm{W}^\pm \to \mu^\pm\nu)$, was already measured in section 7.1.2, for the full phase-space.

The charged W^+ and W^- cross-sections, and the ratio of those, were also presented in that section. The associated systematic uncertainties were summarised in Table 7.6.

$$\begin{aligned}
\sigma(\mathrm{pp} \to \mathrm{W}^{\pm} + X \to \mu^{\pm}\nu + X) &= 9.93 \pm 0.09(\mathrm{sta}) \pm 0.25(\mathrm{exp}) \pm 0.17(\mathrm{theo}) \pm 1.09(\mathrm{lumi})\ \mathrm{nb}, \\
\sigma(\mathrm{pp} \to \mathrm{W}^{+} + X \to \mu^{+}\nu + X) &= 5.84 \pm 0.07(\mathrm{sta}) \pm 0.14(\mathrm{exp}) \pm 0.11(\mathrm{theo}) \pm 0.64(\mathrm{lumi})\ \mathrm{nb}, \\
\sigma(\mathrm{pp} \to \mathrm{W}^{-} + X \to \mu^{-}\bar{\nu} + X) &= 4.09 \pm 0.06(\mathrm{sta}) \pm 0.11(\mathrm{exp}) \pm 0.09(\mathrm{theo}) \pm 0.45(\mathrm{lumi})\ \mathrm{nb}, \\
\frac{\sigma(\mathrm{pp} \to \mathrm{W}^{+} + X \to \mu^{+}\nu + X)}{\sigma(\mathrm{pp} \to \mathrm{W}^{-} + X \to \mu^{-}\bar{\nu} + X)} &= 1.43 \pm 0.03(\mathrm{sta}) \pm 0.04(\mathrm{exp}) \pm 0.03(\mathrm{theo})
\end{aligned}$$

Systematic uncertainties (2.5% experimental and 1.7% theoretical for the inclusive W cross-section) dominate over the statistical uncertainty of the measurement (0.9%), already for this initial data-sample. The largest uncertainty comes from the determination of the integrated luminosity of the data sample (11%), and concerns only the measurement of the cross-sections. The W^+/W^- ratio is not affected by it.

The measurement can be restricted to a reduced phase-space, $p_T > 20$ GeV, $|\eta| < 2.1$, thus avoiding the kinematic acceptance correction used in the analysis. As a result, these reduced cross-sections are not affected by PDF uncertainties. The measured W, W^+ and W^- cross-sections are:

$$\begin{aligned}
\sigma(\mathrm{pp} \to \mathrm{W}^{\pm} + X \to \mu^{\pm}\nu + X)|_{red} &= 5.21 \pm 0.05(\mathrm{sta}) \pm 0.13(\mathrm{exp}) \pm 0.07(\mathrm{theo}) \pm 0.57(\mathrm{lumi})\ \mathrm{nb}, \\
\sigma(\mathrm{pp} \to \mathrm{W}^{+} + X \to \mu^{+}\nu + X)|_{red} &= 3.16 \pm 0.04(\mathrm{sta}) \pm 0.07(\mathrm{exp}) \pm 0.04(\mathrm{theo}) \pm 0.35(\mathrm{lumi})\ \mathrm{nb}, \\
\sigma(\mathrm{pp} \to \mathrm{W}^{-} + X \to \mu^{-}\bar{\nu} + X)|_{red} &= 2.05 \pm 0.03(\mathrm{sta}) \pm 0.06(\mathrm{exp}) \pm 0.03(\mathrm{theo}) \pm 0.22(\mathrm{lumi})\ \mathrm{nb}
\end{aligned}$$

Given the different production mechanims of the W^+ and W^-, they are affected by different acceptance corrections. Therefore, the ratio of their cross-sections in the reduced phase-space has no real meaning, and it is not quoted.

The production cross-section of Z bosons, multiplied by the branching ratio of the decay of the Z boson to muons $\sigma(\mathrm{pp} \to \mathrm{Z} + X) \times BR(\mathrm{Z} \to \mu^+\mu^-)$ has also been measured by CMS, and published in [91]:

$$\sigma(\mathrm{pp} \to \mathrm{Z}(\gamma^*) + X \to \mu^+\mu^- + X) = 0.92 \pm 0.03(\mathrm{sta}) \pm 0.01(\mathrm{exp}) \pm 0.02(\mathrm{theo}) \pm 1.11(\mathrm{lumi})\ \mathrm{nb}$$

The total W cross-section measured here can be combined with this Z cross-section to compute the ratio of W/Z cross-sections. This measurement is, as the ratio of W^+/W^-, not affected by the luminosity error, and therefore it is very precise.

$$\frac{\sigma(\mathrm{pp} \to \mathrm{W}^{\pm} + X \to \mu^{\pm}\nu + X)}{\sigma(\mathrm{pp} \to \mathrm{Z}(\gamma^*) + X \to \mu^+\mu^- + X)} = 10.7 \pm 0.4(\mathrm{sta}) \pm 0.3(\mathrm{exp}) \pm 0.19(\mathrm{theo})$$

The experimental transverse mass distribution, M_T, is again displayed in Figure 8.1, together with the fitted contributions of the different processes. The $W^{\pm}$, W^+ and W^- distributions are shown in linear and logarithmic scale. The agreement between data and the result of the fit is remarkably good, with only some small discrepancies at $M_T \approx 30$ GeV. This overlap region between signal and background is the most delicate one to model. From $M_T \gtrsim 100$ GeV onwards the fitted signal shape deviates slightly from the experimental distribution, due to the low $Z \rightarrow \mu^+\mu^-$ statistics available for template modelling, but with no impact on the cross-section measurement.

The transverse momentum distribution of the muons coming from the decay of the W boson is shown in Figure 8.2. The distribution is shown twice, for the full candidate data-sample, and only for those candidates with a reconstructed transverse mass larger than $M_T = 50$ GeV, in linear and logarithmic scale. The agreement data-MC is again excellent even in the tails, and we can see how after the M_T requirement the distribution is almost completely free of hadronic background. This allows a purer comparison of the observed data with the predicted distributions, with only some residual electroweak background contamination.

Figure 8.3 shows the ϕ and η distributions of the muons in events with a transverse mass $M_T > 50$ GeV. The yield shows no dependence on the azimuthal angle ϕ and shows a good agreement with Monte Carlo. On the other hand η shows dips in the overlap regions of the different systems of the muon-spectrometer, due to event losses in this region at the trigger level. Although the Monte Carlo follows qualitatively this behaviour, the agreement data-MC is not perfect in this case. As we saw in Chapter 6, the available $Z \rightarrow \mu^+\mu^-$ statistics only allowed for an average efficiency correction over the whole y region.

The missing transverse energy distribution is shown in Figure 8.4, for the data-sample and only for those candidates with a reconstructed transverse mass larger than $M_T = 50$ GeV. The shape of the E_T^{miss} distribution is corrected using the same templating procedure applied used to model the M_T shape. The agreement data-MC is again excellent, with only some discrepancies in the tails due to the low statistics available for template modelling. We can again see how after the requirement in M_T the result is practically background-free, and the distributions correspond almost solely to the neutrino transverse momentum.

Acoplanarity is shown in Figure 8.5, both for the full data-sample and only for events with a transverse mass over $M_T > 50$ GeV. All distributions except for the signal are taken from Monte Carlo simulation. Signal is modelled using the templates described in Chapter 6, and the agreement found between data and the templates is very good both in the signal-only region (low acoplanarity, high M_T) and in the high acoplanarity QCD-dominated region.

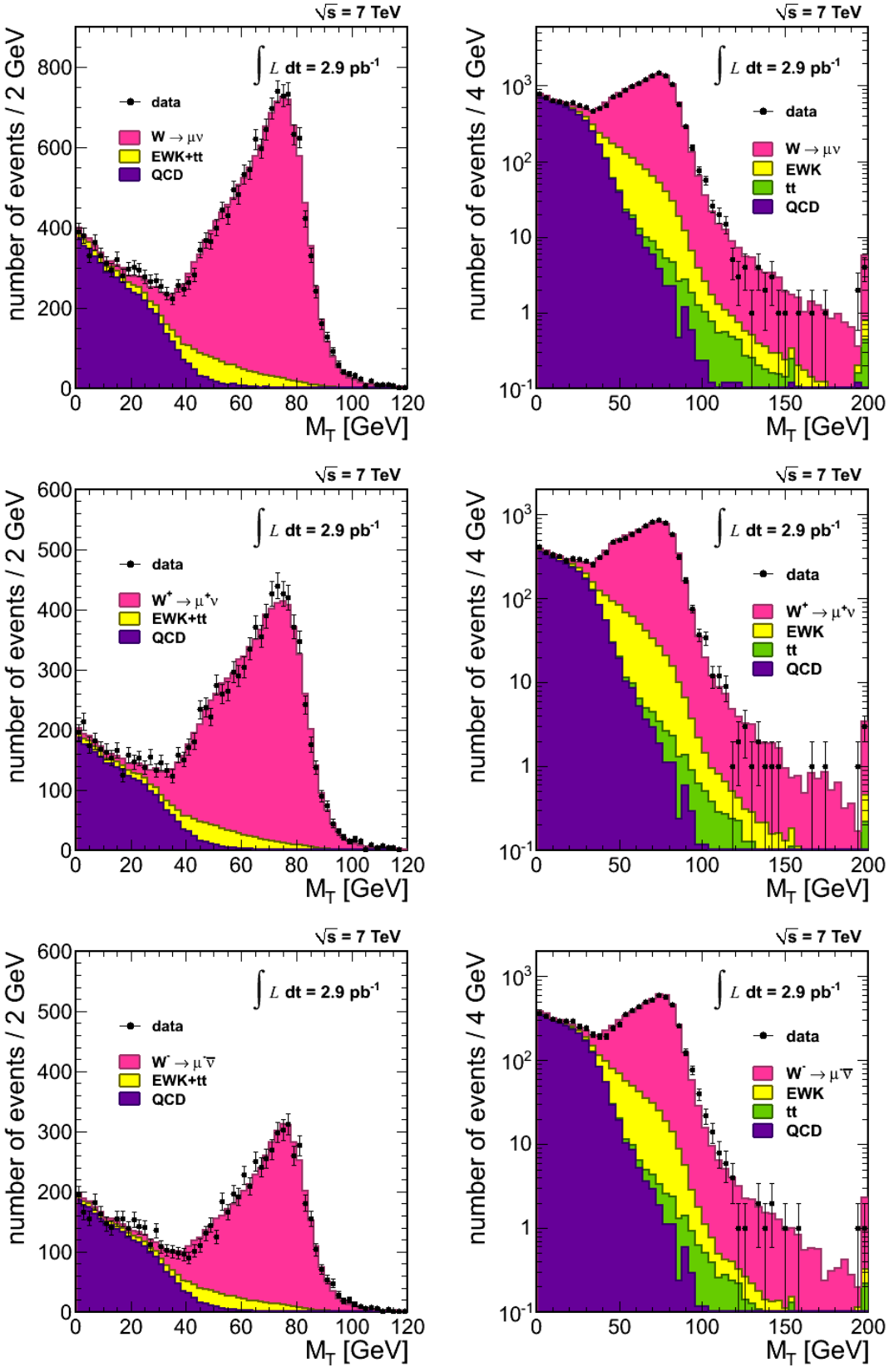

Figure 8.1: Experimental M_T distributions, together with the result of the fit, for $W^{\pm}$ bosons (top), W^+ (centre) and W^- (bottom). They are shown both in linear (left) and logarithmic (right) scales.

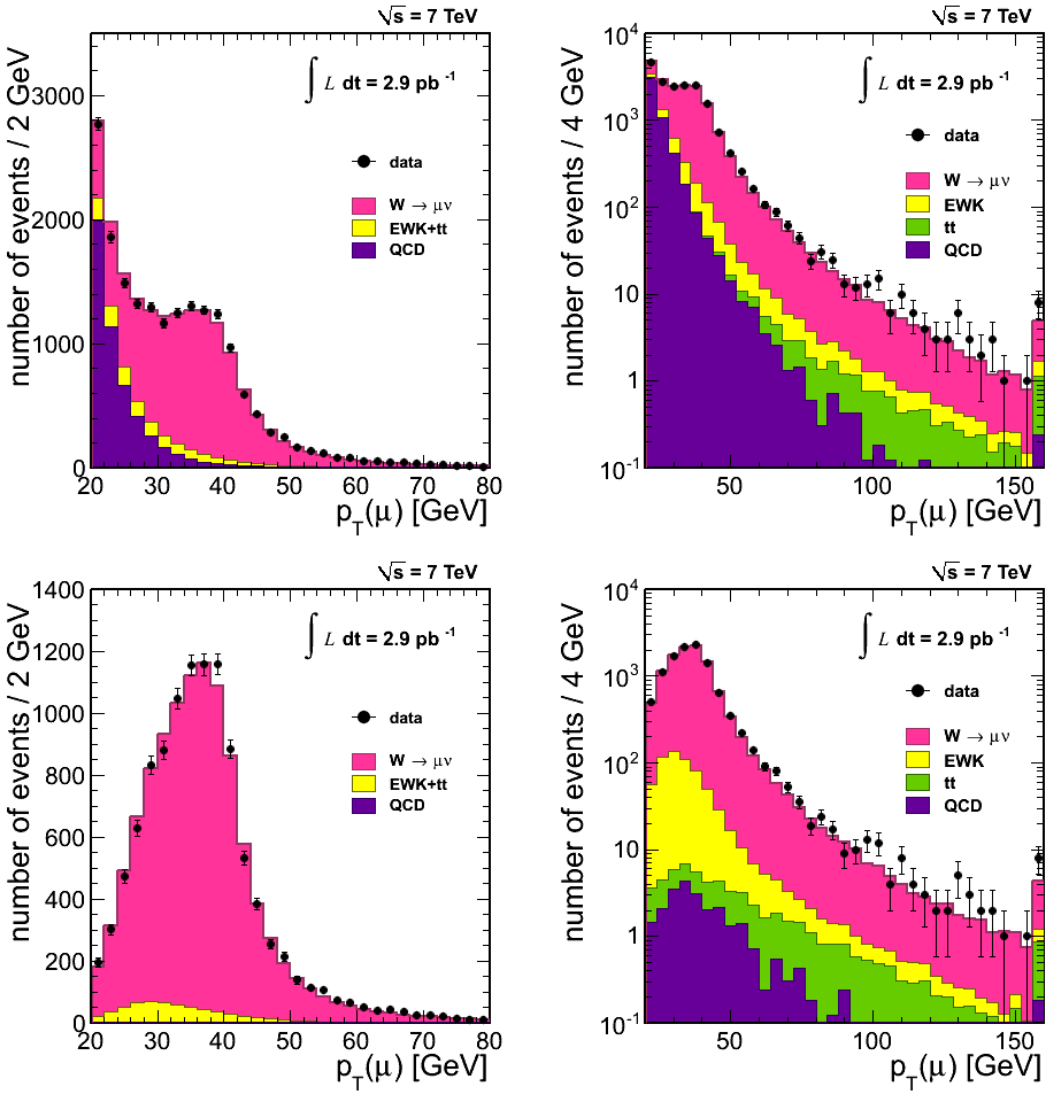

Figure 8.2: Distribution of the transverse momentum p_T of the muon, in linear and logarithmic scale. Top: Full data-sample, Bottom: candidates with a $M_T > 50$ GeV. The different contributions are normalized to the measured cross-sections.

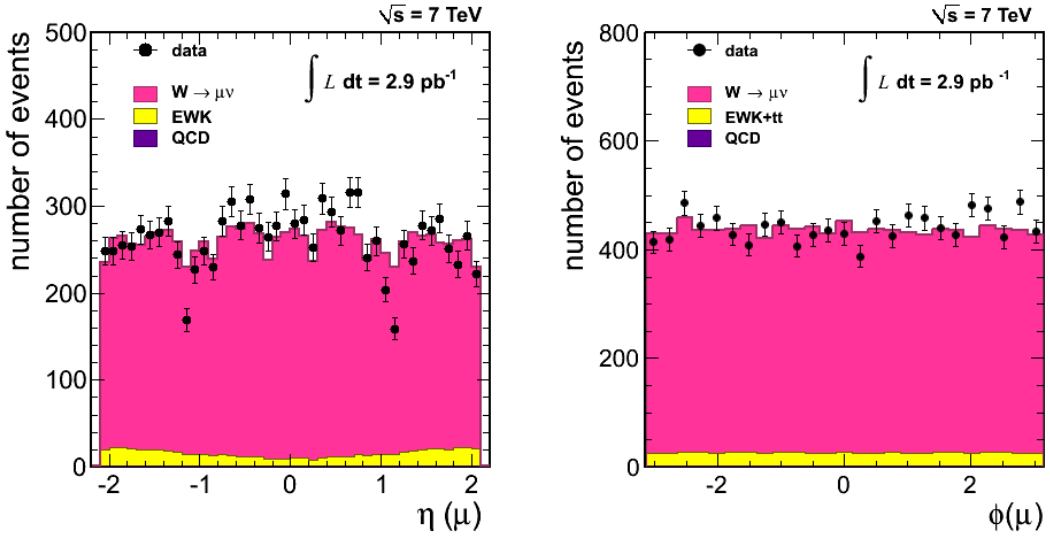

Figure 8.3: Muon η (left) and ϕ (right) distributions after a cut in $M_T > 50$ GeV.

Finally, the reconstructed p_T of the W boson is shown in Figure 8.6, using templates to describe signal and background, for events with $M_T > 50$ GeV. Some differences between the data and the expected distribution can be observed. At low momentum this is a physical meaningful difference from our current Monte Carlo description, which does not reproduce accurately the data as it does not include the resummation of low$-p_T$(W) logarithm terms contributing to the total W production cross-section.

There exist already programs such as ResBos [82] which take them into account in the calculations, but they are not event generators, and thus not useful for event simulation. In the future with the help of an increased set of collected data, the MonteCarlo descriptions may be improved tuning their parameters accordingly to the data.

On the other hand at high momentum this is basically a statistical effect. Since the template used to describe the signal shape is based on the behaviour of E_T^{miss} versus boson p_T in $Z \rightarrow \mu^+\mu^-$ data as described in Chapter 6, the modelling in the high momentum range is still limited by the small amount of Z candidates available to model E_T^{miss} in the highest p_T bins. This will be automatically improved when larger samples of $Z \rightarrow \mu^+\mu^-$ data are collected. Keeping these two comments in mind, although the agreement is not as good as for the other variables shown in this section, it is still rather reasonable with only minor differences at the very low and very high limits of the spectrum.

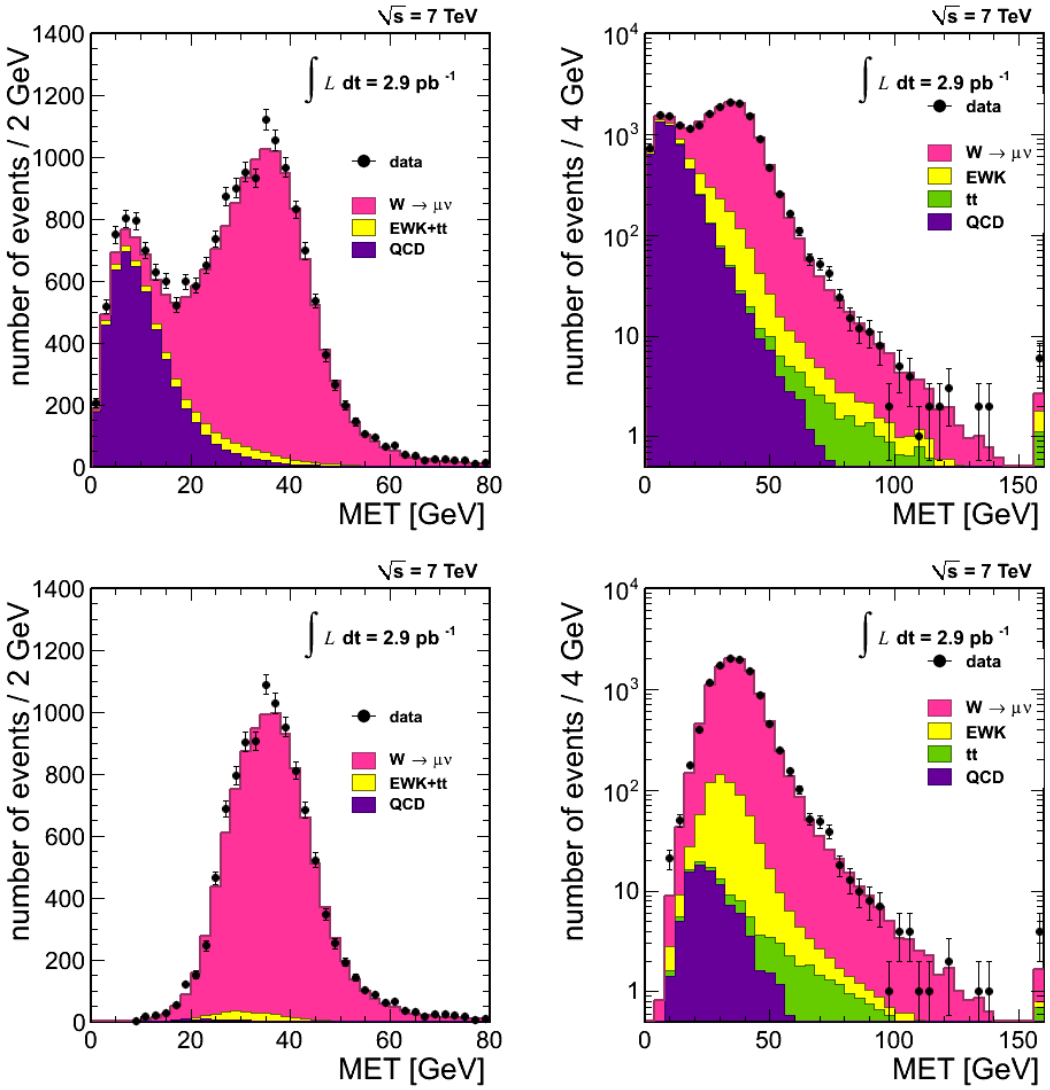

Figure 8.4: E_T^{miss} distributions, in linear and logarithmic scale, using the fitted values. Top: Full data-sample, Bottom: events with $M_T > 50$ GeV.

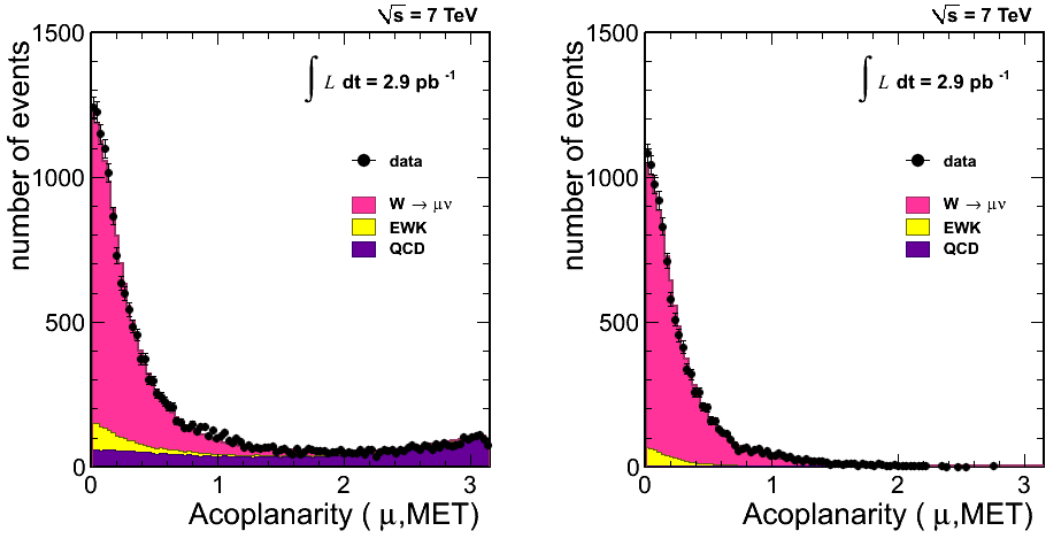

Figure 8.5: Acoplanarity distributions. Left: Full data-sample, Right: events with $M_T > 50$ GeV.

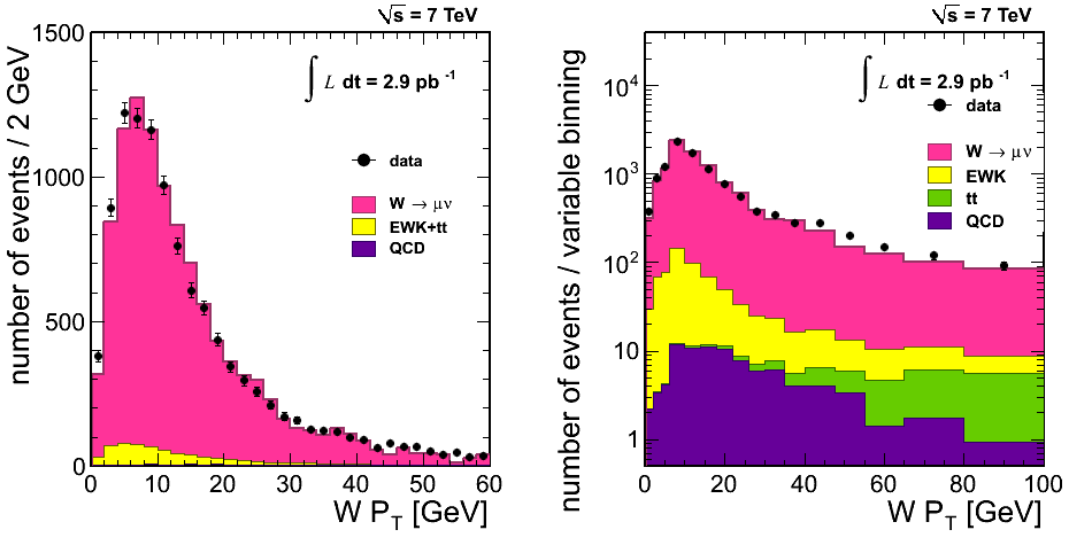

Figure 8.6: $p_T(W)$ distribution for events with $M_T > 50$ GeV, in linear and logaritmic scales.

8.2 Comparison with published results and theoretical predictions

The measured values of the cross-sections presented in this thesis are in full agreement with the two published measurements from CMS, for $L_{int} = 198$ nb^{-1} [92] and $L_{int} = 2.9$ pb^{-1} [91].

The analysis method here reported has been the basis of the one presented in [91], the official CMS result. There is only a small difference between both results, with lies in the method used to describe W signal M_T distribution.

In the published CMS result, W signal modelling is done through a parametrisation of the hadronic recoil to Z $\rightarrow \ell\ell$ bosons. The same information used in Chapter 6 to sample the distributions, the paralell and perpendicular projections of the E_T^{miss} in Z $\rightarrow \mu^+\mu^-$ events (see Chapter 6), is used in this implementation, with a slightly different approach. Instead of directly sampling this information to build the template, the mean and width of the distributions are parametrized as a funcion of the Z boson p_T. The same variables are studied in Monte Carlo in order to derive a data/Monte Carlo correction factor, which is afterwards used to correct the W Monte Carlo prediction. This way a realistic W signal template is obtained.

Both methods describe the signal identically well and have been found to give almost identical results. Residual differences between them may arise from the fact that the sampling method here described may be more affected by the low statistics available in the high Z p_T range; while the parametrization approach may be less precise if non-gaussian tails are found.

Furthermore, in order to present a consistent analysis in the muon and in the electron channels (where the sampling method was not developed), the method chosen for publication has been the parametrisation of the recoil. The method described in this thesis has been used as a cross-check of the measurement.

The values measured in this thesis are shown in Figures 8.7, together with the published CMS values for the electron and muon channels separately, and for their combination. The different graphics in the Figure show the value of (a) W cross-section, (b) W^+ cross-section, (c) W^- cross-section, (d) Ratio of W^+/W^- cross-sections and (e) Ratio of W/Z cross-sections, with their corresponding statistic (black line), systematic (blue line) and luminosity (green line) uncertainties.

As it has just been mentioned the results of this thesis agree with the CMS values. The theoretical predictions, computed using the program FEWZ [37], are also shown. The mean

value is obtained using NNLO MSTW PDFs [9]. The yellow band in the plot corresponds to the uncertainty in this theoretical prediction.

The measured cross-sections are consistently smaller by a $\approx 5\%$ than the theoretical prediction, but well within the luminosity systematic error. The ratio between the CMS published values and the theoretical prediction is shown in Figure 8.8, where the hatched area corresponds to the 11% uncertainty on the luminosity measurement. This systematic behaviour may hint to a overestimation of the luminosity in this first period of the LHC, or to an overestimation of the theoretical predictions of the cross-section. On the other hand, the luminosity independent cross-section ratios W^+/W^- and W/Z show an impressively good agreement with the predicted value.

Finally, the measured values can be compared with the measurements carried out at lower centre-of-mass, in proton-antiproton collisions at $\sqrt{s} = 576$ GeV and $\sqrt{s} = 630$ GeV in the experiments UA1 [93] and UA2 [94] of the SPS, and at $\sqrt{s} = 1.96$ TeV in the CDF and D0 experiments at the Tevatron [95]. This comparison is shown in the left panel of Figure 8.9, where the theoretical curve of the cross-section as a function of centre-of-mass energy, computed with FEWZ using NNLO MSTW pdfs, is also shown. The agreement between the theoretical prediction and the experimental results at different centre-of-mass energies is once again very good.

In the right window of the same Figure, the CMS measurement (red) is shown together with the values measured by the ATLAS collaboration [96] (green), and compared to the theoretical prediction. The ATLAS measurement was derived with a data sample of $\mathcal{L}_{int}(\text{ATLAS}) = 300\ \text{nb}^{-1}$. The 11% luminosity uncertainty, common to the measurements of both experiments, is shown as a hatched blue area. The measured values are in agreement taking into account the systematic uncertainties of the measurements.

8.3 Revision of the luminosity estimation

It must be noted that a revision of the luminosity estimation of the experiment has been performed recently [89], thanks to Van der Meer scans performed in October 2010 to determine the effective crossing area of the beams at the CMS intersection point. This study overrides the previous estimation of the luminosity, used for all analysis published in 2010 and based in Van der Meer scans performed in July [88].

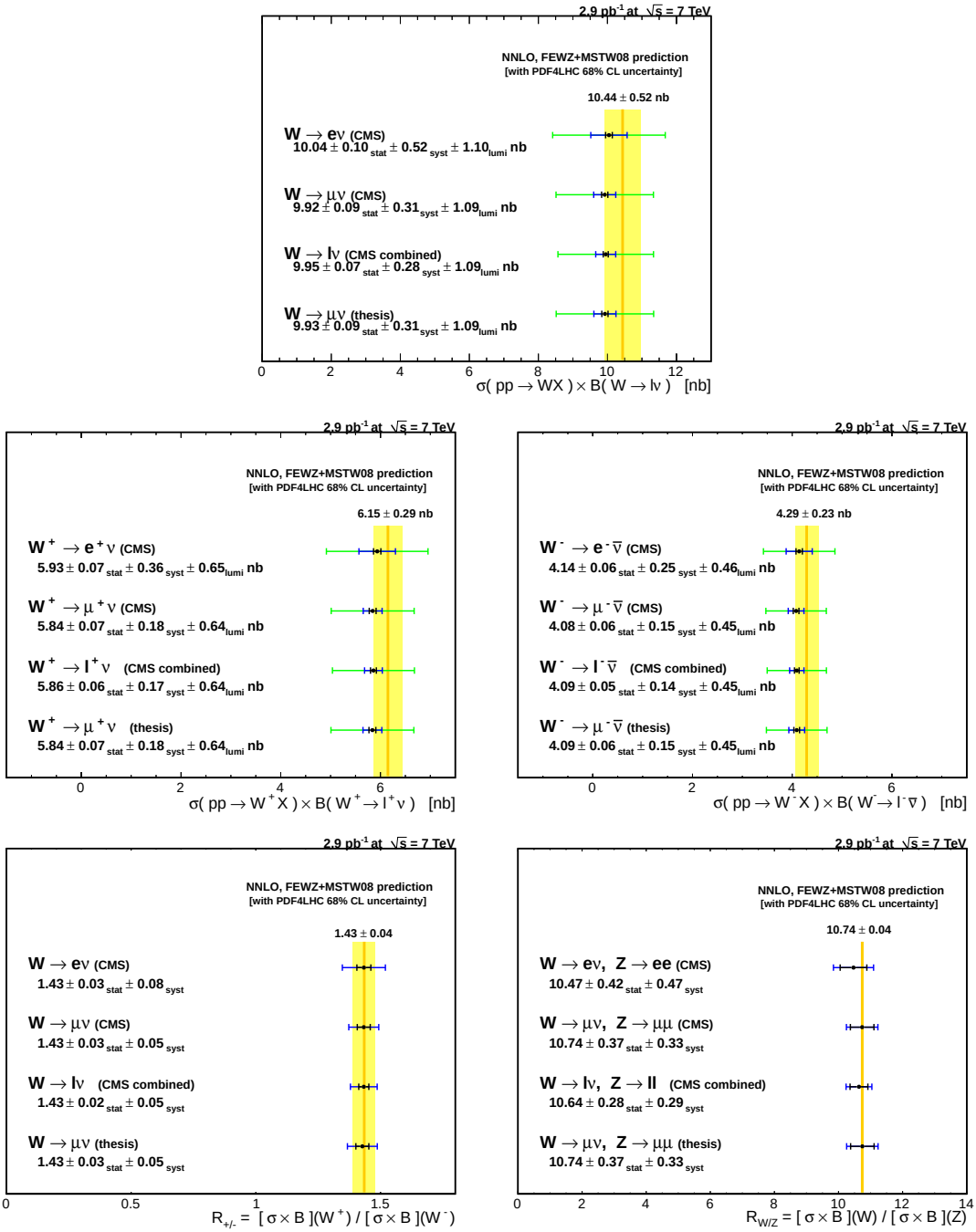

Figure 8.7: Measurements presented in this thesis and published CMS results. The theoretical predictions are also shown for comparison (yellow band).

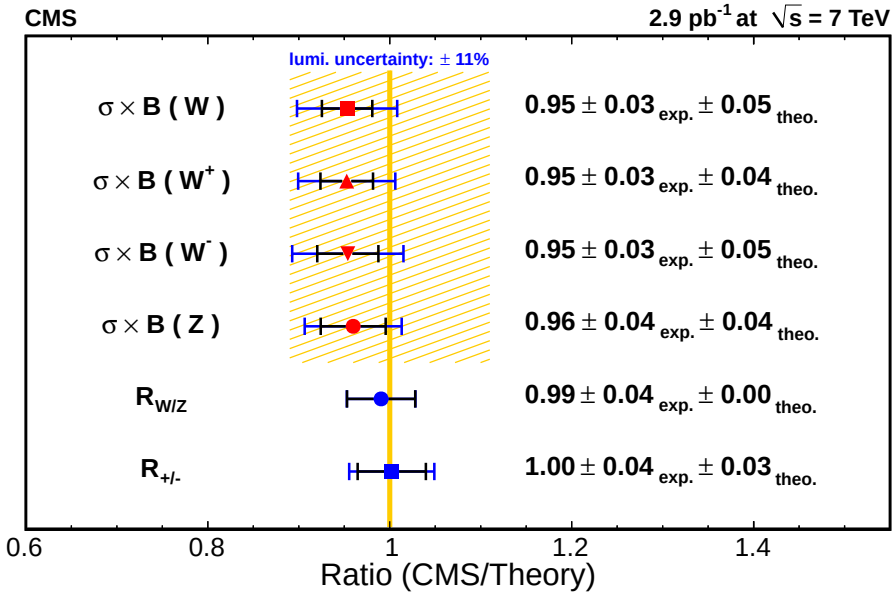

Figure 8.8: Comparison of our measurements with the theoretical prediction, computed as a ratio of the CMS published results over the expected values (CMS/Theory).

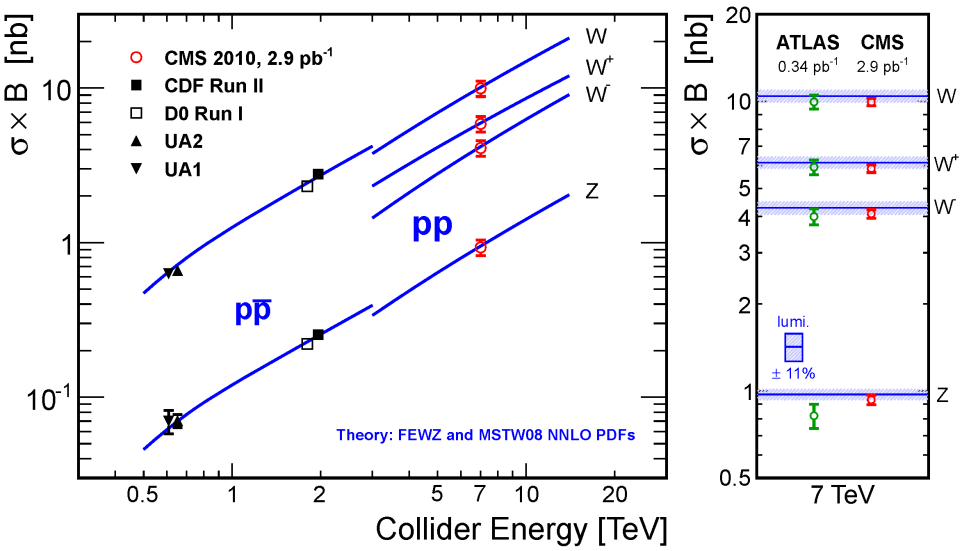

Figure 8.9: Published CMS W and Z cross-sections, compared to past experiments at lower centre of mass energies (left), and to the published ATLAS result (right).

This revision has a minor impact on the integrated luminosity of the data. Cross-sections must be increased by a 0.7%, and the associated systematical error reduced from a 11% to a 4%.

This change implies that measured inclusive cross-section in the full phase-space would be increased to:

$$\begin{aligned}
\sigma(\mathrm{pp} \to \mathrm{W}^{\pm} + X \to \mu^{\pm}\nu + X) &= 10.00 \pm 0.09(\mathrm{sta}) \pm 0.25(\mathrm{exp}) \pm 0.17(\mathrm{theo}) \pm 0.40(\mathrm{lumi})\ \mathrm{nb}, \\
\sigma(\mathrm{pp} \to \mathrm{W}^{+} + X \to \mu^{+}\nu + X) &= 5.88 \pm 0.07(\mathrm{sta}) \pm 0.14(\mathrm{exp}) \pm 0.11(\mathrm{theo}) \pm 0.24(\mathrm{lumi})\ \mathrm{nb}, \\
\sigma(\mathrm{pp} \to \mathrm{W}^{-} + X \to \mu^{-}\bar{\nu} + X) &= 4.12 \pm 0.06(\mathrm{sta}) \pm 0.11(\mathrm{exp}) \pm 0.09(\mathrm{theo}) \pm 0.16(\mathrm{lumi})\ \mathrm{nb},
\end{aligned}$$

The measurements in the restricted phase-space, $p_T > 20$ GeV, $|\eta| < 2.1$ with this new calibration would be:

$$\begin{aligned}
\sigma(\mathrm{pp} \to \mathrm{W}^{\pm} + X \to \mu^{\pm}\nu + X)|_{red} &= 5.25 \pm 0.05(\mathrm{sta}) \pm 0.13(\mathrm{exp}) \pm 0.07(\mathrm{theo}) \pm 0.21(\mathrm{lumi})\ \mathrm{nb}, \\
\sigma(\mathrm{pp} \to \mathrm{W}^{+} + X \to \mu^{+}\nu + X)|_{red} &= 3.18 \pm 0.04(\mathrm{sta}) \pm 0.07(\mathrm{exp}) \pm 0.04(\mathrm{theo}) \pm 0.13(\mathrm{lumi})\ \mathrm{nb}, \\
\sigma(\mathrm{pp} \to \mathrm{W}^{-} + X \to \mu^{-}\bar{\nu} + X)|_{red} &= 2.06 \pm 0.03(\mathrm{sta}) \pm 0.06(\mathrm{exp}) \pm 0.03(\mathrm{theo}) \pm 0.08(\mathrm{lumi})\ \mathrm{nb}
\end{aligned}$$

The luminosity independent ratios, $\sigma(W^+)/\sigma(W^-)$ and $\sigma(W)/\sigma(Z)$ remain unchanged.

The luminosity uncertainty is therefore still the dominant systematical effect on the measurement.

This small shift does not alter any of the conclusions already presented. Therefore in order to give the results of this thesis it has been prefered to maintain the luminosity calibration used at the time this analysis was performed, in order to compare with the results published in [91].

8.4 Outlook

CMS has collected an integrated luminosity of $L_{int} > 40$ pb^{-1} during the full 2010 run, of which ≈ 36 pb^{-1} meet the data-quality filters required for analysis.

The W cross-section measurement presented here, performed with a relatively small data-sample of $L_{int} = 2.88$ pb^{-1} ($\approx 10^4\ Ws$) is currently being updated using the full statistics collected in the first year of operation.

The strategy to analyze this full data-set follows closely the one presented in this thesis. Since the measurement is already dominated by systematic effects, one might conclude that a ten-fold increase in statistics will not signify a major improvement of the measurement.

However, some possible improvements will be possible thanks to a better understanding of the detector, which will reflect in a more accurate description of efficiencies, muon momentum resolution effects, and better modelling of signal shapes, as already discussed through this work. They will consequently imply smaller systematic errors.

In particular, higher integrated luminosity implies higher $Z \rightarrow \mu^+\mu^-$ statistics to study efficiencies, thus reducing one of the largest experimental uncertainties. A binned muon efficiency in terms of η, ϕ and/or p_T will improve the Monte Carlo description of the detector, therefore yielding a better agreement with the experimental distributions for each one of the variables shown in this chapter.

Muon momentum scale will also be better understood once the $Z \rightarrow \mu^+\mu^-$ data sample is large enough, and it may be able to obtain a correction factor for Monte Carlo instead of just quoting an upper limit of the possible distortion of the measurement. In addition to this, since signal modelling is based on $Z \rightarrow \mu^+\mu^-$ candidates as well, a larger data sample will allow for a more precise template, and for a reduction of the systematic uncertainty associated to E_T^{miss} scale and resolution.

The last large experimental systematic error (background subtraction) is clearly unaffected by the statistics of the data sample available. In order to reduce its current value ($\Delta\sigma = 2\%$, see Table 7.6), the easiest and safest choice is to tighten the selection criteria, therefore minimizing the QCD background contamination. The main reason for keeping a loose selection at the LHC start-up (maximising signal yield) will not be so critical with a factor 10 of increase in integrated luminosity. Therefore, it will be beneficial to choose a tighter selection which will provide a purer sample for analysis, as explained in Section 6.1.1. This tighter selection could be obtained setting a higher threshold in the p_T of the muons ($p_T > 25$ GeV) and a stricter isolation criteria ($I_{comb}^{rel} < 10\%$).

These improvements may lead to a reduction of the experimental uncertainties from the current 2.5% to $\approx 1\%$. Some other effects, which have not been discussed here due to their negligible size compared with the current uncertainties, will have to be looked into if one wants to reach a precision below the 1% level. For example, finer details on W p_T or PDF effects on the determination of the signal shape.

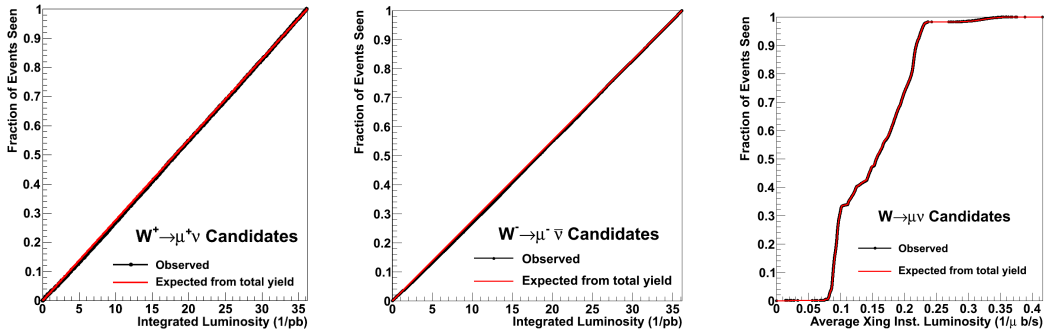

Figure 8.10: Cumulative observed number of positive (left) and negative (center) W Candidates in the 2010 dataset versus integrated luminosity, compared to the average number of events per picobarn obtained from the total number of events. The plot on the right shows the observed W candidates as a function of the average instantaneous luminosity per bunch crossing, also in the full 2010 dataset.

In addition to this, a larger data-sample will enable not only an update of the cross-section analysis presented here, but also new electroweak results (charge asymmetries, differential measurements), to be published in 2011.

An update of the final M_T distributions presented in this thesis, with the same selection criteria, is shown in Figure 8.11 for L_{int}(certified) = 35 pb^{-1}. In the region $M_T > 50$ GeV, the number of candidates observed in data is 144718, whereas the number of expected events (taking into account the theoretical predictions for each cross-section) is 144995.

The evolution of the number of positive and negative candidates observed with time, for the full data-set collected in 2010 and with the same selection applied in the thesis, is shown in Figure 8.10 as a function of the integrated luminosity collected (left plot for candidates with positive charge, and center for candidates with negative charge). Both graphics show a constant slope, which signifies a monotonous increase of the candidate sample, and very good agreement with the averaged prediction for the total number of observed events superimposed in red. The plot on the right shows the number of observed candidates in the 2010 run as a function of the average instantaneous luminosity per bunch crossing. In this case the behaviour is not constant, as expected, but once again the predicted curve from the total number of events (in red) agrees perfectly well with the collected data.

It must be noted that during the years of analysis preparation for the measurement of the cross-section with the first data, the goal was to reach an experimental uncertainties of the order of $4 - 5\%$. With a current systematic uncertainty of 3.1% in the total W cross-section (3.7%

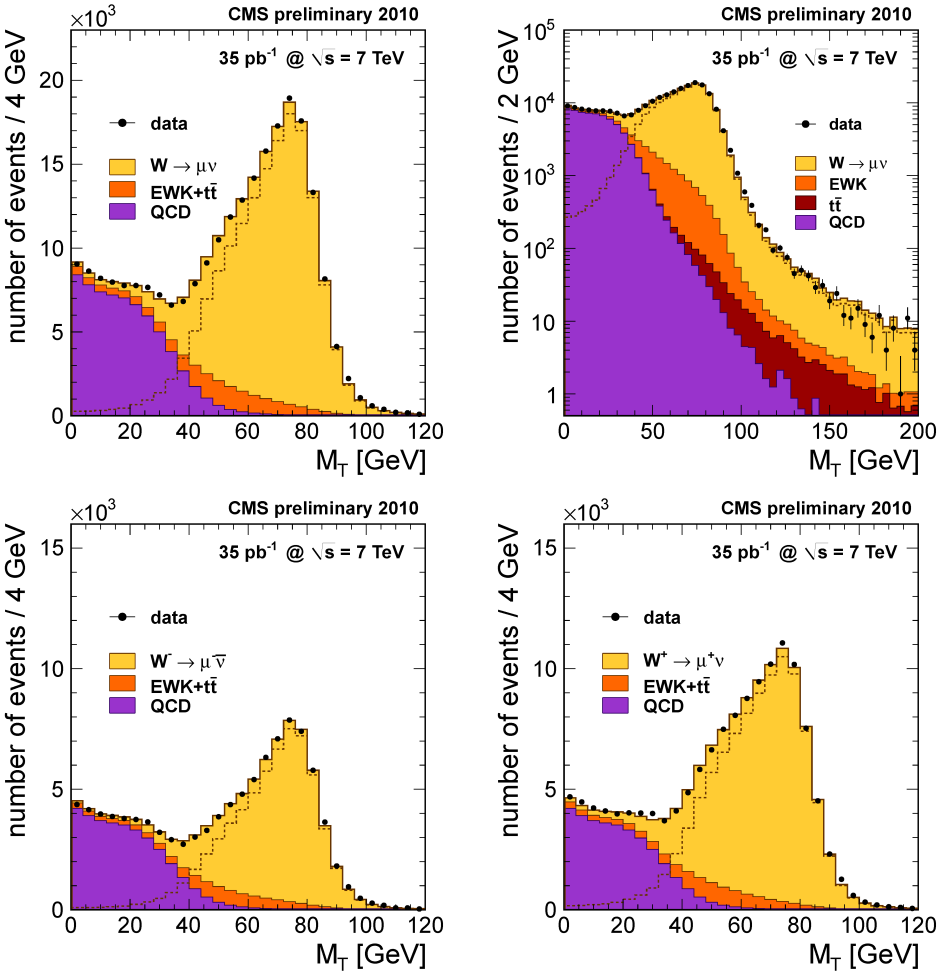

Figure 8.11: W $\rightarrow \mu\nu$ distributions for the full 2010 data-sample (L_{int}(certified) = 35 pb^{-1}). in linear (top left) and logarithmic scales (top right). The distributions separated by candidate charge are also shown in the bottom: W$^+ \rightarrow \mu^+\nu$ (left) and W$^- \rightarrow \mu^-\bar{\nu}$ (right).

including the statistical error), this objective has been clearly fulfilled within the fist year of operation of the detector.

In the future, the cross-section measurement may be used with an additional purpose. With a theoretical error on the prediction of the cross-section $\approx 4\%$, and a experimental uncertantiy on the measured cross-section of $< 2\%$, the luminosity of a given data sample could be determined through W counting: $\mathcal{L} = \frac{N^W/(A_{kin}\times\epsilon_\mu)}{\sigma_{theo}}$. Propagating uncertainties, $\Delta\mathcal{L} < 5\%$ is already within reasonable reach. This measurement could therefore be used as alternative luminosity monitor able to cross-check the standard measurements of the luminosity (expected to be of 4% for the 2011 run).

Chapter 9

Conclusions

The W production cross-section 7 TeV presented in this thesis is one of the first Electro Weak physics results achieved by the CMS experiment, and in a more general scenario, by the Large Hadron Collider.

We have measured the total inclusive production $W^{\pm}$ cross-sections, together with the cross-sections of positive W^{+} and negative W^{-} bosons, and their ratio W^{+}/W^{-}. The total cross-section has been also combined with the inclusive Z boson cross-section measurement to determine the W/Z ratio:

$$
\begin{aligned}
\sigma(\mathrm{pp} \to \mathrm{W}^{\pm} + X \to \mu^{\pm}\nu + X) &= 10.00 \pm 0.09(\mathrm{sta}) \pm 0.25(\mathrm{exp}) \pm 0.17(\mathrm{theo}) \pm 0.40(\mathrm{lumi})\ \mathrm{nb}, \\
\sigma(\mathrm{pp} \to \mathrm{W}^{+} + X \to \mu^{+}\nu + X) &= 5.88 \pm 0.07(\mathrm{sta}) \pm 0.14(\mathrm{exp}) \pm 0.11(\mathrm{theo}) \pm 0.24(\mathrm{lumi})\ \mathrm{nb}, \\
\sigma(\mathrm{pp} \to \mathrm{W}^{-} + X \to \mu^{-}\bar{\nu} + X) &= 4.12 \pm 0.06(\mathrm{sta}) \pm 0.11(\mathrm{exp}) \pm 0.09(\mathrm{theo}) \pm 0.16(\mathrm{lumi})\ \mathrm{nb}, \\
\frac{\sigma(\mathrm{pp} \to \mathrm{W}^{+} + X \to \mu^{+}\nu + X)}{\sigma(\mathrm{pp} \to \mathrm{W}^{-} + X \to \mu^{-}\bar{\nu} + X)} &= 1.43 \pm 0.03(\mathrm{sta}) \pm 0.04(\mathrm{exp}) \pm 0.03(\mathrm{theo}), \\
\frac{\sigma(\mathrm{pp} \to \mathrm{W}^{\pm} + X \to \mu^{\pm}\nu + X)}{\sigma(\mathrm{pp} \to \mathrm{Z}(\gamma^{*}) + X \to \mu^{+}\mu^{-} + X)} &= 10.7 \pm 0.4(\mathrm{sta}) \pm 0.3(\mathrm{exp}) \pm 0.19(\mathrm{theo})
\end{aligned}
$$

The measurement in 2010 has been dominated by the rapidly changing conditions of the data-taking. Instantaneous luminosity increased continously, and presented a challenge to the analysis, which had to evolve with it. This results correspond to an experimental data sample of $\mathcal{L} = 3\ \mathrm{pb}^{-1}$, from which a signal yields of $N_W = 12269 \pm 111$ $W^{\pm}$ bosons ($N_{W^+} = 7439 \pm 86$, $N_{W^-} = 4830 \pm 69$ negative) and $N_Z = 911 \pm 30$ Z bosons was extracted.

Theoretical predictions, calculated at the next-to-next-to-leading order in QCD using recent parton distribution functions, are in good agreement with the measured values of cross-sections and ratios.

The total uncertainty of the measurements, excluding the luminosity since it is an external element of the analysis, is at the $3-4\%$ level, thus allowing us to qualify these measurements as precision physics. In particular, the luminosity-independent ratios, are very precise measurements whose agreement with the theoretical prediction is indeed remarkable.

The excellent agreement with the Standard Model obtained is a successful test of its validity in the new energy frontier, and clears the way towards discovery. The measurement of the product cross-section is the first step towards the full characterization of physics processes involving W bosons, which in many cases constitute a major background for New Physics searches.

The methods and algorithms developed in the context of this analysis will serve as a basis for future Electroweak analysis.

From the detector point of view, the analysis described in this thesis constitutes a benchmark process, extremely useful to establish the performance of the detector. The strong emphasis put on the use of data themselves to improve the understanding of the detector (from the measurement of efficiencies in data, to the re-modelling of the final distributions of the analysis using information obtained from control data-samples) is one of the key pieces of the measurement.

Its contribution to the understanding of muon muon triggering, reconstruction and isolation, and of E_T^{miss} reconstruction and measurement are specially important. The full analysis chain of CMS, from the definition of datasets and the simulation of Monte Carlo samples, to the final analysis details, has been thoroughly validated. The techniques and lessons learnt will be invaluable in the future.

The cross-section of W and Z may provide the experiment with an alternative clean measurement of the luminosity. Since the systematical errors of the measurement are well under control, and already better than 3%, the measurement could be reversed. A competitive cross-check of the absolute value of the luminosity of future data can be obtained from the constant yield of W and Z detected by the experiment.

Appendices

Appendix A

Evolution of the $\mathrm{W} \rightarrow \mu\nu$ analysis

This thesis in entirely based on the data sample collected by CMS up to September of 2010.

However, it has to be noted that the techniques here described are based on previous Monte Carlo studies performed in the CMS collaboration, for different centre-of-mass energies, public at 14 and 10 TeV.

In addition to this, to get to the full analysis here described, CMS went through a weak boson candidate-hunting phase, and showed a first measurement of the crosssection already in the ICHEP conference in July.

Finally, the experiment has continued taking data up to November 2010, collecting a final integrated luminosity over 40 pb^{-1} of 7 TeV data.

This appendix tries to summarise the $\mathrm{W} \rightarrow \mu\nu$ analysis performed through through the first year of LHC operation.

A.1 Monte Carlo studies at 14 TeV and 10 TeV

A similar analysis strategy to the one presented in this thesis, with minor differences, was performed on CMS Monte Carlo samples at 14 TeV and 10 TeV.

The selection criteria are almost identical, with some differences in the isolation variable used (only based in track activity), transverse momentum cut applied (25 GeV) and the missing transverse energy algorithm used (calorimetric E_T^{miss}).

The final transverse mass plots are shown in Figure A.1, from the CMS Physics Analysis Summaries [71; 72].

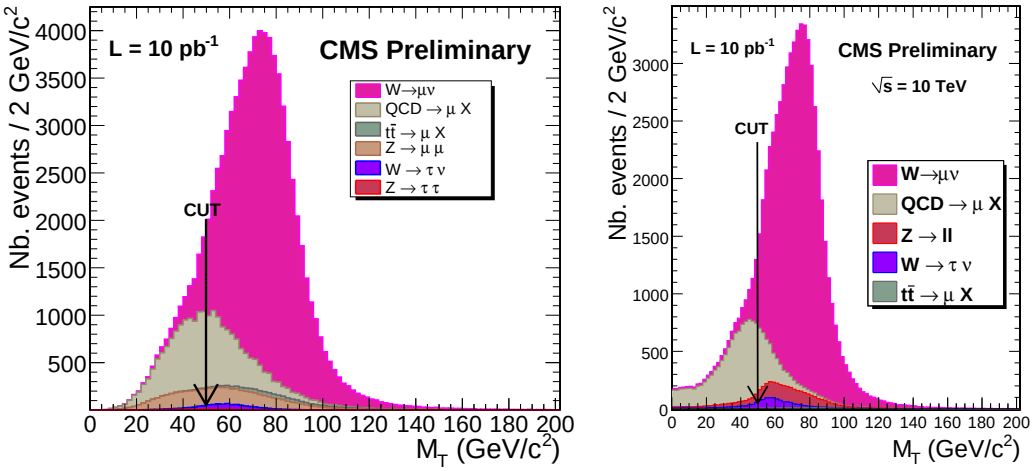

Figure A.1: Monte Carlo expectations for the M_T distributions at 14 (right) and 10 (left) TeV, for a similar selection to the one used in this thesis.

A.2 Candidate Hunting Era

The first W and Z candidates observed in CMS appeared in the first months of LHC operation (Spring 2010). Limited by statistics, the analysis concentrated on identifying possible candidates and testing the selection criteria on the available data (specially those criteria dedicated to identifying "good" muons and rejecting misreconstructed muons and punchthrough).

Examples of the first candidates observed are shown Figures A.2 and A.3 as reconstructed by the graphical event display software of CMS Fireworks (REF).

These first events were studied in detail. The first result of CMS for Vector Boson physics, corresponding to the integrated luminosity of $\approx 1\text{nb}^{-1}$, was the distribution of the first W candidates superimposed to MC predictions. Figures A.2 shows the transverse mass (M_T) distribution of these first candidates together with their purity (estimation of the Signal/(Signal+Background) proportion in Monte Carlo) in the $M_T - P_T$ plane.

A.2.1 Data quality for ElectroWeak analysis

For this task it was specially important the use of online data quality monitoring programs. They provide a first, fast, automatic look at the data before any offline study is performed - invaluable for validation and first results.

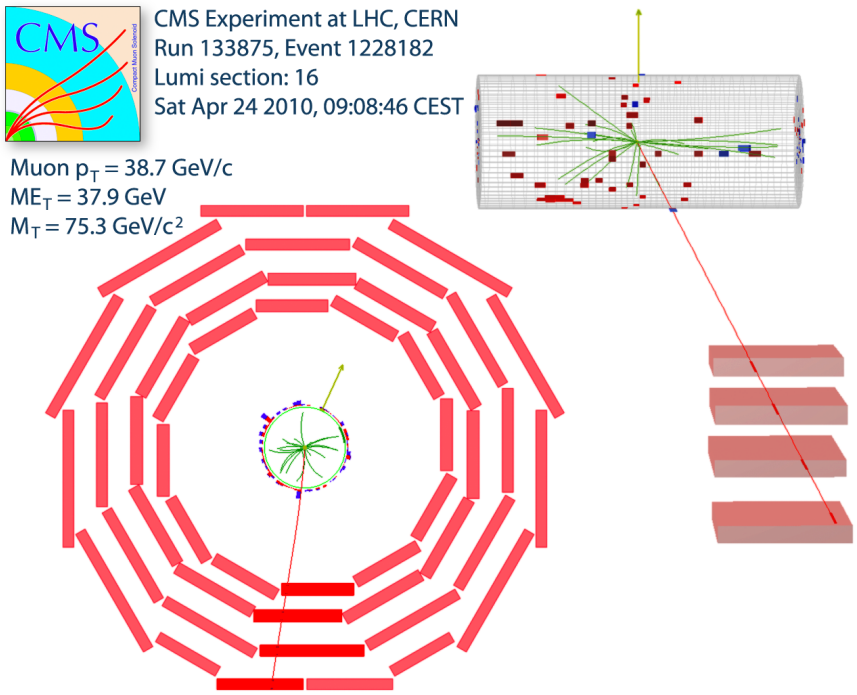

Figure A.2: Examples of one of the first $W \to \mu\nu$ candidates in CMS.

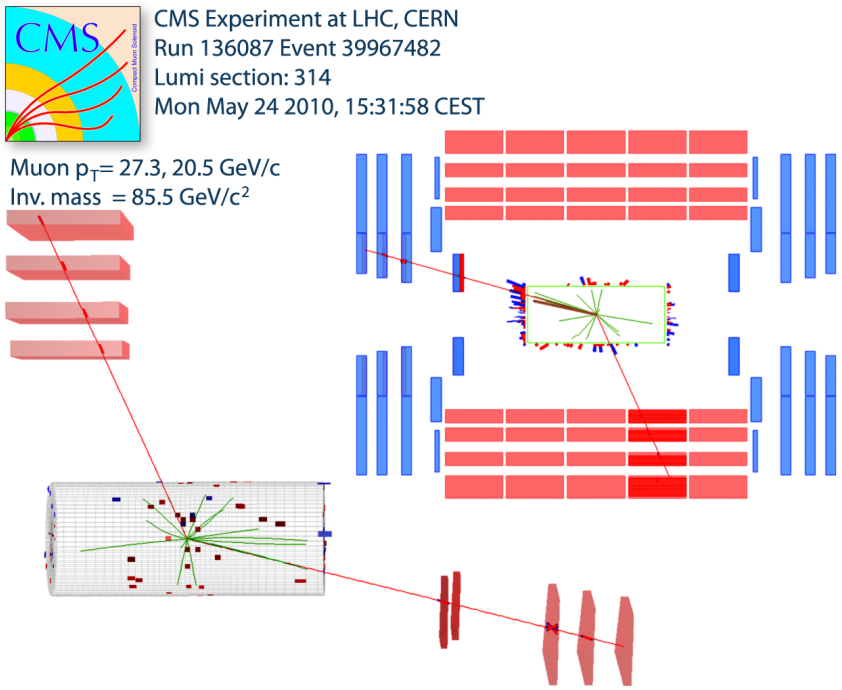

Figure A.3: Examples of one of the first $Z \to \mu^+\mu^-$ events in CMS.

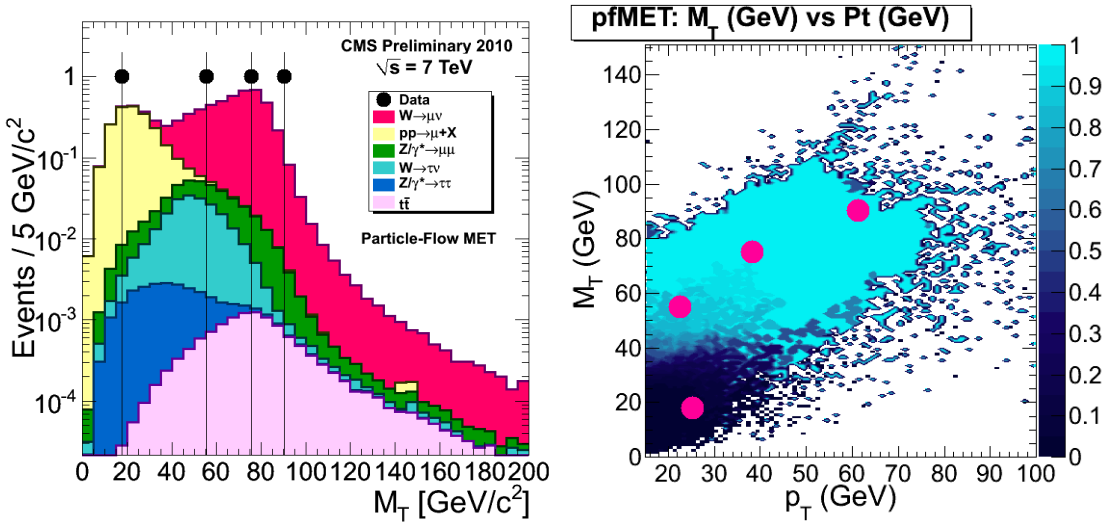

Figure A.4: First W Candidates in CMS, and associated Monte Carlo predictions. a) M_T distribution of the candidates and b) purity associated to them

The ElectroWeak Data Quality Monitoring is divided in several different packages, per reconstructed object (taus, electrons, muons). Focused on the monitoring of muon objects, through the study of W and Z bosons decaying into muons:

- **EwkMuDQM** - Basic module for validation of the variables used in analysis, both before any cut has been applied and after the default selection for W → $\mu\nu$ and Z → $\mu^+\mu^-$ events has been applied. As a first check on the quality of the data, and on the validity of the selection cuts applied, it had an changing role with luminosity. In the first days of "Candidate hunting" (the first era of data-taking in which the identification and study of the first W and Z events was one of the key efforts of the ElectroWeak) it was extremely useful as a tool to identify interesting events to be further studied offline; as well as to control the performance of our selection as a rejection tool against background (mostly muons coming from bb events and decays in flight). As luminosity increased, it also provided a first look on the distributions of the analysis, serving as a check of differences between the releases of software used for data-taking

- **EwkMuLumiMonitor** - Module for Luminosity counting. Based on the fact that vector boson production is one of the best known processes theoretically, as well as very clean experimentally, it is an excellent tool to provide information about the luminosity. Once instantaneous luminosity is high enough to provide a sizeable flow of W and Z candidates

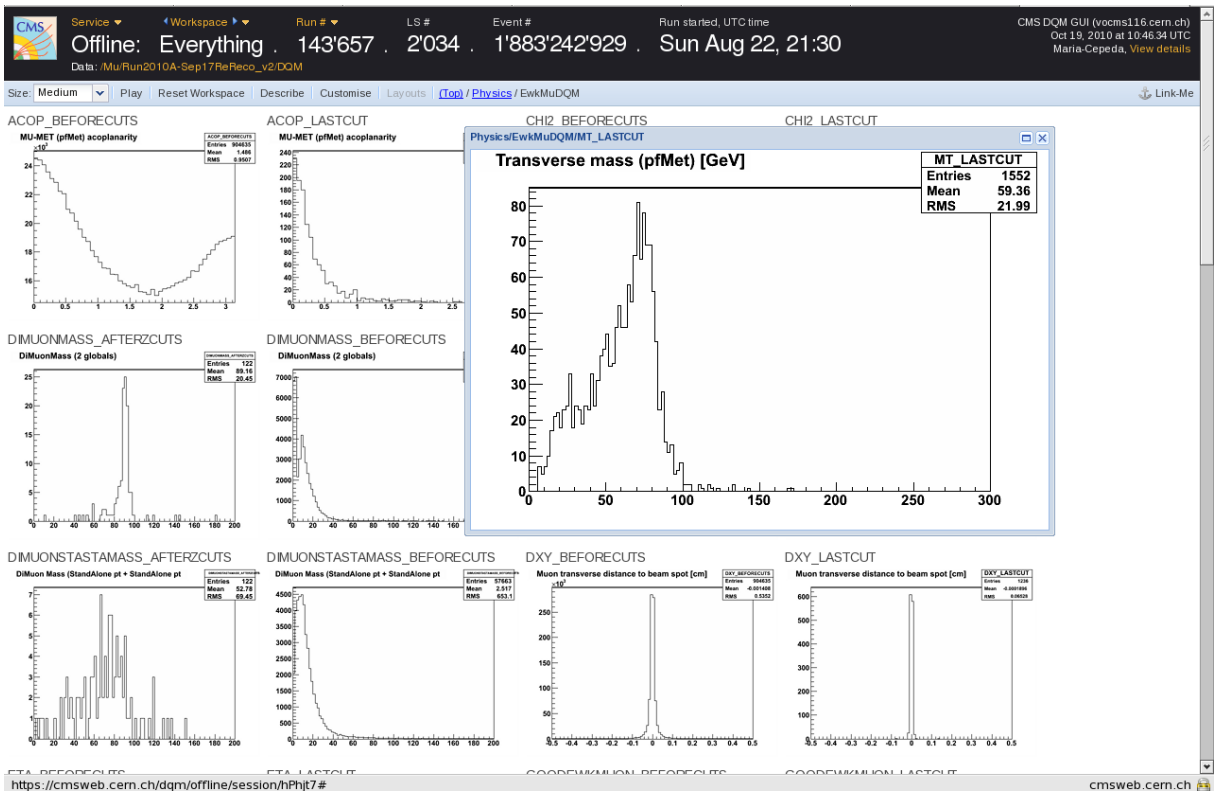

Figure A.5: Screenshot of the Data Quality Monitoring module for ElectroWeak-Muon physics

per run, a simple counting can be performed in order to give an estimative measure of the integrated luminosity recorded. This counting is done based on the final distributions of the analysis, invariant mass for $Z \rightarrow \mu^+\mu^-$ candidates, and transverse mass for $W \rightarrow \mu\nu$ candidates.

A screenshot of the web interface of one of the monitoring modules is shown on Figure A.2.1.

A.3 Summer 2010

The first measurement of the W crosssection by CMS was made public at the ICHEP conference, in Paris, for an integrated luminosity of $L_{int} = 198$ nb^{-1}.

The selection criteria applied and basic analysis strategy are basically identical to the one showed in this thesis.

The most important difference is given by the small amount of Z candidates available for systematic uncertainty calculation and signal modelling. This implied that not only part of the efficiencies had to be calculated using inclusive muons instead of tag-and-probe techniques, but also signal was modelled directly from Monte Carlo.

Lepton reconstruction, identification, online selection and isolation efficiencies were calculated using clean Z → ℓℓ data samples as well as random cone techniques for isolation efficiencies, and inclusive muon studies for identification and trigger efficiencies.

Lepton energy/momentum scale and resolution have been studied using the position and width of reconstructed resonances in data (Z, J/Ψ, Υ) as well as cosmic muons.

$\overrightarrow{E_T}^{miss}$ scale and resolution uncertainties effects were estimated from the recoil distribution against leptons in W events.

Finally, again due to the smaller size of the data sample, QCD was modelled directly from the M_T shape of the anti-isolated sample. Background subtraction uncertainty has been conservatively assigned to the difference in the fit between the modelling of QCD in each channel and the true Monte Carlo prediction.

The final M_T spectra for W bosons and $M_{\mu\mu}$ spectra for Z bosons is show in Figure A.6.

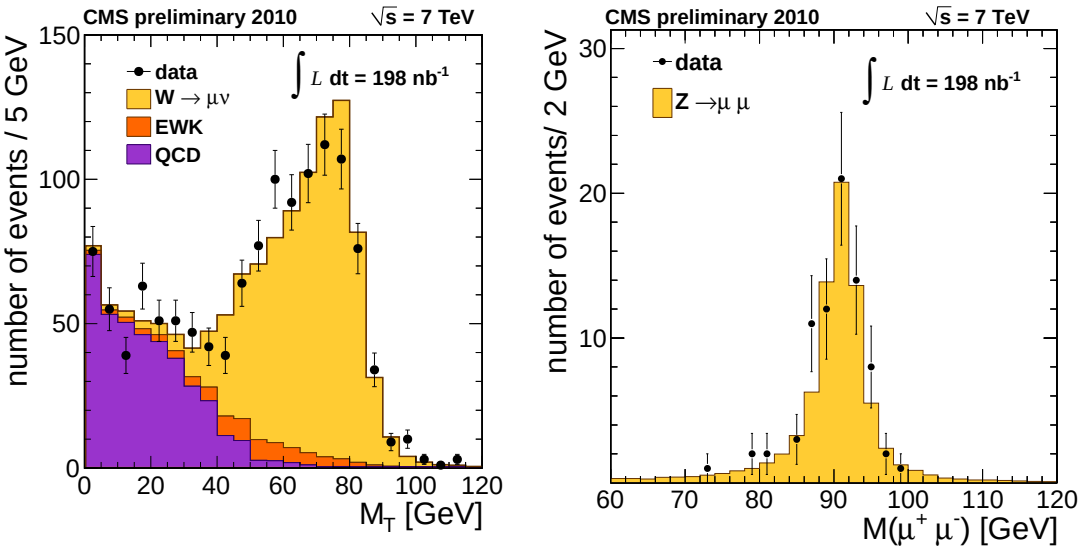

Figure A.6: W → ℓν (left) and Z → ℓℓ (right) distributions. Experimental distributions (points) are compared to the predictions for signal and background components, normalised to the theoretical cross-sections in the Z channel and to the fitted cross-sections for the W channel.

The measured signal yields were $N(\mathrm{W}^+ \to \mu^+\nu) = 529 \pm 24$, $N(\mathrm{W}^- \to \mu^-\bar{\nu}) = 289 \pm 13$, and $N(\mathrm{Z} \to \mu^+\mu^-) = 77$. Cross-sections are calculated from these yields correcting by the lepton selection efficiencies and the acceptance of the phase space used, computed using POWHEG.

This first measurement of production cross-section of W and $Z(\gamma^*)$ bosons and their ratios (combining muon and electron results) yielded

$$\begin{aligned}
\sigma(\mathrm{W} \to \ell\nu) &= 9.22 \pm 0.24(\text{stat.}) \pm 0.47(\text{syst.}) \pm 1.01(\text{lumi.}) \text{ nb.} \\
\sigma(\mathrm{W}^+ \to \ell^+\nu) &= 5.50 \pm 0.18(\text{stat.}) \pm 0.29(\text{syst.}) \pm 0.61(\text{lumi.}) \text{ nb.} \\
\sigma(\mathrm{W}^- \to \ell^-\bar{\nu}) &= 3.60 \pm 0.13(\text{stat.}) \pm 0.19(\text{syst.}) \pm 0.40(\text{lumi.}) \text{ nb.} \\
\sigma(\mathrm{Z} \to \ell\ell) &= 0.882^{+0.077}_{-0.073}(\text{stat.})^{+0.042}_{-0.036}(\text{syst.}) \pm 0.097(\text{lumi.}) \text{ nb..} \\
\sigma(\mathrm{W} \to \ell\nu)/\sigma(\mathrm{Z} \to \ell\ell) &= 10.46^{+0.99}_{-0.88}(\text{stat.})^{+0.65}_{-0.56}(\text{syst.}). \\
\sigma(\mathrm{W}^+ \to \ell^+\nu)/\sigma(\mathrm{W}^- \to \ell^-\bar{\nu}) &= 1.51^{+0.08}_{-0.07}(\text{stat.}) \pm 0.04(\text{syst.}).
\end{aligned}$$

These values are in perfect agreement with the result presented in this thesis, taking into account the much larger statistical uncertainties involved in the measurement.

Appendix B

Results with track-corrected E_T^{miss}

The analysis shown in this thesis has been performed using the baseline E_T^{miss} algorithm for Electro Weak studies in CMS, particle-flow E_T^{miss}.

As shown in Section 5.3, this is not the only E_T^{miss} algorithm that can be used in analysis. In fact, the performance and resolution of the "track corrected E_T^{miss}" (tcMet) algorithm is basically equivalent.

Therefore, as a consistency check the analysis has been repeated with this alternative reconstruction algorithm.

The templates for signal and background developed in Chapter 6, the cross-section results obtained in Chapter 7, and the experimental distributions shown in Chapter 8, are repeated in in this Appendix.

B.1 Signal Templates

In Section 5.3, the procedure to obtain a signal template that combines Monte Carlo resolution for the description of the kinematic of a W boson and the reconstruction of muons with a realistic detector description of the E_T^{miss} reconstruction was developed.

This study was shown using particle-flow in order to describe E_T^{miss} reconstruction. The method is transparent to the kind of E_T^{miss} used, and the conclusions and results obtained using track-corrected E_T^{miss} are equivalent.

Figure B.1 compares Monte Carlo expectations and the template obtained from $Z \rightarrow \mu^+\mu^-$. The broadening of the E_T^{miss} and M_T distributions observed in data (see Chapter 5) is well reproduced by the template. In the linear plot we can see how there is a clear broadening of

the shapes in data, due to a worsening of met scale and resolution with respect to Monte Carlo predictions. In the logarithmic plot we can see how the tails agree, although this part of the distribution will have virtually no effect on the cross-section measurement

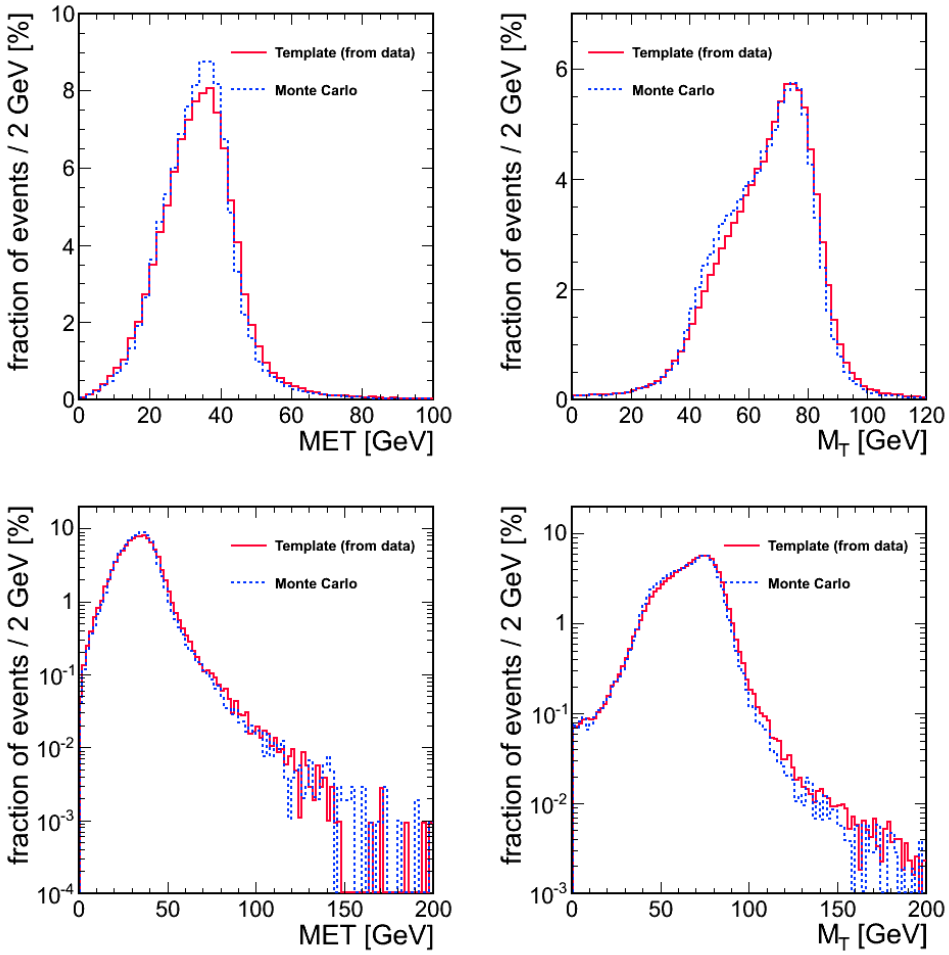

Figure B.1: Linear and logarithmic E_T^{miss} (left) and M_T (right) shape comparison. W Monte Carlo (POWHEG) in blue and the template from a $Z \rightarrow \mu^+\mu^-$ data-sample in red, using track-corrected E_T^{miss}.

The comparison of the resolution observed in data and in Monte Carlo can be also repeated using this E_T^{miss} reconstruction algorithm. A similar plot to Figure 6.15 but using track-corrected E_T^{miss} is shown in B.2.

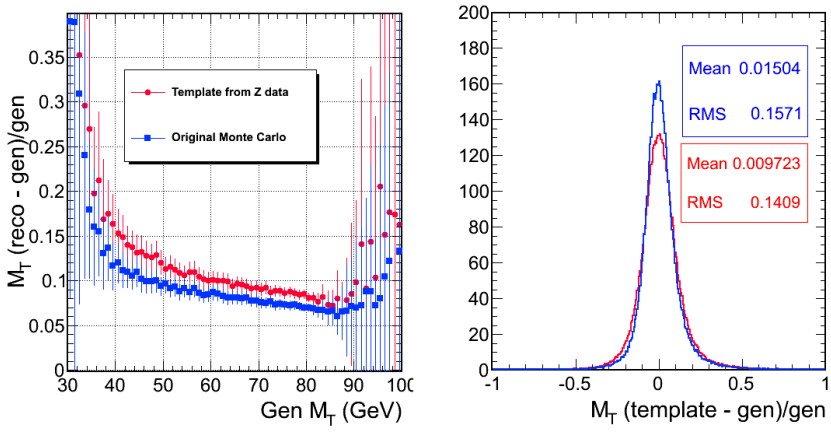

Figure B.2: Estimation of the $\sigma(M_T)$ resolution versus generated transverse mass (top), computed through the width of the distribution in an event by event basis. In blue, from the original Monte Carlo information and in red, from the described sampled template in data. Track-corrected E_T^{miss} used to describe the missing energy of the event and related variables.

B.2 QCD Templates

A template for the E_T^{miss} / M_T QCD background distributions using tcMet can be obtained using the same procedure as the one one shown in Chapter for particle flow. The mathematical formulation of the correction is equivalent, although the α (Table B.1) depends on the E_T^{miss} algorithm used.

$$E_T^{miss}(cor) = E_T^{miss}/(1 + \alpha \times I_{comb}^{rel})$$

$$M_T(cor) = \begin{cases} \sqrt{2p_T E_T^{miss}(cor) * (1 + \cos(acop))} & \text{if } acop < 2.0 \\ \sqrt{2p_T E_T^{miss} * (1 + \cos(acop))} & \text{if } acop > 2.0 \end{cases}$$

E_T^{miss}	Data	MC
pfMet	$\alpha = 0.19 \pm 0.02$	$\alpha = 0.24 \pm 0.02$
tcMet	$\alpha = 0.21 \pm 0.02$	$\alpha = 0.26 \pm 0.02$

Table B.1: Correction values on data and on Monte Carlo.

Once again these corrected distributions are intermediate between the Monte Carlo prediction and the experimental distributions for non-isolated ($I_{comb}^{rel} > 0.20$) events, as shown in

Figure B.3. The left panel shows the fitted slope of the mean of the E_T^{miss} distribution versus isolation (red) and the slope of the mean (black) and width (green) of Gaussian fits to the E_T^{miss} distribution versus isolation (black). The three slopes agree on a $\alpha = 0.21 \pm 0.02$ correction. This values are used to correct E_T^{miss}. The right pannel shows the mean and width of the M_T distribution after the correction to E_T^{miss} has been applied, showing an almost linear behaviour versus isolation. In Figure B.4 the resulting E_T^{miss} (left) and M_T (right) distributions are shown, in linear and logarithmic scale. The Monte Carlo predictions for the isolated distribution (black triangles) and the anti-isolated distribution in data (pink squares) are compared to the corrected anti-isolated distribution (blue squared). We see how the corrected template is in between the Monte Carlo prediction and the plain inversion template. Bottom left shows the mean and width of the M_T distribution after the correction to E_T^{miss} has been applied, showing an almost linear behaviour versus isolation.

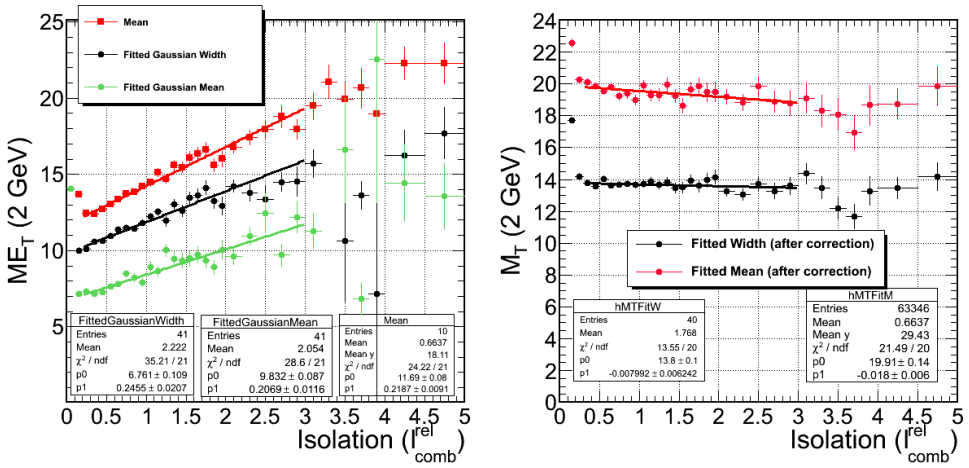

Figure B.3: Method applied on data to particle-flow E_T^{miss}. Left shows the fitted slopes used to obtain the correction. Right shows the mean and width of the M_T distribution after the correction to E_T^{miss} has been applied.

B.3 Cross-Section Results

The signal extraction procedure described in Section 7.1.2 is applied here to the experimental tcMET M_T distribution. Since none of the selection criteria applied make use of any E_T^{miss} related variable, the acceptance and efficiency factors necessary for the measurement are the same as those given in Chapter 7. The measured cross-sections, ratios and QCD normalisation

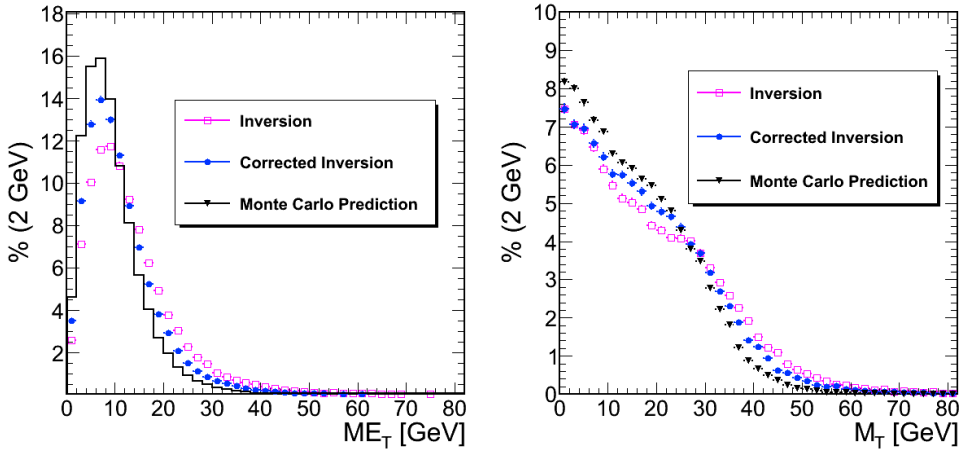

Figure B.4: Comparison of Monte Carlo predictions with the templates, for E_T^{miss} (left) and M_T (right).

are therefore:

$$\begin{aligned}
\sigma(\mathrm{pp} \to \mathrm{W}^{\pm} + X) \times BR(\mathrm{W}^{\pm} \to \mu^{\pm}\nu) &= 9.95 \pm 0.09(\mathrm{stat.})\ \mathrm{nb}, \\
\sigma(\mathrm{pp} \to \mathrm{W}^{+} + X) \times BR(\mathrm{W}^{+} \to \mu^{+}\nu) &= 5.85 \pm 0.07(\mathrm{stat.})\ \mathrm{nb}, \\
\sigma(\mathrm{pp} \to \mathrm{W}^{-} + X) \times BR(\mathrm{W}^{-} \to \mu^{-}\bar{\nu}) &= 4.11 \pm 0.06(\mathrm{stat.})\ \mathrm{nb}, \\
\frac{\sigma(\mathrm{pp} \to \mathrm{W}^{+} + X) \times BR(\mathrm{W}^{+} \to \mu^{+}\nu)}{\sigma(\mathrm{pp} \to \mathrm{W}^{-} + X) \times BR(\mathrm{W}^{-} \to \mu^{-}\bar{\nu})} &= 1.42 \pm 0.03(\mathrm{stat.}) \\
f_{QCD} &= 864 \pm 14(\mathrm{stat.})
\end{aligned}$$

Results using track-corrected E_T^{miss} and particle-flow E_T^{miss} are compatible within systematical uncertainties. The difference in total cross-section is of 0.2%, in the negative and positive charged cross-sections of 0.5% and $< 0.1\%$, and in the ratio of 0.7%. These differences are therefore covered by the signal and background shape uncertainties calculated for each measurement.

The result of performing the fit over the experimental distribution is shown in Figure B.5. The template shapes used for each one of the physical processes involved are shown, together with the final fit result. Data agrees well with the fitted shape over the full range of M_T, with small discrepancies in the tails, due to the lack of statistics available.

The yields for the different processes involved in the full M_T range are shown in Table B.2.

The systematic study for the treatment of the signal and background shape in the analysis presented in Sections 7.2.3 and 7.2.4.

Table B.2: Total, negative and positive yields for each one of the physical processes involved in the fit.

	$W \to \mu\nu$	$W^+ \to \mu^+\nu$	$W^- \to \mu^-\bar{\nu}$
Observed Candidates	18571	10682	7889
$W \to \mu\nu$ yield	12289 ± 111	7437 ± 86	4854 ± 69
QCD yield	4975 ± 80	2488 ± 40	2488 ± 40
$Z \to \mu^+\mu^-$ yield	573 ± 24	297 ± 17	276 ± 17
$W \to \tau\nu$ yield	570 ± 24	342 ± 18	228 ± 15
$Z \to \tau^+\tau^-$ yield	99 ± 10	52 ± 7	48 ± 7
$t\bar{t}$ yield	49 ± 7	24 ± 5	24 ± 5
WW, WZ, ZZ	15 ± 4	8 ± 2	7 ± 2
Fitted Result	18574 ± 142	10648 ± 98	7925 ± 83

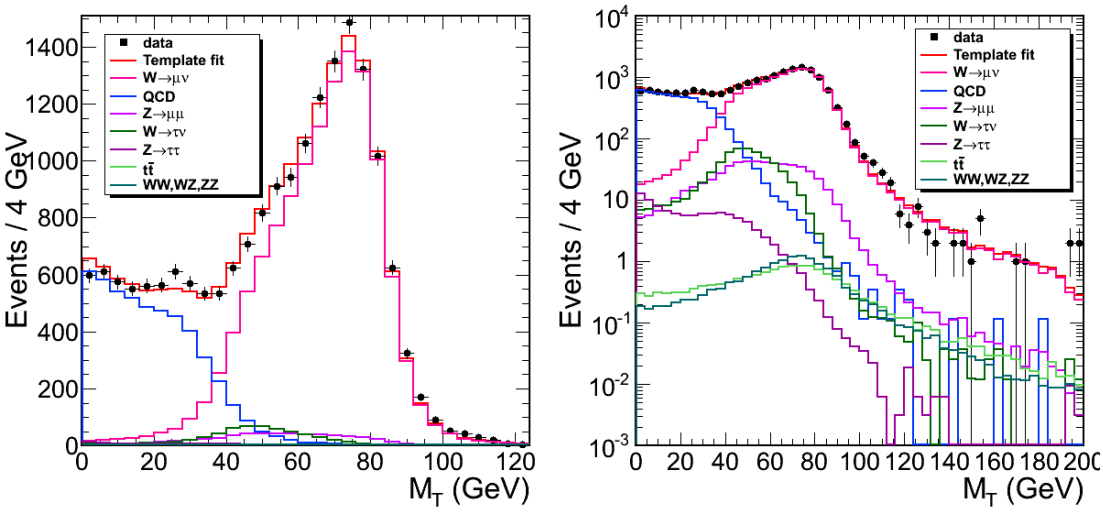

Figure B.5: Final fit using track-corrected E_T^{miss}, showing individual background contributions. Linear and logarithmic scales.

Comparing the results obtained fitting with the signal template or with the original Monte Carlo shape we can obtain an upper limit on the impact of the signal shape (E_T^{miss} scale and resolution) on the result. This effect is of 0.4% on the three measured cross-sections.

Comparing the results obtained fitting with Monte Carlo as opposed to using a template for QCD background we obtain an upper limit of the systematic error on QCD modelling, 2% for the total spectrum, 1.5% for positive Ws and 2.4% for negative Ws (this includes a check on the charge symmetry of this background contribution). The effect on the ratio is measured to be of 0.7%. We still observe that all the results are compatible (and in fact very close) to the equivalent Table shown for particle flow E_T^{miss} in Chapter 7 taking into account systematic uncertainties.

Table B.3: Systematic study on background and signal shape, comparing the results obtained with different template shapes for signal (with and without E_T^{miss} modelling) and QCD background (Monte Carlo predicted shape, M_T distribution for the anti-isolated sample, and corrected M_T distribution). The results are shown floating one and two parameters for QCD background normalisation in order to measure the impact of charge asymmetries in this background. These results have been computed using track-corrected E_T^{miss} reconstruction.

tcMet	QCD	MonteCarlo	Inverted Isolation	Corrected Template
Symm.	MC Signal	$\sigma_W = 10.09 \pm 0.09$ nb $\sigma_{W^+} = 5.90 \pm 0.07$ nb $\sigma_{W^-} = 4.19 \pm 0.06$ nb $R = 1.41 \pm 0.03$	$\sigma_W = 9.72 \pm 0.09$ nb $\sigma_{W^+} = 5.72 \pm 0.07$ nb $\sigma_{W^-} = 4.01 \pm 0.06$ nb $R = 1.43 \pm 0.03$	$\sigma_W = 9.90 \pm 0.09$ nb $\sigma_{W^+} = 5.80 \pm 0.07$ nb $\sigma_{W^-} = 4.09 \pm 0.06$ nb $R = 1.42 \pm 0.03$
QCD	Template Signal	$\sigma_W = 10.14 \pm 0.09$ nb $\sigma_{W^+} = 5.93 \pm 0.07$ nb $\sigma_{W^-} = 4.21 \pm 0.06$ nb $R = 1.41 \pm 0.03$	$\sigma_W = 9.77 \pm 0.09$ nb $\sigma_{W^+} = 5.75 \pm 0.07$ nb $\sigma_{W^-} = 4.03 \pm 0.06$ nb $R = 1.43 \pm 0.03$	$\sigma_W = 9.95 \pm 0.09$ nb $\sigma_{W^+} = 5.84 \pm 0.07$ nb $\sigma_{W^-} = 4.11 \pm 0.06$ nb $R = 1.42 \pm 0.03$
Assym.	MC Signal	$\sigma_W = 10.09 \pm 0.09$ nb $\sigma_{W^+} = 5.86 \pm 0.07$ nb $\sigma_{W^-} = 4.20 \pm 0.06$ nb $R = 1.40 \pm 0.03$	$\sigma_W = 9.72 \pm 0.09$ nb $\sigma_{W^+} = 5.70 \pm 0.07$ nb $\sigma_{W^-} = 4.02 \pm 0.06$ nb $R = 1.42 \pm 0.03$	$\sigma_W = 9.89 \pm 0.09$ nb $\sigma_{W^+} = 5.79 \pm 0.07$ nb $\sigma_{W^-} = 4.01 \pm 0.06$ nb $R = 1.42 \pm 0.03$
QCD	Template Signal	$\sigma_W = 10.14 \pm 0.09$ nb $\sigma_{W^+} = 5.92 \pm 0.07$ nb $\sigma_{W^-} = 4.21 \pm 0.06$ nb $R = 1.41 \pm 0.03$	$\sigma_W = 9.77 \pm 0.09$ nb $\sigma_{W^+} = 5.73 \pm 0.07$ nb $\sigma_{W^-} = 4.04 \pm 0.06$ nb $R = 1.42 \pm 0.03$	$\sigma_W = 9.94 \pm 0.09$ nb $\sigma_{W^+} = 5.82 \pm 0.07$ nb $\sigma_{W^-} = 4.12 \pm 0.06$ nb $R = 1.41 \pm 0.03$

B.4 Experimental Distributions

The experimental transverse mass distribution, M_T, is again displayed in Figure B.6, together with the fitted contributions of the different processes. The total W, W^+ and W^- distribution are shown in linear and logarithmic scale. The agreement between data and the fitted templates for signal and backgrounds is remarkably good, with only some small discrepancies at ≈ 30 GeV. This discrepancy in the overlap region between signal and background was already observed in the particle flow fit, although in a less noticeable way.

The missing transverse energy distribution is shown in Figure B.7, for the full spectra (without charge separation), both for the full M_T spectra and only for those candidates with a reconstructed transverse mass larger than $M_T > 50$ GeV. E_T^{miss} is corrected using the same templates applied to the M_T fit. The agreement data-MC is again excellent, with only some discrepancies in the tails due to the low statistics available for template modelling. We can again see how after the requirement in M_T the result is practically background-free, and the distributions correspond almost solely to the neutrino transverse momentum.

Finally, the reconstructed p_T of the W boson is shown in Figure B.8, using templates to describe signal and background, for events with $M_T > 50$ GeV. In this case some differences between the data and the expected distribution can be observed. The explanation is identical to the one given for the particle flow plot, in Figure 8.6.

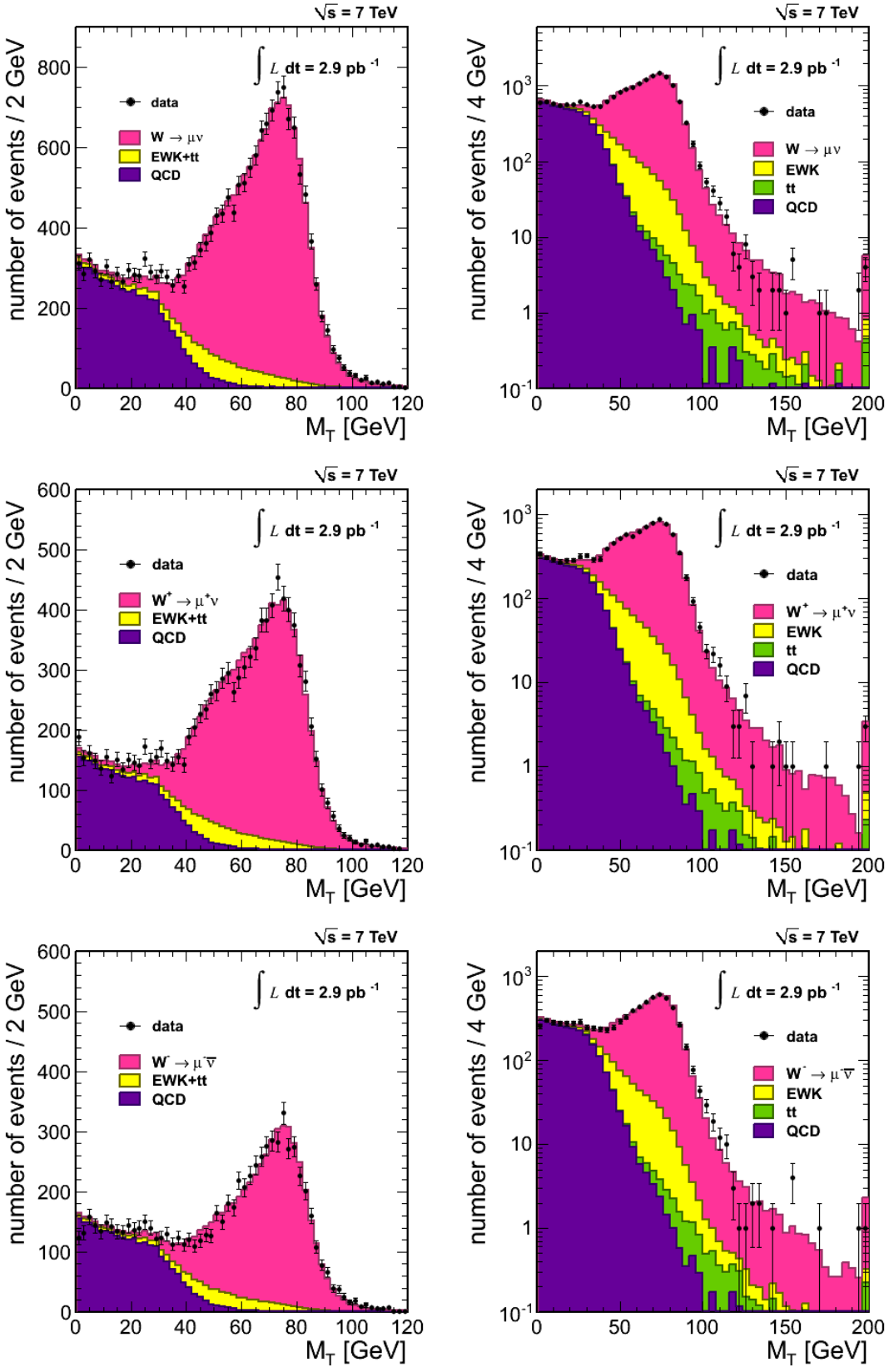

Figure B.6: Fitted M_T distributions, in linear and logarithmic scale. Top: Full distribution, Centre: W^+ fit, Bottom: W^-.

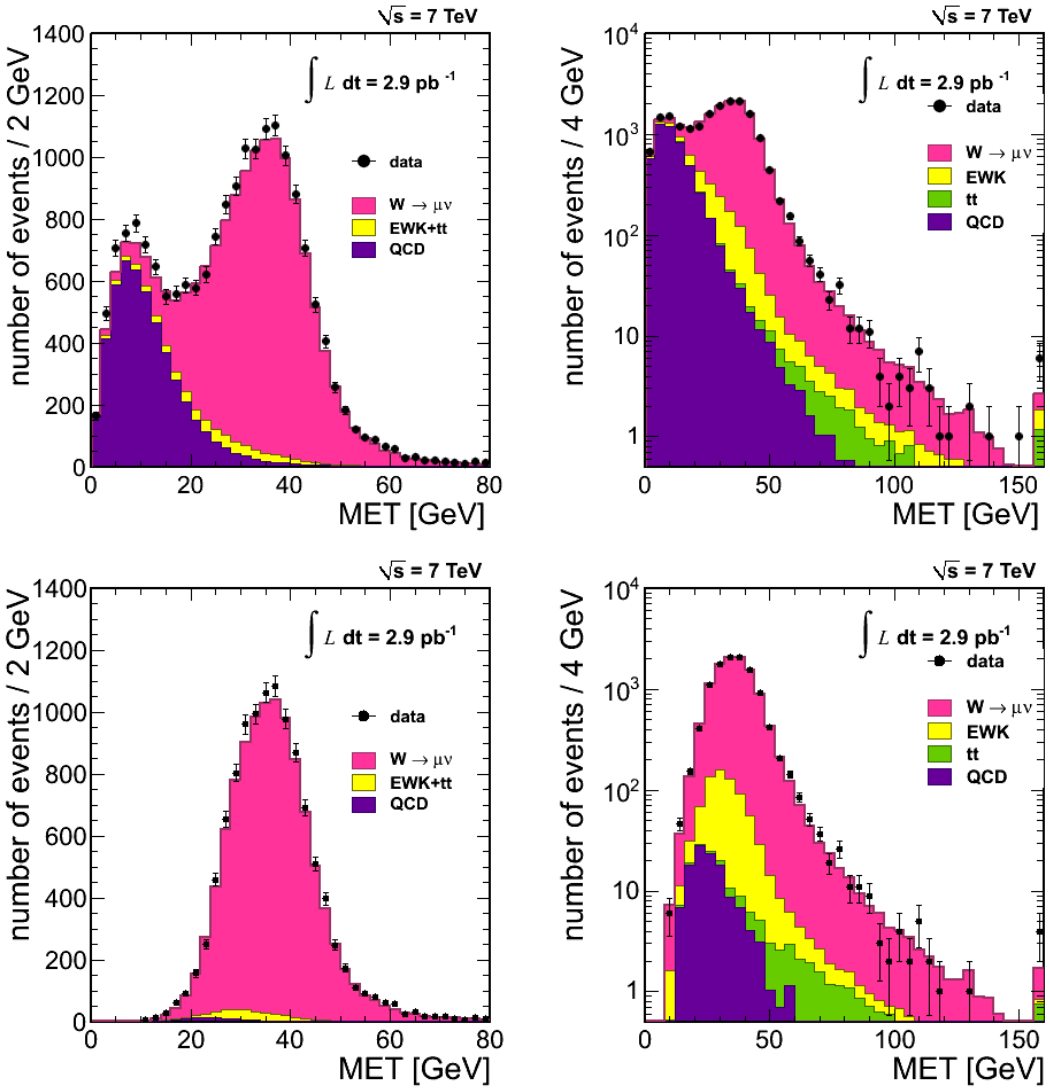

Figure B.7: E_T^{miss} distributions, in linear and logarithmic scale, using the fitted values. Top: Full distribution, Bottom: after a cut in $M_T > 50$ GeV.

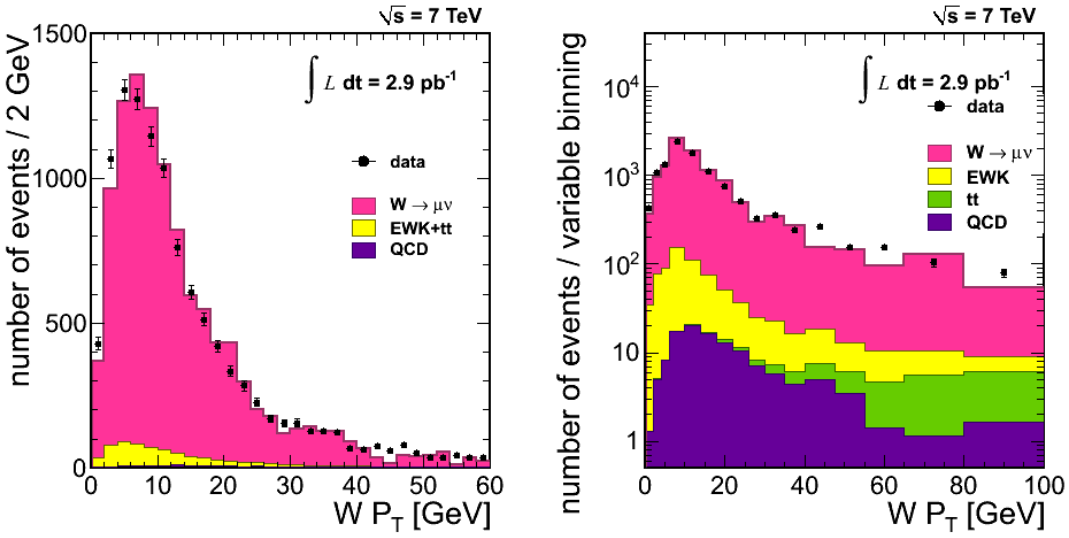

Figure B.8: $p_T(W)$ distribution after a cut in $M_T > 50$ GeV.

Appendix C

Medida de la sección eficaz de producción del bosón W en colisiones protón-protón a $\sqrt{s} = 7$ TeV

En esta tesis se presenta la primera medida de la sección eficaz de producción del bosón W en colisiones protón-protón, a una energía en centro de masas de 7 TeV. La medida ha sido realizada con los datos recogidos por el experimento CMS del LHC.

El acuerdo obtenido con las últimas predicciones teóricas de la sección eficaz, y con otros resultados experimentales, es excelente.

Esta medida no sólo constituye la primera medida de precisión electrodébil en la escala del TeV, sino que es la mejor prueba del buen funcionamiento del experimento y del acelerador ya en sus primeros meses de toma de datos, garantizando la calidad de sus resultados científicos futuros.

C.1 Física Electro-débil en el LHC

El Modelo Estándar de la física de partículas e interacciones es una teoría gauge renormalizable, que describe las interacciones fuertes, débiles y electromagnéticas bajo el grupo de simetría $SU(3) \times SU(2) \times SU(1)$.

Los experimentos llevados a cabo en los aceleradores LEP (*Large Electron Positron machine*) del CERN (1990-2001) y Tevatron de Fermilab (en funcionamiento desde 1988) han permitido

confirmar su validez hasta energías del orden de $\sim 10^2$ GeV (escala electro-débil), llegando a un nivel de precisión del 0.1% o mejor.

Sin embargo, el ME no consigue explicar ciertas observaciones experimentales, como pueden ser las asimetrías materia-antimateria, las oscilaciones de neutrinos o la violación de CP. Por ello hoy se le considera una teoría efectiva de otra más fundamental, comprobada experimentalmente hasta el rango de energías accesibles hasta la fecha.

El objetivo del LHC será alcanzar y explorar esta escala, cubriendo todo el rango de energías hasta 5-6 TeV. Con sus experimentos se espera encontrar la respuesta a muchas de las preguntas actuales de la física de partículas, empezando por el mecanismo de rotura de símetría electro-débil, que en el Modelo Estándar se explica gracias a un campo escalar conocido como "campo de Higgs". La determinación de la existencia del bosón de Higgs es por tanto uno de los objetivos prioritarios del LHC, que lo buscará en todo el rango de masas permitido teóricamente para la partícula. De ésta forma o bien su existencia (y masa) o bien su inexistencia quedará definitivamente establecida.

En este proceso hacia el descubrimiento, el papel de las medidas de precisión electrodébiles es crucial para verificar la validez del modelo en el nuevo rango energético, y para comprobar experimentalmente el funcionamiento del detector.

Las desintegraciones leptónicas de los bosones W y Z estuvieron entre las primeras señales físicas detectadas por el LHC en 2010. Estos procesos se caracterizan por su sección eficaz de produccion relativamente alta, por la precisión alcanzada en las predicciones teóricas asociadas a ésta, y por la limpieza y claridad de sus señales experimentales. Por ello son herramientas insustituibles no sólo para calibrar el detector y calcular eficiencias de detección e identificación, sino también para aportar las primeras medidas Electro-débiles de precisión en el LHC. Sólo tras esta primera comprobación de la validez del ME se puede abrir el camino hacia la búsqueda de física más allá de sus límites actuales.

Los bosones vectoriales W y Z son las partículas elementales encargadas de mediar en las interacciones débiles. Son, a excepción del quark top y el bosón de Higgs, las más masivas de las partículas elementales descubiertas a día de hoy ($M_W = 80.4$ GeV y $M_Z = 91.2$ GeV). Se diferencian por su carga eléctrica, ± 1 para el bosón W^+ y su anti-partícula el W^- y 0 para el Z.

Principalmente se desintegran produciendo hadrones (que experimentalmente se detectan como jets). Sin embargo, estos canales, pese a constituir casi un 70% de las desintegraciones de los bosones W y Z, son mucho más dificiles de estudiar experimentalmente que los canales de desintegración en leptones. Los modos de desintegración leptónica del bosoón W tienen representan un $BR(e,\nu_e) = BR(\mu,\nu_\mu) = BR(\tau,\nu_\tau) = 10.80 \pm 0.09\%$ del total, mientras que para el bosón Zs la fracción es menor, un $BR(l^-,l^+) = (3.3658 \pm 0.0023)\%$ [4]. Aunque menos abundantes, la signatura experimental de las desintegraciones muónicas y electrónicas de Ws y Zs ($\sigma(\mathrm{pp} \to \mathrm{W}^\pm + X) \times BR(\mathrm{W}^\pm \to l^\pm\nu)$, $\sigma(\mathrm{pp} \to \mathrm{Z} + X) \times BR(\mathrm{Z} \to \ell\ell)$) (uno o dos muones o electrones de alto momento) las convertirán en un canal estrella tanto de medida física como de calibración de los detectores.

En el LHC, funcionando en condiciones de diseño ($\sqrt{s} = 14$ TeV, alta luminosidad), se producirán más de 100 bosones vectoriales por segundo. Sin un conocimiento preciso de los mecanismos de producción de W y Zs, sus secciones eficaces y distribuciones cinemáticas no es posible abordar gran parte de los descubrimientos en el programa científico del LHC. Por ejemplo, la producción de dibosones es un fondo residual irreducible para muchas de las búsquedas del Higgs del modelo estándar y la producción de bosones vectoriales acompañados por jets tiene la misma signatura experimental que la desintegración de nuevas partículas supersimétricas pero una sección eficaz de producción órdenes de magnitud mayor.

El primer paso en la caracterización de la producción de bosones vectoriales es por lo tanto la medida de las secciones eficaces de producción en el canal leptónico, el tema de esta tesis.

Los bosones W son producidos en las colisiones protón-protón del LHC por interacción entre partones, los constituyentes de los protones. Pueden ser tanto los quarks de partida de los que está formado el protón (uud) como gluones radiados, u otros quarks producidos por dichos gluones. Por lo tanto, todas las posibles interacciones entre quarks y antiquarks tienen lugar, aunque en distinta proporción. En el LHC el diagrama dominante para la producción de W^+ es el $u\bar{d}$ y para W^- el $d\bar{u}$.

La sección eficaz total vendrá dada por la convolución de la función de estructura interna de los protones en una escala de energías Q (que nos dará la probabilidad de encontrar un partón en concreto con una determinada fracción de momento x_1), y la sección eficaz de interacción

entre dos quarks (σ_{ab}) a esa energía [31].

$$\sigma_{pp\to VX} = \sum_{a,b} \int dx_1 dx_2 f_a(x_1, Q^2) f_b(x_2, Q^2) \sigma_{ab\to VX}(x_1, x_2, Q^2, \alpha_S(Q))$$

La sección eficaz partónica se puede calcular teóricamente con gran precisión, hasta segundo orden en teoría de perturbaciones (NNLO, "next-to, next-to leading order").

La parametrización de la estructura interna del protón, dada por las funciones de densidad partónica (*PDFs*, "parton density functions") son calculadas por distintos grupos teóricos, como CTEQ o MSTW a partir de ajustes a datos de experimentos anteriores. La información de la estructura interna se parametriza a una determinada escala Q_0 y se hace evolucionar hasta otra escala Q utilizando las ecuaciones de Altarelli-Parisi [33].

Combinando esta información se obtienen distintas predicciones teóricas de la sección eficaz de producción de $\sigma(\mathrm{pp} \to \mathrm{W}^{\pm} + X) \times BR(\mathrm{W}^{\pm} \to \mu^{\pm}\nu)$, dependiendo de la parametrización concreta escogida para las PDFs. Las distintas predicciones tienen una incertidumbre sistemática asociada en torno a un $\approx 4\%$, y los valores centrales de los mismos se diferencian entre sí en menos que esta incertidumbre total.

Como ejemplo, la Figura C.1 muestra la comparación entre la sección eficaz de producción de W^+ y W^-, y de W total y Z^0, calculada por el grupo MSTW [9]. En esta gráfica se puede ver cómo la sección eficaz de producción de W^+ es en torno a 1.4 veces la de W^- (por el diferente contenido en quark u y quarks d del protón), y la producción de Zs es unas 10 veces menor que la producción de Ws, todo ello para una energía en centro de masas de 7 TeV. Las predicciones teóricas de distintos grupos (CTEQ, MSTW, NNPDF), cada uno con una parametrizaciones independiente de la estructura interna del protón, se encuentran en buen acuerdo entre si tanto para las secciones eficaces de producción como para el cociente de estas ($\sigma(W)/\sigma(Z)$ y $\sigma(W^+)/\sigma(W^-)$).

La referencia usada en esta tesis es la estándar de CMS. Está calculada a NNLO usando el programa FEWZ [44; 45], y las ya citadas PDFs a NNLO de MSTW [9]. El cálculo de errores asociado sigue las recomendaciones del grupo de trabajo de PDFs para el LHC (PDF4LHC, [39]), y están calculados al 68% de confianza usando las parametrizaciones de los grupos MSTW08 [9], CTEQ66 [40] y NNPDF2.0 [41] a NLO, añadiendo las incertidumbres de escala de NNLO en cuadratura. Estas referencias se resumen en la Tabla C.1 [46]i.

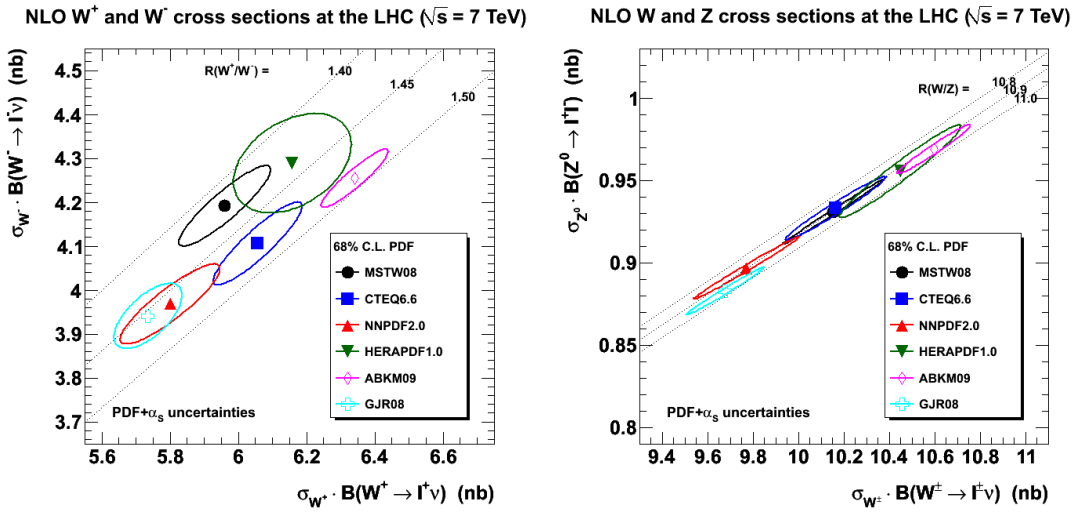

Figure C.1: Predicciones teóricas para la sección eficaz inclusiva de $W^{\pm}$ y Z en el LHC, con una energía en centro de masas del sistema de 7 TeV, calculadas por el grupo MSTW [9; 43].

Bosón	Sección eficaz de producción
$Z/\gamma*$ ($M_{\mu\mu} > 20$ GeV)	0.97 ± 0.04 nb
W^+	6.15 ± 0.29 nb
W^-	4.29 ± 0.23 nb
W	10.44 ± 0.52 nb

Table C.1: Predicciones teóricas de la sección eficaz para $\sigma(\mathrm{pp} \to \mathrm{W}^{\pm} + X) \times BR(\mathrm{W}^{\pm} \to \mu^{\pm}\nu)$ y $\sigma(\mathrm{pp} \to \mathrm{Z} + X) \times BR(\mathrm{Z} \to \mu^{+}\mu^{-})$ a 7 TeV, usada como referencia en CMS

C.2 El LHC y el experimento CMS

El LHC está situado en el antiguo túnel de LEP, un anillo de 26.6 km de circunferencia en la frontera entre Francia y Suiza. Es un colisionador protón-protón, formado por dos anillos independientes pero inmersos en un campo magnético y sistema criogénico común, por los que circulan los dos haces de protones en sentidos opuestos (y durante breves periodos haces de iones plomo).

El LHC está diseñado para funcionar a una energía en centro de masas de 14 TeV, lo que permite alcanzar energías del orden de 1 TeV para cada partón (quark o gluón) que entra en la colisión. Debido a ello, el LHC permitirá sobrepasar los límites actuales del Modelo Estandar, ya que se espera encontrar indicios de física más allá de sus límites a esta escala de energías.

Dado que la sección eficaz de los fenónemos que deseamos observar es muy baja, para garantizar su observación se ha buscado que el número de colisiones por segundo sea lo mayor posible.

C. MEDIDA DE LA SECCIÓN EFICAZ DE PRODUCCIÓN DEL BOSÓN W EN COLISIONES PROTÓN-PROTÓN A $\sqrt{S} = 7$ TEV

El número de colisiones que se producen por unidad de tiempo y de área en un colisionador viene dada por un parámetro conocido como *luminosidad* ($\mathcal{L}$). De este modo, para cualquier proceso con sección eficaz de producción σ_{prod}, se tiene que el número de sucesos producidos para un tiempo t de funcionamiento del acelerador será

$$N_{sucesos_{pp\to X}} = \sigma_{prod}(pp \to X) \int \mathcal{L}\ dt$$

El LHC alcanzará una luminosidad de 10^{34} cm^{-2}s^{-1} a pleno rendimiento, superando en un factor 100 el valor máximo alcanzado hasta la fecha en otros aceleradores.

Los haces son acelerados en todo el complejo de aceleradores del CERN antes de ser inyectados al túnel del LHC a una energía de 450 GeV. La red magnética del LHC cuenta con más de 6000 imanes, entre ellos 1232 dipolos capaces de proporcionar un campo magnético de 8,32 T.

Durante 2010, el LHC ha operado a una energía en centro de masas y luminosidad menores de las de diseño (7 TeV y $\mathcal{L} = 10^{32} cm^{-2} s^{-1}$). Durante los próximos dos años los haces se mantendrán a esta energía, con una subida gradual de la luminosidad instantánea. La máquina llegará a los valores nominales de energía y luminosidad después de una parada técnica en 2013.

Los dos haces de protones sólo se cruzan en cuatro puntos, los llamados "puntos de interacción", en los que están sitos los experimentos ALICE, ATLAS, CMS y LHCb. Dos de ellos (ATLAS y CMS), son experimentos multipropósito, con objetivos similares pero diferente diseño, y están situados diametralmente opuestos en el anillo. LHCb y ALICE son experimentos especializados en física de quarks b y estudios de iones pesados respectivamente, y están situados a ambos lados del experimento ATLAS. Otros dos experimentos de menor tamaño (TOTEM y LHC-f) se encuentran en el tunel, cerca de los dos grandes detectores multipropósito (TOTEM junto a CMS y LHC-f junto a ATLAS).

El "Compact Muon Solenoid" (CMS) [12] se basa, como su propio nombre indica, en un intenso campo magnético solenoidal, en cuyo interior se alojan los diversos subdetectores de los que está compuesto. Éstos se encuentran situados de forma concéntrica. Desde el punto de interacción, situado en el centro del cilindro, hasta el exterior se encuentran:

- El detector central de trazas (TK), que se encarga de medir con alta precisión el momento y la carga de las partículas cargadas generadas en la colisión. Está dividido en dos partes: un detector de píxeles de silicio y uno de bandas del mismo material.

- El calorímetro electromagnético (ECAL), que se encarga de detectar e identificar partículas con interacción electromagnética (fotones y electrones). Se trata de un calorímetro homogéneo, compuesto por cristales de $WPbO_4$.
- El calorímetro hadrónico (HCAL), que se encarga de la detección e identificación de cascadas hadrónicas. Es un calorímetro de muestreo de hierro y plástico centelleador.
- El imán solenoidal, que proporciona un campo magnético uniforme de 3.8 T en su interior, y de hasta 1.8 T en el hierro de retorno.
- El espectrómetro de muones, inserto en el hierro de retorno del imán y encargado de la detección e identificación de muones. Está compuesto por tres tipos de cámaras distintos: cámaras de deriva (DT) en la zona centrali o barril, cámaras de tiras catódicas (CSC) en las zonas laterales a pequeño ángulo respecto de la línea del haz, y cámaras de placas resistivas (RPC) en ambas zonas.

Longitudinalmente, en la dirección del haz, podemos dividir el detector en dos zonas: la central, conocida como Barril, y los discos de cierre a sus extremos o "Endcaps". En conjunto, tiene 21,6 m metros de longitud y 14 m de diámetro, y pesa 12000 toneladas.

CMS es un detector hermético y con buena cobertura angular, lo que asegura la detección y medida precisa de todas las partículas presentes en el estado final de una colisión protón-protón. El detector central mide la carga y el momento de toda partícula cargada creada en la colisión. Fotones y electrones son absorbidos en el calorímetro electromágnetico, dónde su energía es medida. El momento de los electrones es medido asimismo en el detector central de trazas, proporcionando una medida más precisa de éste, mientras que los fotones lo atraviesan sin dejar rastro. Los hadrones (cargados o neutros) llegan hasta el calorímetro hadrónico, donde son absorbidos en forma de cáscada. Finalmente sólo muones y neutrinos son capaces de atravesar el hierro del imán y llegar a la zona más externa del detector. Los primeros son identificados y medidos gracias a sus señales en las cámaras de muones. Los segundos no pueden ser medidos directamente, sólo inferidos a partir de la conservación de energía y momento de cada suceso.

La sección eficaz inelástica protón-protón en el LHC, en condiciones de diseño, superará los 100 mb. Esto supone que con las condiciones nominales del acelerador, en cada punto de interacción se producirán aproximadamente 10^9 colisiones por segundo, imposibles de procesar y almacenar con la tecnología actual. Esta altísima tasa de colisión contrasta con las mucho menores predichas para la producción de procesos físicos de interés científico como el Higgs o

partículas supersimétricas. Por tanto una parte imprescindible de CMS es su sistema de "filtrado" o *trigger*, encargado de seleccionar únicamente los sucesos potencialmente interesantes. De esta forma se consigue reducir el número de colisiones original a unos 10^2 sucesos por segundo, que son almacenados en disco para su posterior análisis.

C.3 Muones en CMS

El estudio del bosón W en su desintegración muónica requiere una buena compresión de los procesos de detección, identificación y reconstrucción de muones en CMS.

La redundancia del sistema de muones de CMS garantiza su detección. Son identificados inequívocamente gracias a las señales dejadas a su paso en los espectrómetros de muones (puesto que son la única partícula detectable capaz de llegar hasta ellos).

Al ser partículas cargadas se reconstruyen y miden como trazas tanto en el detector central de silicio como en las cámaras gaseosas de muones, en un proceso independiente. A continuación la información de ambos subdetectores se combina en una medida final de la trayectoria y momento del muón, alcanzando una gran precisión en su medida en un amplo rango de momento transverso.

La selección de muones en tiempo real durante la toma de datos (*trigger*) en 2010 ha ido evolucionando, de forma que el mínimo momento transverso requerido para que no haga falta aplicar ningun factor de preselección fue aumentando a medida que la luminosidad instantánea crecía. Finalmente, la selección con el umbral más bajo disponible para los datos analizados en esta tesis es la llamada "HLT_Mu9". El muón debe por tanto haber sido reconstruido por el sistema online (y haber sido detectado en dos de los sistemas de muones), tener un momento transverso al menos superior a $p_T > 9$ GeV y provenir de un candidato en el *trigger* de más bajo nivel (hardware) con $p_T > 7$ GeV.

La medida del momento de estos muones, en el rango de momentos estudiado en esta tesis, está dominado por la resolución del detector central de trazas. CMS garantiza una medida de momento con una precisión mejor que el 0.1% hasta los 10 GeV, y de 0.5% hasta los 100 GeV. Esta precisión ha sido comprobada tanto a partir de estudios realizados con muones cósmicos, como con las primeras resonancias dimuónicas producidas en las colisiones pprotón-protón (J/Ψ, Υ, Z^0).

Los muones provenientes de una desintegración de bosones W o Z se caracterizan por su alto momento (valores en torno a 30 o 40 GeV), y por provenir del vértice del suceso. Una vez que un muón ha sido reconstruido, se le exigen los siguientes criterios de calidad:

1. El muón debe ser reconstruido de forma independiente por dos algoritmos distintos, *Global Muon* (que comienza en la parte más externa del detector acercándose hasta el punto de interacción, combinando la información de las trazas reconstruidas en el detector central y en el espectrómetro de muones) y *Tracker Muon* (que comienza con la traza del detector central que se extrapola buscando segmentos coincidentes en las cámaras de muones). De esta forma se asegura una buena medida del momento, y se disminuye la presencia de contaminación de muones procedentes de desintegraciones en vuelo de hadrones o hadrones cargados que pudieran alcanzar el espectrómetro. El momento del muón vendrá dado por la traza reconstruida en el detector central.

2. El ajuste combinado (global) debe ser de buena calidad, expresada en términos de su χ ($\chi^2/\text{ndof} < 10$).

3. Para asegurar una buena determinación del momento y el parámetro de impacto de la traza reconstruida se exigen como mínimo 10 impactos en el detector central; y al menos uno de ellos en la parte más interna de éste, el detector de pixeles.

4. Por otra parte, se exige que el muón penetre profundamente en las cámaras de muones, cruzando al menos dos cámaras y dejando al menos un impacto utilizado en el ajuste final. De este modo se suprime el fondo de falsos muones, incapaces de adentrarse en el sistema de muones debido a sus pérdidas de energía en el hierro de retorno del imán.

5. La contaminación residual de muones cósmicos se elimina asegurando que el muón ha sido producido en una colisión, exigiendo para ello que su parámetro de impacto en el plano transverso sea menor que 2 mm.

Estas medidas garantizan la calidad de los muones reconstruidos, y eliminan la contribución de fondos instrumentales o muones mal reconstruidos. La eficiencia de reconstrucción e identificación de muones de alto momento es cercana al 100%.

La muestra de muones resultante está formada por una combinación de muones procedentes de procesos electrodébiles (como las desintegraciones de bosones W y Z que estudiamos) con otros procedentes de procesos hadrónicos (principalmente, producción de pares $b\bar{b}$).

Los primeros se caracterizan además de por su alto momento, por no encontrarse rodeados de actividad en el detector, por estar *aislados* tanto en el detector central de trazas como en los calorímetros. En cambio, los muones "QCD" típicamente se encuentran dentro de jets de bajo momento, y vienen acompañados de un alto número de trazas en el detector central y de depósitos energéticos en los calorímetros.

Por lo tanto una herramienta muy útil para la identificación de estos procesos será el *aislamiento*. La actividad presente en el detector en un cono $R = \sqrt{(\Delta\phi)^2 + (\Delta\eta)^2)}$ alrededor del muón se cuantifica para poder distinguir de forma numérica entre ambos tipos de procesos. En concreto en este análisis se utiliza un radio $R = 0.3$, y se elige una variable combinada que tiene en cuenta el momento de las trazas en torno al muón y la energía en ambos calorímetros, expresadas de forma relativa al momento del muón:

$$I^{rel}_{comb} = \frac{\sum_{\text{tracks}} p_T + \sum_{\text{ECal}} E_T + \sum_{\text{HCal}} E_T}{p^{\mu}_t}$$

Aquellos sucesos en los que la variable combinada de aislamiento tenga un valor menor que el 15% del momento del muón serán considerados "aislados" (y por tanto candidatos de provenir de un proceso electrodébil). El comportamiento de esta variable en datos, comparada con las predicciones Monte Carlo para ambos tipos de sucesos, se muestra en la Figura C.2.

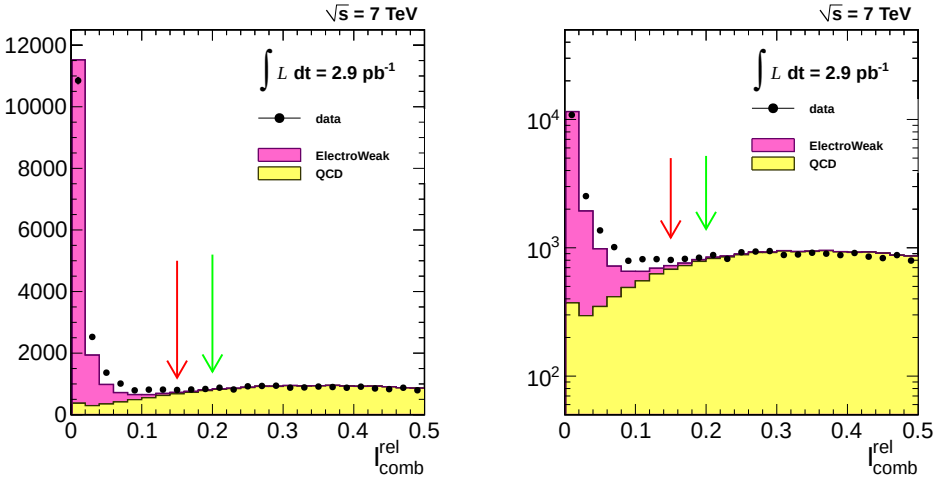

Figure C.2: Aislamiento (relativo, combinado) en escalas logaritmica y lineal, comparando datos y las predicciones Monte Carlo para procesos electródebiles y hadrónicos. La flecha roja en $I^{rel}_{comb} < 0.15$ marca la región definida como "señal". La flecha verde la región de control, dominada por el fondo QCD.

C.4 Energía transversa faltante, E^{miss}_T, en CMS

Los neutrinos no interactúan con la materia de los detectores. Su presencia en una interacción sólo puede ser detectada indirectamente.

La hermeticidad y amplio volumen angular del detector CMS aseguran la detección de casi cualquier partícula. Por ello, estudiando la conservación de energía y momento en el plano

transverso del suceso podemos inferir la presencia de partículas no detectadas, y asignarles una energía y una dirección (por medio de un ángulo azimuthal).

Esta "falta de energía" en el suceso, $\overrightarrow{E_T}^{miss}$, es por lo tanto una estimación del momento del neutrino. Tanto ella como sus variables derivadas son cruciales para el estudio del canal $W \rightarrow \mu\nu$, no sólo para asegurar una buena resolución para el pico jacobiano del W, sino también para distinguir la señal de Ws de otros procesos de fondo.

CMS utiliza tres algoritmos distintos para reconstruir la E_T^{miss}.

El más sencillo de todos es la medida calorimétrica, basada únicamente en el cómputo de la suma negativa de la energía depositada en los calorímetros. Los muones son partículas de mínima ionización, por lo que su momento debe substraerse vectorialmente de éste cálculo para proporcionar un balance de la energía perdida en el suceso:

$$\overrightarrow{E_T}^{miss}(caloMet) = -\sum_{\text{CaloTowers}} \overrightarrow{E_T} - \sum_{\text{muons}} \overrightarrow{p_T}^{\mu} + \sum_{\text{muons}} \overrightarrow{E_T}^{\mu}$$

Esta medida básica puede corregirse teniendo en cuenta la excelente resolución del detector central de trazasr de CMS. El algoritmo conocido como *track-corrected* E_T^{miss} substituye la medida de la energía calorimétrica por el momento cálculado en el detector central para todos aquellos depósitos calorimétricos que se correspondan con una traza en el detector central (salvo electrones, bien medidos por el calorímetro electromagnético), asumiendo que son piones.

$$\overrightarrow{E_T}^{miss}(tcMet) = -\sum_{\text{CaloTowers}} \overrightarrow{E_T} - \sum_{\text{muons}} \overrightarrow{p_T}^{\mu} + \sum_{\text{muons}} \overrightarrow{E_T}^{\mu} - \sum_{\text{good tracks}} \overrightarrow{p_T}^{track} + \sum_{\text{good tracks}} \overrightarrow{E_T}^{track}$$

Finalmente, el método más completo tiene en cuenta todos los detectores de forma conjunta, mediante la técnica conocida como *Particle Flow* o flujo de partículas, que realiza una reconstrucción inclusiva de todo el suceso, identificando al mismo tiempo todas las partículas presentes. De esta forma,

$$\overrightarrow{E_T}^{miss}(pfMet) = -\sum_{\text{AllPF}-\text{Particles}} \overrightarrow{p_T}$$

El comportamiento de estos tres algoritmos para la reconstrucción de la E_T^{miss} de sucesos W en los datos analizados se muestra en la Figura C.3, tras seleccionar muones de alto momento que pasen los criterios de calidad, aislamiento y *trigger* descritos en la sección anterior. Los histogramas sólidos representan la predicción Monte Carlo para la señal.

En esta figura se comprueba cómo la señal del W está mucho más definida, y tiene más separación del resto de procesos, tanto en datos como en Monte Carlo, en los dos últimos

algoritmos presentados. La mejor resolución es la dada por el tercer algoritmo (*Particle Flow*), que será por tanto el utilizado en el análisis posterior.

Por otra parte también podemos observar que los datos son en los tres casos más anchos que la predicción Monte Carlo, que no reproduce de forma exacta el comportamiento observado. Este efecto será corregido a la hora de obtener la medida de la sección eficaz.

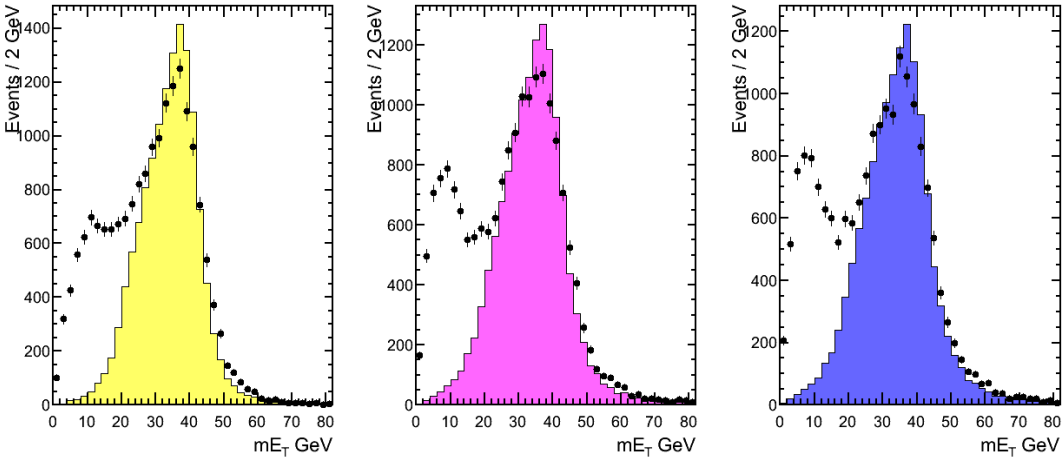

Figure C.3: Comparación de la E_T^{miss} medida en datos (puntos) y en Monte Carlo (histogramas solidos), para una muestra de muones aislados de alto momento. Los tres algoritmos de reconstrucción de energía presentados se muestran en amarillo (calorimétrico), rosa (E_T^{miss} corregida por trazas) y azul (Particle flow).

C.5 Estrategia de Análisis

Experimentalmente, medir la sección eficaz de producción de cualquier partícula se basa en contabilizar cuántas de ellas se han producido en un tiempo dado; teniendo en cuenta la aceptancia geométrica del detector, la eficiencia de los procesos de selección y reconstrucción de muones, la posible contaminación de otros procesos en la muestra experimental, y la luminosidad integrada analizada.

$$\sigma(\mathrm{W} \to \mu\nu) = \frac{N^{obs} - N^{bckg}}{\epsilon_\mu A_{kin} \times \int \mathcal{L} dt}$$

Por tanto el primer paso del análisis supone un estudio de las propiedades cinemáticas de señal y fondo, con objeto de identificar aquellas variables que permitan obtener una muestra lo más pura posible de candidatos a W.

La producción de bosones W desintegrándose en muon-neutrino se caracteriza por la presencia en el detector de un muón aislado de alto momento, acompañado por una falta de conservación de la energía del suceso debida al neutrino. Por ello, la muestra experimental utilizada para análisis queda constituida por aquellos sucesos que han sido seleccionados por los *triggers* de muones, en concreto por el HLT_Mu9 (*trigger* de alto nivel con un muón de al menos 9 GeV). Posteriormente se exige que exista un muón en el suceso contenido dentro del rango de pseudorapidez $\eta < 2.1$ (dado por el *trigger* a nivel hardware), que cumpla los criterios de calidad de reconstrucción de muones detallados anteriormente, que tenga un momento de al menos $p_T > 20$ GeV y que demás esté aislado en el detector ($I^{rel}_{comb} < 0.15$). Los sucesos en los que haya un segundo muon de $p_T > 10$ GeV serán vetados, por proceder de la desintegración de un bosón Z.

El efecto de cada uno de los cortes aplicados en la muestra experimental y en la simulación Monte Carlo se ve en la Tabla C.2. Este proceso de selección conserva un 46% de los sucesos originales.

Table C.2: Candidatos a sucesos W $\rightarrow \mu\nu$ observados, en una muestra experimental de $L_{int} = 2.88$ pb^{-1}, comparados con las predicciones Monte Carlo para esta estadística, distinguiendo la señal del total de procesos con signaturas similares. Los cortes han sido aplicados sucesivamente sobre una muestra preseleccionada de muones seleccionados por el HLT_Mu9, con un momento transverso de mas de $p_T > 15$ GeV y de la que se han eliminado los sucesos con un segundo muón de más de 10 GeV.

	MC (Todos)	MC (Señal)	Datos
Preselección	201465	16884	232286
$\lvert d_{xy}\rvert < 2\ mm$	201172	16884	231507
Criterios de Calidad	194235	16504	192297
$\lvert\eta\rvert < 2.1$	187797	15606	185503
$p_T > 20$ GeV/c	69358	14117	63346
Iso ($I^{rel}_{comb} < 0.15$)	19053	13890	18571

El resto de características cinématicas del W serán usadas para la descripción final de la señal. La energía transversa faltante del suceso ($\overrightarrow{E_T}^{miss}$) y sus variables asociadas serán clave para esta tarea. En concreto en el análisis se utilizarán la acoplanaridad (ángulo en el plano transverso entre el muón y la $\overrightarrow{E_T}^{miss}$) y la masa transversa o M_T del par μ-$\overrightarrow{E_T}^{miss}$:

$$m_{T(\mu,\nu)}(W) = \sqrt{2p_T^{\mu}p_T^{\nu}(1-\cos(\Delta\phi(\mu,\nu)))}$$

Tras este proceso de selección obtenemos una muestra bastante pura de candidatos a W. No obstante hay una contribucón residual de otros procesos de "fondo".

El principal es el fondo hadrónico (en su mayor parte, sucesos $b\bar{b}$), muy distinto cinemáticamente de la señal y caracterizado principalmente por muones de bajo momento contenidos en jets y por tanto no aislados. La alta sección eficaz de producción de estos sucesos ($\sigma_{LO}(QCD) \approx 80$ mb, exigiendo a nivel generador la existencia de de un muón de $p_T > 15$ GeV y $|\eta| < 2.5$) asegura que incluso después de aplicar los mencionados criterios de selección (alto p_T, aislamiento) a la muestra experimental, siga habiendo una contribución no despreciable de estos sucesos.

Hay una contribucón menor, aunque irreducible debido a su similitud con la señal, de otros procesos electrodébiles. Los principales son procesos Drell-Yan ($Z/\gamma* \rightarrow l^+l^-$, $l = \mu, \tau$) y la producción de bosones W desintegrándose en $\tau \rightarrow \mu\nu_\mu\nu_\tau$ (W $\rightarrow \tau\nu$). En menor proporción aparecen también procesos $t\bar{t}$ y de producción de dibosones (WW, WZ, ZZ).

Las eficiencias de selección de sucesos hadrónicos y del conjunto de procesos electrodébiles son de $\approx 1.6\%$ y $\approx 3.7\%$ respectivamente. Teniendo en cuenta las predicciones de sus secciones eficaces teóricas, la contaminación final de fondo se estima en un $N_{bckg}/(N_{bckg} + N_{sig}) \approx 27\%$ (principalmente debido al fondo QCD, $N_{QCD} = 2.5N_{EWK}$).

C.5.1 Determinación de aceptancias y eficiencias

La aceptancia cinemática del proceso de selección (A_{kin}, muones con $p_T > 20$ GeV y en la región angular $\eta < 2.1$) se calcula utilizando una muestra Monte Carlo de alta estadística, teniendo en cuenta el diferente comportamiento de los bosones W^+ y W^-. Esta aceptancia, para la muestra Monte Carlo de referencia utilizada, se muestra en la Tabla C.3, comparada con la eficiencia final de selección A_W, que tiene en cuenta no sólo esta aceptancia cinemática sino también la eficiencia de detección de muones ϵ_μ ($A_W = A_{kin} * \epsilon_\mu$).

Los distintos valores obtenidos para W^+ y W^- (un poco menores para la segunda) se deben a diferencias en los mecanismos de producción de ambas partículas ($u\bar{d} \rightarrow W^+$, $d\bar{u} \rightarrow W^-$), que resultan en espectros de pseudorapidez y momento ligeramente distintos y por tanto diferentes aceptancias.

CMS pretende minimizar la dependencia de sus análisis con cualquier tipo de modelización Monte Carlo. Las eficiencias de selección, identificación, reconstrucción y aislamiento de muones se calculan con una muestra limpia de muones provenientes de desintegraciones de Zs, con un método que se conoce como "Tag and Probe".

	W^+ (%)	W^- (%)
Aceptancia cinemática (A_{kin})	54.13 ± 0.07	50.23 ± 0.06
Eficiencia final de selección (A_W)	47.65 ± 0.07	44.13 ± 0.06

Table C.3: Aceptancia a nivel generador (A_{kin}, $p_T > 20$ GeV, $\eta < 2.1$) y eficiencia final de selección ($A_W = A_{kin} * \epsilon_\mu$) para W^+ y W^-. Los erroes son estadísticos.

Para ello, una vez un suceso es identificado gracias a su masa invariante cercana a la masa del boson Z, se exige que uno de los dos muones de la pareja cumpla estrictos criterios de selección. A continuación se computa la eficiencia a partir del estudio del muón restante, y se tabula en función de su pseudorapidez y momento transverso para incorporarla posteriormente al análisis. De este modo se pueden obtener eficiencias directamente a partir de los datos, y con muones con una cinemática muy próxima a los procedentes de la señal.

Dada la pequeña muestra de candidatos a Z (≈ 1000) disponible en el momento de escritura de esta tesis, en lugar de la medida tabulada recien descrita se usará una sola eficiencia global. De forma práctica, esta eficiencia en datos se incorporará al análisis como una corrección a la eficiencia predicha por las simulaciones Monte Carlo utilizadas, $\rho_{eff} = \epsilon_{DATA}/\epsilon_{MC}$.

Esta eficiencia global (*trigger* x reconstrucción de trazas x reconstruccion de muones x identificación x aislamiento) de selección de muones en datos es de un $82.8 \pm 1.1\%$, y en Monte Carlo de un $88.74 \pm 0.13\%$. Por lo tanto obtenemos un factor de corrección de eficiencias de muones de $\rho_{eff} = 93.3 \pm 1.2\%$. Cada una de las eficiencias en datos y en Monte Carlo se muestra en la Tabla C.4.

Table C.4: Eficiencias y factores de corrección, calculados a partir de una muestra limpia de dimuones [91]

	Datos	Simulacción	Factor de corrección ρ_{eff}
ϵ_{HLT}	$88.3 \pm 0.8\%$	$93.19 \pm 0.14\%$	$94.7 \pm 0.9\%$
$\epsilon_{stand-alone}$	$96.4 \pm 0.4\%$	$97.24 \pm 0.06\%$	$99.2 \pm 0.5\%$
ϵ_{track}	$99.4 \pm 0.5\%$	$99.27 \pm 0.07\%$	$99.8 \pm 0.3\%$
$\epsilon_{isolation}$	$98.5 \pm 0.4\%$	$99.14 \pm 0.04\%$	$99.4 \pm 0.4\%$
ϵ_{id}	$99.7 \pm 0.3\%$	$99.67 \pm 0.05\%$	$100.0 \pm 0.3\%$
$\epsilon_\mu(W)$	$82.8 \pm 1.1\%$	$88.74 \pm 0.13\%$	$93.3 \pm 1.2\%$

Este 7% de ineficiencia en datos comparados con Monte Carlo se debe básicamente a problemas de sincronización en el *trigger* de muones en esta primera etapa, y se reducirá en el

futuro.

Un estudio separando por carga las eficiencias descarta utilizar distintos valores de corrección para μ^+ y μ^-, al no observarse diferencias estadísticamente significativas. Estudiando la ineficiencia en rangos de η (barril central, zona de solape, extremos) se ven diferencias entre los valores de esta correción (la diferencia entre MC y datos es más acusada en la zona de solape). Sin embargo, los errores estadísticos en esta medida en rangos son demasiado grandes. Una corrección diferencial tendrá que esperar a una muestra de bosones Z disponible para análisis mayor.

Un último detalle a tener en cuenta es la posibilidad de que haya efectos que causen la pérdida del suceso en su totalidad, esto es, que estén totalmente correlacionados entre los dos muones y por tanto sean imposibles de medir utilizando la técnica "Tag and Probe" descrita. Uno de estos efectos es el de *pre-triggering*, en el que el suceso no se asigna al cruce de haces que le corresponde sino al anterior, y por lo tanto no es correctamente registrado por el sistema. La probabilidad de *pre-triggering* en el sistema de muones se ha calculado utilizando canales de selección independientes (basados en $\overrightarrow{E_T}^{miss}$ y jets) y se ha calculado un factor adicional de corrección de $99.5 \pm 0.5\%$.

C.5.2 Modelado de Señal y Fondo

Para obtener un modelado realista de las distribuciones finales (E_T^{miss} o M_T) de señal y fondo, puede ser necesario incorporar efectos del detector (resolución, escala) para corregir las simulaciones Monte Carlo que se utilizan.

El proceso de producción de Ws y Zs es uno muy bien comprendido a nivel teórico. Por ello, las simulaciones de la señal de $W \rightarrow \mu\nu$ (y de los demás procesos electrodébiles), son realistas y una base razonable para el análisis. De hecho, el excelente acuerdo en las distribuciones de momento de los muones y la posición y anchura del pico de $Z \rightarrow \mu^+\mu^-$ indican que los procesos de reconstrucción de muones están correctamente simulados en el Monte Carlo, y no es necesario corregir su resolución o escala.

No es ese el caso de la energía transversa. Se observa en datos una pérdida de resolución en la E_T^{miss}, que debe ser tenida en cuenta para modelar correctamente la señal. Para ello se utilizará de nuevo una muestra experimental limpia de desintegraciones $Z \rightarrow \mu^+\mu^-$ de la que se obtiene información de la forma y resolución de la distribución de E_T^{miss} en datos, en función del momento del bosón Z. Esta información se reinterpreta e introduce en el Monte Carlo de $W \rightarrow \mu\nu$, a partir de la distribución obtenida para el valor concreto del momento del bosón W

en cada suceso simulado. Se modela por tanto el comportamiento del neutrino a partir de datos y se combina después con la información del muón en MonteCarlo. De esta forma se reconstruye el bosón W de forma realista teniendo en cuenta el comportamiento del detector.

De este modo obtenemos "patrones" de las variables necesaria para el análisis final, E_T^{miss} y M_T. Estos se muestran en la Figura C.4 comparados con la distribución Monte Carlo sin corregir. Se puede observar un ensanchamiento de las distribuciones corregidas, especialmente apreciable en el pico de la distribución.

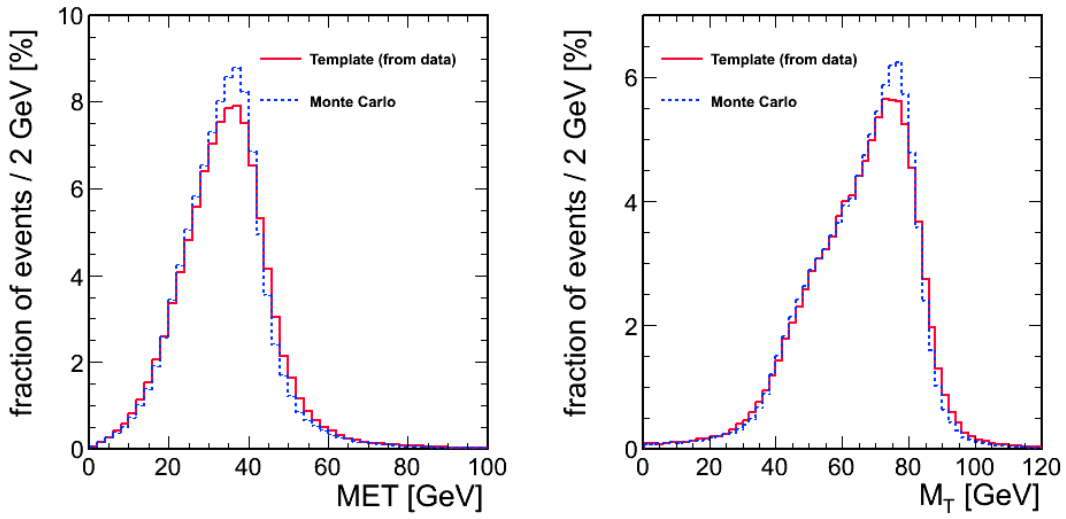

Figure C.4: Comparación entre la distribución Monte Carlo y el patrón obtenido para la señal, en E_T^{miss} y M_T.

Este tratamiento efectuado para la señal sería igualmente aplicable a los distintos fondos electrodébiles ($Z \rightarrow \mu^+\mu^-$, $W \rightarrow \tau\nu$, $Z \rightarrow \tau^+\tau^-$, etc) del análisis. No obstante, dada su pequeña contribución a la composición final de la muestra experimental analizada, el impacto de esta corrección sería insignificante.

En el caso del fondo hadrónico, "QCD", la complejidad de los procesos asociados impiden obtener una simulación Monte Carlo en la que apoyar la modelización de estos fondos. Toda la información será por tanto extraida a partir de muestras de control en datos.

Para ello se busca una variable no correlacionada con las distribuciones de M_T / E_T^{miss} que queremos modelar, y que proporcione una adecuada separación entre señal y fondo. El candidato óptimo es la variable de aislamiento, dado que seleccionando datos no aislados, por ejemplo la region $I_{comb}^{rel} > 0.2$, obtenemos una muestra muy pura de sucesos QCD. A partir de la

distribución de M_T de esta submuestra obtenemos en primera aproximación la forma del fondo hadrónico requerida.

Sin embargo, dado que hay una pequeña correlación residual, necesitamos corregir esta distribución para modelar más adecuadamente los sucesos QCD aislados que queremos eliminar de la muestra experimental.

Para ello estudiamos la variación de la forma de los espectros de E_T^{miss} y M_T en función del valor de la variable de aislamiento I_{comb}^{rel} y del ángulo entre el muón y la E_T^{miss}. Teniendo en cuenta la variación de la posición del valor medio y la anchura de las distribuciones, podemos obtener un factor α de relación entre energía transversa y aislamiento. Esta correlacción medida en datos a partir de la distribución bidimensional de E_T^{miss}-I_{comb}^{rel} resulta ser lineal, y permite obtener una masa transversa corregida:

$$E_T^{miss}(cor) = E_T^{miss}/(1 + \alpha \times I_{comb}^{rel})$$

$$M_T(cor) = \begin{cases} \sqrt{2p_T E_T^{miss}(cor) * (1 + \cos(acop))} & \text{si } acop < 2.0 \\ \sqrt{2p_T E_T^{miss} * (1 + \cos(acop))} & \text{si } acop > 2.0 \end{cases}$$

De este modo se puede extrapolar el comportamiento de la zona aislada a partir de la zona no aislada.

La distribución corregida resultante está comprendida entre la esperada a partir de la simulación Monte Carlo (que predice una contribución del fondo más centrada en valores bajos de M_T y por tanto más alejada de la zona de señal) y la obtenida directamente a partir de la muestra de control (más desviada hacia valores altos de M_T).

La Figura C.5 compara la forma de la distribución de este fondo predicha por la simulación Monte Carlo, con los dos patrones (con y sin correción en función del aislamiento), para la energía transversa faltante y la masa transversa.

C.6 Medida de la Sección Eficaz

La medida de la sección eficaz se realiza a partir de una minimización de la función de verosimilitud entre la distribución experimental de M_T y una distribución suma de los patrones descritos en la sección anterior para la señal y los distintos fondos.

$$N(DATA) = N(W) + N(QCD) + \sum_i N(EWK_i)$$

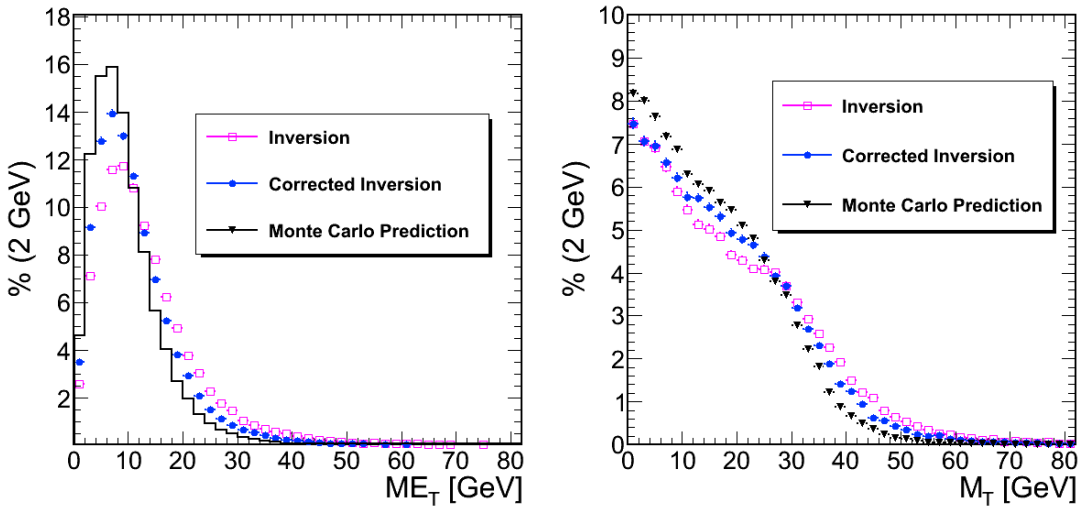

Figure C.5: Comparación entre la distribución Monte Carlo y el patrón obtenido para el fondo hadrónico, para E_T^{miss} y M_T.

Las contribuciones de señal y de los tres principales fondos electrodébiles ($Z \rightarrow \mu^+\mu^-$, $W \rightarrow \tau\nu$, $Z \rightarrow \tau^+\tau^-$) se expresan a partir de su sección eficaz y de su aceptancia y eficiencia de selección ($A_W = A_{kin}(W) \times \epsilon_{sel}(W)$, y equivalentemente para cada proceso EWK). Para ello se usan los patrones de M_T descritos previamente, $\mathcal{F}(M_T)$ para la señal y $\mathcal{G}_i(M_T)$ para cada uno de los fondos citados. A partir de las predicciones teóricas de las secciones eficaces de los distintos procesos podemos normalizar la contribución de cada fondo electrodébil a la del W, a través de un factor $k_{EWK_i} = \sigma_{EWK_i}/\sigma_W$. De este modo,

$$\begin{aligned} N(W)(M_T) &= A_W \mathcal{F}(M_T)\sigma_W \int \mathcal{L}dt \\ N(EWK_i)(M_T) &= A_{EWK_i}\mathcal{G}_i(M_T)\sigma_{EWK_i} \int \mathcal{L}dt \\ &= A_{EWK_i}\mathcal{G}_i(M_T)\sigma_W k_{EWK_i} \int \mathcal{L}dt \\ &(i = Z \rightarrow \mu^+\mu^-, Z \rightarrow \tau^+\tau^-, W \rightarrow \tau\nu) \end{aligned}$$

Las contribuciones correspondientes a producción de pares top-antitop y dibosones (WW, WZ, ZZ) son lo suficientemente pequeñas comparadas con la señal como para que la contribución de estos fondos (N_{Other}) pueda ser directamente estimada a partir de predicciones Monte Carlo.

Finalmente, el fondo QCD se modela a partir del patrón $\mathcal{H}(M_T)$ obtenido con la distribución de M_T en la región no-aislada. Su normalización se obtiene en el ajuste. Matemáticamente esto

Table C.5: Resumen de los números necesarios para la extracción de la sección eficaz.

	$W \to \mu\nu$	$W^+ \to \mu^+\nu$	$W^- \to \mu^-\bar{\nu}$
A_W	46.20 ± 0.07	47.65 ± 0.07	44.13 ± 0.06
ρ_{eff}	$\rho_{MC} = (99.5 \times 93.3 \pm 1.2 \otimes 0.5)\%$		
$\mathcal{L}$	2.88pb^{-1}		

se expresa según

$$N(QCD) = f_{QCD}\mathcal{H}(M_T)\int \mathcal{L}dt$$

Con objeto de calcular no sólo la sección eficaz total, sino también las correspondientes a W^+ y W^-, las expresiones anteriores se duplican, separando los candidatos en positivos y negativos.

$$N_{fit^+} = N(W^+) + N(QCD^+) + \sum_i N(EWK(i)^+) + N(Other^+)$$
$$N_{fit^-} = N(W^-) + N(QCD^-) + \sum_i N(EWK(i)^-) + N(Other^-)$$

El fit tendrá por lo tanto tres parámetros libres: la normalización del fondo QCD (f_{QCD}, asumido simétrico por carga), la sección eficaz total $\sigma(W)$ y el cociente de las secciones eficaces de bosones W positivos y negativos $R = \sigma(W^+)/\sigma(W^-)$. La función de verosimilitud que será ajustada usando MINUIT [79] es la siguiente:

$$\begin{aligned} -\frac{1}{2}\log L = \quad & \textstyle\sum_{M_T}\left(N_{DATA^+}\log\left(N_{fit^+}\left(M_T, f_{QCD}, \sigma_W, R\right)\right) - \left(N_{fit^+}\left(M_T, f_{QCD}, \sigma_W, R\right)\right)\right. \\ & \left. + \textstyle\sum_{M_T}\left(N_{DATA^-}\log\left(N_{fit^-}\left(M_T, f_{QCD}, \sigma_W, R\right)\right) - \left(N_{fit^-}\left(M_T, f_{QCD}, \sigma_W, R\right)\right)\right. \end{aligned}$$

Los valores de la Aceptancia x Eficiencia de la señal, y el factor de corrección de eficiencias necesarios para el ajuste se resumen en la Tabla C.5.

Los valores obtenidos de sección eficaz, cociente y normalización de QCD son

$$\begin{aligned} \sigma(\text{pp} \to \text{W}^\pm + X) \times BR(\text{W}^\pm \to \mu^\pm\nu) &= 9.93 \pm 0.09(\text{stat.})\ \text{nb}, \\ \sigma(\text{pp} \to \text{W}^+ + X) \times BR(\text{W}^+ \to \mu^+\nu) &= 5.84 \pm 0.07(\text{stat.})\ \text{nb}, \\ \sigma(\text{pp} \to \text{W}^- + X) \times BR(\text{W}^- \to \mu^-\bar{\nu}) &= 4.09 \pm 0.06(\text{stat.})\ \text{nb}, \\ \frac{\sigma(\text{pp} \to \text{W}^+ + X) \times BR(\text{W}^+ \to \mu^+\nu)}{\sigma(\text{pp} \to \text{W}^- + X) \times BR(\text{W}^- \to \mu^-\bar{\nu})} &= 1.43 \pm 0.03(\text{stat.}), \\ f_{QCD} &= 868 \pm 13(\text{stat.}) \end{aligned}$$

Table C.6: Número de sucesos para cada uno de los procesos físicos involucrados obtenidos a partir del ajuste a los datos.

	$W \to \mu\nu$	$W^+ \to \mu^+\nu$	$W^- \to \mu^-\bar{\nu}$
Candidatos observados	18571	10682	7889
Ajuste	18575 ± 142	10663 ± 98	7912 ± 83
$W \to \mu\nu$	12269 ± 111	7439 ± 86	4830 ± 69
QCD	5002 ± 80	2501 ± 40	2501 ± 40
$Z \to \mu^+\mu^-$	571 ± 24	297 ± 17	275 ± 17
$W \to \tau\nu$	569 ± 24	342 ± 18	227 ± 15
$Z \to \tau^+\tau^-$	99 ± 10	52 ± 7	48 ± 7
$t\bar{t}$	49 ± 7	24 ± 5	24 ± 5
WW, WZ, ZZ	15 ± 4	8 ± 2	7 ± 2

Las distribuciones ajustadas de M_T se muestran, en escala lineal y logarítmica, en la Figura C.6. El acuerdo entre los datos y las distribuciones ajustadas es excelente en todo el rango de M_T, con sólo pequeñas desviaciones en la zona de solape entre señal y fondo ($M_T \approx 30$ GeV) y a alto M_T.

El número de sucesos correspondiente a cada proceso, en todo el rango de masa transversa, se muestra en la Tabla C.6. Las funciones de verosimilitud ajustadas se muestran en la Figura C.7, para la sección eficaz, el cociente, y las secciones eficaces de W^+ y W^-. Una línea marca la incertidumbre estadística del ajuste (0.5 sobre el valor mínimo).

C.7 Cálculo de incertidumbres sistemáticas

Diferentes efectos sistematicos afectan la medida.

Por un lado, están los errores teóricos (PDFs, radiación de estado inicial y final, efectos electrodébiles y de QCD de mayor orden), que sólo intervienen en la medida a través de la aceptancia cinemática del proceso A_{kin}. Un estudio dedicado de cada uno de ellos permite asignar un sistemático global de un 1.8% para la medida de la sección eficaz total (1.9% para W^+ y 2.3% para W^-). La incertidumbre teórica en la razón de secciones eficaces es de un 2.4%.

Por otro lado, hay que tener en cuenta las distintas incertidumbres experimentales asociadas a la medida.

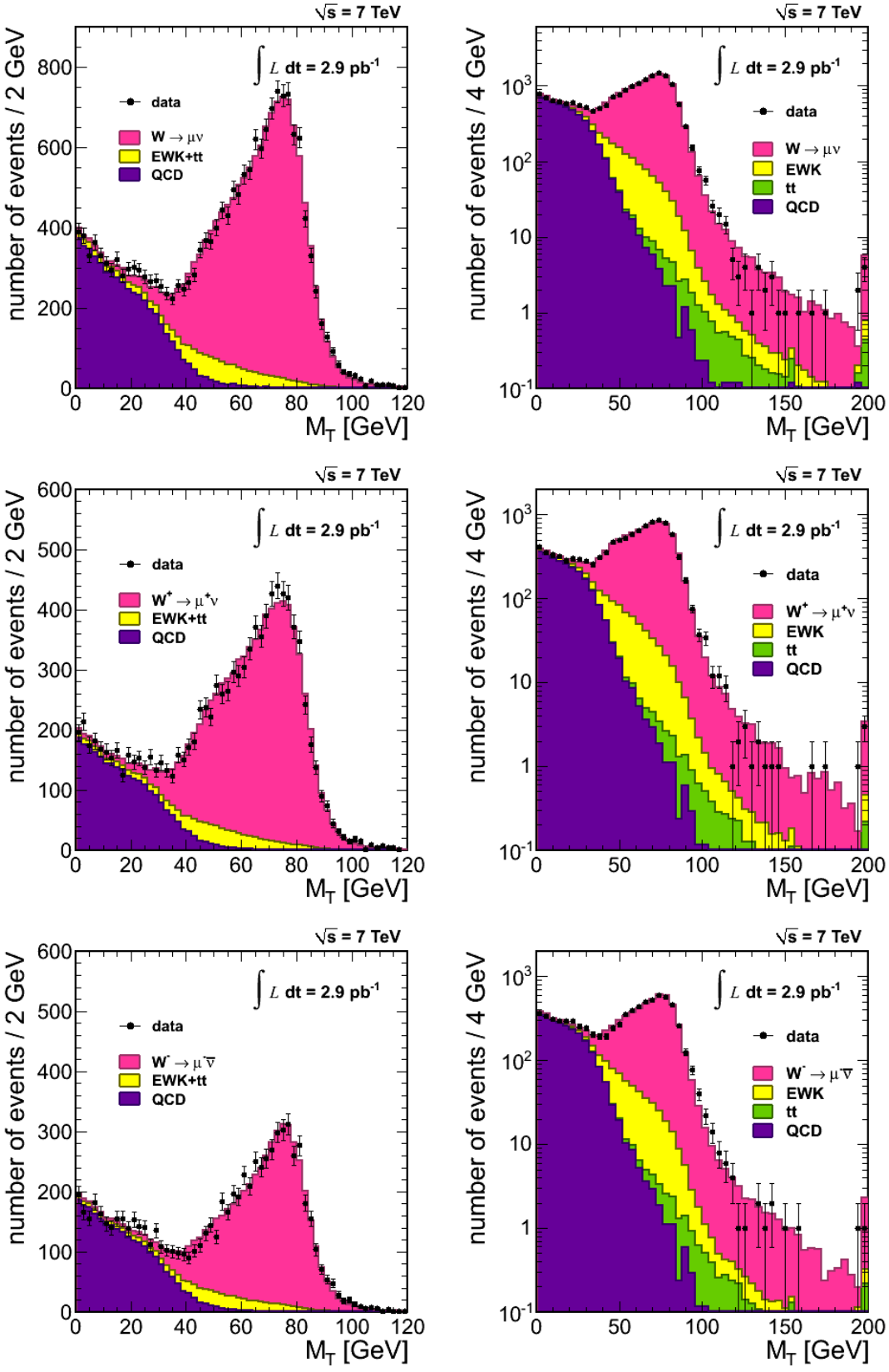

Figure C.6: Distribuciones ajustadas de M_T, en escala lineal y logarítmica, para todos los candidatos (figura superior), y diferenciando los de carga positiva (central) y negativa (inferior).

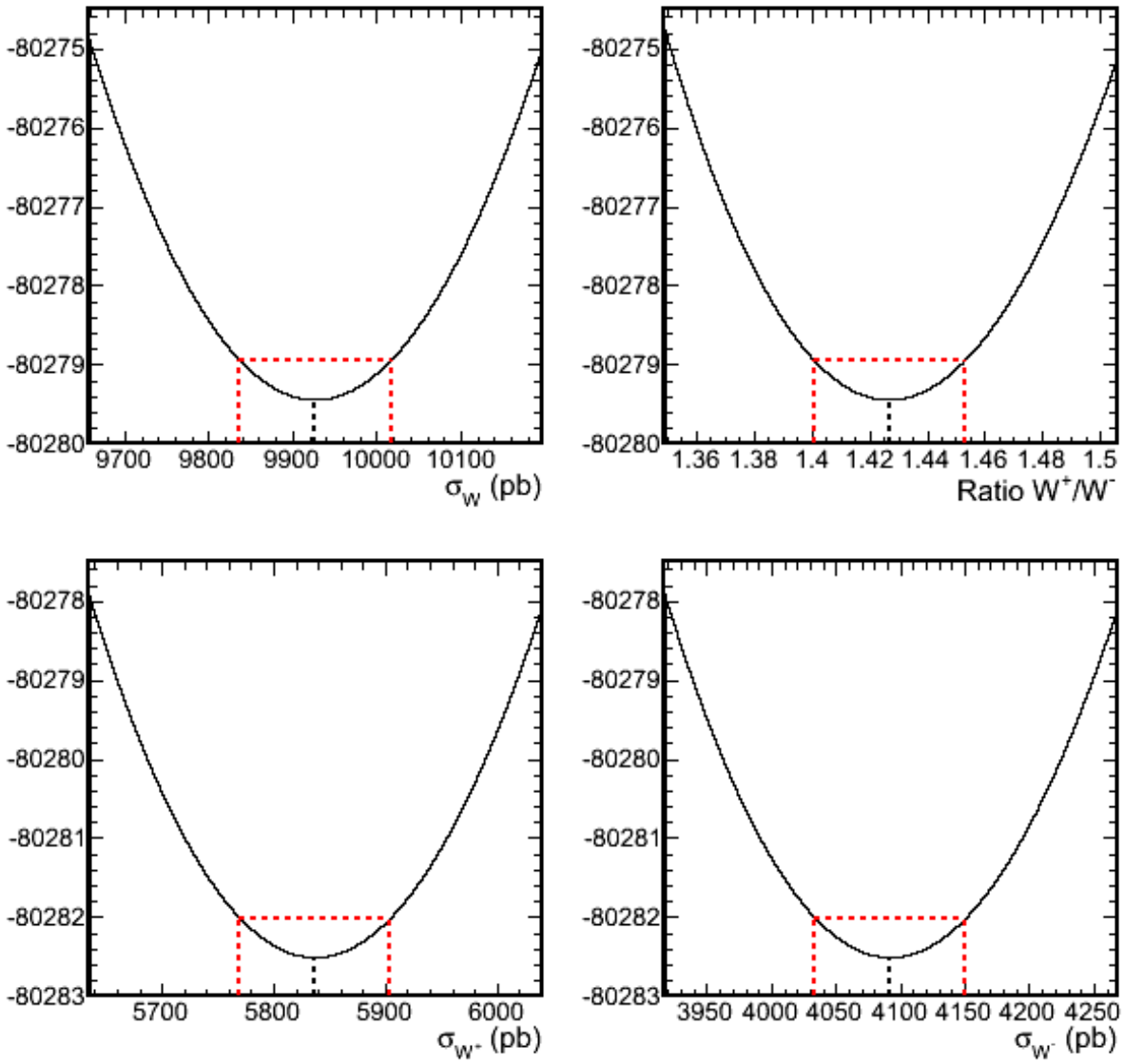

Figure C.7: Funciones de verosimilitud ajustadas, para las cuatro medidas involucradas (σ_W, $R = \sigma_W^+/\sigma_W^-$, σ_W^+ y σ_W^-).

En primer lugar, las asociadas a la determinación de la eficiencia de selección de muones (reconstrucción, identificación, aislamiento, *trigger*), obtenidas con el método de "Tag and Probe". El error sistemático asociado a estas medidas se estima a partir de la propagación del error estadístico asociado al factor de corrección ρ_{eff}, un 1.2%. Un factor adicional de un 0.5% debido a los efectos de *pre-triggering* se añade en cuadratura.

Hay que tener en cuenta que aunque la cinemática de los muones provenientes de la desintegración de bosones Z y W es muy similar, hay una pequeña diferencia entre ambos procesos. Se calcula que el efecto de esta diferencia en cinemática es menor que un 0.5%. El sistemático final asociado a las eficiencias de muones será por tanto de un 1.5%.

En cuanto a posibles efectos de escala y resolución en la medida del momento de los muones, estudios basados en diferentes resonancias (J/Ψ, Zs, Υs) permiten descartar efectos de escala superiores a 0.40% para muones con un $p_T \approx 40$ GeV [67; 80].

Este tipo de efectos se trasladan a la medida de la sección eficaz, mediante un reprocesado de los datos incluyendo una distorsión de este calibre, y estudiando el impacto producido en el resultado del ajuste experimental. Este factor de escala produce un efecto muy pequeño, de sólo un 0.3%, que será utilizado como un límite superior al error sistemático correspondiente.

La resolución y escala de medida de la energía transversa faltante (E_T^{miss}) se estudia a través de la comparación entre el patrón de señal utilizado en el ajuste, y la distribución Monte Carlo original. Esta comparación conduce a un límite superior para el sistemático asociado de un 0.4%, valor conservador puesto que sabemos que el Monte Carlo original se desvía bastante de la distribución experimental.

La extracción de los distintos fondos electrodébiles presentes en la muestra experimental puede afectar a la medida tanto por las incertidumbres en la determinación de la aceptancia de cada proceso como por el modelado imperfecto de la E_T^{miss}. No obstante, dada la pequeña contribución de estos fondos al total de sucesos esperados, la incertidumbre en la medida de la sección eficaz se considera sólo de un 0.2%.

Por otra parte, los errores debidos a la forma de la contribución del fondo hadrónico no son en absoluto despreciables. La auténtica forma del fondo QCD es imposible de determinar, y el sistemático asociado se calcula (de nuevo de forma relativamente conservadora) comparando el resultado del ajuste con la forma corregida, la forma de la región no-aislada del espectro, y la forma predicha por la distribución Monte Carlo. Esta comparación lleva a la asignación de un límite superior para el error cometido de un 2% para la sección eficaz total (1.7% para la sección eficaz positiva, 2.3% para la negativa, y 0.7% para el cociente).

Table C.7: Incertidumbres en la sección eficaz de W, W^+, W^- y la razón de secciones eficaces cargadas

Origen	$W \to \mu\nu$	$W^+ \to \mu^+\nu$	$W^- \to \mu^-\bar{\nu}$	$\frac{W^+\to\mu^+\nu}{W^-\to\mu^-\bar{\nu}}$
Estadístico	0.9	1.2	1.5	2.1
Reconstrucción e identificación de muones	1.5	1.5	1.5	2.8
Escala y resolución de momento	0.3	0.3	0.3	0.3
Escala y resolución de E_T^{miss}	0.4	0.4	0.4	-
Substracción y modelado de fondo	2.0	1.7	2.3	0.7
Incertidumbre teórica debida a las PDF	1.1	1.3	1.9	2.1
Otras incertidumbres teóricas	1.4	1.4	1.3	1.2
Sistemático (Teoría + Experimento)	3.1	3.0	3.6	3.8
Luminosidad	11.	11.	11.	-

El último error experimental a tener en cuenta es el debido a la determinación de la luminosidad integrada de los datos, que para los primeros datos del LHC es del 11%.

Todas las fuentes de incertidumbre están resumidas en la Tabla C.7. Se puede comprobar como los errores sistemáticos (3.1% combinando teóricos y experimentales sin tener en cuenta el debido a la luminosidad) dominan claramente sobre los estadísticos (0.9% para la sección eficaz total).

C.8 Resultados

Las secciones eficaces $\sigma(\mathrm{pp} \to \mathrm{W}^\pm + X) \times BR(\mathrm{W}^\pm \to \mu^\pm\nu)$, $\sigma(\mathrm{pp} \to \mathrm{W}^+ + X) \times BR(\mathrm{W}^+ \to \mu^+\nu)$ y $\sigma(\mathrm{pp} \to \mathrm{W}^- + X) \times BR(\mathrm{W}^- \to \mu^-\bar{\nu})$ medidas a 7 TeV en centro de masas, y la razón de secciones eficaces cargadas, para todo el espacio de fases, son las siguientes:

$$
\begin{aligned}
\sigma(\mathrm{pp} \to \mathrm{W}^\pm + X \to \mu^\pm\nu + X) &= 9.93 \pm 0.09(\mathrm{est}) \pm 0.25(\mathrm{exp}) \pm 0.17(\mathrm{teo}) \pm 1.09(\mathrm{lumi})\ \mathrm{nb}, \\
\sigma(\mathrm{pp} \to \mathrm{W}^+ + X \to \mu^+\nu + X) &= 5.84 \pm 0.07(\mathrm{est}) \pm 0.14(\mathrm{exp}) \pm 0.11(\mathrm{teo}) \pm 0.64(\mathrm{lumi})\ \mathrm{nb}, \\
\sigma(\mathrm{pp} \to \mathrm{W}^- + X \to \mu^-\bar{\nu} + X) &= 4.09 \pm 0.06(\mathrm{est}) \pm 0.11(\mathrm{exp}) \pm 0.09(\mathrm{teo}) \pm 0.45(\mathrm{lumi})\ \mathrm{nb}, \\
\frac{\sigma(\mathrm{pp} \to \mathrm{W}^+ + X \to \mu^+\nu + X)}{\sigma(\mathrm{pp} \to \mathrm{W}^- + X \to \mu^-\bar{\nu} + X)} &= 1.43 \pm 0.03(\mathrm{est}) \pm 0.04(\mathrm{exp}) \pm 0.03(\mathrm{teo})
\end{aligned}
$$

Esta medida puede restringirse al espacio de fases dado por los cortes cinématicos utilizados ($p_T > 20$ GeV, $|\eta| < 2.1$). De esta forma se suprimen los errores teóricos debidos al conocimiento

actual de las PDFs. Estas secciones eficaces restringidas son las siguientes

$$\begin{aligned}
\sigma(\mathrm{pp} \to \mathrm{W}^{\pm} + X \to \mu^{\pm}\nu + X)|_{red} &= 5.21 \pm 0.05(\mathrm{est}) \pm 0.13(\mathrm{exp}) \pm 0.07(\mathrm{teo}) \pm 0.57(\mathrm{lumi})\mathrm{nb}, \\
\sigma(\mathrm{pp} \to \mathrm{W}^{+} + X \to \mu^{+}\nu + X)|_{red} &= 3.16 \pm 0.04(\mathrm{est}) \pm 0.07(\mathrm{exp}) \pm 0.04(\mathrm{teo}) \pm 0.35(\mathrm{lumi})\mathrm{nb}, \\
\sigma(\mathrm{pp} \to \mathrm{W}^{-} + X \to \mu^{-}\bar{\nu} + X)|_{red} &= 2.05 \pm 0.03(\mathrm{est}) \pm 0.06(\mathrm{exp}) \pm 0.03(\mathrm{teo}) \pm 0.22(\mathrm{lumi})\mathrm{nb}
\end{aligned}$$

La diferencia de producción de bosones W^+ y W^- afecta a la aceptancia cinemática, por lo que el cociente de secciones eficaces cargadas no puede ser medido en el espacio de fases de los cortes aplicados.

Por otra parte, si combinamos este resultado con la sección eficaz de producción de bosones Z publicada por CMS, [91], podemos obtener una nueva razón de secciones eficaces, W/Z:

$$\begin{aligned}
\sigma(\mathrm{pp} \to \mathrm{Z}(\gamma^*) + X \to \mu^+\mu^- + X) &= 0.92 \pm 0.03(\mathrm{est}) \pm 0.01(\mathrm{exp}) \pm 0.02(\mathrm{teo}) \pm 1.11(\mathrm{lumi})\ \mathrm{nb}, \\
\frac{\sigma(\mathrm{pp} \to \mathrm{W}^{\pm} + X \to \mu^{\pm}\nu + X)}{\sigma(\mathrm{pp} \to \mathrm{Z}(\gamma^*) + X \to \mu^+\mu^- + X)} &= 10.7 \pm 0.4(\mathrm{est}) \pm 0.3(\mathrm{exp}) \pm 0.19(\mathrm{teo})
\end{aligned}$$

Estas medidas están en excelente acuerdo con los resultados publicados por CMS en [91]. De hecho la medida aquí presentada es básicamente idéntica a la de esta referencia. La muestra experimental, la estrategia de selección, el método de ajuste es idéntico. La única diferencia radica en el método usado para modelizar la distribución en M_T de la señal.

En el resultado publicado, la señal se modela también a partir de la información obtenida en una muestra de $\mathrm{Z} \to \mu^+\mu^-$. Sin embargo en este caso en vez de utilizar la distribución experimental en cada rango de momento, se realiza una parametrización de la resolución que se incorpora al Monte Carlo. Los dos métodos son plenamente compatibles y describen la señal con la misma precisión. Las pequeñas diferencias existentes entre ambos métodos son en todo caso mucho menores que el sistemático asociado a la escala y resolución de E_T^{miss}. El método presentado en esta tesis podría verse afectado por la escasa muestra experimental de sucesos de $\mathrm{Z} \to \mu^+\mu^-$ disponible, que hace que las distribuciones de E_T^{miss} de partida esten poco pobladas; mientras que el método de la parametrización puede no ser capaz de describir adecuadamente las colas de la señal si estas no son gausianas. Disponer de ambos métodos permite su validación a través del buen acuerdo obtenido entre sus resultados.

La principal razón por las que en el resultado públicado se optó por el modelado a partir de una parametrización fue la búsqueda de una mayor homogeneidad entre los resultados en el canal $\mathrm{W} \to \mu\nu$ y el canal $\mathrm{W} \to \mathrm{e}\nu$, presentados en paralelo en el citado artículo. El método gausiano se desarrolló para ambos canales, y por tanto se seleccionó en lugar del método de

muestreo. En cualquier caso el resultado de esta tesis se utilizo cómo una comprobación auxiliar en el cálculo de incertidumbres sistemáticas.

La comparación final entre las medidas mostradas en esta tesis, las públicadas por CMS, y las predicciones teóricas, se muestran en la Figura C.8: (a) sección eficaz de W, (b) sección eficaz de W^+, (c) sección eficaz de W^-, (d) razón W^+/W^- y (e) razón W/Z.

La predicción teórica a NNLO ha sido calculada con el programa FEWZ [37], utilizando pdfs a NNLO del grupo MSTW [9].

Los valores de sección eficaz medidos están todos un $\sim 5\%$ por debajo de la predicción teórica, pero son compatibles con ella teniendo en cuenta la incertidumbre debida a la luminosidad de los datos (línea externa, verde en la gráfica). Sin embargo los dos cocientes de secciones eficaces, que no están afectadas por esta incertidumbre, están en perfecto acuerdo con lo predicho por el modelo. Esta comparación entre la medida publicada por CMS y la predicción teórica (CMS/TEO) se muestra en la Figura C.9, y puede apuntar a una sobreestimación de la medida de la luminosidad integrada en este primer periodo del LHC.

C.9 Conclusiones

La medida de la sección eficaz de producción de bosones W, y los cocientes de producción de W^+/W^- y W/Z, en colisiones protón-protón a 7 TeV es la primera medida Electrodébil de precisión realizada en el LHC.

$$\begin{aligned}
\sigma(\mathrm{pp} \to \mathrm{W}^{\pm} + X \to \mu^{\pm}\nu + X) &= 9.93 \pm 0.09(\mathrm{est}) \pm 0.25(\mathrm{exp}) \pm 0.17(\mathrm{teo}) \pm 1.09(\mathrm{lumi})\ \mathrm{nb}, \\
\frac{\sigma(\mathrm{pp} \to \mathrm{W}^{+} + X \to \mu^{+}\nu + X)}{\sigma(\mathrm{pp} \to \mathrm{W}^{-} + X \to \mu^{-}\bar{\nu} + X)} &= 1.43 \pm 0.03(\mathrm{est}) \pm 0.04(\mathrm{exp}) \pm 0.03(\mathrm{teo}), \\
\frac{\sigma(\mathrm{pp} \to \mathrm{W}^{\pm} + X \to \mu^{\pm}\nu + X)}{\sigma(\mathrm{pp} \to \mathrm{Z}(\gamma^*) + X \to \mu^{+}\mu^{-} + X)} &= 10.7 \pm 0.4(\mathrm{est}) \pm 0.3(\mathrm{exp}) \pm 0.19(\mathrm{teo})
\end{aligned}$$

El excelente acuerdo de los resultados experimentales con las últimas predicciones teóricas no sólo sirven para validar en esta nueva escala de energías los modelos teóricos subyacentes, sino también la cadena de ánalisis de CMS.

La precisión obtenida con esta medida (3.1% de error sistemático, sin tener en cuenta la incertidumbre debida a la luminosidad integrada de los datos) son la mejor garantía del buen funcionamiento de los sistemas de selección de datos, reconstrucción e identificacción de muones y reconstrucción de la energía total del suceso.

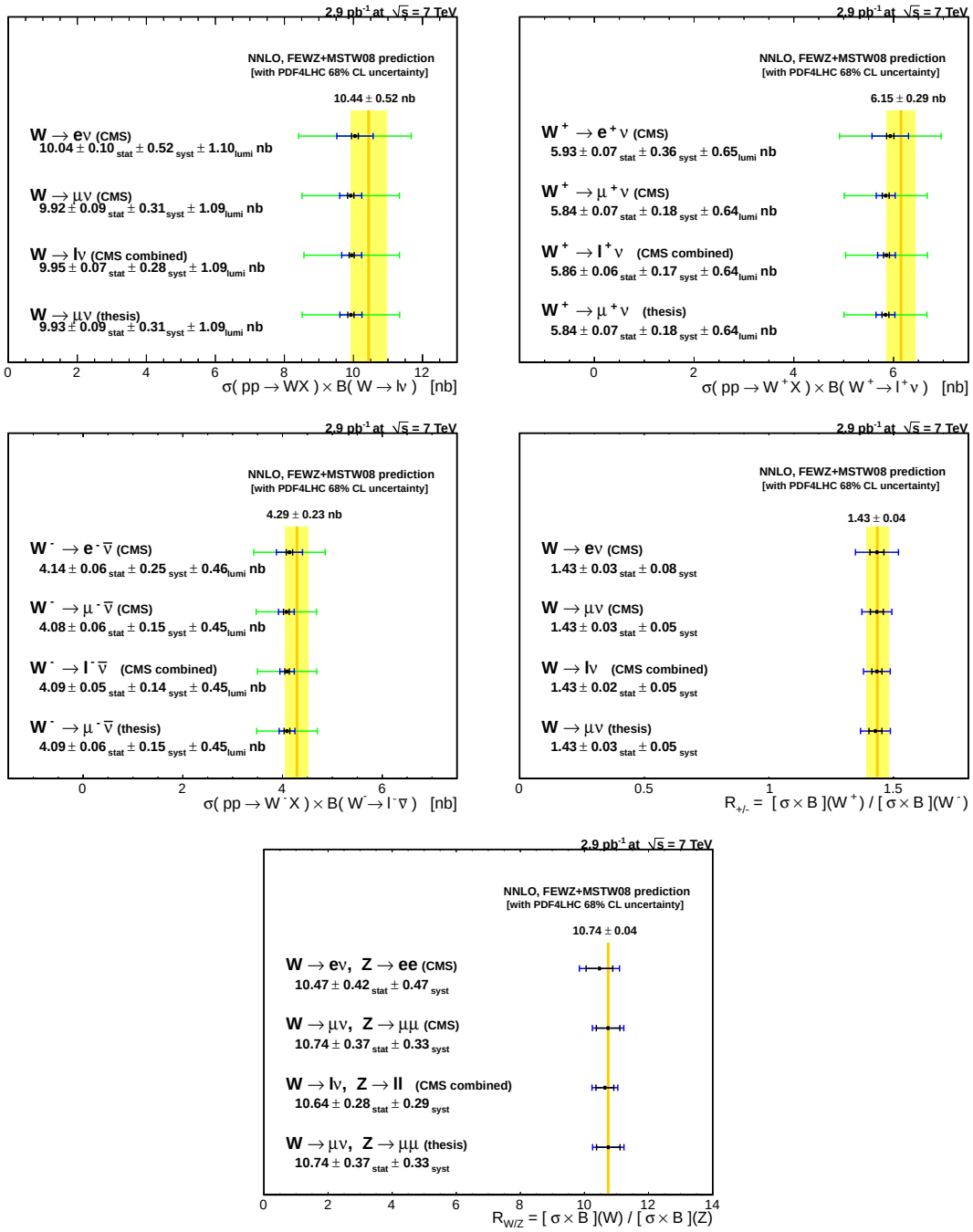

Figure C.8: Comparación de la sección eficaz medida con la teoría y el resultado públicado por CMS.

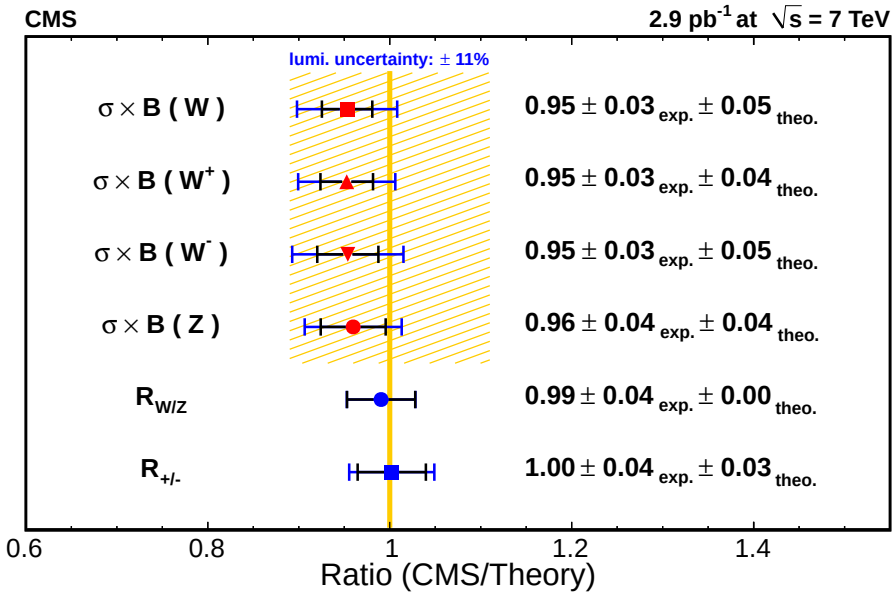

Figure C.9: Comparación en forma de cociente (CMS/Teoría) de los resultados aqui presentados con las predicciones teóricas.

C. MEDIDA DE LA SECCIÓN EFICAZ DE PRODUCCIÓN DEL BOSÓN W EN COLISIONES PROTÓN-PROTÓN A $\sqrt{S} = 7$ TEV

References

[1] O. Bruning *et. al.*, *The LHC design report v.1: the LHC Main Ring*, *CERN-2004-003-V-1* (2004). 5

[2] O. Bruning *et. al.*, *The lhc design report v.2 : the lhc infrastructure and general services*, *CERN-2004-003-V-2* (2004). 5

[3] B. Benedikt *et. al.*, *The LHC design report v.3 : the LHC Infrastructure and General Services*, *CERN-2004-003-V-3* (2004). 5

[4] C. Amsler *et. al.*, *Review of particle physics*, *Phys. Lett.* **B667** (2008) [http://pdg.lbl.gov/]. 6, 47, 53, 179

[5] LEP Electroweak Working Group, http://lepewwg.web.cern.ch/LEPEWWG/. 7, 8, 9, 57

[6] R. Barate *et. al.*, *Search for the standard model Higgs boson at LEP*, *Phys. Lett.* **B565** (2003) 61–75, [hep-ex/0306033]. 7, 8

[7] Tevatron New Phenomena and Higgs Working Group, *Combined CDF and D0 Upper Limits on Standard Model Higgs-Boson Production with up to 6.7 fb-1 of Data*, *webpage, arXiv:1007.4587 [hep-ex]* (2010). 8, 9

[8] **CMS** Collaboration, *The CMS physics reach for searches at 7 TeV*, *CMS Note 2010/008* (2010). 9

[9] A. D. Martin, W. J. Stirling, R. S. Thorne, and G. Watt, *Parton distributions for the LHC*, *Eur. Phys. J.* **C63** (2009) 189–285, [arXiv:0901.0002]. 11, 47, 51, 52, 54, 133, 146, 180, 181, 203

[10] **ALICE** Collaboration, *ALICE: Technical proposal for a large ion collider experiment at the CERN LHC*, . 15

[11] **ATLAS** Collaboration, *The ATLAS Experiment at the CERN Large Hadron Collider*, *JINST 3 S08003* (2008). 15

[12] **CMS** Collaboration, "The CMS experiment at the CERN LHC." 15, 16, 23, 31, 182

[13] **CMS** Collaboration, *CMS physics: Technical Design Report*, *CERN-LHCC-2006-001* (2006). 15

[14] **LHCb** Collaboration, *LHCb technical design report: Reoptimized detector design and performance*, *CERN-LHCC-2003-030* (2003). 15

[15] **CMS** Collaboration, *CMS Physics Technical Design Report Volume 1: Detector Performance and Software*, *CERN-LHCC-2006-001, http://cdsweb.cern.ch/record/922757.* 16, 24, 26, 28

[16] **CMS** collaboration, *CMS Physics Technical Design Report Volume 2: Physics Performance*, *J. Phys. G 34 995* **CERN-LHCC-2006-021, http://cdsweb.cern.ch/record/942733.** (2006). 16, 58, 59, 71

[17] **CMS** Collaboration, *Precise Mapping of the Magnetic Field in the CMS Barrel Yoke using Cosmic Rays*, *J. Instrum.* **5** (Oct, 2009) T03021. 37 p. 18, 20, 38

[18] **CMS** Collaboration, *The CMS tracker system project : Technical design report*, . 18

[19] **CMS** Collaboration, *The CMS tracker: addendum to the Technical Design Report*, . 18

[20] **CMS** Collaboration, *The CMS electromagnetic calorimeter project : Technical Design Report*, . 24

[21] **CMS** Collaboration, *The CMS hadron calorimeter project : Technical Design Report*, . 26

[22] **CMS-HCAL** Collaboration, *Design, performance and calibration of the CMS forward calorimeter wedges*, *Eur. Phys. J. C53* **139. doi:10.1140/epjc/s10052-007-0459-4.** (2008). 27

[23] **CMS-HCAL** Collaboration, *Design, performance, and calibration of CMS hadron-barrel calorimeter wedges*, *Eur. Phys. J. C55* (2008). 27

[24] **CMS** Collaboration, *The CMS muon project : Technical Design Report*, . 28

[25] G. L. Bayatyan, M. Della Negra, L. Foá, A. Herv, and A. Petrilli, *CMS computing: Technical Design Report*, . 33

[26] R. Brun and F. Rademakers, *Root - an object oriented data analysis framework*, *Inst. Meth. in Phys. Res. A 389* **81** (1997). 34

[27] **CMS** Collaboration, *Performance of CMS Muon Reconstruction in Cosmic-Ray Events*, *J. Instrum.* **5** (Nov, 2009) T03022 . 47 p. 38

[28] **CMS** Collaboration, *Alignment of the CMS silicon tracker during commissioning with cosmic rays*, *J. Instrum.* **5** (Oct, 2009) T03009. 41 p. 38

[29] **CMS** Collaboration, *Aligning the CMS muon chambers with the muon alignment system during an extended cosmic ray run*, *J. Instrum.* **5** (Nov, 2009) T03019. 35 p. 38

[30] **CMS** Collaboration, *Transverse momentum and pseudorapidity distributions of charged hadrons in pp collisions at $\sqrt{s}$ = 0.9 and 2.36 tev. oai:cds.cern.ch:1237408*, *J. High Energy Phys.* **02** (Feb, 2010) 041. 33 p. 39

[31] A. D. Martin, W. J. Stirling, R. S. Thorne, and G. Watt, *Uncertainties on α_S in global PDF analyses*, `arXiv:0905.3531`. 49, 180

[32] W. Stirling, *Progress in parton distribution functions*, *DIS08, London* (2008). 50

[33] S. Catani *et. al.*, *QCD*, *CERN-TH/2000-131, arXiv:hep-ph/0005025v1* (2000). 50, 56, 180

[34] S. Goy López, *Parton density functions in ElectroWeak processes at the LHC*, *DIS08, London* (2008). 51

[35] J. Alcaraz, *Thoughts on the measurement of the inclusive $w \to \mu\nu$ cross-section in pp collisions at $\sqrt{s} = 10$ tev*, *CMS-IN* (2009). 51

[36] S. Frixione and M. Mangano, "How accurately can we measure the W cross-section?." 51

[37] K. Melnikov and F. Petriello, *FEWZ*, 2006. 54, 133, 145, 203

[38] J. Campbell and R. Ellis, "Monte Carlo for FeMtobarn processes." `http://mcfm.fnal.gov/`. 54

[39] PDF4LHC Working Group, `http://www.hep.ucl.ac.uk/pdf4lhc/PDF4LHCrecom.pdf`. 54, 133, 180

[40] P. Nadolsky *et. al.*, *Implications of CTEQ global analysis for collider observables*, *Phys. Rev.* **D78** (2008) 013004, [`arXiv:0802.0007`]. 54, 133, 180

[41] R. D. Ball *et. al.*, *A first unbiased global NLO determination of parton distributions and their uncertainties*, arXiv:1002.4407. 54, 133, 180

[42] H.-L. Lai *et. al.*, *New parton distributions for collider physics*, *Phys. Rev.* **D82** (2010) 074024, [arXiv:1007.2241]. 54

[43] A. D. Martin, W. J. Stirling, R. S. Thorne, and G. Watt. http://projects.hepforge.org/mstwpdf/. 54, 181

[44] K. Melnikov and F. Petriello, *Electroweak gauge boson production at hadron colliders through O(alpha(s)**2)*, *Phys. Rev.* **D74** (2006) 114017, [hep-ph/0609070]. 54, 180

[45] K. Melnikov and F. Petriello, *The W boson production cross section at the LHC through* $O(\alpha_s^2)$, *Phys. Rev. Lett.* **96** (2006) 231803, [hep-ph/0603182]. 54, 180

[46] CMS Generator Group, https://twiki.cern.ch/twiki/bin/view/CMS/StandardModelCrossSections. 54, 66, 180

[47] M. Dittmar, F. Pauss, and D. Zurcher, *Towards a precise parton luminosity determination at the CERN LHC*, *Phys. Rev.* **D56** (1997) 7284–7290, [hep-ex/9705004]. 56

[48] **CMS** Collaboration, *Measurement of the W-boson charge asymmetry*, *CMS PAS EWK-10-006* (2011). 57

[49] **CMS** Collaboration, *Study of the process* $pp \to WZ \to \ell\ell$ *(*ℓ*= e,* μ*) at CMS*, *CMS PAS EWK-08-003* (2008). 59

[50] **CMS** Collaboration, *Prospects for the first measurement of the WW production cross-section in pp collisions at* $\sqrt{s}$*=10 TeV center of mass energy with the CMS detector*, *CMS PAS EWK-09-002* (2009). 59

[51] **CMS** Collaboration, *First measurement of WW production and search for Higgs boson in pp collisions at* $\sqrt{s}$ *= 7 TeV*, *CMS PAS EWK-10-009* (2011). 59

[52] **CMS** Collaboration, *Measurement of inclusive* $W\gamma$ *and* $Z\gamma$ *cross sections and limits on anomalous trilinear gauge boson couplings at 7 TeV*, *CMS PAS EWK-10-008* (2011). 59

[53] **CMS** Collaboration, *Measurement of Drell-Yan Cross Section (*$d\sigma/dM$*)*, *CMS PAS EWK-10-007* (2011). 59

[54] **CMS** Collaboration, *Measurement of the inclusive $Z \to \tau\tau$ cross section in pp collisions at $\sqrt{s}$ = 7 TeV*, *CMS PAS EWK-10-013* (2011). 59

[55] **CMS** Collaboration, *First measurement of the polarization of W bosons with large transverse momentum in W +Jets events at a pp collider*, *CMS PAS EWK-10-014* (2011). 59

[56] **CMS** Collaboration, *Measurement of the Forward-Backward Asymmetry of Lepton Pairs*, *CMS PAS EWK-10-011* (2011). 59

[57] **GEANT4** Collaboration, S. Agostinelli *et. al.*, *GEANT4: A simulation toolkit*, *Nucl. Instrum. Meth.* **A506** (2003) 250–303. 60

[58] J. Allison *et. al.*, *Geant4 developments and applications*, *IEEE Trans. Nucl. Sci.* **53** (2006) 270. 60

[59] T. Sjostrand, S. Mrenna, and P. Skands, *PYTHIA 6.4 Physics and Manual*, *JHEP* **05** (2006) 026, [hep-ph/0603175]. 60, 65, 96

[60] S. Frixione, P. Nason, and C. Oleari, *Matching NLO QCD computations with Parton Shower simulations: the POWHEG method*, *JHEP* **11** (2007) 070, [arXiv:0709.2092]. 60, 65, 96

[61] S. Alioli, P. Nason, C. Oleari, and E. Re, *NLO vector-boson production matched with shower in POWHEG*, *JHEP* **07** (2008) 060, [arXiv:0805.4802]. 65

[62] P. Nason, *A new method for combining NLO QCD with shower Monte Carlo algorithms*, *JHEP* **11** (2004) 040, [hep-ph/0409146]. 65

[63] VBTF TWiki, Reference MC samples: Reference Monte Carlo Samples. 66

[64] N. Kidonakis, *Higher-order corrections to top-antitop pair and single top quark production*, *Proceedings of the DPF-2009 Conference, Detroit, MI* **arXiv:0909.0037v1 [hep-ph]** (2009). 66

[65] **CMS** Collaboration, *Performance of CMS muon identification in pp collisions at $\sqrt{s} = 7$ TeV*, *CMS PAS* **MUO-2010-002** (2010). 67, 72

[66] W. Adam, B. Mangano, T. Speer, and T. Todorov, *Track reconstruction in the cms tracker*, Tech. Rep. CMS-NOTE-2006-041. CERN-CMS-NOTE-2006-041, CERN, Geneva, Dec, 2006. 68

[67] **CMS** Collaboration, *Measurement of momentum scale and resolution of the CMS detector using low-mass resonances and cosmic ray muons*, *CMS PAS* **TRK-10-004** (2010). 70, 71, 129, 200

[68] **CMS** Collaboration, *Particle-flow commissioning with muons and electrons from J/ψ, and W events at 7 TeV*, *CMS PAS* **PFT-2010-003** (2010). 82

[69] **CMS** Collaboration, *Missing transverse energy performance in minimum-bias and jet events from proton-proton collisions at $\sqrt{s} = 7$ TeV*, *CMS PAS* **JME-2010-004** (2010). 82, 83

[70] **CMS** Collaboration, *Cms MET performance in events containing electroweak bosons from pp collisions at $\sqrt{s}$=7 TeV*, *CMS PAS* **JME-2010-005** (2010). 83

[71] **CMS** Collaboration, *Towards a measurement of the inclusive $W \to \mu\nu$ cross-section in pp collisions at $\sqrt{s}$ = 14 TeV*, *CMS PAS* **EWK-07-002** (2007). 91, 99, 100, 157

[72] **CMS** Collaboration, *Towards a measurement of the inclusive $W \to \mu\nu$ cross-section in pp collisions at $\sqrt{s}$ = 10 TeV*, *CMS PAS* **EWK-09-005** (2009). 91, 157

[73] C. Diez-Pardos *et. al.*, *Establishing the method to measure the single muon efficiency from z events with the first data*, *CMS Note* **2010/233** (2010). 100

[74] M. de Gruttola, *The $Z \to \mu\mu$ decay channel in the CMS experiment at LHC: from cross section measurement with the 2010 7 TeV collision dataset to offline machine luminosity monitor*. PhD thesis, Universit degli Studi di Napoli Federico II, December, 2010. 100, 101

[75] M. de Gruttola and *et al., Determination of the* $Z \to \mu^+\mu^-$ *inclusive cross section with a simultaneous fit of Z yield, muon reconstruction efficiencies and High Level Trigger efficiency with the first 2.9 pb-1 of 7 TeV collision data,* CMS Note **2010/345** *(2010). 101*

[76] C. Battilana, "talk at the CMS L1 DPG meeting." `http://indico.cern.ch/conferenceDisplay.py?confId=108729`. *102*

[77] C. Farrell, "talk at the CMS L1 DPG meeting." `http://indico.cern.ch/conferenceDisplay.py?confId=110505`. *102*

[78] J. Alcaraz, "talk at the CMS L1 DPG meeting." `http://indico.cern.ch/conferenceDisplay.py?confId=110505`. *102*

[79] F. James, MINUIT function minimization and error análisis reference manual, CERN Program Library. *121, 196*

[80] S. Santaolalla et. al.*, Understanding the muon transverse momentum resolution in CMS using $pp \to \mu\mu + x$ events,* CMS AN-2010/105 *(2010). 129, 200*

[81] M. Soares et. al.*, Studies on Missing Transverse Energy for events with muons,* CMS AN-2010/197 *(2010). 129*

[82] C. Balazs, C.P. Yuan, Phys. Rev. D56 (1997) 5558-5583. 133, 142

[83] C. M. Carloni Calame, G. Montagna, O. Nicrosini, and A. Vicini, Precision electroweak calculation of the production of a high transverse-momentum lepton pair at hadron colliders, JHEP **10** *(2007) 109, [*arXiv:0710.1722*]. 133*

[84] C. M. Carloni Calame, G. Montagna, O. Nicrosini, and M. Treccani, Multiple photon corrections to the neutral-current Drell- Yan process, JHEP **05** *(2005) 019, [*hep-ph/0502218*]. 133*

[85] C. M. Carloni Calame, G. Montagna, O. Nicrosini, and A. Vicini, Precision electroweak calculation of the charged current Drell-Yan process, JHEP **12** *(2006) 016, [*hep-ph/0609170*]. 133*

[86] C. M. Carloni Calame, G. Montagna, O. Nicrosini, and M. Treccani, Higher-order QED corrections to W-boson mass determination at hadron colliders, Phys. Rev. **D69** *(2004) 037301, [*hep-ph/0303102*]. 133*

[87] J. Alcaraz et. al.*, Updated Measurements of InclusiveW and Z Cross Sections at 7 TeV,* CMS Note **2010/264** *(2010). 133*

[88] ***CMS*** *Collaboration, Measurement of CMS luminosity,* CMS PAS **EWK-2010-004** *(2010). 134, 135, 136, 146*

[89] N. Adam et. al.*, Absolute calibration of luminosity measurement in CMS,* CMS Analysis Note **2011/093** *(2010). 134, 135, 146*

[90] S. Van der Meer, Calibration of the efective beam height in the ISR, Internal CERN Report **ISR-PO/68-31** *(1968). 134*

[91] ***CMS*** *Collaboration, Measurements of Inclusive W and Z Cross-Sections in pp Collisions at $\sqrt{s}$ = 7 TeV,* Journal of High Energy Physics **2011** *(2011) 1–40. 10.1007/JHEP01(2011)080. 135, 138, 145, 149, 191, 202*

[92] ***CMS*** *Collaboration, Measurement of the W and Z inclusive production cross sections at $\sqrt{s} = 7$ TeV with the CMS experiment at the LHC,* CMS PAS **EWK-2010-002** *(2010). 145*

[93] **UA1** *Collaboration, C. Albajar* et. al.*, Studies of Intermediate Vector Boson Production and Decay in UA1 at the CERN Proton - Antiproton Collider,* Z. Phys. **C44** *(1989) 15–61. 146*

[94] **UA2** *Collaboration, J. Alitti* et. al.*, Measurement of W and Z Production Cross-Sections at the CERN $\bar{p}p$ Collider,* Z. Phys. **C47** *(1990) 11–22. 146*

[95] **CDF II** *Collaboration, D. Acosta* et. al.*, First measurements of inclusive W and Z cross sections from Run II of the Tevatron collider,* Phys. Rev. Lett. **94** *(2005) 091803, [*hep-ex/0406078*]. 146*

[96] ***ATLAS*** *Collaboration, Measurement of the $w \to l\nu$ and $z/\gamma* \to ll$ production cross sections in proton-proton collisions at $\sqrt{s} = 7$ tev with the atlas detector. oai:cds.cern.ch:1299479, . Comments: 38 pages plus author list (57 pages total), 16 figures, 15 tables. 146*